Fall 2009

Separation of endogenous fluorophores in normal and cancer cells

Ye Li
University of Iowa

Recommended Citation

Li, Ye. "Separation of endogenous fluorophores in normal and cancer cells." PhD (Doctor of Philosophy) thesis, University of Iowa, 2009.
http://ir.uiowa.edu/etd/396.

SEPARATION OF ENDOGENOUS FLUOROPHORES IN NORMAL AND CANCER CELLS

by

Ye Li

An Abstract

Of a thesis submitted in partial fulfillment
of the requirements for the Doctor of
Philosophy degree in Chemistry
in the Graduate College of
The University of Iowa

December 2009

Thesis Supervisor: Professor M. Lei Geng

ABSTRACT

In the development of noninvasive optical biopsy, normal tissues can be statistically differentiated from precancerous and cancerous tissues by analyzing their autofluorescence spectra. The observed cancer hallmarks in the spectra are manifestations of biochemical and morphological changes in tissue during cancerous transformation. For detection of colorectal cancers, it has been hypothesized that the major contributors to tissue fluorescence are three endogenous fluorophores – reduced nicotinamide adenine dinucleotide (NADH), flavin adenine dinucleotide (FAD) and collagen. Separating and identifying endogenous fluorophores in cells/tissues using capillary electrophoresis (CE) with laser-induced fluorescence (LIF) detection holds promise as a simple and fast method to analyze fluorophore compositions in tissues during the cancerous transformation.

To this end, we have established the extraction and separation protocols for quantifying endogenous fluorophores in Chinese Hamster Ovary (CHO) cells, human colorectal adenocarcinoma cells (HT-29) and human normal colon cells (FHC). Flavin mononucleotide (FMN), FAD, NADH and nicotinamide adenine dinucleotide phosphate (NADPH) have been identified in the cell extracts by spiking them with standards and quantified by standard addition methods. The influence of cell densities and cell growth stages on fluorophore composition has been closely examined.

Two-dimensional (2D) correlation coefficient mapping of electropherograms of HT-29 and FHC cell extracts reveals that the HT-29 cell extracts with higher cell density can be differentiated from FHC and HT-29 cell extracts with lower cell density, which is also demonstrated by the comparison of peak area ratios of NADH and NADPH. The electropherograms for 2D correlation analysis are pretreated by aligning their prominent peaks to account for peak shifting.

A challenge in biological spectroscopy of cells and tissue is the identification of endogenous components that contribute to the overall complex spectra and the diagnostic signature. We propose 2D generalized correlation of CE-LIF electropherograms and fluorescence spectra in order to resolve the overlapped fluorescence spectra into their individual components.

Separation of the endogenous fluorophores in normal and cancer cells by CE-LIF has provided us insight into fluorophore compositions and tools for classifications of cells. It has also prepared us for extraction and separation of tissues under different physiological conditions to assist cancer diagnosis.

Abstract Approved: __________________________________
Thesis Supervisor

____
Title and Department

____
Date

SEPARATION OF ENDOGENOUS FLUOROPHORES IN NORMAL AND CANCER CELLS

by

Ye Li

A thesis submitted in partial fulfillment
of the requirements for the Doctor of
Philosophy degree in Chemistry
in the Graduate College of
The University of Iowa

December 2009

Thesis Supervisor: Professor M. Lei Geng

Graduate College
The University of Iowa
Iowa City, Iowa

CERTIFICATE OF APPROVAL

PH.D. THESIS

This is to certify that the Ph.D. thesis of

Ye Li

has been approved by the Examining Committee
for the thesis requirement for the Doctor of Philosophy
degree in Chemistry at the December 2009 graduation.

Thesis Committee: ___________________________________
M. Lei Geng, Thesis Supervisor

____
Gary W. Small

____
Amnon Kohen

____
Leonard R. MacGillivray

____
Alan R. Kay

To my grandfather, my parents and my husband.

Life is not easy for any of us. But what of that? We must have perseverance and above all confidence in ourselves. We must believe that we are gifted for something and that this thing must be attained.

Marie Sklodowska Curie

ACKNOWLEDGMENTS

I would like to thank Dr. M. Lei Geng for his unconditional support throughout my graduate career. Dr. Geng inspires me with his passion, guides me with his patience and grants me the freedom to explore science. I treasure the five and a half years of being a Geng Research Group member as my most valuable learning experience. I am also grateful to Dr. Gary Small, Dr. Amnon Kohen, Dr. Leonard MacGillivray, Dr. Alan Kay, Dr. Claudio Margulis and Dr. Don Cannon for their input to my project and support during my graduate career.

I deeply appreciate all the help and friendship from the past and present Geng group members: Gufeng Wang, Jinfu Zhao, Zhenming Zhong, Edward Crowell, Alice Eck, Anamika Mubayi, Yi Gao, Yulia Skvortsova, Chester Duda, Mark Brewer, Rui Zhang, Reygan Freeney, Claudiu Brumaru and Jamesha Wills. Special thanks to Piyanka De Silva and Lu Xi who started the separation project and Carrie Fisk for her input. I have learned a lot from everyone and their encouragement is irreplaceable.

Thanks to Dr. Jim Jung-Ching Lin and Alissa van Winkle for helping us to establish the cell culture facility in Geng lab. Thanks to the Center for Biocatalysis and Bioprocessing for awarding me the graduate fellowship from 2006 to 2009.

I wish to thank my aunt, Guoqing Lan, who lost her life to colon cancer in 2007, for encouraging me to go further with cancer diagnosis research. May she rest in peace.

Finally, I would like to thank my grandfather, Menglin Li, my father, Xikong Li, and my mother, Yingping Wu, who are living in China, half an earth away from their single child, me. I owe them a lot for not being around for them. They may never be able to read this dissertation but they must see that their love to me has crystallized in this work. I am deeply grateful to my beloved husband, Dr. Jianquan Yang. His unconditional support and endless love have been carrying me through all the happiness and difficulties in life. We have come this far and will go farther only because we are together.

TABLE OF CONTENTS

LIST OF TABLES

LIST OF FIGURES

CHAPTER 1

INTRODUCTION

Cancer, the second most common life-threatening disease in the US, is a group of diseases characterized by uncontrollable growth of abnormal cells and their invasions of other organs/tissues [1]. Some basic concepts about cancer are summarized in Figure 1.1 [2]. The survival rate from cancer would be significantly improved if the disease could be identified at its earlier stage and treated appropriately. For example, as the third most common cancer, colorectal cancer incidence rates have been decreasing with the increase in screening and removing of colorectal polyps before they further develop into cancer [1, 3]. The five-year relative survival rate is as high as 90% when the disease is diagnosed at the localized stage while the rate is as low as 11% when it is diagnosed at the distant stage (Figure 1.2) [3]. However, symptoms of cancer usually appear as certain types of functional failures, which usually happen at later stages of cancer. Thus, it has been a long-standing challenge to diagnose cancer at its early stage.

Testing in individuals with no symptoms, but at risk, for a particular disease is defined as screening. Screenings for colorectal, breast, and uterine cervical cancer have been proved to reduce the mortality rates of these cancers [4]. Screening for cervical and colorectal cancers can even identify the precancerous abnormalities. Therefore, the early detection for these cancers has always been a research area of intense interest. For example, besides the six recommended screening methods (flexible sigmoidoscopy, colonoscopy, barium enema with air contrast, computed tomographic colonography, fecal occult blood test, and stool DNA [4]), optical biopsy has also been extensively explored as an early detection method for colon cancer and has the potential to further increase the sensitivity and specificity of the screening [5-8].

With the noninvasive optical biopsy technologies, the nondiseased (normal and hyperplastic) and diseased (adenomatous and adenocarcenomatous) colonic tissues can be statistically differentiated by analysis of their autofluorescence spectra [6, 9-15]. Based on spectral analysis, it is believed that the observed tissue fluorescence arises from the superposition of fluorescence produced by biological fluorophores such as collagen, reduced nicotinamide adenine dinucleotide (NADH) and flavin adenine dinucleotide (FAD), which exist in the mucosa and submucosa layers of colonic tissue. However, it is not clear whether the observed spectral differences are due to changes in molecular composition of tissue fluorophores specific to dysplasia or simply from morphological differences between dysplastic and normal tissues. Knowledge about tissue composition of these fluorophores at different tissue stages will provide valuable insight into this issue. To this end, separation and identification of endogenous cellular fluorophores, FAD, NADH and collagen by capillary zone electrophoresis (CZE) with laser-induced fluorescence (LIF) detection holds great promise as a simple and fast method to analyze fluorophore composition in tissues at different physiological stages during the cancerous transformation.

This introduction will provide a brief overview of optical biopsy and its application in cancer diagnosis, extraction and separation of endogenous fluorophores, and capillary electrophoresis and its application to biological samples.

1.1 Optical biopsy in cancer diagnosis

As a clinical method providing the “final” diagnosis of cancer, biopsy usually involves the removal of a sample tissue and the histological classification of the tissue. Inevitably, biopsy is invasive and highly dependent on the pathologist’s experience. Optical biopsy, as a complimentary method to biopsy, offers a noninvasive and quantitative possibility for cancer diagnosis. This technique, which employs tissue spectroscopy and spectroscopic imaging to classify tissues at different physiological stages, has the potential to improve the safety, sensitivity and specificity of cancer diagnosis [5].

In order to understand how the morphological and biochemical changes could be reflected by the changes of tissue optical properties, the biopsy pathology and the cancer biochemistry are briefly discussed and followed by the introduction to cancer diagnosis with optical biopsy.

1.1.1 Biopsy pathology of cancer

Biopsy offers the definitive diagnosis for many types of cancer. Tissue/organ samples can be obtained by endoscopy, punch biopsy, fine-needle aspiration biopsy, or open biopsy, depending on different locations and conditions of various lesions [16]. For example, biopsies of mucosal lesions like colorectal dysplasia are usually obtained by colorectal endoscopy. Since the colorectal cancer is the primary focus of this dissertation, the biopsy pathology of colorectal dysplasia is briefly reviewed in this section.

In order to examine colon tissue samples microscopically, the process of biopsy pathology for colon tissue usually includes obtaining the sample by endoscopic biopsy, fixing the tissue sample in formaldehyde, embedding it in paraffin, slicing it into sections, staining it with dyes, and eventually observing the tissue sections under the microscope. For diagnosing cancer, the tissue sections are evaluated by pattern recognition based on tissue structural changes, cell size and shape changes, cell reproduction rate changes and tissue necrotic changes [8].

As shown in Figures 1.3(a) and (b), the normal mucosa, normally 500-1000 µm thick is composed of crypts. Crypts are parallel-sided, straight, narrow, unbranched tubes which are formed by epithelium cells and separated from each other by a thin rim of lamina propria. The crypts extend into the muscularis mucosae, which consists of elastic fibers and an inner circular and outerlongitudinal layer of smooth muscle. Under the mucosa layer, the submucosa (Figure 1.3 (c)), normally, consists of areolar connective tissue with loosely arranged collagen fibers and scanty elastic fibers [17]. The muscularis propria is under the submucosa.

Figures 1.4 and 1.5 illustrate the progression of malignancy in the colorectal tissue. From hyperplasia (Figure 1.4(a)) to dysplasia (Figures 1.4(b) and (c)), and then to adenocarcinoma (Figure 1.5), the most indicative changes in the tissue section are the enlargement of the cell nuclei and the disorganization of the crypts structure. At the later stage of adenocarcinoma (Figure 1.5(c)), the crypt structure is poorly differentiated and the tissue structure barely assembles the normal epithelium structure [17]. Figure 1.6 depicts how the abnormal proliferation of colorectal epithelial cells leads to the development of neoplasia [18]. Briefly, in the normal tissue, the cell proliferation is controlled in the proliferative zone and the transitional zone at the bottom of the crypt close to the lamina propria mucosae. Once the cells become abnormal, they undergo mitosis even in the mature cell zone thus causing the accumulation of cells at the top of the crypt. Then, the accumulated cells result in the branches of crypts. Eventually, the tissue becomes neoplastic.

1.1.2 Biochemistry of cancer

In the 1920’s, Otto Warburg, one of the pioneers in cancer biochemistry research, discovered high glucose consumption in tumors and the Warburg effect [19]. The Warburg effect refers to the cancer cells’ increased dependency on glycolysis to obtain energy, even in the presence of high oxygen concentration [20]. From the beginning, the abnormal metabolism of cancer has been an important focus of cancer biochemistry research [21-22]. With the technology development, the genetic basis of cancer has also become an important research focus in cancer biochemistry [23-24]. Among the two focuses, the cancer metabolism research will be briefly discussed in this section since the genetic basis of cancer is not the focus of this dissertation.

Gatenby and Gillies proposed that the upregulation of glycolysis confers a powerful growth advantage for pre-malignant lesions to grow progressively further from their blood supply and prompts the revolution of the cancer cells to become resistant to acidic microenvironments [25]. To explain how cancer cells show the increased glycolysis flux, various mechanisms have been suggested: (1) the increase of the glycolytic enzymes and glucose transporters isoform expression, such as hexokinase(HK), phosphofructokinase type I and Type II (PFK-1 and PFK-2), and glucose transporters (GLUT); (2) the decrease of mitochondrial oxidative enzymes and transporters expression; (3) lowering of the amount of mitochondria per cell; (4) inhibition of oxidative phosphorylation by glycolysis activation; (5) increase of natural inhibitor protein (IF1) of the mitochondrial ATP synthase; and (6) hightened sensitivity of mitochondrial DNA to oxidative stress [22]. Not all the six mechanisms apply for a particular type of tumor cell. In addition, for some types of cancer cells, glycolysis is not the main ATP supplier. For example, in human lung carcinoma, the oxidative phosphorylation offers 95% of the ATP needed [26].

The high consumption and metabolism of glucose produces ATP, reduced nicotinamide adenine dinucleotide(NADH), reduced nicotinamide adenine dinucleotide phosphate(NADPH), and acids[27]. For example, in colorectal cancers, the Pentose Phosphate Pathway is upregulated resulting in increased glycolysis. As shown in Figure 1.7, the generation of cofactor NADPH as the by-product is also increased [28]. The NADPH can be further used for reducing glutathione and synthesizing fatty acids [29]. Comparatively, the Embden–Meyerhoff Pathway (EMP) is not upregulated thus the by-product NADH is not increased. NADH can be used to reduce pyruvate to lactate or assist oxidative phosphorylation [29].

From the physiological point of view, “six hallmarks” have been suggested for recognition of cancer, including self-sufficiency in growth signals, insensitivity to growth-inhibitory signals, evasion of programmed cell death, limitless replicative potential, sustained angiogenesis, and tissue invasion and metastasis [30]. These hallmarks are essentially caused by genetic alteration in cancer cells. The abnormal metabolism of cancer cell is not considered as a “hallmark” because the progress in oncogenesis apparently drives the belief that cancer is a genetic disease while the metabolic changes are only the consequences [31]. However, some recent developments show that the metabolic changes and genetic changes are connected and both contribute to cancer development [32-33]. Therefore, the complete understanding of Warsburg effect and related cancer metabolism will still be crucial in cancer research. Ultimately, this understanding will be connected to the detection and treatment of cancer so that humans can conquer this life-threatening disease.

1.1.3 Optical biopsy in cancer diagnosis

As discussed in section 1.1.2, excisional biopsy is currently the "gold standard" for cancer diagnosis in clinical practice. However, the invasive biopsy has many limitations [8].

- Invading into lesions leads to risk of complications, limits of tissue sample amount, sampling error (not representative enough), and biochemical changes after excision.
- Preparing tissue samples is time, cost and manpower intensive.
- Evaluating tissue samples based on pathologists' experiences is only qualitative and relatively arbitrary.

Therefore, many non-invasive technologies have been developed for cancer diagnosis. For example, X-rays (plain film and computed tomography (CT)), magnetic resonance imaging (MRI), ultrasound (US), single-photon emission computed tomography (SPECT), or positron emission tomography (PET) are clinically available [34-35]. Among them, CT, MRI, SPECT, and PET can offer three dimensional images but only PET and MRI can be used for molecular level imaging [34, 36]. Besides these traditional imaging techniques, optical imaging shows great potential for cancer diagnosis and possibility for molecular imaging [5, 34, 36-37]. The relative sensitivity and potential directions of application of the above techniques are shown in Figure 1.8 [38]. As summarized by Weissleder and Pittet in 2008 [39], optical imaging systems will allow doctors to visualize the expression and activity of particular molecules, cells and biological processes thus bringing deeper understanding of tumor cells and their responses to treatment. Optical imaging is one of the important techniques in optical biopsy.

Optical biopsy employs the analysis of absorbed, scattered and reemitted light from an optically excited tissue to reveal chemical and physiological changes undergoing in the tissue while diseases progressing [5]. Combined with fiber optics, this minimally invasive/noninvasive technique is safer, cost and time efficient, and potentially offers high sensitivity and specificity for tissue classification because [8]:

1. All parts of the body can be accessed remotely through catheters, needles, cannulas or endoscopes, which allow *in situ* data collection and avoid complications and sampling errors caused by traditional biopsy.
2. Data can be collected in seconds to allow the real-time feedback for a particular tissue site.
3. Biochemical changes of tissue, which sometimes happen much earlier than morphological changes, can be reflected in signals to assist early detection of disease.
4. Possibilities of making quantitative classification of disease stages and phases ensures the objectivity of diagnosis when compared to the judgment based on experience only in traditional biopsy pathology.

These advantages make the optical biopsy an excellent choice for monitoring these optical features to identify the biochemical and morphological changes in tissue, and eventually determine the physiological conditions of the tissue.

Various spectroscopic techniques have been applied for cancer diagnosis [6-8], for example, fluorescence spectroscopy [6-7, 9-15, 40-53], optical coherence tomography [54-56], photon migration spectroscopy [57], light scattering spectroscopy [58-59], reflectance spectroscopy [60] and Raman spectroscopy [61-62]. Recently, fluorescence endoscopic imaging, confocal laser endomicroscopy [63-65] and multiphoton excitation microscopy [66] have also been used for cancer diagnosis and shown great potential in the functional and molecular imaging of tissue.

Among these techniques, fluorescence spectroscopy and imaging, especially using the endogenous fluorescence, have been extensively studied for the detection of neoplasia [10-11, 40-45, 48-49, 67]. Fluorescence spectroscopy in the ultraviolet and visible spectral regions has proved to be effective in colorectal cancer diagnosis as early as the 1990's [10-11, 50]. To address the biological and experimental variation in the spectral information, mathematical algorithms have been developed and optimized to classify tissues according to their respective physiological conditions [9-15, 50-53], i.e., the nondiseased (normal and hyperplastic) and diseased (adenomatous and adenocarcenomatous) colonic tissues can be statistically differentiated by analysis of their autofluorescence spectra.

Many types of endogenous fluorophores exist in tissue, such as amino acids, structural proteins, enzymes, coenzymes, vitamins, lipids and porphyrins [45]. Most of these endogenous fluorophores at the excitation wavelength range between 250 and 450 nm are summarized by Ramanujam, N. as shown in Table 1.1. Under the UV-Vis excitation wavelength used in tissue autofluorescence spectroscopy, the endogenous fluorophores making the major contributions to tissue spectra are intracellular small molecules, such as nicotinamides, flavins and vitamins, and extracellular matrices, such as collagen or elastin. This attribution is based on the statistical analysis of the tissue fluorescence spectra [6, 9, 47]. For example, Table 1.2 shows the result of statistical decomposing of tissue spectra at different physiological conditions performed by Schomacker et al. [11]. Figure 1.9 shows the wavelength-wavelength correlation coefficient mapping calculated by Crowell et al., which indicates that the contribution from FAD, NADH, collagen and hemoglobin (negative contribution) can be attributed to the different wavelength range of the spectra.

In fact, tissue fluorescence can depend on the concentration and distribution of tissue fluorophores. Also, the biochemical environment of fluorophores may change the fluorophores' quantum yield and lifetime. The absorption and scattering of non-fluorescent absorbers and scatters within the different sub-layers of the tissue may also alter the tissue fluorescence. With the development of dysplasia, morphological changes will alter the fluorophore distribution and their environment thus altering the fluorescence. Therefore, separation of tissue fluorophores will assist differentiation of the tissue spectra changes due to the biochemical changes from those changes due to the morphological changes. This information will further our understanding on the development of cancer.

1.2 Separation of endogenous fluorophores

Spectroscopy and imaging methods based on endogenous fluorophores have been widely used for cancer diagnosis research. Among these fluorophores, two types of cofactors, nicotinamides and flavins, make the major contribution to the intracellular fluorescence under UV excitations. In fact, besides being used in cancer diagnosis research, fluorescent spectroscopy and imaging of these two types of molecules have also been used for research on metabolism, such as redox fluorometry and redox confocal imaging [68-69]. For the cofactors like nicotinamides and flavins, the ratio of their oxidized form and reduced form usually represents the metabolism status of the cell, since these cofactors carry the electron transport in the energy conversion process through their oxidation/reduction [29]. Because of these important roles, separation of these cofactors has been extensively studied [70-110].

The structures of endogenous fluorophores flavin (including riboflavin (RF), flavin mononucleotides (FMN) and FAD) and nicotinamides (including NADH and

NADPH) are shown in Figure 1.10. Only the oxidized forms of flavins, not the reduced forms, are fluorescent while only the reduced forms of nicotinamides are fluorescent. The absorption and fluorescence emission spectra of RF, FMN, FAD, NADH and NADPH are shown in Figure 1.11.

The oxidized forms of RF, FMN and FAD have the maxima of excitation at ~450 nm and the maxima of emission at ~525 nm. For FAD, the flavin fluorescence can be quenched by the adenine moiety by forming intramolecular complexes or colliding between molecules [111-113]. Once bound to flavoproteins, FAD shows decreased fluorescence [111, 114]. FAD shows strongest fluorescence intensity at pH 2.7-2.8 [113]. However, in diluted acid, the ester bond of flavin nucleotides tends to be hydrolyzed [115]. RF, FMN and FAD are all sensitive to light of wavelength shorter than 600 nm. The photochemical degradation products are lumiflavin and lumichrome. In neutral solution, FAD forms intramolecular complex thus more stable than RF and FMN while it does not form such complex in alkaline or organic solvent [115].

The reduced forms of NADH and NADPH have the maxima of excitation at ~340 nm and emission at ~460 nm. The oxidized form NAD^+ and $NADP^+$ are not fluorescent. The fluorescence of the reduced nicotinamide ring can also be quenched by the adenine moiety by collision or stacking just as in FAD [111]. The fluorescence of NADH can increase or decrease as binding to the various types of protein.

Because of the nucleotide moiety, FAD and NAD(P)H are often discussed in the separation of nucleotides [70-71, 95-97]. Also, since cofactor is a part of metabolism, they are discussed in the development of metabolomics. For example, Liquid Chromatography with Mass Spectrometry detection (LC-MS) and Capillary Electrophoresis with Mass Spectrometry detection (CE-MS) have been intensively studied to approach the ultimate goal—the identification and quantification of all metabolites in a given system [116-120]. Between the two types of methods, Capillary Electrophoresis (CE) separation usually requires a smaller sample size and is more suitable for ionic and highly hydrophilic molecules than Liquid Chromatography (LC) [121]. Compared to the "global view" of the metabolomics, this dissertation focuses on the endogenous fluorophores via laser-induced fluorescence detection to offer direct comparison with optical biopsy results. Therefore, this section will discuss the separation of flavins and nicotinamides as well as simultaneous separation of both molecules.

Since flavins are important cofactors, separation and purification of flavins are crucial for biochemical research on enzyme mechanisms. Between the 1930's and the 1970's, paper electrophoresis [73-74] and paper chromatography [75] were used for the separation of flavins, including FAD, FMN, RF and other derivatives from microorganisms such as yeast and bacteria. Since the 1980's, High Performance Liquid Chromatography (HPLC) [76-78, 88-89] and CE [80-87, 90, 104] have been widely used for separation of flavins and its derivatives. In recent years, CE separations of RF, FMN and FAD were performed by dynamic pH junction sweeping CE [82, 104], microchip CE [86, 90], and CZE [81, 83-85, 87], all with LIF detection. CE-LIF (excitation at 488 nm) was also used to determine riboflavin vitamers in human plasma [109] and other biological tissue samples [81].

As important cofactors closely related to energy metabolism, nicotinamide nucleotides are also separated by LC [91-94, 99-100] and CE [98, 101] for various purposes. They are also often identified as components of metabolites separated from biological extracts with CE. For example, Markuszewski determined the pyridine and adenine nucleotide concentrations in *Bacillus subtilis* cell extracts by sweeping borate complexation CE with UV detection [105] . Casey determined 18 metabolites from rats' heart extracts in a single CE run with UV detection at 200 nm [108]. In particular, NADH was identified in the electropherogram of ethanolic extraction. More recently, a two-dimensional separation system coupling capillary liquid chromatography to CE has been used for the analysis of *Bacillus subtilis* and *Escherichia coli* metabolites [106-107] although the nicotinamide nucleotides were not identified in the extracts. Soga et al.

successfully identified NADH, NAD^+, NADPH, $NADP^+$ and 24 other metabolites from *Bacillus subtilis* JH642 cell extracts [122]. For tissue extracts, Dillon and Sears measured the metabolites in rabbit bladder extracts by CE with UV detection at 195 nm and identified NAD and NADH [97].

The stability of nicotinamide cofactors has been a challenge in separation of NADH and NADPH. Both compounds are sensitive to the pH, ionic strength and nature of the buffer used to dissolve them [102-103, 123-132]. Generally speaking, the reduced form of nicotinamides, which gives fluorescence, is more stable at higher pH around 9-11 [127]. Also, the decomposition of the reduced factors can be caused by the acetate or phosphate buffer when the concentration is higher than 100 mM [103, 123, 128, 130-132].

Due to the different pH preferences of oxidized flavins and reduced nicotinamide nucleotides, simultaneously separating and detecting both of them with fluorescence detection from biological sample has been a challenge. Gostkowski developed a method to separate FAD, NADH and serotonin by multiphoton-excitation fluorescence detection in CE [133]. The report demonstrated excellent mass detection sensitivity through optimization of the multiphoton-excitation LIF detector, while not emphasizing separation aspects. Also, the FAD and NADH were not identified simultaneously from a biological sample. To the best of our knowledge, the simultaneous identification of flavins, NADH and NADPH in cell extracts was first demonstrated by Wise and Shear [98, 134-135] from immortalized SCN 2.2, RN33B, NG108-15 cell extracts and neuronal extracts using CE with multiphoton-excited fluorescence. In this thesis, we present a detailed study of separating endogenous fluorophores by CZE with single photon-excitation fluorescence detection, which is instrumentally simpler and readily available with CE instruments. We will also explore the separation of normal and cancer cell extracts with this method to provide guidance to optical biopsy.

1.3 Capillary electrophoresis and its application on metabolites and small biomolecules

"Electrophoresis" as a term was first used by Michaelis in 1909 for separation of proteins using their isoelectric points [136]. Half a century later, Hjertén published the pioneering work for running electrophoresis in open tubes [137]. In the late 1970's and 1980's, capillary electrophoresis (CE) started to show the potential for providing high resolution in the separation of analytes ranging from small molecules to macromolecules such as proteins and biopolymers [138-140]. After that, capillary coating and surface modifications, micellar electrokinetic chromatography (MEKC), new detectors like laser induced fluorescence (LIF) and mass spectrometry (MS), sample processing prior to CE, new separation media like gels or ionic liquids, microfluidic devices and other technological developments have significantly widened the application of CE in biological samples [141-144]. In this section, the CE principles and recent developments in the application of CE on biological samples, especially metabolites and small biomolecules, will be introduced.

1.3.1 Capillary Electrophoresis

Capillary electrophoresis (CE) is a simple but powerful separation technique. The instrumentation for CE consists of a high voltage power supply with two electrodes, a capillary, inlet and outlet buffer reservoirs, and a detector (Figure 1.12). The capillary is usually a polyimide coated fused silica capillary. The separation process of capillary zone electrophoresis (CZE) includes the following steps. First, the buffer reservoirs and the capillary are filled with buffer. Next, a small plug of sample is introduced into the capillary using pressure or electric fields. When the high voltage is applied across the capillary through the buffer reservoirs, the charged molecules from the sample are separated according to their size-to-charge ratio. Ultimately, the molecules will be detected at the window or at the end of the capillary. Signals corresponding to different analytes from the detector will be recorded as peaks versus migration time on the electropherogram. Nowadays, this process has been highly automated. Various detectors have been coupled with CE, including ultraviolet absorbance (UV), fluorescence, mass spectrometry (MS), amperometric, conductivity, radiometric, Raman-based, and refractive-index detectors etc. [145-146].

The advantage of performing electrophoresis in a capillary is mainly the fast dissipation of Joule heat generated as a result of the electric current passing through the electrophoresis buffer [137, 140]. The large surface-area-to-volume ratio and the coolant circulating around the capillary ensure the efficiency of Joule heat removal thus allowing CE to be run with a very high electrical field (usually up to 30 kV). The low Joule heating minimizes natural convection caused by temperature gradients, reduces band dispersion, and avoids the degradation of the analytes or buffer.

In CZE, the combination of electroosmotic flow (EOF) and different electrophoretic mobilities of analytes determines the apparent mobilities of analytes. As shown in Figure 1.13, on the surface of silica capillary, the silanol groups are ionized and negatively charged when the buffer pH is above ~3. The cations in the buffer are attracted tightly by the SiO^- layer and form a layer of cations on the capillary wall called the stern layer. The positive charge of the stern layer decreases exponentially as the distance from the wall increases. Then, a diffused layer of cations loosely forms as the mobile layer. When the electric field is applied, the cations in the mobile layer are moved towards the negative electrode (cathode) and drag the water molecules around them together. Thus, we can observe the electroosmotic flow towards the cathode [145].

Due to the exponential decrease of charges of the stern layer, there is a zeta potential, ζ, which can be expressed as

$$\zeta = \frac{4\pi\delta\sigma}{\varepsilon} \qquad [1.1]$$

where δ is the thickness of the diffuse double layer, σ is the charge density on the silica surface and ε is the dielectric constant of the buffer. The value of δ is usually inversely proportional to the square root of the buffer concentration. The electroosmotic mobility and the electroosmotic flow velocity can be calculated by equations 1.2 and 1.3, respectively.

$$\mu_{EOF} = \frac{\varepsilon\zeta}{4\pi\eta} \qquad [1.2]$$

$$v_{EOF} = \mu_{EOF} E = \frac{\delta\sigma E}{\eta} \qquad [1.3]$$

Here, η is the viscosity of the separation medium. An increase in temperature usually leads to a decrease of the medium viscosity thus accelerating the EOF.

When the electric field is applied, each analyte in the capillary shows its own electrophoretic mobility, which is determined by its charge-to-size ratio. The electrophoretic mobility (μ_{ep}) can be calculated by equation 1.4.

$$\mu_{ep} = \frac{q}{6\pi\eta r} \qquad [1.4]$$

In equation 1.4, q is the charge of the analyte, η is the buffer viscosity, and r is the radius of the analyte molecule. Besides the charge-to-size ratio, the electrophoretic mobility also depends on the viscosity of the buffer. Cations have positive μ_{ep} thus moving towards the negative electrode (cathode) while anions have negative μ_{ep} thus moving towards the positive electrode (anode). Neutral molecules have μ_{ep} as 0.

The apparent mobility of an analyte in the capillary depends on the combination of electroosmotic flow (μ_{EOF}) and the electrophoretic mobility (μ_{ep}):

$$\mu_{app} = \mu_{EOF} + \mu_{ep} \qquad [1.5]$$

The apparent velocity of the analyte can be calculated by,

$$v_{app} = \mu_{app} E \qquad [1.6]$$

where E is the electric field strength. Since the μ_{EOF} is larger than the electrophoretic mobilities of analytes when the buffer pH and concentration are appropriate, cations, neutral molecules, and anions all move towards the cathode at different velocities thus being detected at different migration times by the detector at the window. The migration time can be calculated by

$$t = \frac{L_d}{v_{app}} = \frac{L_d}{\mu_{app} E} = \frac{L_d L_t}{\mu_{app} V} \qquad [1.7]$$

In equation 1.7, L_t is the total length of the capillary, L_d is the effective length (the distance from the origin to the detector window), and V is the high voltage applied.

When the electric field increases, the apparent velocity is increased thus reducing the migration time. However, the high voltage applied to the system cannot be too high to generate more Joule heat than can be dissipated instantaneously. Otherwise, it would eventually lead to band broadening and irreproducibility of migration times.

The nature, pH and concentration of the running buffer closely relate to the charge density of the silica surface. When the pH is lower than 2, there are few negatively charged sites on the capillary surface thus no EOF flow is generated. When the pH is higher, there are more negative charges on the surface, thus corresponding to stronger zeta potential and EOF. In practice, it is crucial that the running buffer has sufficient capacity to form a constant EOF flow during separation. Also, preconditioning of the capillary before separation ensures the homogeneity of the capillary surface and the constant EOF. In addition, interaction between analytes and the running buffer has to be taken into account when choosing the running buffer for a specific separation task.

Because the driving force of the electroosmotic flow is the electric field rather than the pressure and the capillary diameter is much larger than the size of the stern layer, the profile of the electroosmotic flow is flat. Compared to the parabolic velocity profile of the pressure-driven flow in HPLC, the plug-like flat velocity profile in CE significantly reduces the peak dispersion. As estimated by Oda et al., for a small molecule, the injection plug width is mostly the largest contributor to the band broadening in CE separation [145] . Therefore, CE can give comparatively narrower peaks than other separation techniques, which is one of the advantages for applying CE to the separation of complicated biological samples.

Assuming the peaks can be fitted by a Gaussian curve and the variance only comes from the diffusion along the migration pathway, the variance of the peak is

$$\sigma = \sqrt{2Dt} \tag{1.8}$$

where D is the diffusion constant and t is the migration time. By substituting equation 1.4 into equation 1.8, we can obtain

$$\sigma = \sqrt{\frac{2DL_d}{\mu_{app}E}} \tag{1.9}$$

Also, to achieve the baseline separation between two adjacent Gaussian peaks ($\sigma_1 = \sigma_2$), the distance between the two peak maxima (Δx) should be equal to 4σ. That is to say, the resolution R can be calculated by equation 1.10.

$$R = \frac{\Delta x}{4\sigma} = \frac{(\Delta\mu_{app}E)t}{4\sqrt{2D_{average}t}} \tag{1.10}$$

Here, $\Delta\mu_{app}$ is the difference between the apparent mobility of the two analytes and the $D_{average}$ is the average diffusion constant of the two analytes. The efficiency of CE can be quantified by the number of theoretical plate N,

$$N = \frac{(\mu_{average}E)^2 t^2}{2Dt} \tag{1.11}$$

where $\mu_{average}$ is the average mobility of the two analytes. The resolution R and plate number N are related by

$$R = \frac{\Delta\mu_{app}}{4\mu_{average}} N^{1/2} \tag{1.12}$$

When R=1,

$$N = 16(\frac{\mu_{average}}{\Delta\mu_{app}})^2 \quad [1.13]$$

Although we can use the plate number N to express the efficiency of CE, N does not possess the physical meaning as the partition equilibrium constant between two phases as in chromatography. The separation in CE depends on the relative mobility of the components, which is a function of their charge-to-size ratio.

1.3.2 CE application on metabolites and small molecules

Since CE is a fast, efficient, easy-to-automated technique requiring very small sample amounts, it has been widely used to separate biological molecules, including nucleic acids, peptides, proteins, lipids, carbohydrates, metabolites and other small molecules [141, 144]. In fact, it has become one of the powerful tools for proteomics [147-150], metabolomics [118, 120] and biomarker discovery [151-153]. Besides these small molecules, CE is also applied for separation of larger biological assemblies like inorganic and polymeric particles, colloidal suspension, cells, organelles, microorganisms and viruses [142-143, 154].

Since metabolites and small molecules involved in metabolism are often charged and hydrophilic, CE is an efficient and flexible tool to separate these molecules. The various detectors available for CE (LIF, MS, and electrochemical detectors etc.) offer good sensitivity and selectivity to research on metabolites, although identification of the metabolites with very diverse structures is still a challenge. The cofactors to the interest of this dissertation often appear in the separation of metabolites from cell/tissue extracts since these cofactors are closely related to metabolism. Thus, the CE separation of metabolites and related small molecules are briefly reviewed here.

Hundreds of metabolic intermediates can be found in the cell, for example, amino acids, amines and their derivatives, carboxylic acids, alcohols, aldehydes, phosphate esters, nucleic acids, carbohydrates, lipids, steroids, fatty acids, vitamins, coenzymes, and some inorganic ions [110]. To investigate these compounds and the dynamics about them, there are mainly five classes of approaches towards their analysis [120].

- Metabolite target analysis – a few specific compounds are targeted.
- Metabolic profiling – a group of metabolites based on a class of compounds or their association with a specific pathway is targeted.
- Metabolic fingerprinting – samples are classified through pattern recognition based on global high throughput, and rapid analysis.
- Metabolomics –all the metabolites are identified and quantified in a biological system without bias.
- Metabonomics – the dynamic multiparametric metabolic response of living systems to physiological stimuli or genetic modification is quantitatively measured.

CE has been applied to all five classes of approaches. The technique of CE-MS offers the high resolving power and peak capacity which metabolomics and metabonomics require. To maximize the coverage of various types of metabolites, Soga and his colleagues designed an approach to divide all metabolites into subgroups and use different conditions to separate each set of metabolites. The results were then combined to show the global view [118]. The first group is composed of amino acids, amines and nucleosides, which can be separated as cations using a 25 mM pH ~2.6 formic acid as the background electrolyte [155]. The second group is composed of carboxylic acids, phosphorylated carboxylic acids, phosphorylated saccharides, nucleotides, and nicotinamide and flavin adenine coenzymes. This group can be separated as anions using a cationic polymer-coated capillary and an electrolyte system consisting of 50 mM ammonium acetate at pH 9.0 [122]. For those multivalent anions, a pressure-assist CE-ESI-MS can be used to provide a neutral capillary surface to avoid anions absorbing onto the wall. With the combination of the above conditions and CE-TOF-MS, 1692 peaks of metabolites can be separated with three runs, which illustrates the high resolving power and peak capacity of the method very well [156]. However, among the 1692 peaks, only 150 peaks were identified due to a lack of standards and limited mass spectral libraries.

For metabolic fingerprinting, improving the reproducibility of CE is important so that pattern recognition is possible when comparing the results from two samples. The sensitivity and identification of peaks are not as crucial as they are for other classes of metabolites analysis. Therefore, using sample pretreatment to concentrate samples and minimize analyte-surface interaction, as well as using chemometrics to make meaningful comparisons, are all highly focused research areas [120, 157]. For example, denoising and baseline correction, alignment of electropherograms and normalization of electropherograms are all useful chemometric data pretreatment methods [158-160].

Metabolic profiling is usually aimed at revealing a biochemical process or a specific pathway with the separation results thus demanding better sensitivity and identification of peaks. For example, dynamic pH junction, sweeping, and dynamic pH junction-sweeping are all classic ways to perform online concentration of samples to increase sensitivity by thousands of folds [161-165]. With the dynamic pH junction sweeping method, the limits of detection for FAD and FMN can be as low as ~4.0×10^{-12}M with CE-LIF using a pH 8.5 borate buffer and 100 mM SDS as the background electrolyte [82]. Peak identification for metabolites profiling is also moving forward. Edwards, et al. identified about 40% of peaks detected (47 out of 118) from *E.coli* extracts by a sheathless negative mode CE-MS [166]. In addition to good sensitivity and peak identification, designing the experiment to focus on the interested pathway is also very important for revealing biochemical processes with separation. For instance, Tanaka et al. suggested that the reduced concentration of acetyl CoA caused the altered concentration of tricarboxylic acid (TCA) cycle metabolites, with their well-designed combination of CE-MS separation and other protein and DNA analysis [167].

In all, although CE-MS is still not perfect to give the global view of metabolites yet, it is undoubtedly a powerful tool which possesses the potential to do so in the near future. In the meantime, CE-LIF also has an important role in the targeted metabolites analysis due to its high sensitivity and availability. To the interest of this dissertation, CE-LIF offers an ideal platform for us to focus on the separation of cofactors related to optical biopsy. The sample preparation and data processing techniques developed in metabolites analysis can be readily transferred to our targeted cofactor separation.

In this dissertation, we present the details of optimizing the extraction and separation of major endogenous fluorophores in cells and the identification and quantification of these fluorophores. We also compare electropherograms of normal and cancer cell extracts with two-dimensional correlation analysis and investigate the factors influencing the comparison. In addition, the implementation of a cell culture facility in the Geng research lab is discussed for future group members' reference. Finally, we discuss the application of two-dimensional generalized correlation analysis in correlation between CE-LIF and fluorescence spectroscopy to open the gate to techniques for hetero-correlation analysis of tissue.

Table 1.1 Potential endogenous fluorophores at the excitation wavelength range from 250 to 450 nm

Endogenous fluorophores	Excitation maxima (nm)	Emission maxima (nm)
Amino acids		
Tryptophan	280	350
Tyrosine	275	300
Phenylalanine	260	280
Structure proteins		
Collagen	325, 360	400, 405
Elastin	290, 325	340, 400
Enzyme and coenzymes		
FAD, flavins	450	535
NADH	290, 351	440, 460
NADPH	336	464
Vitamins		
Vitamin A	327	510
Vitamin K	335	480
Vitamin D	390	480
VitaminB6 compounds		
Pyridoxine	332, 340	400
Pyridoxamine	335	400
Pyridoxal	330	385
Pyridoxic acid	315	425
Pyridoxal 5’-phosphate	330	400
Vitamin B12	275	305
Lipids		
Phospholipids	436	540, 560
Lipofuscin	340-395	540, 430-460
Ceroid	340-395	430-460, 540
Porphyrins	400-450	630, 690

Source: Ramanujam, N. (2000). Fluorescence spectroscopy of neoplastic and non-neoplastic tissues. *Neoplasia*, 2(1-2), 89-117.

Table 1.2 Mean contribution of spectral components to the fluorescence of colonic tissue *in vivo* with standard errors (%)

Tissue	N*	Collagen	NADH	FAD	Hemoglobin
Normal	86	87.4±1.4	11.6±1.3	1.0±0.2	22.0±0.5
Hyperplastic	35	64.4±3.3	32.6±3.1	3.1±0.5	22.8±1.1
Adenomatous	49	49.1±3.6	47.9±3.5	3.0±1.5	26.3±1.4
Adenocarcinomas	7	42.8±6.8	53.8±7.0	4.7±2.1	35.7±6.0

Source: Schomacker, K. T., Frisoli, J. K., Compton, C. C., Flotte, T. J., Richter, J. M., Nishioka, N. S., et al. (1992). Ultraviolet Laser-Induced Fluorescence of Colonic Tissue - Basic Biology and Diagnostic Potential. *Lasers in Surgery and Medicine*, 12(1), 63-78.

Note: *N is the number of spectra used for decomposing.

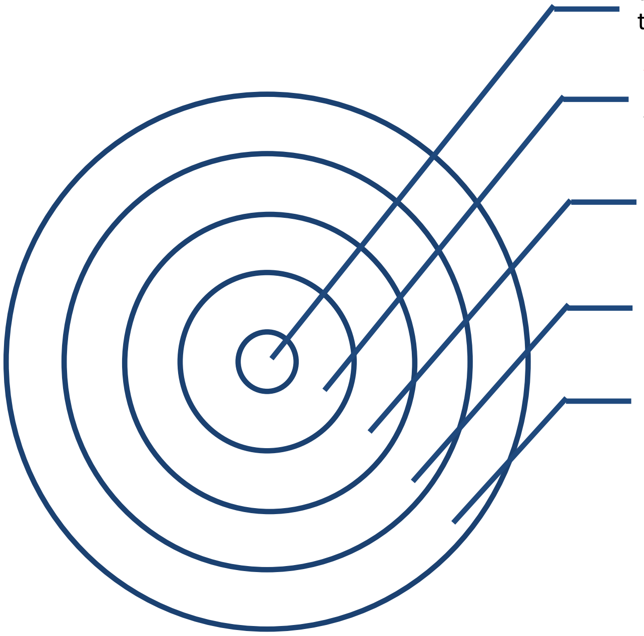

Cancer or **malignant tumor** or **neoplasia** – substantial alterations in the tissue structure and in particular the presence of tumor cell invasion

Preneoplastic change – dysplasia proceeds malignant tumor

Dysplasia – extensive hyperplasia or hyperplasia with additional changes such as altered differentiation. (Benign tumor)

Hyperplasia – an increased number of cells

Tumor – abnormally large structure in the human body, also including swelling or fluid-filled cysts

Carcinoma – a solid malignant tumor formed from cells of epithelial origin

Adenoma – a benign tumor displaying a glandular structure (often originated from gland tissue)

Adenocarcinoma – a malignant tumor showing resemblance to glandular structures (often originated from gland tissue)

Tumor stage – a measure of the physical extension (invasion) of a (malignant) tumor

Tumor grade – a measure of the cellular an/or architectural atypia of a tumor (differentiation status)

Figure 1.1 Basic concepts related to cancer

Source: The above concepts are excerpted from Schulz, W. A., *Molecular biology of human cancers : an advanced student's textbook*. Springer: Dordrecht; Norwell, MA, 2005.

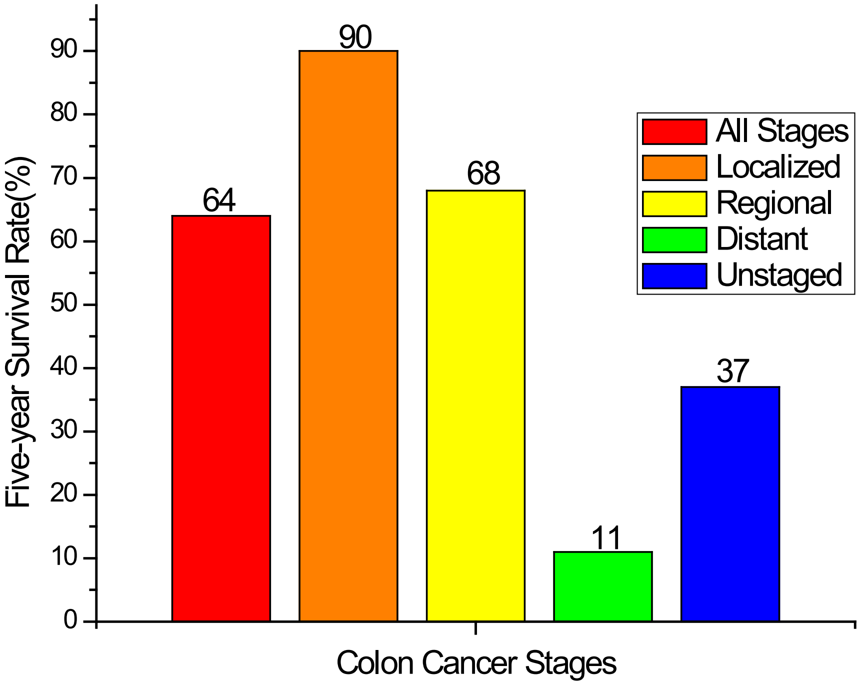

Figure 1.2 Five-year relative survival rate for colorectal cancer by stages at diagnosis, 1996-2004.

Source: American Cancer Society *Colorectal Cancer Facts & Figures 2008-2010*; American Cancer Society: Atlanta, GA, 2008.

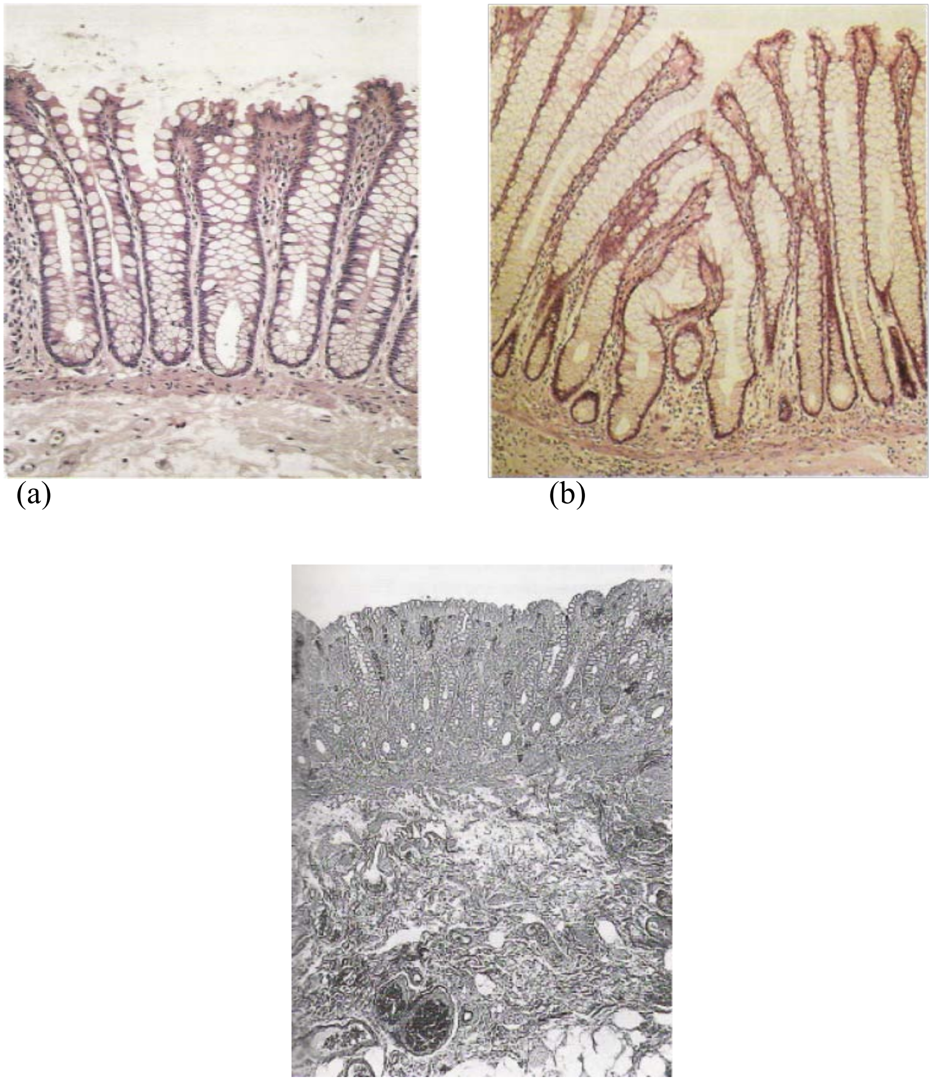

(a) (b)

(c)

Figure 1.3 Colorectal tissue biopsy examples (a) Normal rectal mucosal biopsy and (b) Normal colonic mucosal biopsy (c) Normal submucosal collagen and elastic fibers

---

Source: Images (a), (b) and (c) are excerpted from pages 6, 19 and 11 of Talbot, I.; Price, A.; Salto-Tellez, M., *Biopsy Pathology in Colorectal Disease*. 2nd ed.; Hodder Arnold: London, Great Britain, 2006, respectively.

Note: In the normal rectal mucosa (a), the straight, parallel crypts lie close together and extend down to the muscularis mucosae. In the normal colonic mucosa (b), crypts branch at the junctions of mucosal undulations. There are 500 to 2000 epithelial cells in each crypt.

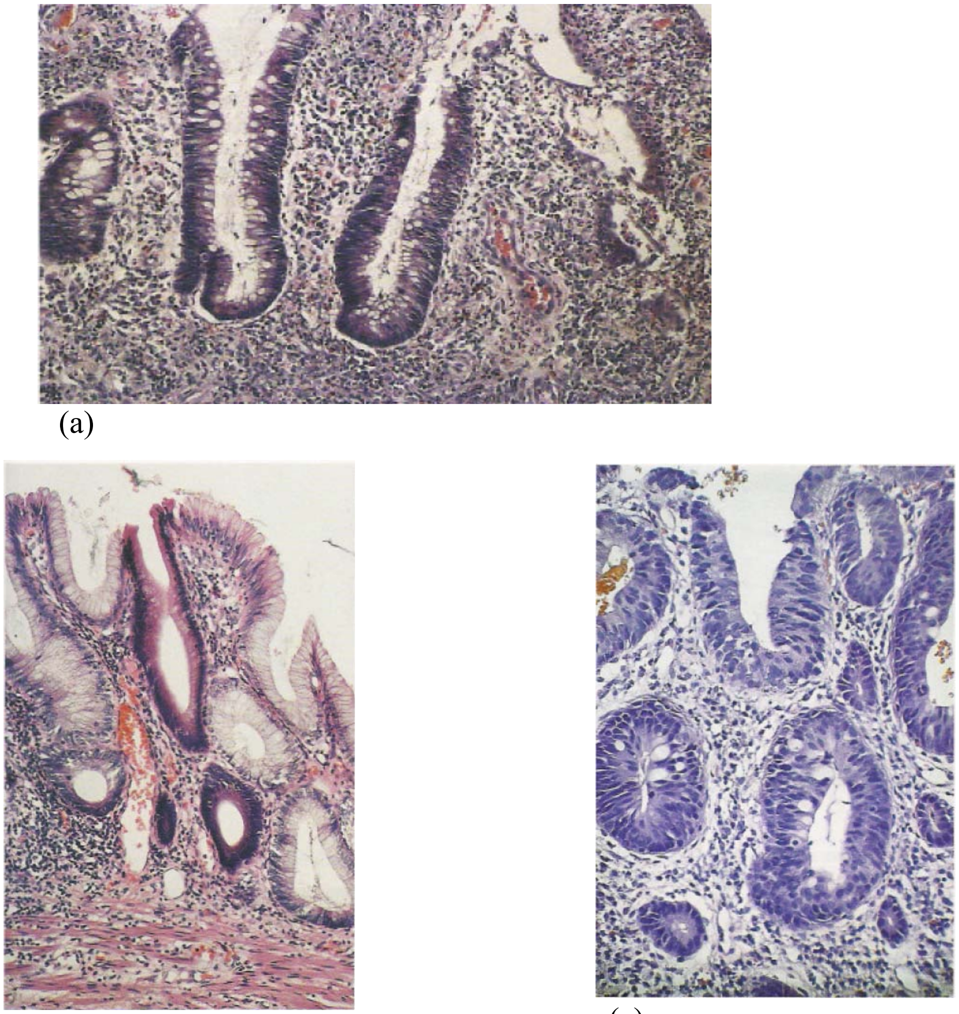

(a)

(b)

(c)

Figure 1.4 Premalignant colorectal tissue biopsy (a) Actively regenerating colorectal epithelium (b) Colorectal dysplasia, low grade (c) Colorectal dysplasia, high grade

---

Source: Images (a), (b) and (c) are excerpted from pages 30, 31 and 31 of Talbot, I.; Price, A.; Salto-Tellez, M., *Biopsy Pathology in Colorectal Disease*. 2nd ed.; Hodder Arnold: London, Great Britain, 2006, respectively.

Note: In regenerative hyperplasia (a), goblet cells are reduced in numbers and the proportion of undifferentiated crypt base cells is increased. The nucleo-cytoplasmic ratio is also increased. In low grade dysplasia (b), a single crypt shows hyperchromasia of epithelial cell nuclei and cytoplasm, mild nuclear enlargement and stratification, and disturbed goblet cells. In high grade dysplasia (c), there is marked nuclear enlargement and stratification as well as hyperchromasia. Goblet cells are greatly reduced.

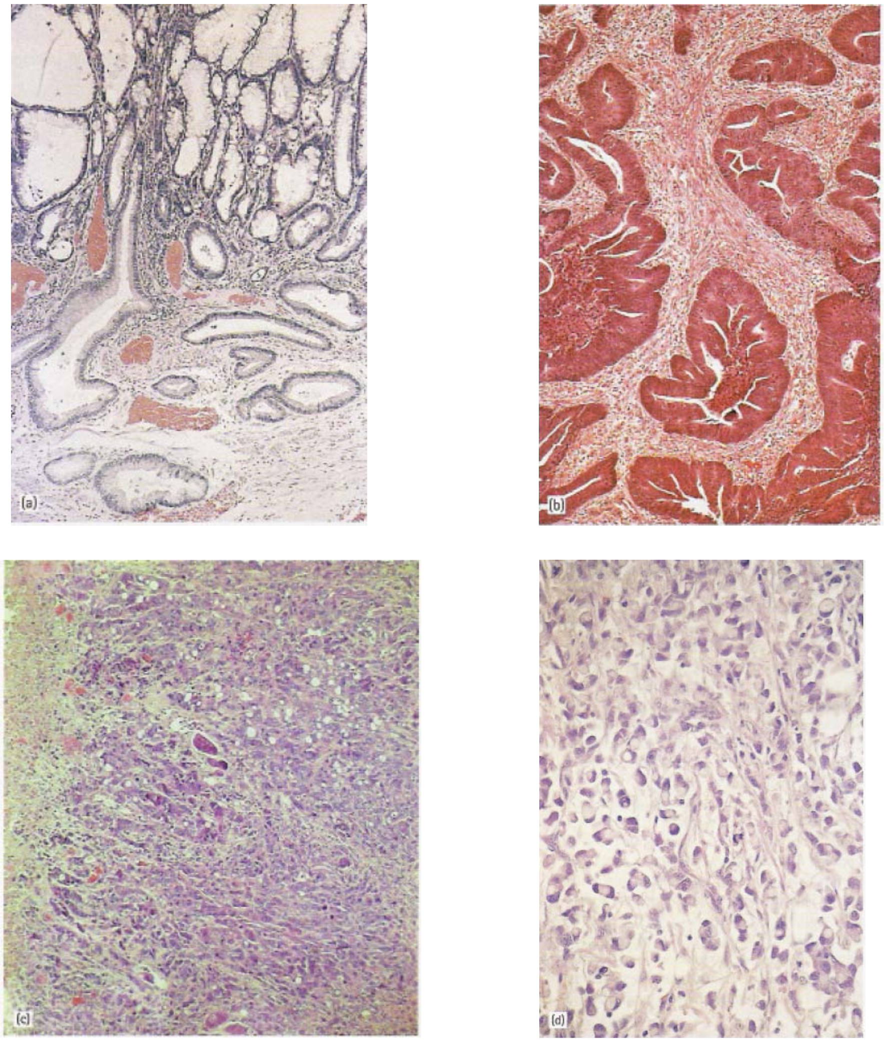

Figure 1.5 Malignant colorectal tissue biopsy (a) Well differentiated adenocarcinoma arising in dysplastic mucosa (b) Moderately differentiated invasive adenocarcinoma of rectum (c) Poorly differentiated adenocarcinoma of rectosigmoid colon (d) Signet ring cell adenocarcinoma of colon

---

Source: Images are excerpted from page 331 of Talbot, I.; Price, A.; Salto-Tellez, M., *Biopsy Pathology in Colorectal Disease*. 2nd ed.; Hodder Arnold: London, Great Britain, 2006.

Note: In (a), the only difference of the well differentiated adenocarcinoma and the dysplastic mucosa is the presence of the paradoxical greater cell pleomorphism in the adenocarcinoma. In (b), well defined glands still exist but deviate considerably from normal rectal mucosa. In (c), the tumor cells lie in sheets and grouped in clumps and cords. The carcinoma barely resembles the normal epithelium, architecturally and cytologically. In (d), the epithelium structure completely disappears.

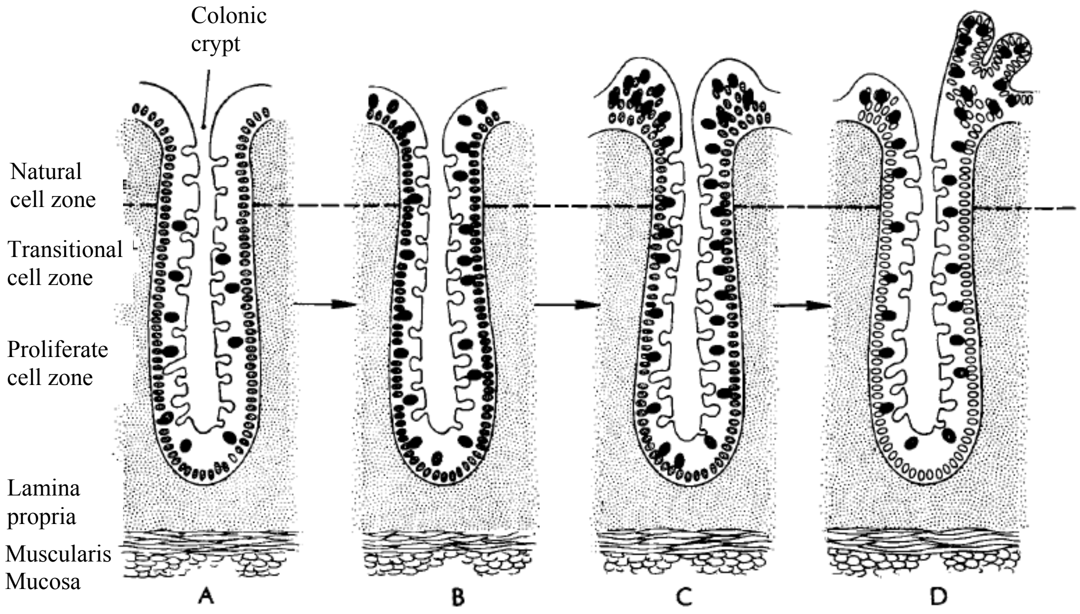

Figure 1.6 One sequence of events to account for the location of abnormally proliferating colonic epithelial cells before and during the formation of polypoid neoplasms

Source: Martin Lipkin, Phase 1 and phase 2 proliferative lesions of colonic epithelial cells in diseases leading to colonic cancer. *Cancer* 1974, 34 (S3), 878-888. Image is retrieved from Images.MD in February 2009 at http://www.images.md.proxy.lib.uiowa.edu/users/Image.asp?ID=GIC0201-03-007&chapID=GIC0201%2D03&fp=8&tf=90&showstyle=1&pagesize=12&contribid

Notes: In normal epithelial tissues (A), the proliferation and differentiation occurs in the proliferative zone. The dark cells incorporate ^{3}H-labeled thymidine, which means they are synthesizing DNA and preparing to undergo cell division. When cells pass through the transitional zone and eventually reach the surface of the mucosa, the DNA synthesis and mitosis activity are gradually decreasing, then cells start normal maturation. In Phase 1 proliferative lesion (B), cells fail to repress the incorporation of thymidine ^{3}H into DNA and continue proliferating even after passing through the transition zone to the mucosa surface. But the mucosa is flat and there is still no excess cell accumulation in the mucosa. In a Phase 2 proliferative lesion (C), cells are able to accumulate in the mucosa. In a neoplastic lesion (D), adenomatous polyps and villous papillomas are formed due to differentiation of abnormally retained proliferating epithelial cells.

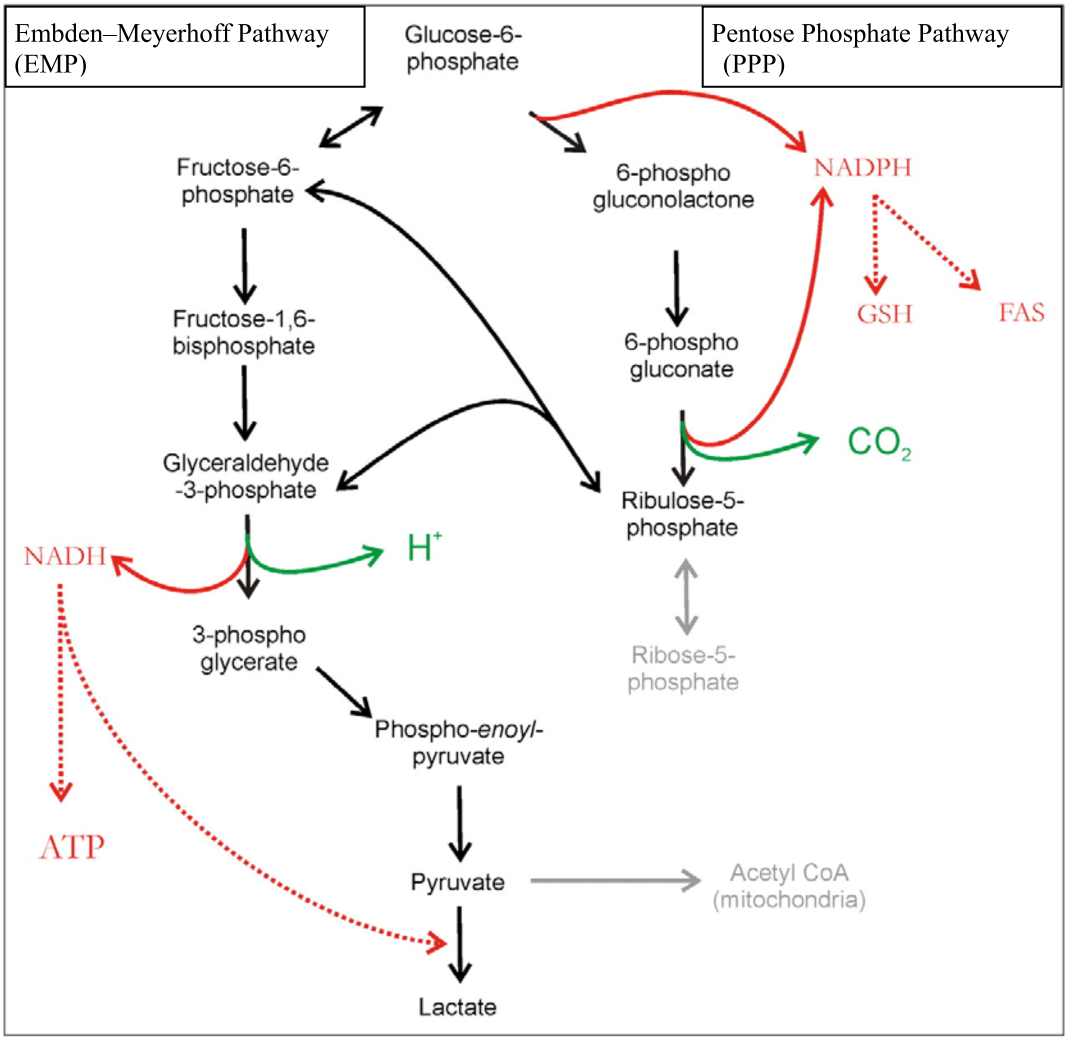

Figure 1.7 Pathways of Glycolysis

Source: Gillies, R. J.; Robey, I.; Gatenby, R. A., Causes and Consequences of Increased Glucose Metabolism of Cancers. *Journal of Nuclear Medicine* 2008, 49 (Suppl_2), 24S-42.

Note: In the Embden–Meyerhoff Pathway (EMP), NADH is produced; while in Pentose Phosphate Pathway (PPP), NADPH is produced as by-product. The generated NADPH will be used to reduce glutathione (GSH) or fatty acid synthase (FAS).

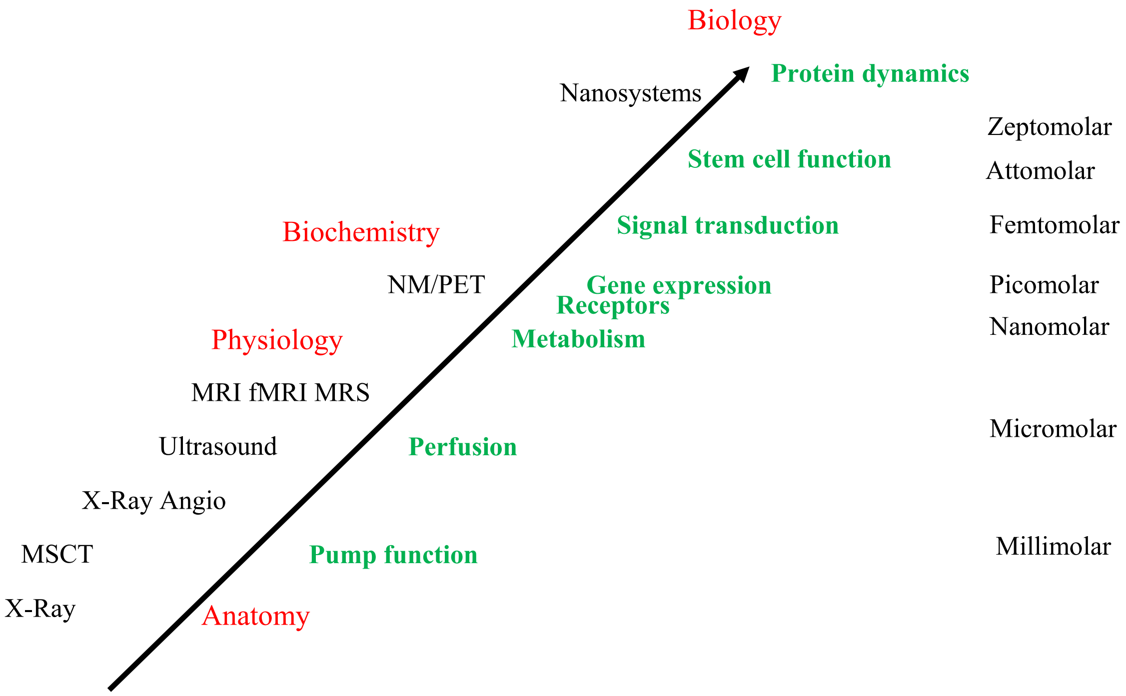

Figure 1.8 Relative sensitivity and directions of application of imaging techniques for cancer diagnosis

---

Source: Fass, L., Imaging and cancer: A review. *Molecular Oncology* 2008, 2 (2), 115-152.

Note: MSCT, Multislice Computational tomography; MRI, Magnetic Resonance Imaging; fMRI, Functional Magnetic Resonance Imaging; MRS, Magnetic Resonance Spectroscopy; NM, Nuclear Medicine; PET, Positive Emission Tomography.

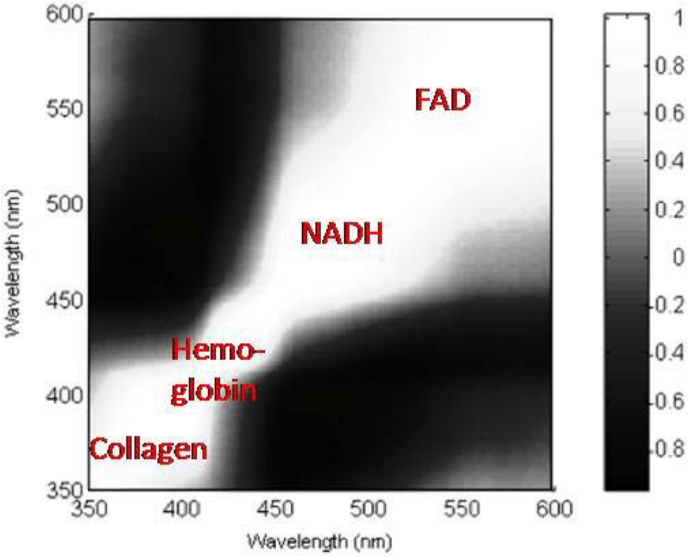

Figure 1.9 Wavelength-wavelength correlation coefficient map of 57 colonic tissue spectra

---

Source: Crowell, E., Wang, G. F., Cox, J., Platz, C. P., & Geng, L. (2005). Correlation coefficient mapping in fluorescence spectroscopy: Tissue classification for cancer detection. *Analytical Chemistry*, 77(5), 1368-1375.

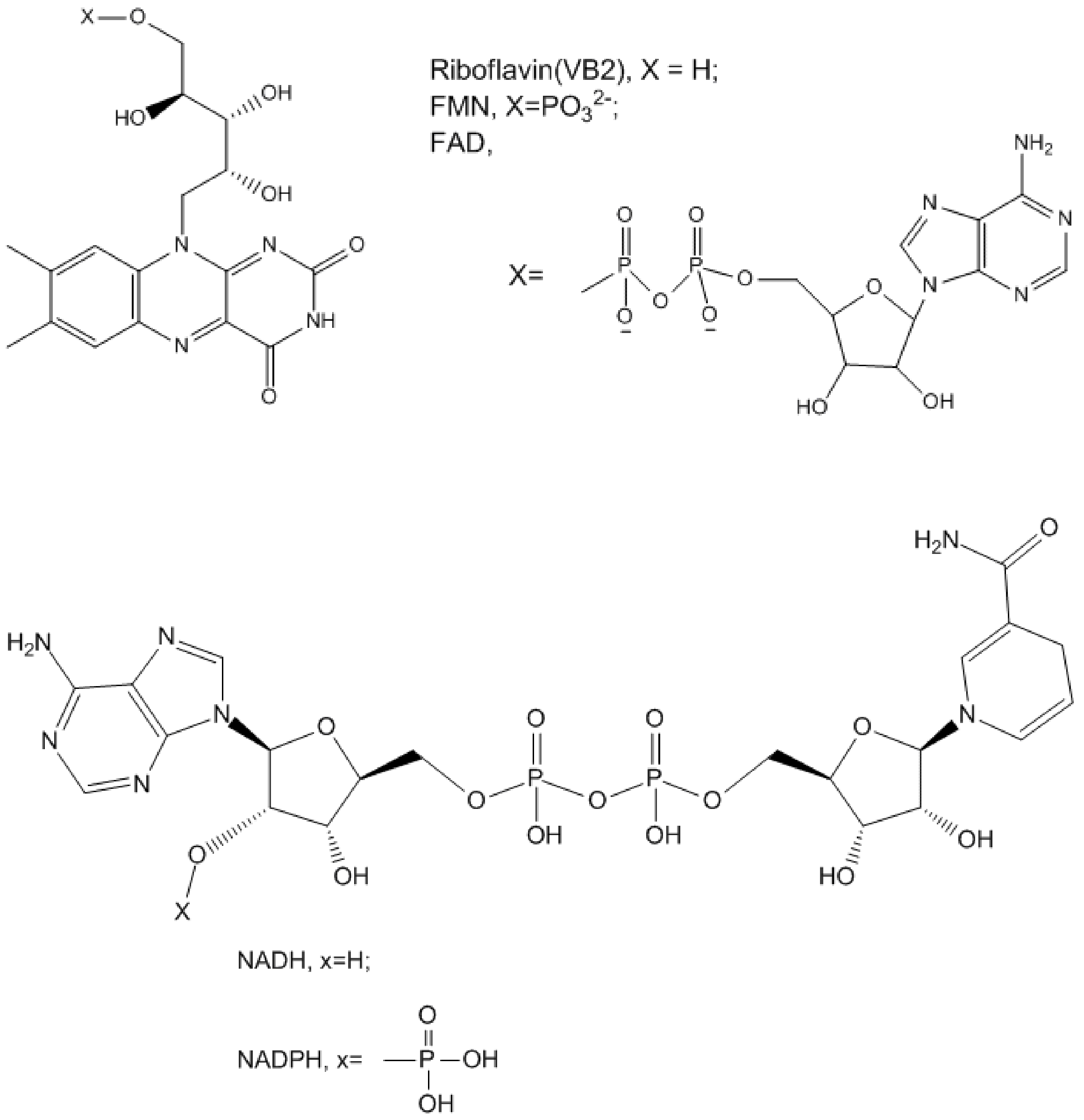

Figure 1.10 Structures of flavins and nucleotides

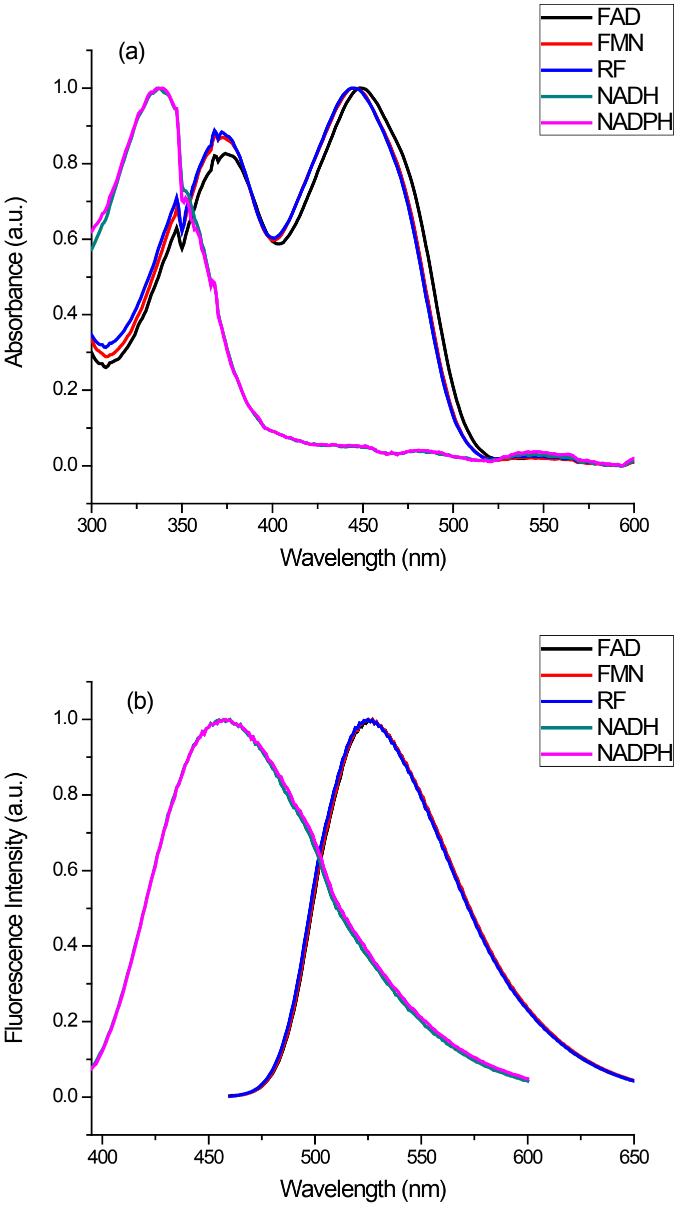

Figure 1.11 The absorption (a) and fluorescence emission (b) spectra of flavins and nicotinamide nucleotides

---

Note: All spectra are normalized to 1 at the maximum. The UV-Vis absorption spectra were collected on a Cary 300 Bio UV-Visible Spectrophotometer. The fluorescence emission spectra were collected on an Aminco Bowman Series 2 Luminescence Spectrometer.

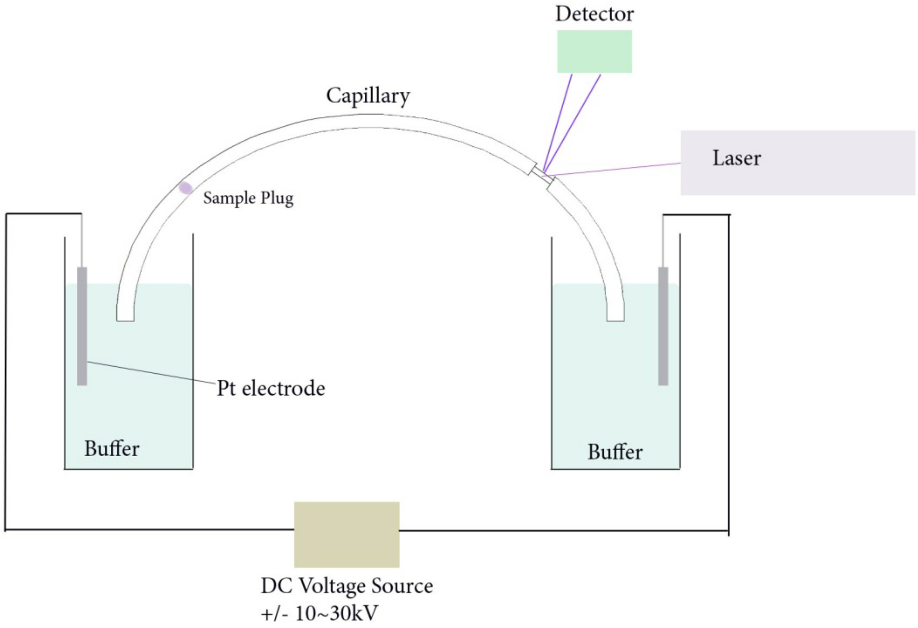

Figure 1.12 A typical setup of capillary electrophoresis

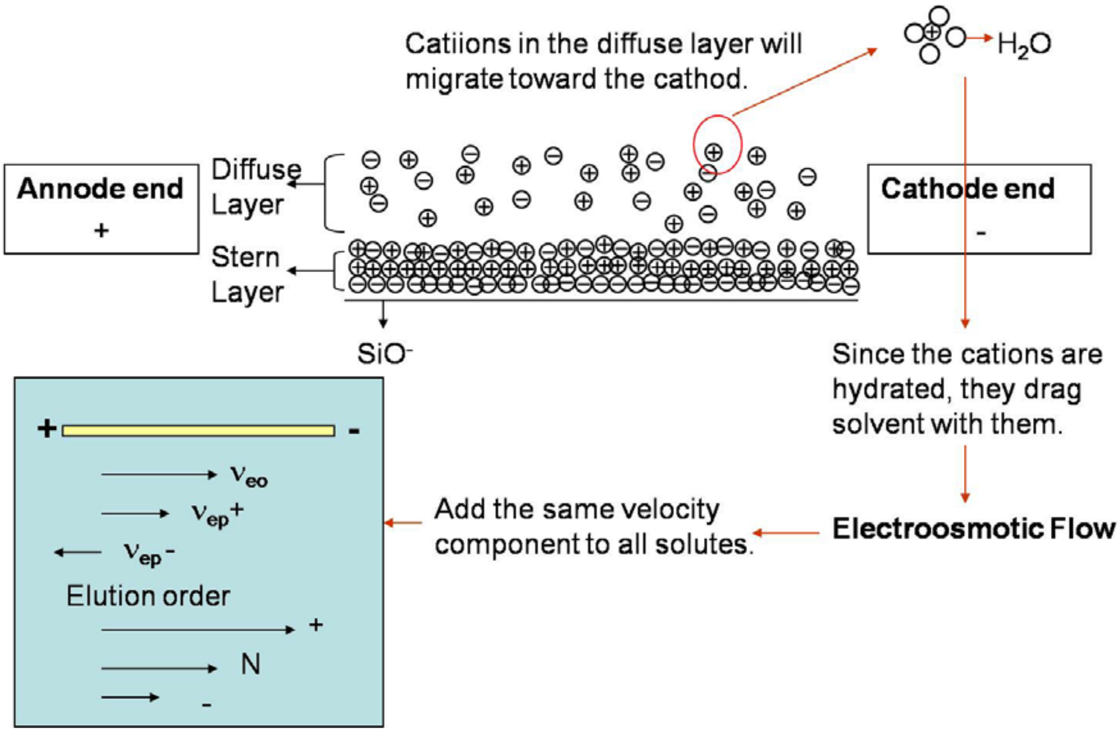

Figure 1.13 Electroosmotic flow and mobility of charged and uncharged molecules in an applied field

CHAPTER 2

OPTIMIZATION OF FLAVINS AND NICOTINAMIDE NUCLEOTIDES SEPARATION

2.1 Introduction

Chemical separation of endogenous fluorophores can bring insight into biochemical changes during cancer development and provide guidance to optical biopsy. The initial focuses of the separation are the fluorescent cofactors in cells including flavin and nicotinamide nucleotides. With its excellent separation efficiency and detection sensitivity, CE-LIF is a suitable technique to accomplish this separation. Separation of metabolites and neurotransmitters by CE has been demonstrated with multiphoton-excitation-laser-induced fluorescence detection and MS detection, where FAD and NADH were among the biochemicals separated. In this chapter, conditions for CE separation and single photon-excitation-laser-induced-fluorescence detection are thoroughly optimized to lay the foundation for the separation of cell and tissue samples. To establish the separation protocols, the detection method, the high voltage, the EOF, the effects of buffer nature, pH and concentration on separation efficiency in terms of sensitivity and resolution, and the day-to-day and within-day variation have been investigated. The optimal conditions were then applied to the separation of RF, FMN, FAD, NADH and NADPH. Quantitative analysis of these five compounds was performed to ensure sufficient sensitivity for detecting these analytes in biological samples.

2.2 Experimental

2.2.1 Chemicals and materials

Flavin adenine dinucleotide (FAD, 95%), β-nicotinamide adenine dinucleotide reduced disodium salt (β-NADH, 98%), flavin mononucleotide sodium salt (FMN, ~95%), Riboflavin (RF, >98%) and β-nicotinamide adenine dinucleotide phosphate reduced tetrasodium salt (β-NADPH, 97%) were obtained at the highest purity from Sigma (St. Louis, MO, USA) and used as received. Sodium dihydrogen phosphate, disodium hydrogen phosphate, boric acid and sodium hydroxide were purchased from Aldrich (Milwaukee, WI, USA). Ultra pure Milli-Q (Millipore, Bedford, MA, USA) water was used to prepare all solutions. Standard stock solutions of FAD and NADH were prepared in dimmed light and stored in dark at 4ºC in amber glass containers with concentrations in the range of 1~2 mM. To avoid errors in analysis from NADH degradation under acidic or neutral conditions [130], stock solutions were prepared daily. Separation with CE was performed no later than 5 hours after sample preparation. Different concentrations and pHs of phosphate and borate buffers were prepared, and the run buffer was adjusted to the target pH using 0.1 M sodium hydroxide solution. All solutions were filtered through 0.20 μm syringe filters (Cole-Parmer Instrument Co., Vernon Hills, IL, USA) to remove any particles and sonicated prior to measurement to remove air bubbles.

2.2.2 Instrumentation and CE separation conditions

A Beckman P/ACE™ MDQ system (Beckman Coulter, Fullerton, CA, USA) was used to perform the CE separations. In LIF detection, the excitation was provided by a He-Cd laser at 325 nm and the fluorescence emission was collected through a 345 nm long pass filter to reduce scattered laser light. The excitation wavelength was selected in tissue spectroscopic measurements, which required the detection of all main tissue fluorophores, collagen, NADH and FAD, simultaneously, while avoiding the excitation of protein fluorescence from the aromatic amino acids. The excitation power was typically 1 mW. Polyimide coated fused silica capillaries (Polymicro Technologies, Phoenix, AZ) with an effective length of 20 cm (30 cm × 50 μm I.D.) were used in the experiment. Prior to use, the capillaries were preconditioned with sodium hydroxide and run buffer. Between runs, the capillary was conditioned consecutively with 0.1 M sodium hydroxide, 0.1 M hydrochloric acid, deionized water and run buffer. Samples were introduced by pressure injection for 5 seconds at 0.5 psi (~3.5 kPa). The CE runs were conducted at voltages ranging from 10 to 30 kV. The temperature of the capillary was maintained at 25ºC with the thermostating system of the instrument.

To better assess the impact of run buffer on CE separation of these molecules, a neutral electroosmotic flow (EOF) marker, DMSO, was used in the system to evaluate the electroosmotic mobility. The apparent mobilities (μ_{app}) were obtained from the migration time (t_m), total length of the capillary (L_t), effective length of the capillary (L_d) and the applied high voltage (V) by equation 2.1.

$$\mu_{app} = \frac{L_t L_d}{t_m V} \qquad [2.1]$$

The electrophoretic mobility (μ_{ep}) of each substance was calculated by subtracting the apparent mobility of the EOF marker (μ_{eo}) from the apparent mobility of the substance.

The effects of buffer pH, buffer concentration and high voltage on the separation performance in terms of electrophoretic mobility, resolution, analysis time and limits of detection were investigated. The limit of detection (LOD) was calculated as the analyte concentration at the signal-to-noise ratio of 3 (equation 2.2).

$$LOD = \frac{3C \cdot N}{S} \qquad [2.2]$$

In equation 2.2, C is the analyte concentration in the sample and S is the signal corresponding to the analyte in the electropherogram, which is represented by its peak area. N is the noise of the electropherogram, which is calculated as the standard deviation of a baseline section in the electropherogram. The same range of each electropherogram was selected as the baseline to calculate the noise. To correct the variation caused by the slope of a baseline, the signals of the baseline section were linearly fitted as $y = a+bx$. Then, $y_i' = a+bx_i$ was calculated for each value of x. The corrected baseline Δy was equal to the difference between the experimental value y and the calculated value y', i.e. $\Delta y_i = y_i$

$-y_i'$ for each data point. The standard deviation of the corrected baseline Δy was calculated as the noise of the electropherogram.

2.3 Optimization of separation conditions for FAD and NADH

2.3.1 Selection of detection method

FAD and NADH were separated by CE with different detection methods to illustrate the advantage of using 325 nm as the excitation wavelength. Figure 2.1 shows electropherograms for separations of FAD (peak at 95 s) and NADH (peak at 100 s) with LIF detection at excitation wavelengths of 325 nm and 442 nm, and UV detection at 280 nm. The limits of detection for FAD and NADH with the three different detection methods are summarized in Table 2.1. An excitation wavelength of 442 nm provided the best sensitivity for FAD detection as the result of the close match between the laser wavelength and the FAD excitation maximum. An excellent detection limit (signal-to-noise ratio of 3), 2 nM, was achieved at this excitation wavelength. However, the other tissue fluorophore, NADH, was not excited at this wavelength (Figure 2.1b). Although 442 nm is the favorable wavelength for LIF detection in CE separations of flavins, it is not effective for our application. The 325 nm laser line was a suitable wavelength for the simultaneous excitation of both tissue fluorophores (Figure 2.1a). Nanomolar detection limits were achieved for both FAD and NADH, at 23 nM and 10 nM, respectively. Although the excitation of NADH came at the cost of a ten-fold decrease in FAD detection sensitivity, it was necessary to probe the tissue composition of these cancer markers simultaneously in cancer detection. In addition, a third important tissue fluorophore, collagen, the connective tissue protein, could also be excited at this wavelength. Shorter wavelength excitation below 300 nm could induce overwhelming protein fluorescence that would mask these cancer markers and was thus not suitable. The

325 nm line of He-Cd laser, on balance, provided the best CW laser choice for detection of colon cancers.

For comparison, we investigated detection sensitivity with UV absorption detection. As shown in Figure 2.1c, UV detection at 280 nm was hundreds of folds lower in detection sensitivity than the LIF method. With the LIF method, FAD and NADH detection limits were higher by factors of 100 and 400, respectively. The improvement for LIF detection of FAD over UV was slightly inferior to NADH, due to the non-optimal excitation at 325 nm. With the 442 nm laser line, the sensitivity improvement was 750-fold for FAD. Clearly, UV absorption does not provide sufficient detection sensitivity for the quantification of FAD and NADH in CE separation of cell extracts.

2.3.2 High voltage and Ohm’s law plot

Joule heating was effectively avoided by thermostating the separation capillary as demonstrated by Ohm’s law plots (Figure 2.2). In testing of Ohm’s law, a 40 cm capillary was conditioned with the 30 mM pH 8.0 phosphate buffer or the 5 mM pH 9.0 borate buffer. The high voltage across the capillary was programmed to ramp up by 2 kV every 4 minutes from 10 kV to 30 kV. The current through the capillary corresponding to each high voltage level was recorded. The dependence of current on applied high voltage was plotted in Figures 2.2 (a) and (b) for phosphate buffer and borate buffer, respectively. According to Ohm’ law, the high voltage (V) should have a linear relationship with the current (I) as long as the resistance (R) of the system does not change.

$$I = \frac{V}{R} \qquad [2.3]$$

If the Joule heating is efficiently dissipated and does not lead to temperature increase and resulting resistance change of the system, the current vs. high voltage curve should be linear. As shown in Figures 2.2 (a) and (b), the I~V curves in both buffer system had r^2 higher than 0.99, demonstrating excellent linearity. The current follows the applied voltage linearly throughout the voltage range of the instrument up to 30 kV in both buffer systems. It demonstrated that the thermostatic system of the CE instrument was controlling the system temperature very efficiently.

The separation voltage was selected based on considerations to achieve high resolution as well as good efficiency. The optimization experiments were conducted under high voltages ranging from 10 to 30 kV in both phosphate buffer (Figure 2.3) and borate buffer (Figure 2.4). Voltages of 15 kV and 20 kV were selected upon optimization for the separation in the 5 mM pH 9.0 borate and 30 mM pH 8.0 phosphate buffers, respectively, ensuring excellent resolution, reasonable efficiency, and reasonable analysis time (less than three minutes). The resolution (R) and efficiency (N) of the separation were calculated with equations 2.4 and 2.5, respectively.

$$R = \frac{t_1 - t_2}{(w_1 + w_2)/2} \qquad [2.4]$$

$$N = 16\left(\frac{t}{w}\right)^2 \qquad [2.5]$$

In equation 2.4, t_1 and t_2 are migration times of FAD and NADH, respectively. w_1 and w_2 are peak widths of FAD and NADH, respectively. In equation 2.5, t and w are the migration time and peak width of the peak to calculate efficiency with. As summarized in Table 2.2, in both buffer systems, the resolution and efficiency were decreasing significantly when the high voltage was increased from 10 kV to 30 kV. In the 30 mM pH 8.0 phosphate buffer, the resolutions were still higher than 2.8 even with the high voltage at 30 kV. But when the high voltage is higher than 20 kV, the efficiency of the separation becomes lower than 10^5, the typical theoretical plate number in CE separations. Since other endogenous fluorophores will be introduced to the system later, the efficiency should be kept close to or higher than 10^5. Therefore, 20 kV was selected as the high voltage for separations in the 30 mM pH 8.0 phosphate buffer. As for the 5 mM pH 9.0 borate buffer, the resolution was close to or lower than 1 when the high voltage was higher than 20 kV. Therefore, the high voltage should be at least 15 kV. In this buffer system, the efficiencies of both peaks were much lower than 10^5 even when the high voltage was 10 kV due to the low concentration of the borate buffer. With this low concentration, the flow in the capillary was not the "plug like" flat profile thus leading to excessive band broadening and low efficiency. It should be noted that this low concentration was selected to show the process of losing resolution and efficiency but not designed for real separation. The buffer concentration and pH optimization will be shown in section 2.3.4.

2.3.3 Effect of EOF marker DMSO and sample matrix

A stable EOF flow is crucial for the reproducibility of CE separation. Measuring the EOF by adding neutral markers to the system allows tracking the changes in EOF and calculation of electroosmotic and electrophoretic mobilities. In our system, DMSO was chosen to be the EOF marker and was added to the sample matrix. To investigate whether the EOF marker DMSO influences the separation of FAD and NADH, a comparison between the separations of FAD and NADH with and without DMSO introduced to the sample matrix was performed in the pH range of 6.0 to 10.0 in 30 mM phosphate buffer. The electrophoretic mobilities of FAD and NADH were calculated for each run and summarized in Table 2.3. As shown in Table 2.3, the average electrophoretic mobilities of FAD were $(1.80\pm0.2) \times 10^{-4}$ cm^2 $V^{-1}s^{-1}$ and $(1.80\pm0.7) \times 10^{-4}$ cm^2 $V^{-1}s^{-1}$ without and with DMSO, respectively. The average electrophoretic mobilities of NADH were $(1.95\pm0.2) \times 10^{-4}$ cm^2 $V^{-1}s^{-1}$ and $(1.94\pm0.4) \times 10^{-4}$ cm^2 $V^{-1}s^{-1}$ without and with DMSO, respectively. Clearly, it demonstrated that DMSO did not significantly influence the mobilities of NADH and FAD in the sample.

Regarding the dilution of the stock solution, if water is used to dilute the stock solution, there can be a strong sample stacking effect due to lower conductivity in the sample matrix. This stacking effect is useful to narrow the band width as shown in Figure

2. 5. However, buffers were still used to dilute the stock solution to mimic our targeted sample matrices, the cell/tissue extracts, which were mostly in buffer. Although the stacking effect would not be as strong as using a water matrix, the sample matrix composed of stock solution and buffer still had lower conductivity than the running buffer thus leading to a certain level of stacking.

During subsequent studies, sample mixtures were prepared by diluting the freshly prepared aqueous stock solution of FAD and NADH with run buffers and adding the DMSO (0.7%) directly to the sample mixture.

2.3.4 Buffer Nature, pH and concentration

Phosphate buffer and borate buffer were chosen to perform the CE separation. These buffers have been shown to be effective media in CE separation of flavins [83]. The buffer pH for FAD and NADH separation was optimized in 30 mM phosphate buffer (pH 6.0, 7.0, 8.0, 9.0, 10.0) and 10 mM borate buffer (pH 7.0, 8.0, 8.5, 9.0, 10.0). The buffer concentration was optimized in 10, 20, 30, or 40 mM phosphate buffer (pH 8.0) and 5, 10, 20, or 40 mM borate buffer (pH 9.0). Sample electropherograms for the optimization are shown in Figures 2.6 and 2.7 for pH optimization and concentration optimization, respectively. The two electropherograms in Figure 2.8 show the separation of FAD and NADH at optimal conditions in phosphate and borate buffers. The unidentified peak consistently appearing at shorter migration time than FAD was previously observed in the separation of riboflavin, flavin mononucleotide (FMN) and FAD [83, 86]. This peak appeared concurrently with FAD, and could be caused by an impurity in the FAD sample such as other flavonoids or a degradation product of FAD. In addition, in the borate buffer system, a small amount of FMN impurity was separated from FAD at 40 mM and pH 9.0. This peak was identified by spiking the sample with an FMN standard.

Buffer pH influences both the fluorescence intensity of FAD and CE separation efficiency. Low pHs are favorable for LIF detection of FAD because the fluorescence intensity of FAD peaks at pH 2.6-2.8 [113]. However, these conditions are not ideal for our application. At such a low pH, NADH displayed a high susceptibility towards degradation [127]. In addition, relatively low surface concentrations of silicate anions existed on the fused silica capillary wall in this pH range thus generating low EOF. Therefore, pH ranges of 6.0-10.0 and 7.0-10.0 were examined for the phosphate (30mM) and borate buffer (10mM) systems, respectively, during optimization. Toward the goal of optimized resolution between FAD and NADH peaks, baseline separation was achieved between the peaks from pH 6.0 to 8.0 for phosphate buffer and from pH 8.0 to 10.0 for borate buffer.

As shown in Figure 2.9, when the pH of borate buffer was elevated, the higher borate anion concentration increased the possibility of forming complex between FAD/NADH with borate anion [168]. The size-to-charge ratios of the complexes were different from those of FAD and NADH molecules. The electrophoretic mobilities were thus affected significantly by the pH variation of borate buffer. In contrast, elevation of the phosphate buffer pH did not influence the electrophoretic mobilities.

When the buffer concentration was changed from 5 mM to 40 mM, the apparent mobilities of FAD and NADH decreased for both phosphate (pH 8.0) and borate buffers (pH 9.0), which was expected due to the lower EOF as a result of a decrease in the zeta potential at the capillary wall-solution interface. As a consequence of decreasing apparent mobilities, the resolution between FAD and NADH was improved at higher buffer concentrations. The gradual increase in the concentration of borate buffer helped resolve another peak in the electropherogram, which was identified as FMN by spiking the sample with a standard. A comparison of the structures of FAD and FMN suggested that FMN had no vicinal diol functional group to complex with borate. Thus, it was separated from FAD in the borate buffer, but remained mixed with FAD in phosphate buffer. This presented a distinct advantage of using borate buffers for the separation of these tissue fluorophores, although the peaks were somewhat broader in this buffer. An additional consideration was that the phosphate buffer tends to accelerate the destruction of NADH, especially when a higher concentration is desired for biological samples later [103, 132]. Therefore, borate buffer is preferred for the separation of cell/tissue extracts. The concentration of the borate buffer may need to be increased to accommodate the cell/tissue extracts buffer concentration.

2.3.5 Day-to-day variation and within-day variation in CE separation

Table 2.4 summarizes the reproducibility study performed in 30 mM phosphate buffer at pH 8.0. The intraday relative standard deviation (RSD) of electrophoretic mobilities was lower than 1.0% (n=10). Day-to-day variation was slightly higher, with an RSD of ~1.5%. These variations are consistent with good CE separations, which tend to be higher than in chromatographic separations.

The intensity ratio between two fluorophores is of central interest in our studies and needs to be measured with high precision. The CE method described here provided excellent separation with small variation, 1.6% of RSD in peak areas ratio between FAD and NADH (n=10). The laser power was varied between 1.0 ~ 1.5mW in the reproducibility examination. The experimental results suggested that the laser power variation between 1.0~1.5 mW did not introduce significant variance in the ratios of their peak areas.

2.4 Calibration and limits of detection

Under the optimized conditions, 40 mM borate buffer at pH 9.0, NADH, NADPH, RF, FMN and FAD were separated by CE-LIF with 325 nm laser excitation. The electropherogram is shown in Figure 2.10, demonstrating baseline separation between all compounds.

To ensure that the concentrations of these species were measured in their linear range, calibrations were performed for the five compounds at the concentration range between 0.05 µM to 50 µM. The calibration curves and regression coefficients are summarized in Table 2.5. FAD, FMN, NADH and NADPH all had coefficients of determination (r^2) higher than 0.99 while RF was slightly lower at 0.984. It suggests that all five compounds showed good linearity at the concentration range calibrated.

The concentration LODs were determined at a signal-to-noise ratio of 3 and found to be 9 nM, 4.5 nM, 23 nM, 10 nM, and 10.5 nM for RF, FMN, FAD, NADH and NADPH, respectively. To estimate the mass LOD, i.e. the on-column LOD, the sample injection volume was estimated by equation 2.6.

$$V_{inj} = \pi r^2 \frac{\Delta \mathrm{P} r^2 t_{inj}}{8 \eta L} \qquad [2.6]$$

Here, the pressure difference ΔP was usually equal to 0.5 psi, i.e. 3.435×10^3 N m^{-2}; the capillary inner radius was usually 5.0×10^{-5} m; the selected injection time t_{inj} was usually 5 seconds; the viscosity of the sample solution η was approximately equal to the water viscosity at 25 °C, 0.9548 cp, i.e. 9.548×10^{-4} N sec m^{-2}; the total length of the capillary was usually 0.30 m. With these parameters,, the estimated injection volume was about 10 nL. With this injection volume, the on-column LODs for RF, FMN, FAD, NADH and NADPH were 90 amol, 45 amol, 230 amol, 90 amol and 103 amol, respectively. The LODs were estimated from the electropherogram under the optimal separation conditions (in 30 mM pH 8.0 phosphate buffer; 20kV).

2.5 Conclusion

The CE separation method established in this chapter offers a solid base for fast, cost-efficient and simultaneous separation of flavins and nicotinamide nucleotides in cell or tissue extracts. The separation conditions for RF, FMN, FAD, NADH and NADPH were optimized to be in 30 mM pH 8.0 phosphate buffer with 20 kV high voltage or in 40 mM pH 9.0 borate buffer with 15 kV high voltage. The separation offers good linearity for all five compounds in the concentration range of 0.05-50 μM. The concentration detection limits for all the five compounds are in the nanomolar range, which ensures sufficient sensitivity for separation of cell extracts.

Table 2.1 Limits of detection for FAD and NADH by CE separation with different detection methods

	LIF detector, λ_{ex}=325nm		LIF detector, λ_{ex}=442nm		UV detector, 280nm	
	FAD	NADH	FAD	NADH	FAD	NADH
Electrophoretic mobility ($\times 10^{-4}$ cm^2 $V^{-1}s^{-1}$)	-1.74	-1.92	-1.74	N/A	-1.77	-1.94
Concentration Limit of Detection (nM)	15	9.0	2.0	N/A	1520	3730
Mass Limit of Detection (amol)	146	92	19	N/A	14900	36600

Note: The electropherogram examples are shown in Figure 2.1. The separation conditions are as following: buffer: 30 mM phosphate buffer (pH 8.0), high voltage: 20 kV, effective capillary length: 20 cm, capillary i.d. 50 µm, injection: 0.5 psi 5 sec.

Table 2.2 High voltage effects on resolution and efficiency of FAD and NADH separation in phosphate buffer and borate buffer

High Voltage	Phosphate Buffer (n=3)			Borate Buffer (n=3)		
	R	$N_{FAD}(\times 10^4)$	$N_{NADH}(\times 10^4)$	R	$N_{FAD}(\times 10^4)$	$N_{NADH}(\times 10^4)$
10 kV	4.92±0.07	11.9±0.3	12.4±0.1	2.45±0.03	3.06±0.03	2.20±0.03
15 kV	4.5±0.2	10.0±0.9	10.1±0.9	2.035±0.03	2.30±0.04	1.58±0.02
20 kV	3.81±0.01	7.43±0.05	7.96±0.02	1.77±0.02	1.94±0.02	1.26±0.02
25 kV	3.43±0.06	6.4±0.2	6.7±0.2	0.40±0.02	0.2±0.1	2.0±1.0
30kV	2.81±0.03	4.58±0.09	4.90±0.07	0.06±0.03	0.0043±0.0009*	

Note: The resolution and efficiency are calculated based on the electropherograms from the same set of experiments as the electropherograms shown in Figure 2.3 and Figure 2.4.

CE separation conditions: buffer: 30 mM phosphate buffer (pH 8.0) or 5 mM borate buffer (pH 9.0), effective capillary length: 30 cm, total capillary length: 40 cm, capillary i.d. 50 µm, injection: 0.5 psi 5 sec, LIF detection with excitation wavelength of 325nm.

*Since the two peaks are almost merged together, there is only one efficiency can be calculated and the efficiency becomes extremely low.

Table 2.3 Effects of EOF marker DMSO on electrophoretic mobility of FAD and NADH

		Electrophoretic mobility ($\times 10^{-4}$ cm^2 V^{-1}s^{-1})						
		Buffer pH					Average	Standard deviation
		6.0	7.0	8.0	9.0	10.0		
Without DMSO	FAD	-1.82	-1.76	-1.80	-1.80	-1.81	-1.80	0.02
	NADH	-1.98	-1.92	-1.96	-1.96	-1.94	-1.95	0.02
With DMSO	FAD	-1.82	-1.72	-1.75	-1.83	-1.91	-1.80	0.07
	NADH	-1.97	-1.89	-1.91	-1.99	-1.96	-1.94	0.04

Note: Separation conditions: buffer: 30 mM phosphate buffer, high voltage: 20 kV, effective capillary length: 20 cm, total capillary length: 30 cm, capillary i.d. 50 μm, sample injection: 0.5 psi 5 sec, LIF detection with excitation wavelength of 325nm.

Without DMSO: the separation was performed without DMSO in the sample. The electroosmotic mobility used to calculate the electrophoretic mobilities were measured by injecting DMSO separately.

With DMSO: the separation was performed with adding 0.7% DMSO into the buffer used to dilute the sample stock solution.

Table 2.4 Intraday and interday reproducibilities of electrophoretic mobilities

Electrophoretic mobility	Intraday (n=10) Day2		Interday (6 days, n=29)	
	FAD	NADH	FAD	NADH
Average ($\times 10^{-4}$ cm^2 V^{-1}s^{-1})	-1.77	-1.93	-1.78	-1.94
RSD	0.7%	0.6%	1.3%	1.2%

Note: Separation conditions: buffer: 30 mM pH 8.0 phosphate buffer, high voltage: 20 kV, effective capillary length: 20 cm, total capillary length: 30 cm, capillary i.d. 50 µm, sample injection: 0.5 psi 5 sec, LIF detection with excitation wavelength of 325nm.

Table 2.5 Linear regression results of calibration curves and detection limits

	Linear regression results		concentration Range /μM**	Limits of Detection***	
	Equations*	r^2		concentration/nM	mass/amol
FAD	y=(0.72±0.01)x-(0.6±0.2)	0.996	0.05-50	23±6	230±60
FMN	y=(3.66±0.04)x-(1.8±0.6)	0.998	0.05-50	4.5±0.2	45±2
RF	y=(2.77±0.09)x-(3±1)	0.983	0.05-50	9±2	90±20
NADH	y=(1.38±0.03)x-(0.8±0.4)	0.995	0.05-50	10±2	90±20
NADPH	y=(1.15±0.02)x-0.7±0.4)	0.995	0.05-50	10.5±0.8	103±7

Note: *y and x stand for peak area and concentration respectively.

**The calibration curve is linear in the entire concentration range of the experiments.

***The limits of detection are estimated at a signal-to-noise ratio of 3.

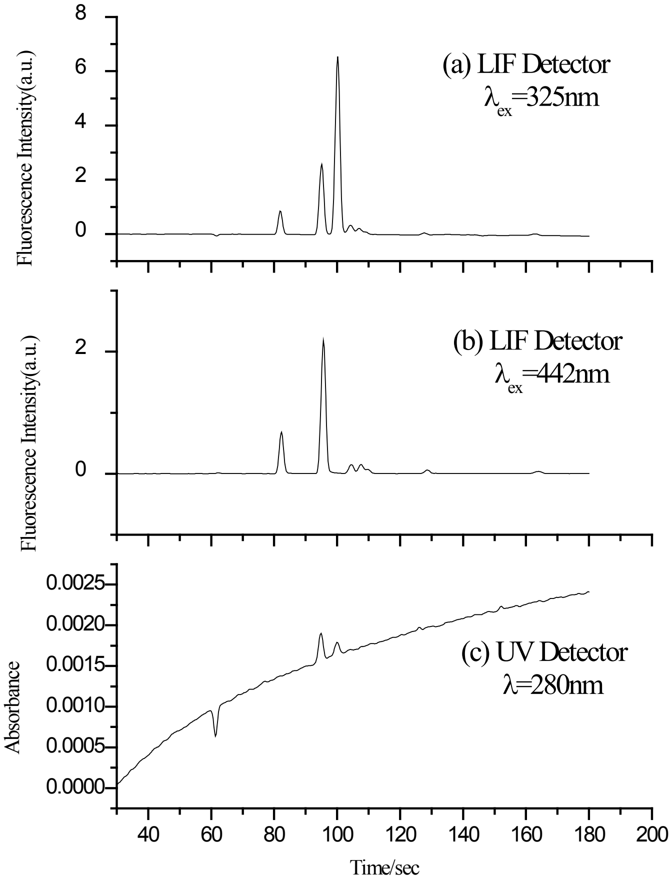

Figure 2.1 CE separation of FAD and NADH with LIF and UV detection

Note: Concentration of FAD: 8.3 µM, concentration of NADH: 9.4µM. Separation conditions: buffer:30 mM phosphate buffer (pH 8.0), high voltage: 20 kV, effective capillary length: 20 cm, capillary i.d. 50 µm, injection: 0.5 psi 5 sec. (a) LIF detection with excitation wavelength of 325nm; (b) LIF detection with excitation wavelength of 442 nm; (c) UV detection at 280 nm.

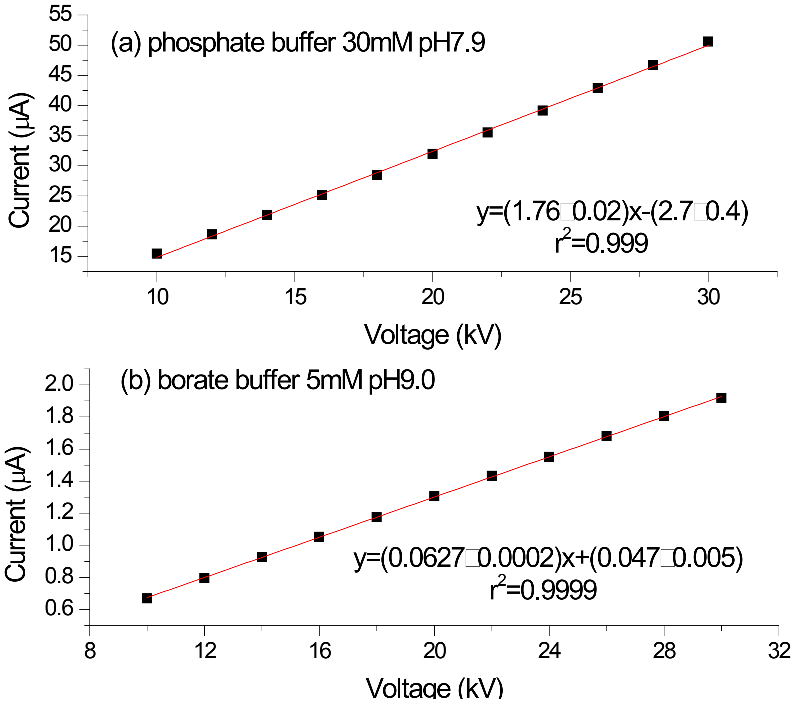

Figure 2.2 Ohm's law plots in CE

Note: CE conditions: capillary total length: 40 cm; Buffer concentration and pH as noted in (a) and (b), respectively.

Each data point in the plot represents a single current value measured under the corresponding high voltage.

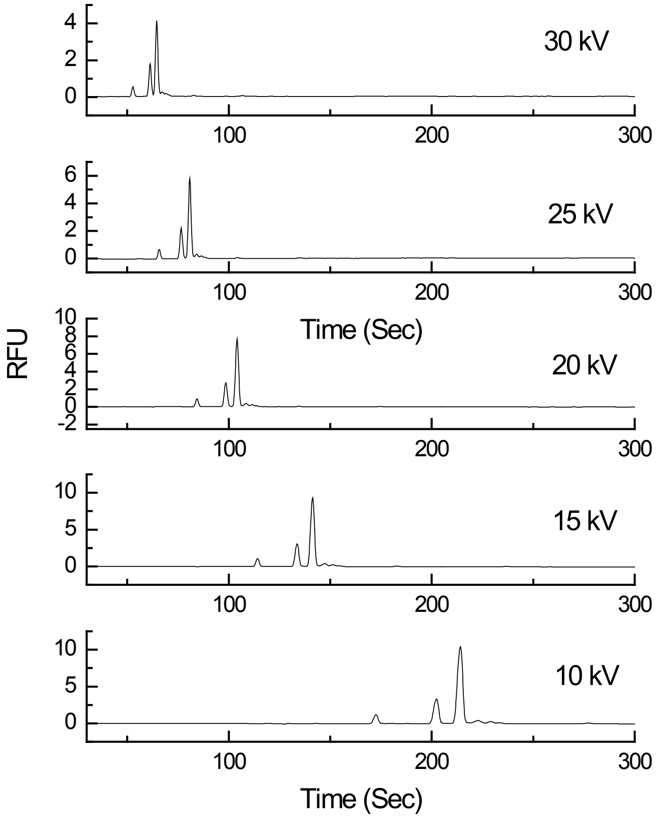

Figure 2.3 High voltage effects on CE separation of FAD and NADH in phosphate buffer

---

Note: CE separation conditions: buffer: 30 mM phosphate buffer (pH 8.0), effective capillary length: 30 cm, total capillary length: 40 cm, capillary i.d. 50 µm, injection: 0.5 psi 5 sec, LIF detection with excitation wavelength of 325nm.

*RFU: relative fluorescence units

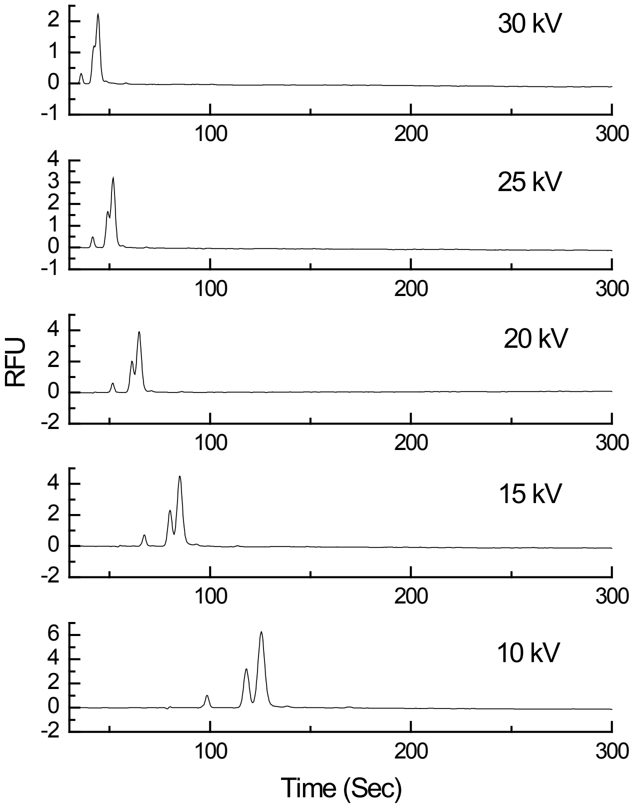

Figure 2.4 High voltage effects on CE separation of FAD and NADH in borate buffer

---

Note: CE separation conditions: buffer: 5 mM borate buffer (pH 9.0), effective capillary length: 30 cm, total capillary length: 40 cm, capillary i.d. 50 µm, injection: 0.5 psi 5 sec, LIF detection with excitation wavelength of 325nm.

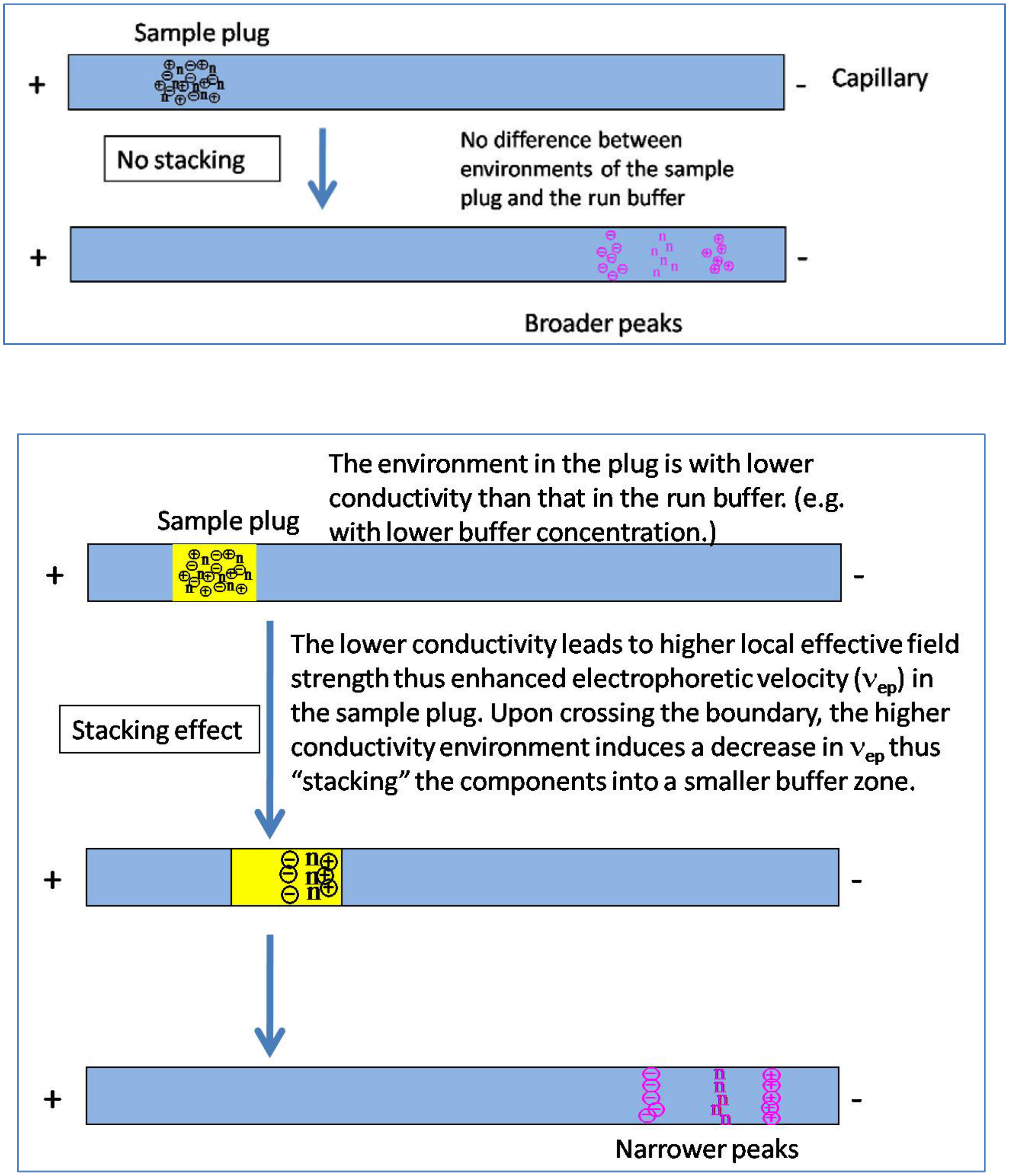

No difference between environments of the sample plug and the run buffer

The environment in the plug is with lower conductivity than that in the run buffer. (e.g. with lower buffer concentration.)

The lower conductivity leads to higher local effective field strength thus enhanced electrophoretic velocity (ν_{ep}) in the sample plug. Upon crossing the boundary, the higher conductivity environment induces a decrease in ν_{ep} thus "stacking" the components into a smaller buffer zone.

Figure 2.5 The sample stacking effect in CE

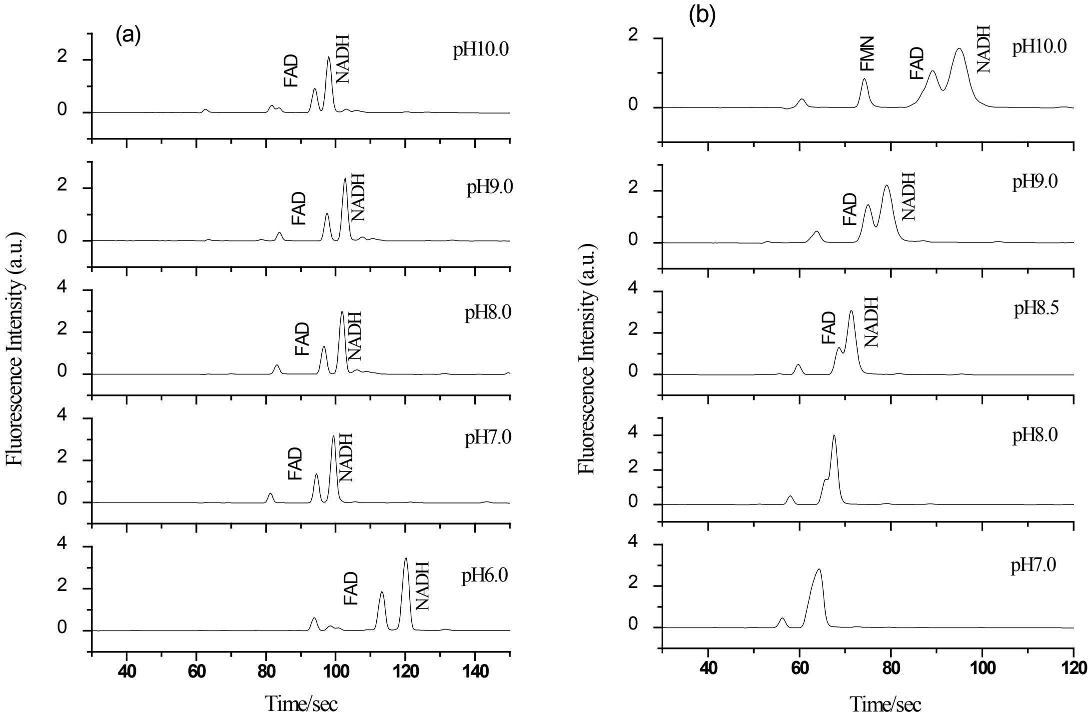

Figure 2.6 Effects of buffer pH on CE separation of FAD and NADH in phosphate buffer and borate buffer

---

Note: Separation conditions: (a) buffer: 30 mM phosphate buffer (pH 6.0, 7.0, 8.0, 9.0, 10.0), high voltage 20 kV, effective capillary length: 20 cm, capillary i.d. 50 µm, injection: 0.5 psi 5 sec, LIF detection with excitation wavelength of 325nm. (b) buffer: 10 mM borate buffer (pH 7.0, 8.0, 8.5, 9.0, 10.0), high voltage: 15 kV, other conditions are the same as in (a).

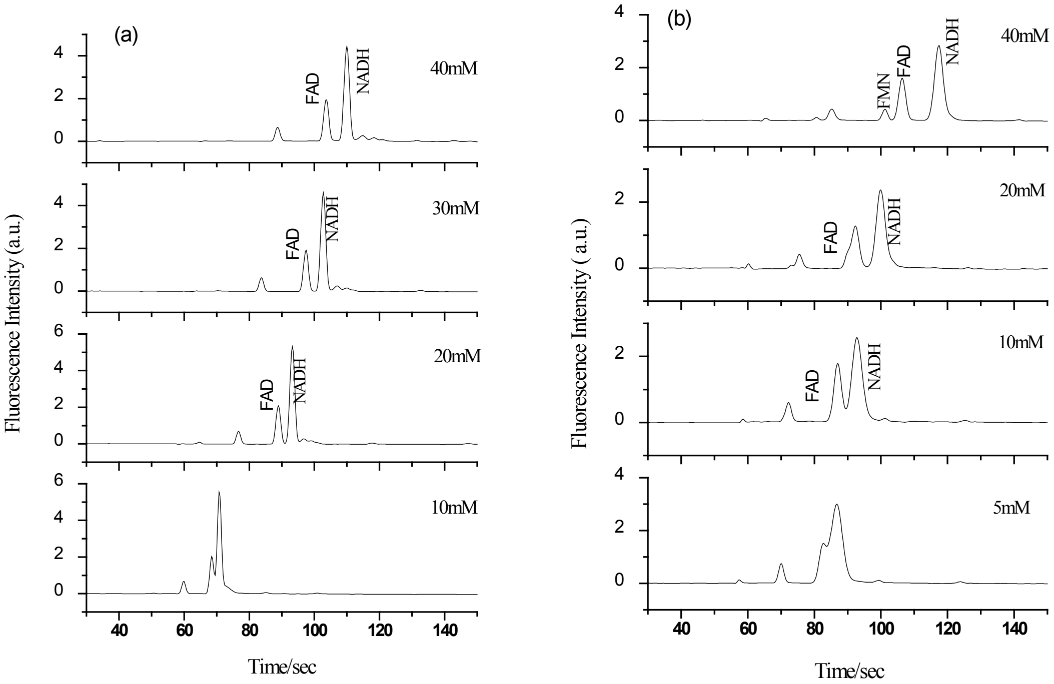

Figure 2.7 Effects of buffer concentration on CE separation of FAD and NADH in phosphate buffer and borate buffer

---

Note: Separation conditions: (a) buffer: 10, 20, 30, or 40 mM phosphate buffer (pH 8.0), high voltage 20 kV, effective capillary length: 20 cm, capillary i.d. 50 µm, injection: 0.5 psi 5 sec, LIF detection with excitation wavelength of 325nm. (b) buffer: 5, 10, 20, or 40 mM borate buffer (pH 9.0), high voltage: 15 kV, other conditions are the same as in (a).

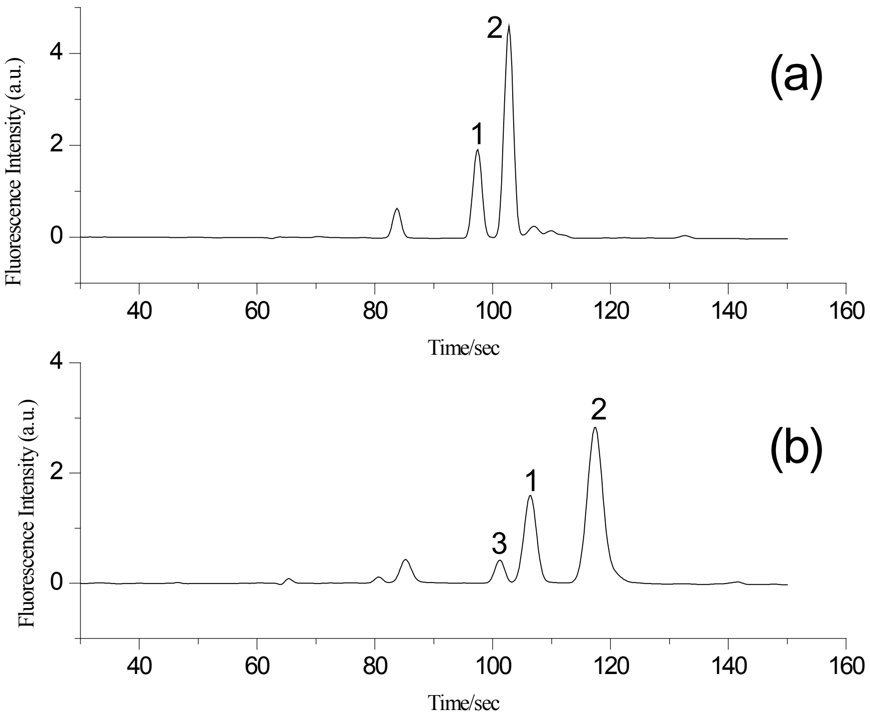

Figure 2.8 Electropherograms of FAD and NADH in phosphate and borate buffer

Note: Peak identities: (1) FAD (10µM) (2) NADH (11µM) and (3) FMN.

Separation conditions: (a) buffer: 30 mM phosphate buffer (pH 8.0), high voltage: 20 kV, effective capillary length: 20 cm, capillary i.d. 50 µm, injection: 0.5 psi 5 sec, LIF detection with excitation wavelength of 325nm. (b) buffer: 40 mM borate buffer (pH 9.0), high voltage: 15 kV, other conditions are the same as in (a).

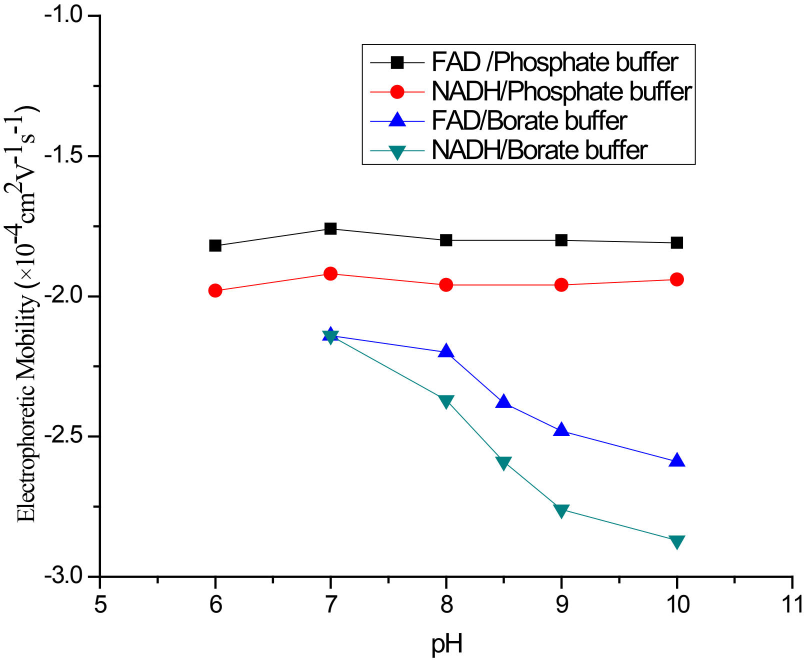

Figure 2.9 Effects of buffer pH on electrophoretic mobilities of FAD and NADH

Note: Separation conditions: 20 cm effective capillary length, 5 s injection at 0.5 psi; 30 mM phosphate buffer, 20 kV; 10 mM borate buffer, 15 kV, LIF detection with excitation wavelength of 325nm.

Each electrophoretic mobility was calculated from one electropherogram.

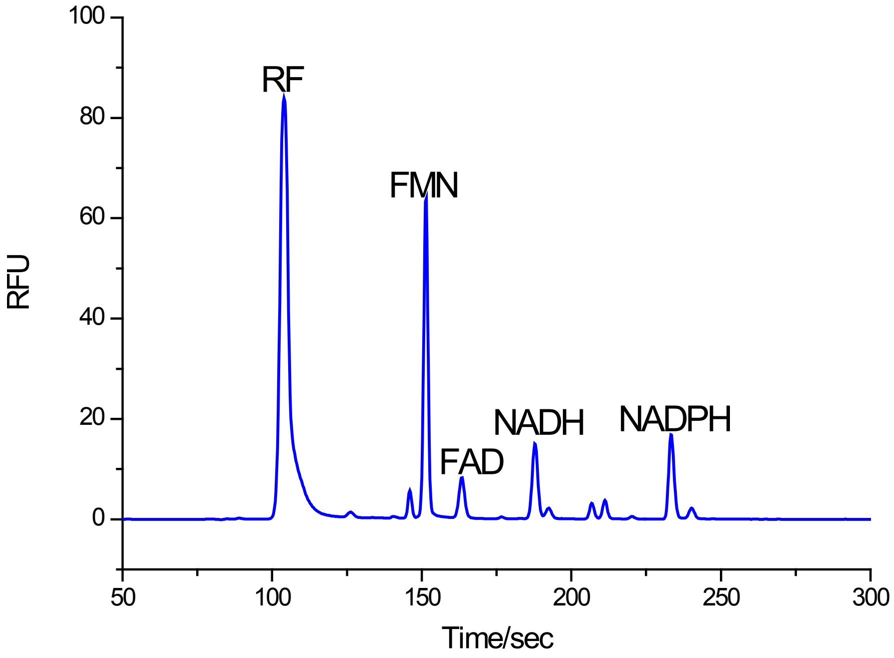

Figure 2.10 Electropherogram of RF, FMN, FAD, NADH, and NADPH

Note: optimized separation conditions: buffer: 40 mM borate buffer (pH 9.0), high voltage: 15 kV, effective capillary length: 20 cm, capillary i.d. 50 μm, injection: 0.5 psi 5 sec, LIF detection with excitation wavelength of 325nm.

Concentrations: RF 110 μM, FMN 31 μM, FAD 22 μM, NADH 42 μM, NADPH 49 μM.

CHAPTER 3

ESTABLISHING CELL/TISSUE CULTURE FACILITY

A central task in this project was to establish the capability of culturing cells and tissue in our laboratory. Setting up a cell/tissue culture facility in our research lab enables us to perform chemical separations and spectroscopic studies of normal and cancer cells as well as presents new possibilities in research on biology, biochemistry and biomedicine chemistry. With a well constructed and maintained cell/tissue culture facility, we can:

- Perform extraction and separation of cell content as planned without relying on other facilities.
- Culture cells in semisolid, such as in a gel like collagen or agar, to construct tissue phantom for imaging experiments.
- Culture and label cells for confocal microscopy imaging, and
- Culture tissues for spectrally-resolved fluorescence correlation imaging.

With these considerations, we commenced on the construction project to establish a cell/tissue culture facility in our research lab in August 2006. In January 2007, the cell/tissue culture facility was established and ready for cell culture. This chapter will briefly discuss the chemical, biological and mechanical considerations and details in the design, construction, and maintenance of the cell/tissue culture facility as a general reference and direction for future group members.

3.1 Safety considerations

The cell lines first cultured in the cell/tissue culture facility are wild type Chinese Hamster Ovary (CHO) cells (ATCC Number CCL-61) [169], human colorectal adenocarcinoma cells HT-29 (ATCC Number HTB-38) [170], and human normal cells FHC (ATCC Number CRL-1831) [171]. According to American Type Culture Collection (ATCC), these three cell lines are all classified as biosafety level 1. According to the

Biological Safety Manual issued by the University of Iowa[172-173] and communication with Health Protection Office staff, culturing these cells should be classified as risk group 2. Also, the Biological Safety Manual also specified that biological safety level 2 should be applied to the cell/tissue culture facility in risk group 2. For the biosafety level 2 facility, autoclave is required on-site and a Class II Type A biosafety cabinet is desired. Other requirements for establishing and running of the biosafety level 2 facility in the Biological Safety Manual are strictly followed. Two aspects are most important. Firstly, personnel who will access the cell/tissue culture facility need to have the hepatitis B vaccine. The hepatitis B vaccine should be offered for free, should be documented, and all post-exposure evaluations and follow-up should also be provided to personnel at no cost. Secondly, the following personal protection equipments (PPE) have to be worn all the time when using the cell/tissue culture facility.

- Gloves
- Face protection equipment (goggles, mask, face shield or other splatter guard)
- Protective clothing (laboratory coats, gowns or uniforms)

3.2 Equipments and cell culture facility enclosure

The major equipments needed [174] for the cell/tissue culture facility are a biosafety cabinet class II, a CO_2 incubator, a CO_2 cylinder, balance, an autoclave, a designated refrigerator and a freezer, an inverted microscope, a water bath, a water purifier, a benchtop centrifuge, pipettes and a hemocytometer. To store cell lines on site, a liquid nitrogen freezer and a liquid nitrogen Dewar are needed.

The biosafety cabinet offers a work surface with sterilized air blown onto it. The laminar flow inside the hood provides a good control of sterility during the manipulation of the culture. Three classes (Class I, II and III) of biosafety cabinets are available selections. For our research projects, the class II type A biosafety cabinet is the appropriate choice. Figure 3.1 shows the air flow directions in this type of biosafety cabinet. The air is filtered by the High Efficiency Particulate (HEPA) Filter to remove >0.3 µm particles with 99.99% efficiency, then it flows vertically down onto the work surface. The front window with a lower edge allows adequate access by arms as well as minimizes turbulence to air drawn in from outside. The exhausting air flows across the cultures, passes through the outlet filter, then cycle within the cabinet or flow out to the lab air. The stainless surface of the cabinet is easy to decontaminate. There is usually an air flow monitor and alarm system which warns when the rate falls below or rises above safe levels. In all, the Class II type A biosafety cabinet protects biological agents and cell culture inside the cabinet from contamination and at the same time protects the lab and the researchers from the biological agents.

The CO_2 incubator provides a constant temperature at 37°C, 5% CO_2 concentration and consistent humidity. The constant CO_2 concentration is important to maintain the pH level in the medium for cells to grow. A pressurized pure CO_2 tank and tubes with 0.22 µm filters are needed to set up the incubator. Frequent cleaning of the incubator and calibration of the temperature sensor and CO_2 sensor are crucial for the incubator to function as desired.

Compared to other sterilization methods like dry heat, irradiation, chemical and filtration, steam sterilization is convenient, inexpensive and multi-purpose. Therefore, the autoclave (steam sterilizer) is necessary for cell/tissue culture. With applying 121 °C at 15 psi (100 kPa) pressure to liquid agent or apparatus, the autoclave sterilizes them to keep cells from contamination.

An upright bright field microscope with 100x objectives allows direct observation of most cells in culture. However, the phase contrast microscope offers better visibility. A centrifuge with 80-100g force can be used to spin down the cells. The hemocytometer is a tool for counting cells, which is an optically flat chamber with a defined area of known depth. As shown in the Figure 3.2, once the cell suspension in medium is added to the defined area, cells can be counted under the microscope with the assistance of the grids on the slide. The procedure of cell counting is described in Section 3.3.4.3.

A designated refrigerator is needed to store the culturing medium and other agents. A designated -20 °C freezer can be used to store serum and other supplements requiring -20 °C storage. The autodefrost feature for the freezer is not desired because the serum, enzyme and antibiotics may deteriorate under the oscillation of the temperature. Other apparatus needed include Pasteur pipettes, plastic pipettes, pipettes can, cell culture flasks, cell culture dishes, sterile containers and sterilization filters.

In order to protect the cell/tissue culture facility, the major equipments is enclosed in a designed plastic enclosure. Importantly, the enclosure isolates the cell culturing facility from the general lab environment to avoid contamination in the cell culture. The design of the enclosure was based on multiple points of consideration: (1) the efficient layout of the major equipment (2) the possibility of multiple personnel working simultaneously, (3) transparency of the facility to ensure lab safety, and (4) structural connections and stability. Figures 3.3 and 3.4 show the design plot and the implemented enclosure, respectively. The air inside the enclosure is circulated to outside through the ceiling.

3.3 Cell culture protocols

To ensure the standardized operation and maintenance of the cell culture facility, protocols on various techniques and instrument operations were established based on introduction in reference [174] and the suggestions from Alissa van Winkle and Professor Jim Jung-Ching Lin in the Department of Biology at the University of Iowa. Here, a selected collection of important protocols are presented for future references.

3.3.1 Protocols for aseptic techniques

3.3.1.1 Remember

The air is dotted and filled with dust, spores and germs. Unless air currents blow them away from the working area, these potential contaminants will descend to the working surface, into open bottles, and onto pipette tips. Microorganisms, such as bacterial, mycoplasma, yeast, and fungal spores, will “fall” from hands and sleeves, and descend to the surface. Arm motions, rapid pipetteing, and people passing by will stir up unpredictable currents that cannot be guarded against.

3.3.1.2 General Rules

- Carefully check the culture by eye and on a microscope every time when they are handled.
- Maintain the culture without antibiotics, preferably at all times but at least for part of the time, to reveal possible contaminations.
- Check reagents for sterility before use.
- Do NOT share bottles of media or other reagents with other people or use for different cell lines.
- Keep the standard of sterile techniques high.

3.3.1.3 Elements of Aseptic Environment

1. Quiet Area
    a. Keep traffic low and motion slowly.
    b. Keep quiet.
    c. Clean the bench top with 70% ethanol daily. Clean the floor with bleach at least weekly. Clean equipment as scheduled.
    d. Non-sterile procedures should be carried elsewhere.
2. Work Surface

   a. Swab the surface liberally with Gauze Sponge damped by 70% alcohol before and after experiment.
   b. Bring only those items required for the application. Minimize movement in and out the hood.
   c. Arrange the work area so that you have
      i. Easy access to all items without having to reach over one to get another
      ii. A wide, clear space at the center of the bench to work on.
      iii. Suggested arrangement in the biosafety cabinet is shown in the Figure 3.5.
   d. Work in clear space with no obstructions between the central work area and the HEPA filter. Do not block the airflow.
   e. Never leave any paper on the work surface. Secure any lightweight material to prevent their entrapment in the exhaust line.
   f. Work within your range of vision. (when inserting pipette, point the tip away from you.)
   g. Do not use constant flame in the hood. Use the Bunsen burner.
   h. Mop up any spillage immediately and swab the area with 70% alcohol.
   i. When finished, remove everything and swab the work surface down again.
   j. Keep the front door shut when not in use.

3. Personal Hygiene and Protection
   a. Wear lab coat and gloves. Tuck cuff of sleeves into gloves if possible.
   b. Spray hands with 70% alcohol often.
   c. Tie long hair back.
4. Reagent and Media
   a. If commercially obtained, just swab the outside of the bottle with 70% alcohol when they come from the refrigerator or from a water bath.

   b. If prepared from powder, the sterilization procedure of liquid should be followed. Still swab the outside before entering the hood.

5. Cultures
   a. Imported cell lines may be contaminated at the source or in transit. So handle separately until it is ensured to be safe.
   b. Antibiotics should not be used for the imported cell lines because they may suppress.
6. Sterile handling
   a. Swabbing – with 70% alcohol; work surfaces, bottles, flasks, boxes from cold storage or water bath etc.
   b. Capping – Screw caps are preferred. Use aluminum foil to protect the neck of the bottle from sedimentary dust when autoclaving and storing.
7. Flaming – Flame glass pipettes, the necks of bottles and screw caps before and after opening and closing a bottle.
   a. Do not leave bottles open.
   b. Screw caps should be placed with the open side down on a clean surface and flamed before being replaced on the bottle. Or just hold them in hand.
   c. Handling bottles and Flasks
      i. Keep bottles and flasks at an angle as shallow as possible without risk spillage.
      ii. Culture flasks should be laid down horizontally.
      iii. Pipetting – With reusable/disposable glass pipettes

5. Glass pipettes are cleaned, autoclaved and stored in pipette cans with tips towards the bottom of the can. Loosen the top of the can. Hold the can in the left hand, and remove the top of the can with the right hand. Flame the top and the open end of the can. Place the top down on its side. Hold the can horizontally in your left hand and gently shake and tip the can so that the tops of one or two pipettes stick out

of the top of the can about an inch and can be easily grasped. Slide a pipette out and hold 2 inches from the top without touching the pipette to the side of the can. Pass the bottom 1/3 of pipette through the flame for 1-3 seconds. Rotate the pipette 180º as you pass it through the flame. Insert the pipette into pipette aid or pipettor. Hold the bottle from which you will pipette at 45 º angle with your left hand. Open the bottle with your left hand and hold the cap in the last two figures. With the left hand, pass the opening of the bottle through the flame. Pass the pipette through the flame again. Place the tip of the pipette into the container from which you are removing liquid. Don't touch the tip to the inside at all, but place it straight into the liquid. Pipette the volume you require and carefully withdraw the pipette. Flame the donor bottle and recap it. Place it to side. While holding the pipette as still as possible, open the receptacle bottle and dispense the liquid as described above. Discard the pipette. Flame the receptacle bottle and recap it.

iv. With disposable plastic pipettes

Unwrap all the plastic of plastic pipettes needed in an experiment and put them with tips up into a sterile beaker. Do the unwrapping under the hood. Pipetting procedure is the same as above, just without flaming.

v. With pipette tips (Useful for small volumes and small vessels.)

Pipettor and tips are sterilized and arrange well in the hood. After sterilizing, the condensation in the pipette box should be removed to avoid contamination. Adjust the pipettor to the volume needed before open the tips box. Never touch the inner surface of any vessel by the pipettor.

vi. With pipette aid

Charge and clean the outside of pipette aid before putting into hood. Make sure the tips are fitted to the aid before starting.

8. Pouring – Do not pour from one sterile vessel to another.
9. Handling Dishes or Plates

   a. Do not leave dishes open for extended
   b. When removing dishes or transporting them to or from the incubator, take care not to tilt them or shake them to avoid the medium entering the capillary space between the lid and the base. (To remove the medium lodged in the space, discard the lid, blot any medium carefully from the outside of the rim with a sterile tissue dampened with 70% alcohol, and replace the lid with a fresh one.)
   c. Use secondary container to dishes and plates for incubator, and swab the box with alcohol when it is retrieved from the incubator.

10. Sterilization of Apparatus
    a. Glassware
       i. Soak glassware into Decon detergent overnight. (Do not let glassware dry after using.)
       ii. Brush glassware by hand and rinse thoroughly in four times of tap water followed by three times of deionized water.
       iii. Invert bottles and dry upside down.
       iv. Cap bottles with aluminum foil when cool and store.
       v. Dry heat sterilization

Attach a small square of sterile-indicating tape or other indicator label to glassware and date. Place glassware in an oven with fan-circulated air and temperature set to 160ºC. Keep the temperature at least 1 hour. Cool the oven and allow it to cool with the door closed. Use glassware within 24-48 hours.

       vi. Autoclave

Bottles may be loosely capped with screw caps and foil, tagged with autoclave tape. Make sure the cap is autoclavable. Autoclave them for 20 min at 121ºC with a dry cycle. Tighten the bottles. Mist left may increase the risks for contamination. Dry heat is better for glassware. Autoclave caps in steam permeable film separately.

b. Sterilization of glass pipette

Put used pipettes into bucket with 300 ppm hypochlorite and detergent (Decon) to disinfect immediately after use. Soak them at least 2 hours, better over night. Remove plugs with compressed air. Transfer pipettes into pipette washer tops uppermost. Rinse thoroughly by siphoning action of pipette washer for a minimum of 4 hours, followed by DI water rinse. Dry them in oven and plug with cotton. Store them dust free and by size. Collect rinsed pipette into pipette can. Attach sterile indicating tape on the can, bridging the cap to the can. Sterilize by dry heat at 160 ºC for an hour. Remove pipettes from oven and allow it to cool. If not to be used in 48 hours, seal cans with adhesive tapes.

For disposable Pasteur pipettes, rinse with DI water if dusted. Then sterilize by autoclave or dry heat.

c. Sterilization of miscellaneous equipment: follow general rules for sterilization. Items which are not fit for autoclave and dry heat can be immersed in 70% alcohol and dry them off under UV light in a laminar flow hood.

11. Sterilization of Liquid
    a. Use autoclave for heat-stable liquids, such as water, salt solution, and some specially formulated media.
    b. Use filtration for heat-labile liquids.
    c. Water:
        i. Purification: reverse osmosis, distillation, deionization and carbon filtration are all applicable. Then, micropore filter should be used. Standard for type I water at a level >=10MΩ/cm. at 25 ºC, total organic carbon should be <=10ppb.
        ii. Sterilize ultra pure water by autoclaving at 121ºC and 15 psi for 20 min. If the bottle is borosilicate glass (Pyrex), the bottle should be

sealed. If the bottles are unsealed, allow 10% extra volume per bottle to allow for evaporation.

d. Medium should be stored in 0~4 ºC fridge. Serum should be stored in -20 ºC freezer in no less than 50 mL aliquot. If -70 ºC freezer is used to store serum, polycarbonate or high density polypropylene bottle should be used.

3.3.2 Protocols for operation and maintenance of biosafety cabinet

3.3.2.1 Biosafety Cabinet Maintenance

1. General Periodic Cleaning or After Spillage
   - a. Personal protection equipments (PPE) should be worn for every exposure parts, including HEPA filtered respirator
   - b. Make sure the cabinet remains in operational mode with the internal blower on.
   - c. Open the view screen and secure in full position. Clean all readily accessible surfaces of cabinet.
   - d. Remove perforated metal diffuser screen from the underside of the supply HEPA filter and place on the cabinet work tray. Clean both sides of the perforated metal diffuser screen and remove it from the cabinet.
   - e. Lift the cabinet work tray, clean both sides and remove it from the cabinet.
   - f. Remove the front perforated grill, place on the cabinet floor and clean both sides. Remove from cabinet.
   - g. Clean work tray supports.

   h. Working from top to bottom, clean all inside surfaces of the cabinet. Take care not to wet the HEPA filter. If liquid collected in the plenum drain, aspirate it using a plastic tube into an evacuated container.
   i. Clean the plenum drain and wipe try.
   j. If the cabinet requires maintenance and/or replacement of the HEPA filters, the operation should be halted at this point to allow trained personnel to complete replacement of the HEPA and/or maintenance action required.
   k. Replace front grill. Replace work tray and carefully tighten the thumbscrews. Replace perforated metal diffuser screen over the underside of the supply HEPA filter.
   l. Wipe down all exposure surface of the work area with 70% alcohol.
   m. Prepare for aseptic operation.

2. Daily Cleaning
   a. Raise the sliding window. (If desired, full-open position is allowed with the audible alarm key off.)
   b. Apply 5% bleach with gauge sponge and 70% ethanol consecutively. Note: since bleach contains chloride and may destroy the stainless steel. Remove it by 70% ethanol wipe. FOR DAILY WORKING, BLEACH WIPE CAN BE SKIPPED.
3. Lamp replacement: Whenever needed. Check manual for information.
4. UV light replacement

   Lifetime: 7000 hours. Check manual for replace information.

3.3.2.2 Biosafety Cabinet Operation

1. Check the panel lights

   a. Circuit Breaker-Blower – should the circuit breaker open, unplug the appliance plugged into the outlet and merely depress the pop-out button to reset. Should not be continuously open.
   b. Circuit Breaker-Outlets – should the circuit breaker open, unplug the appliance plugged into the outlet and merely depress the pop-out button to reset.
   c. Blower Indicator Light – should be on.
   d. Audible Alarm Enable – should be on.
   e. Minihelic Gauge – should read 0.5” w.g. ± 0.1” w.g.

2. Preparation of work area
   a. Keep everything in “safe working area” – middle to back part of work tray.
   b. Minimize penetration of “air curtain”. – All materials needed for a procedure should be placed in the cabinet before starting. Unnecessary raisin of the hands inside the cabinet above the level of the work opening should be avoided.
   c. Minimize Room Activity!
   d. Aseptic technique – See section 3.4.1
3. Operation
   a. Turn on the UV light about 20 min before operation. Allow the blower to operate at least 15min before aseptic manipulations.
   b. Wipe the interior surface with 70% alcohol.
   c. Put apparatus and materials into the cabinet. No items are placed over the front intake grills. Material should be arranged so that the “clean”, “dirty” are well separated.
   d. Additional purge of the workspace without disturbing should be allowed for 2-3 minutes after materials are put in.

   e. Perform work.
   f. Terminal purge and wipe down – Following completion of work, allow the cabinet to run for 2-3 minutes without disturbing. Remove all the materials. Wipe the interior with 70% alcohol again. Check grills and diffuser grids for spilled or splashed liquid.
   g. Shut down – shut the front window to stop the blower. Do not use cabinet as a depository of anything.

3.3.3 Protocols for operation and maintenance of CO_2 incubator

3.3.3.1 CO_2 incubator maintenance

1. Chamber and Shelf (Perform the following steps before turning on the incubator whenever incubator has been shut down or contamination is concerned.)
   a. Remove all the shelves and water pan from the incubator. Wipe the interior with 70% ethanol. Try to reach all the corners and crevices.
   b. Restore heat and leave the door open until the chamber is dry.
   c. Rinse the shelves and water pan in detergent, rinse them in water, and wipe the shelves and humidity water pan with 70% ethanol.
   d. Return the shelves and water pan to the incubator. The water in humidity water pan should be changed (Fill it with sterile water +1% CuSO4 to act as fungicides).
   e. Close the door and restore CO2.
2. Water-Jacket: Fill the water-jacket with DI water whenever the “Low water” light is on. No anti-bacterial agents are needed.
3. Filter Maintenance
   a. CO_2 supply filter: change it every fifth empty CO2 tanks or when the filter is visibly discolored (yellow-brown).

   b. Air Inlet Filter: change it very three to six months or visibly discolored.
   c. Air pump filter: change it every two years.
   d. CO_2 sensor filter: change it when discolored (yellow-brown).
4. The chamber temperature, door temperature, air injection, CO_2 control, CO_2 sensor and CO_2 injection should all be calibrated regularly. See manual of the instrument for details.

3.3.3.2 CO_2 incubator operation

1. After cleaning with detergent and 70% alcohol, install shelf brackets, shelves and water pan.
2. Fill water pan with sterile DI water.
3. Plug in the incubator to the wall outlet. Turn on the incubator via the power switch on the back panel. Make sure run/setup key indicates blinking green LED with incubator in Setup mode.
4. Check filters. Attach CO_2 gas supply to the CO_2 inlet on the incubator back panel. TURN ON THE CO_2 CYLINDER. (Reading of the cylinder pressure should be 700 to 800 psi (48-55 bar) and the low-pressure gauge reads 20 psi or 1.4 bar.)
5. Enter temperature, CO2 percentage setpoints as shown below.
   a. Setpoint values are entered by pressing the “SEL” key until the LED is lit next to the desired parameter indicator. The value of the selected parameter will be shown in the display in the form “XX.X”.
   b. Press and hold run/setup key for three seconds to Setup.
   c. Press SEL to indicate green LED next to CHMABER TEMPERATURE display or CO_2 PERCENT display.
   d. Press ↑ or ↓ to indicate desired temperature or CO_2 percentage.
   e. Press run/setup key back to run.

6. Press run/setup key to run and let incubator stabilize for 24 hours. The CO_2 percent will indicate “dly” until the incubator reaches within 2 ºC of setpoint temperature. Note: then the CO2 setpoint is set for 0.0%, the CO2 control system is turned off and all alarms are inhibited.
7. Shutting down the incubator
    a. Prior to shutting down the incubator, open the inner and outer doors and remove the water pan. Leave doors open for at least 5 min to purge the chamber, circulating system and the sensors of humidity that could condense and cause faulty readings when the incubator is turned back on.
    b. Be sure to empty the water pan prior to putting it back into the chamber if the incubator is going to be shut off for any length of time.

3.3.4 Protocols for basic cell culture techniques

3.3.4.1 Protocol for Feeding a Monolayer Culture

1. Preparation:
    a. Prepare the hood as protocol for biosafety cabinet.
    b. Pre-warm medium to 37ºC in water bath (15min).
    c. Take the sterilized Pasteur pipette in pipette can and pipette aid or bulb to the cabinet.
    d. Unwrap needed plastic pipettes under the hood and put them into a sterilized beaker in the hood.
    e. Take the beaker with funnel for waste, marker pen into the cabinet.
2. Bring reagents and material necessary for the procedure, swab bottles with 70% alcohol.
3. Take the culture vessel out from the incubator. Examine the culture carefully for signs of contamination or deterioration.
4. Decide whether to change the medium based on pH, cell density and experience.

5. Take the culture into the hood. Uncap the flask.
6. Take a sterile pipette and insert it into bulb or pipetting aid to withdraw the medium and discard into waste beaker. Discard pipette.
7. Uncap the medium bottle. Take a fresh pipette and add the same volume of fresh medium as was removed, and recap the bottle. Discard the pipette.
8. Recap the flask and the medium bottle.
9. Return the culture to the incubator.
10. Complete record of observations and feeding on record sheet and note book.
11. Clear away all pipettes, glassware and swab down the work surface.

3.3.4.2 Protocol for Monolayer Subculture (CHO cells as example)

1. Preparation:
   a. Warm up the nutritional media (10% FBS in high glucose 1x DMEM, 1x PBS and 0.05%trypsin in 37ºC water bath for 15 min.
   b. Observe dishes under microscope and determine passage concentrations based on experiments target and confluency of dish and the overall cell health. (e.g. for CHO cells in 100 mm dish with 100% confluency, if split in 1:4, after 2½ days, the cultures will be confluent again.)
2. Prepare the hood and bring reagents and materials to the hood.
3. While things are warming up, prepare conical tubes and Petri dishes for use later by labeling them appropriately (including cell line, passage number, date and passage dilution for each Petri dish and cell line for conical tubes).
4. Take the culture into the hood. Uncap the flask.
5. Take sterile pipette and insert into bulb or pipetting aid to withdraw the medium and put into corresponding conical tubes. If media is yellowish and it seems dirty,

add fresh warmed media into the conical tube and discard the old media into the waste beaker. Discard the pipette.

6. Wash dishes with enough 1× PBS to fill the surface – shake for 1 min. If use flask, add the 1 × PBS to the side of the flasks opposite the cells so as to avoid dislodging cells. Rinse the prewash over cells and discard by pipetting. This rinse is to remove traces of serum that would inhibit the action of the trypsin and to deplete the divalent cations.
7. After discarding the PBS by pipetting, add 0.05% trypsin to help separating the cells and incubate in 37 ºC incubator for 5 min. (for dishes: 35 mm needs 0.8 ml, 60 mm needs 1.5ml, 100 mm needs 3.0 ml. Or if 0.25% trypsin, 0.2mL/cm^2.) If flask is used, add to the side of the flasks opposite the cells. Turn the flasks over and lay them down. Ensure the monolayer is completely covered.
8. Break up clumps of trypsinized cells by sucking up and down with pipette 40-50 times. If use flask, pipette the cell suspension up and down a few times, with the tip of the pipette at the bottom corner of the bottle, taking care not to create a foam. (If counting cell is needed now, change the trypsin to fresh media and count.)
9. Transfer the broken up trypsinized cells to corresponding conical tubes containing media. Balance the tubes and centrifuge for 5 min at 80-100g.
10. While tubes are spinning, add new warmed media to Petri dishes or flasks. (Petri dish: 35mm needs 1.8 -2.5 ml, 60mm needs 4-5 ml, 100mm needs 9-10ml.) These are total volumes. If you deduct the volume of cell suspension which will be added later from the total, you will get the media volume needed. (For flasks, 10 cm^2, 2ml; 25 cm^2, 5ml; 75 cm^2, 25ml.)
11. After spinning, suck away media to the waste, add 1.8 ml or volume as calculated dilute times media to the tube. And breakup pellet by sucking up and down approx. 40-50 times with trying to avoid creating bubbles.

12. Transfer appropriate amount of cell/media mixture to dishes or flasks. Shake the dish or flask at the horizontal level to four directions. (To the left and right 50 times and up and down 50 times.
13. Take a look at the dish under the microscope and make sure this looks like what you expected in terms of your passaging calculation.
14. Put the dish or flask into incubator. Record the culture on the data sheet on the incubator and your notebook.

3.3.4.3 Protocol for Cell Counting with Hemocytometer

1. Preparation:
    a. Trypsinize the monolayer as for routine subculture and re-suspend in medium to give an estimated 1×10^6 /ml. (When samples are counted in a growth experiment, the trypsin need not be removed and the cells can be dispersed in the trypsinate and counted directly, or after diluting 50:50 with medium containing serum if the cells tend to re-aggregate.)
    b. Transfer a small sample (~1ml) to a vial.
    c. Clean the surface of the slide with 70% alcohol, taking care not to scratch the semi-silvered surface.
    d. Clean the coverslip and wet the edges very slightly, press it down over the grooves and semi-silvered counting area. The appearance of interference patterns (rainbow) indicates that the coverslip is properly attached.
2. Mix the cell sample thoroughly, pipette vigorously to disperse any clumps and collect 20 µL into the tip of a pipette.
3. Transfer the cell suspension immediately to the edge of the hemocytometer chamber, and expel the suspension and let it be drawn under the coverslip by capillary. Do not overfill or underfill the chamber. The fluid should run only to the edges of the grooves.

4. Mix the cell suspension, reload the pipettor, and fill the second chamber.
5. Blot off any surplus fluid (without drawing from under the coverslip), and transfer the slide to the microscope stage.
6. Select a 10× objective, and focus on the grid lines in the chamber. If focusing is difficult because of poor contrast, close down the field iris, or make the lighting slightly oblique by offsetting the condenser.
7. Move the slide so that the field you see is the central area that you can see bounded by three parallel lines. This area is 1 mm^2. With a standard 10× objective, this area will almost fill the field, or the corners will be slightly outside the field, depending on the field of view.
8. Count the cells lying within this 1 mm^2 area, using the subdivisions (also bounded by three parallel lines) and single grid lines as an aid for counting.
9. Count cells that lie on the top and left-hand lines of each square, but not those on the bottom or right-hand lines, to avoid counting the same cell twice. For routine subculture, attempt to count between 100-300 cells per mm^2; the more cells that are counted, the more accurate the count becomes. For more precise quantitative experiment, 500-1000 cells should be counted.
    a. If there are very few cells, count one or more additional squares surrounding the central square.
    b. If there are too many cells, count only five small squares across the diagonal of the larger square.
10. If the slide has two chambers, move to the second chamber to do a second count. If not, rinse the slide and repeat the count with a fresh sample.
11. Calculating: c = n (cells number counted) × 10 × 1000. Use the original total volume to calculate the total cells number.

3.3.4.4 Protocol for Cryopreservation

3.3.4.4.1 Freezing cells

1. Preparation:
    a. Warm up 1 × PBS and trypsin for 15 min in 37 ºC water bath.
    b. Prepare the freezing medium by adding either 10-20% DMSO or 20-30% glycerol to growth medium. (Usually medium with 10% DMSO is only good for 1 month after preparation. Cover with foil and store in fridge. Remember to filter after mixing.)
    c. Look at the culture dish or flask under microscope to make sure that the 100 mm dish for freeze back is 100% confluency. It should also (1) show healthy appearance; (2) show normal morphological characteristics; (3) be at late log phase of growth cycle; (4)be free from contamination.
    d. While things are warming up, prepare conical tubes and cryostasis vials – label freeze vial with cell line, dish or flask size used before freezing, % of confluency, passage number, place to freeze it down, initials and date.
2. Suck away the media from the culture vessel to corresponding conical tubes. If the media is yellowish and dirty, throw them away and add the fresh media into the conical tube.
3. Wash dishes or flasks with enough 1× PBS to fill surface of dish or flask. Shake for 1 min. Suck away PBS.
4. Add 0.05% trypsin to help and separate the cells and incubate for 5 min. For 100 mm dish, 3 ml trypsin should be added.
5. Break up clumps of trypsinized cells by sucking up and down with pipette 40-50 times. See protocol for subculture about this step.

6. Transfer broken up trypsinized cells to corresponding conical tubes containing media. Balance to make sure the conical tubes are at an even weight when centrifuge. Centrifuge it for 5 min at 80-100g.
7. After centrifugation, suck the old media away and add 1 ml only of freeze media and quick 1-2 times of sucking up and down then add to cryostasis vial. Make sure the final concentration is 1×10^6~1×10^7cells/ml.
8. Put the vials into cotton wool in a polystyrene foam box with a wall thickness of ~15 mm. Then put the box into the -80 ºC freezer over night. To control the temperature decreasing rate to 1 ºC /min.
9. Transfer the frozen cells to liquid nitrogen tank if applicable. Or let it stay in -80 ºC freezer (not preferred).
10. Keep good records including exact position of all the frozen cells. Keep one copy of the freezer record at the cell culture area with the incubator.

3.3.4.4.2 Thawing frozen cells

1. Preparation:
    a. Warm up media and add 9 ml into a 15 ml conical tube.
    b. Find the frozen cell line and warm it up in the 37 ºC water bath until just a very tiny bit of ice is left over.
2. Wipe the vial with 70% alcohol. Open the vial under the hood.
3. Pipette the cells into the 15 ml conical tube with warm media.
4. Balance the tube and centrifuge them for 5 min at 80-100 g.
5. Suck away the old media and resuspend the pellet in 2 ml medium.
6. Add 7 ml of warmed media to a new sterile 100 mm dish or proper volume of media to a flask.
7. Transfer the resuspended pellet and 2 ml of media to new 100 mm dish or flask. Shake the dish 50 times at horizontal level back and forth, left and right.

8. Incubate in 37 ºC incubator.

Alternate for step 3: transfer the cell suspension to a conical tube and slowly add (10ml over 2 min) warm medium to the tube to dilute the cryoprotectant. Centrifuge them for 2 min under 100g. Discard the supernatant medium with the cryoprotectant. Resuspend the cells in fresh medium. Seed them in flask for culture.

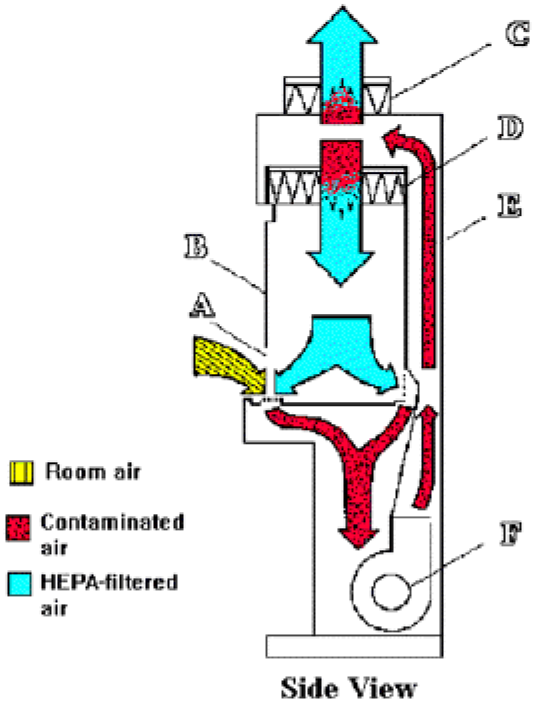

A. front opening
B. sash
C. exhaust HEPA filter
D. rear plenum
E. supply HEPA filter
F. blower

Figure 3.1 Air flow in the Class II type A Biosafety Cabinet

Source: http://oregonstate.edu/ehs/LVSG-BSC-type

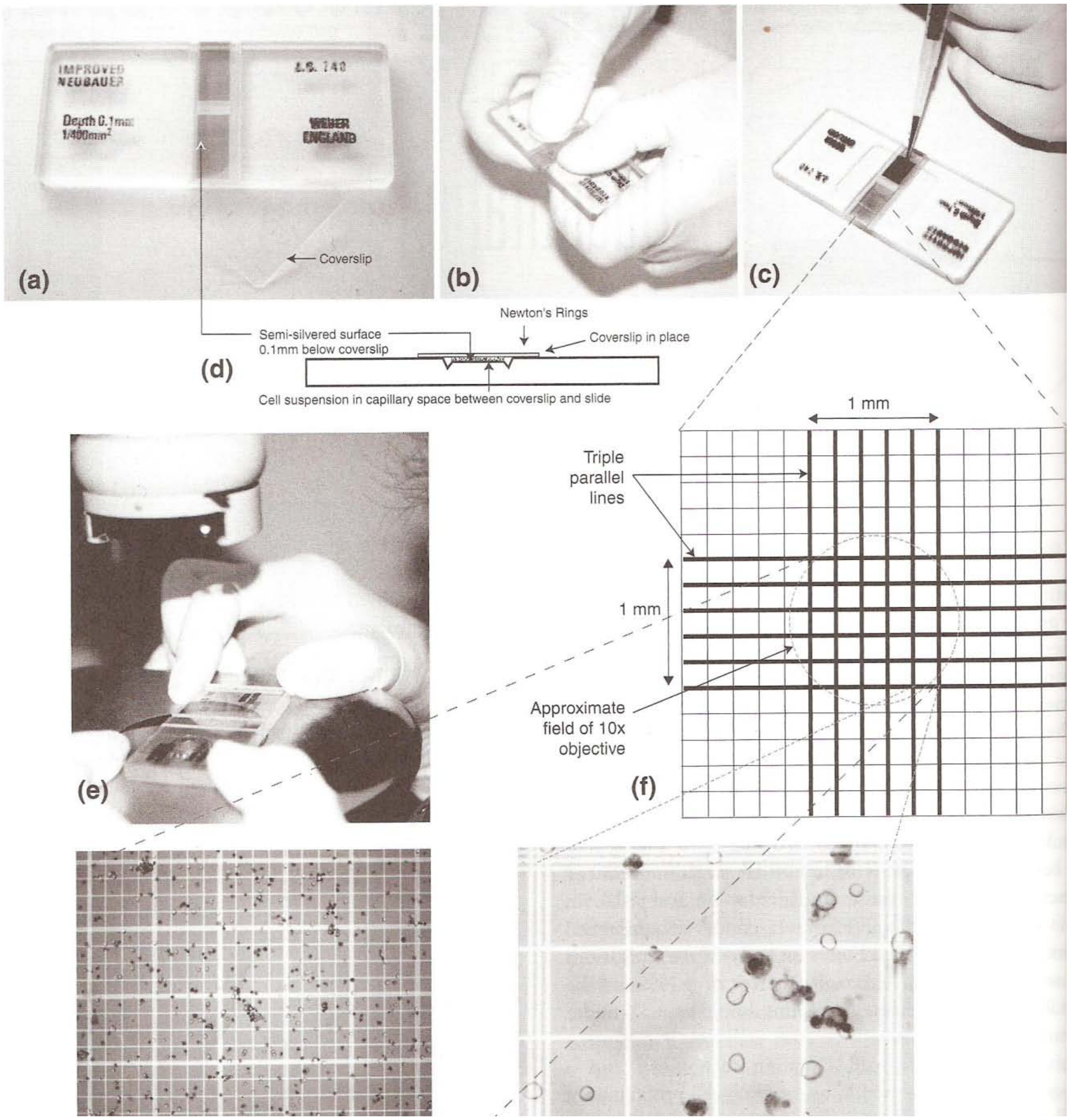

Figure 3.2 Counting cells with a hemocytometer

Source: Freshney, R. I. (2005). *Culture of animal cells : a manual of basic technique.* Hoboken, N.J.: Wiley-Liss.

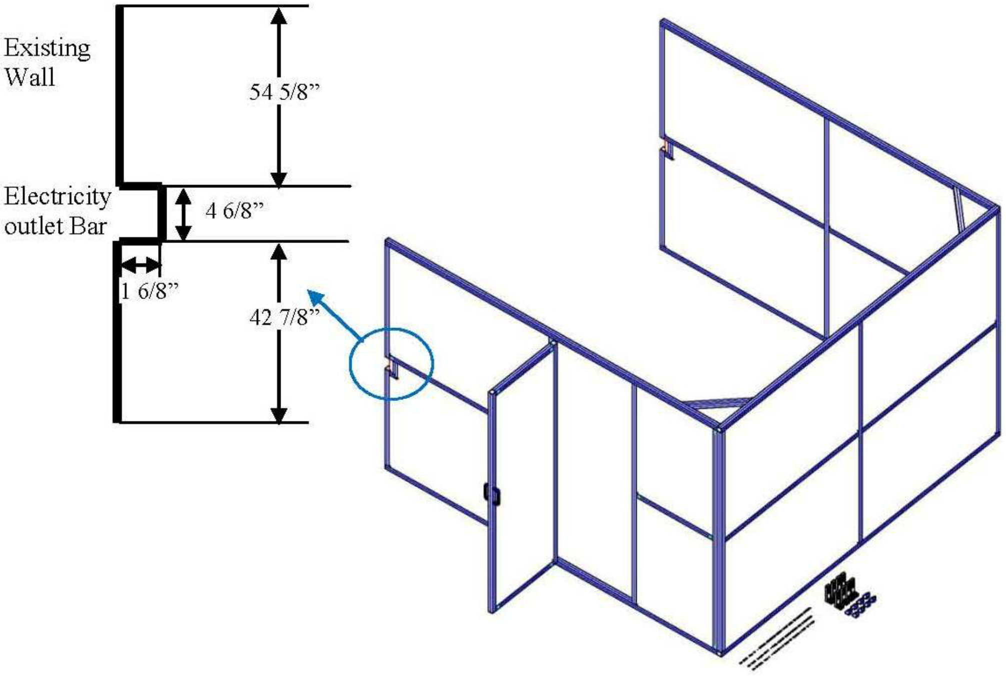

Figure 3.3 Design of the cell culture facility enclosure

Note: The enclosure is designed with assistance from Complete Motion Control Systems and Solutions, 345 South 26th St., Omaha, NE 68131 PO Box 3832 Omaha, NE 68103, Ph: (402) 346-6480 (402) 422-0430 (800) 228-9750 Fax (402) 345-1567, www.cmdimotion.com

Figure 3.4 The cell culture facility in the lab

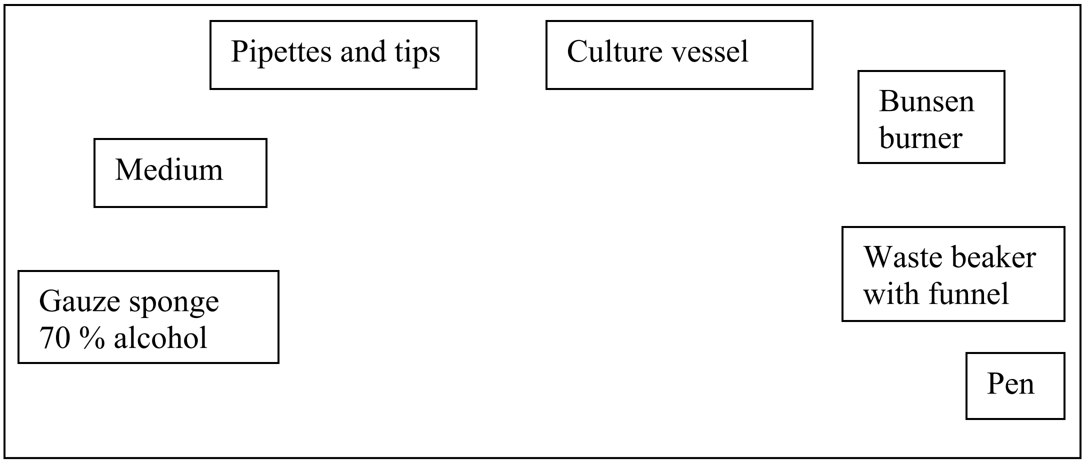

Figure 3.5 Recommended arrangements inside the Biosafety Cabinet

CHAPTER 4

E.COLI CELL AND CHINESE HAMSTER OVARY CELL EXTRACTION AND SEPARATION

4.1 Introduction

In order to establish the protocol for extraction and separation of endogenous fluorophores from cells, two types of easily accessible cells, *Escherichia coli* (*E. coli*) cells and Chinese Hamster Ovary (CHO) cells, have been used as models to study the extraction and separation.

The extraction and CE separation of metabolites from the bacterial cells, such as *Bacillus subtilis* (*B. subtilis*) and *E. coli*, have been widely studied [104-105, 107, 110, 122, 166, 175]. The typical extraction methods include cold methanol, hot methanol, perchloric acid or formic acid, alkaline, or methanol/chloroform extraction [175]. For example, ice-cooled methanol extraction followed by removal of phospholipids liberated from the cell membrane with chloroform and removal of proteins and other debris by ~5000 Dalton cutoff filter allows the identification of $NAD(P)^+$ and NAD(P)H in the separation results of the extracts [105, 107, 122, 166]. The formic acid extraction usually allows the identification of FAD and FMN in the separation results of the extracts [104, 110]. However, to the best of our knowledge, there is no extraction method for bacterial cells to allow identification of both flavins and nicotinamide nucleotides in the extracts.

Since CHO cells and derivative cell lines have been widely used as models in biomedical investigation including cancer research [176-177], the wild type CHO cell is used as a model for normal cells versus cancer cells. Extraction and separation of CHO cells have been studied for nucleotides and nucleotide sugars identification [178-179]. Kochanowski et al. used cold 0.5 M perchloric acid extraction and identified 13 nucleotides and nucleotide sugars in CHO cell extracts with RP-HPLC separation [178]. Feng et al. used 5% Triton X-100, acetonitrile and chloroform to extract CHO cells and identified 19 nucleotides and nucleotide sugars with CE separation [179]. Neither flavins nor nicotinamide nucleotides were identified in these two reports. Based on the extraction method used for immortalized SCN 2.2, RN33B, NG108-15 cells extraction [98, 134-135], we developed an extraction and separation method for simultaneously identifying flavins and nicotinamide nucleotides in CHO cell extracts [180].

In this chapter, the extraction and separation of *E. coli* cells and CHO cells with the motivation to identify flavins and nicotinamide nucleotides simultaneously are discussed in detail to illustrate the process of establishing our cell extraction and separation protocols.

4.2 Experimental

4.2.1 Chemicals and Materials

FAD (95%), β-NADH (98%), FMN (~95%), RF (>98%) and β-NADPH (97%) were obtained at the highest purity from Sigma (St. Louis, MO, USA) and used as received. Sodium dihydrogen phosphate, disodium hydrogen phosphate, boric acid and sodium hydroxide were purchased from Aldrich (Milwaukee, WI, USA). EDTA disodium salt (Amresco, Solon, OH, USA), Tris[hydroxymethyl] aminomethane (>99.9%, Sigma, St. Louis, MO,USA), [3-[3-chloramidopropyl]-dimethylamminio]-1-propanesulfonate (CHAPS, >99.0%, Research Products International Corp. Mt. Prospect, IL, USA), LB broth base (LENNOX L broth base, Invitrogen, Carlsbad, CA, USA), methanol (optima, FisherChemical, Fairlawn, NJ, USA), and chloroform (FisherChemical, Fairlawn, NJ) were used as received. Ultra pure Milli-Q (Millipore, Bedford, MA, USA) water was used to prepare all solutions. Stock solutions were prepared daily and CE separation was performed no later than 5 hours after sample preparation. Different concentrations and pHs of phosphate and borate buffers were prepared, and the run buffer was adjusted to the target pH using 0.1 M sodium hydroxide solution. All solutions were filtered through 0.20 μm syringe filters (Cole-Parmer Instrument Co., Vernon Hills, IL, USA) and sonicated prior to experiment.

4.2.2 *E.coli* cells culture and extraction

The *E.coli* cells were cultured in 20g/L LB broth at 37 °C by shaking (200 rpm). The cell growth was monitored by measuring the optical density (OD) at 600 nm. The growth was discontinued when the OD reached 0.7, which could be translated as a cell concentration of 2.0×10^{11} living cells per mL. Then, the cells were evenly distributed in 10 mL aliquots to 15 mL centrifuge tubes and centrifuged at 4 °C and 5000 rpm for 5 minutes. The media were withdrawn from the cell pellets. The cell pellets were washed by 2 mL 10 mM pH 7.0 phosphate buffer for two times with centrifugation at 4 °C and 5000 rpm. To each cell pellet, 2 mL ice-cooled methanol was added to the tube and incubated at room temperature for 10 min followed by 30 min in the -20 °C freezer. After this period of incubation, the mixture was centrifuged at 4 °C and 5000 rpm for 10 minutes. The supernatants were transferred to another tube and a 2 mL mixture of chloroform and water (2.5 : 1) was added to the methanol solution. The solution was mixed thoroughly by vortexing for 30 seconds and stored at room temperature for 10 minutes. Following this, the solution was centrifuged at 4 °C and 5000 rpm for 10 min and the upper layer solution was loaded to a 3000 Dalton cutoff centrifuge filter. The filter was centrifuged at 4°C 5000 rpm (~4500 g) for 1 hour. The resulting 1~2 mL solution was lyophilized and then dissolved in 50 μL H_2O for separation.

4.2.3 CHO cells culture and extraction

Wild type Chinese Hamster Ovary (CHO) cells were obtained from Professor Jim Jung-Ching Lin's Lab, Department of Biology at the University of Iowa. The CHO cells were maintained in Dulbecco's Modified Eagle Medium High Glucose (Invitrogen, Carlsbad, CA, USA) supplemented with 10% fetal bovine serum (Atlanta Biologicals, Lawrenceville, GA, USA) and seeded in 25 cm^2 canted tissue culture flasks with vent cap (Corning Incorporated, Corning, NY, USA). The cells were cultured in a 37°C incubator with 5% CO_2 until they reached the 100% confluency. For each batch of extraction, one flask of cells was digested by 0.05%/Trypsin/EDTA (Invitrogen, Carlsbad, CA, USA) and counted with a hemocytometer to assist the quantification of compounds per cell. Adapted from extraction methods by Wise and Shear [98], the metabolites were extracted from the cell monolayer without being digested by Trypsin. As depicted in Figure 4.1, after the medium was removed with pipettes and cotton swabs, the cell monolayer in the flask was rinsed by iced 20mM glucose in Delbecco's phosphate buffered saline without Calcium and Magnesium (Invitrogen, Carlsbad, CA, USA). The DPBS was then removed thoroughly with pipettes and cotton swabs. The extraction buffers (120 mM Tris, 10 mM EDTA, and 7 mM CHAPS) were added into the flask. Then, the flasks were put on ice in a Branson 2210 sonicator (Branson Ultrasonics Corporation, Danbury, CT, USA) to sonicate for 3 min and the pHs of the extracts were immediately adjusted to ~9.0 by iced 1.2 M HCl, followed by 60 sec sonication for mixing. The resulted extracts were transferred into Millipore Amicon® Ultra-4 30kD NMWL 4mL centrifugal filter units (Millipore, Bedford, MA, USA) and filtered for 15 min at 4500 rpm using a Beckman Coulter Allegra 21R Centrifuge (Beckman Coulter, Fullerton, CA, USA). The centrifugal filter units were rinsed with water and 0.1 M NaOH to remove glycerol before use. The filtrate was collected and analyzed by CE-LIF immediately.

4.2.4 Instrumentation and CE separation conditions

A Beckman P/ACE™ MDQ system (Beckman Coulter, Fullerton, CA, USA) was used to perform the CE separations. The separation conditions were described in Chapter 2. Briefly, in LIF detection, the excitation was provided by a He-Cd laser at 325 nm and the fluorescence emission was collected through a 345 nm long pass filter to reduce scattered laser light. The excitation power was typically 1 mW. Polyimide coated fused silica capillaries (Polymicro Technologies, Phoenix, AZ) with an effective length of 20 cm (30 cm × 50 μm I.D.) were used in the experiment. Prior to use, the capillaries were preconditioned with sodium hydroxide and run buffer. Between runs, the capillary was conditioned consecutively with 0.1 M sodium hydroxide, 0.1 M hydrochloric acid, deionized water and run buffer. Samples were introduced by pressure injection for 10 seconds at 0.5 psi (~3.5 kPa). The temperature of the capillary was maintained at 25ºC with the thermostating system of the instrument. Separation of *E. coli* cell extracts was performed with 30 mM pH 8.0 phosphate buffer and 40 mM pH9.0 borate buffer. Separations of CHO cell extracts were performed under15 kV in 170 mM, pH 9.0 borate buffer, which was the optimized condition.

4.2.5 Identification and quantification of endogenous fluorophores in cell extracts

The flavins and NAD(P)H were identified by spiking the cell extracts with standard solutions of NAD(P)H, RF, FMN and FAD. To quantify the identified compounds in the cell extracts, the standard addition method was used for each compound. Briefly, 0.5 μL, 1.0 μL, 1.5 μL, and 2.0 μL standard solutions with appropriate concentration were added into 50 μL cell extracts. Since the added volumes (V_s) were much smaller than the initial volume ($V_{initial}$), there was a linear relationship between the ratio of peak areas after (I_{x+s}) and before (I_x) standard additions and the added volume (V_s) as shown in equation 4.1.

$$\frac{I_{x+s}}{I_x} = \frac{[s]_{initial}}{[x]_{initial} V_{initial}} V_s + 1 \tag{4.7}$$

In equation 4.1, $[s]_{initial}$ is the concentration of the added standard solution and $[x]_{initial}$ is the initial concentration of the analyte in the sample. After CE-LIF runs, the peak area ratios were plotted vs. the added volumes of the standard and fitted by linear regression.

The initial concentration of the analyte in the sample can be calculated by the slope of the line I_{x+s}/I_x vs. V_s as shown in equation 4.2.

$$[x]_{initial} = \frac{[s]_{initial}}{slope \times V_{initial}} \qquad [4.8]$$

The mass of each compound in a cell was estimated according to the cell numbers obtained from parallel cell counting as shown in equation 4.3.

$$\text{Moles of a compund per cell} = \frac{\text{Concentration in extracts} \bullet \text{Volume of extracts}}{\text{Number of cells}} \qquad [4.9]$$

4.3 *E. coli* cells extraction and separation

The cold methanol/chloroform extraction of *E. coli* cells uses cold methanol to break the cell wall, chloroform to extract the phospholipids from the cell membrane, and a 3000 Dalton cutoff centrifugal filter to remove the larger protein molecules. Since there are no mitochondria in the bacterial cells, once the cell wall is broken, our targeted molecules, the flavins and nicotinamide nucleotides cofactors, as well as other enzyme and metabolites are released to the solution. However, there is no protection designed to preserve the cofactors. Considering the instability of these cofactors discussed in Chapter 1 and the complicated enzyme reactions that may happen once the cell wall is broken, it is unlikely that we could preserve most of the cofactors in the cell extracts. The separation results of the *E. coli* cell extracts shown in Figures 4.2 and 4.3 demonstrate that neither FAD nor NADH are identified in the cell extracts. In the Figure 4.3 electropherogram in borate buffer, a peak from the cell extracts at migration time of 94 seconds has very close migration time with the FAD spiking peak. However, in the electropherogram in phosphate buffer shown in Figure 4.2, there is no peak co-migrating with the FAD spiking peak. Therefore, there is no firm evidence to identify any of the peaks as FAD or NADH. Under our experimental conditions, the cold methanol/chloroform extraction does not allow us to identify our targeted molecules. An extraction method with more gentle conditions and more protection for flavins and nicotinamide nucleotides is needed.

4.4 CHO cells extraction and separation

The CHO cells were extracted with the method depicted in Figure 4.1. The extracts were separated by CE-LIF to identify the flavins and nicotinamide nucleotides. The conditions for separation and detection are thoroughly investigated to ensure sufficient detection sensitivity for cell contents, reliable reproducibility and valid quantification for cell extracts.

4.4.1 Separation of CHO cell extracts

4.4.1.1 Optimization of buffer nature and concentration

Although the buffer nature, pH and concentration have been optimized for the flavins and nicotinamide nucleotides as described in Chapter 2, the buffer conditions need to be modified and optimized to accommodate the high ionic strength and complex matrix of the cell extracts. Both the phosphate and borate buffer systems have been used to test their applicability.

Figure 4.4 shows the electropherograms of CHO cell extracts separated in pH 8.0 phosphate buffers with different concentrations ranging from 50 mM to 120 mM. With all these concentrations, the electropherograms in the phosphate buffer do not show a stable baseline and the peaks are not well differentiated, thus appearing as broad bands. The baseline tends to be more stable for the separation with 120 mM phosphate buffer than with the 50 mM phosphate buffer. There is a possibility that the baseline can become more stable if the concentration of phosphate buffer is further elevated. But considering the potential destruction of NAD(P)H in phosphate buffer with concentrations higher than 100 mM [103, 130], no further attempts were made to use phosphate buffer with higher concentrations to separate the CHO cell extracts.

Following the effective separations demonstrated in Chapter 2, the CHO cell extracts were separated in pH 9.0 borate buffers at concentrations 50 mM, 100 mM, and 175 mM (Figure 4.5). The electropherograms clearly show that the 175 mM pH 9.0 buffer yielded a more stable baseline and better resolution than buffers at lower concentrations. Since the flavins and nicotinamides nucleotides are stable in borate buffer, 175 mM pH 9.0 buffer was used for separation of cell extracts thereafter.

4.4.1.2 Optimization of injection duration

To avoid overloading, the sample injection volume is usually controlled between 1-5% of the total capillary volume as the preference in traditional chromatography [145]. But since the phenomenon of sample stacking could occur in CE separation, as a result of a difference between the ionic strengths of the sample plug and the buffer environment, the length of the sample plug sometimes can be as long as the capillary length. In our experiment, since the cell extracts contain extraction buffer as well as the cell content, estimation of the exact ionic strength is not straightforward. Therefore, we studied the effects of sample injection time on separation to determine the optimized injection volume.

Figure 4.6 shows the sample electropherograms with different injection volumes of CHO cell extracts. The injections are performed under 0.5 psi pressure for 3, 5, 10, 15 and 20 seconds, respectively. Estimated by Equation 2.5, these injection durations correspond to injected sample volumes of 6, 10, 20, 30, and 40 nL, respectively. The lengths of these injection plugs are approximately 1.5%, 2.5%, 5.0%, 7.5%, and 10.0% of the effective length of the capillary (length to the window), respectively.

As expected, with the increment of sample loading, the intensities of the peaks increased. In fact, the signal-to-noise ratios are improved from 6, 13, 293, and 105 with 3-second injection to 99, 239, 2527, and 1287 with 20-second injection for FMN, FAD, NADH and NADPH, respectively. However, with increased sample loading, peak resolution and separation efficiency can deteriorate. The resolution of the two most prominent peaks, NADH and NADPH, and the efficiency of the two peaks were calculated by Equations 2.3 and 2.4 and summarized in Table 4.1. The resolution of the two peaks decreased over 30% when the injection time lengthened from 3 seconds to 20 seconds. The efficiency for NADH was reduced to below 10^5 for the 20-second injection while the efficiency for NADPH did not change significantly with the extended injection duration. In all, considering that a 10-second injection offered the sample plug with a length about 5% of the effective length, reasonable resolution and efficiency for the two peaks examined, and signal-to-noise ratios higher than 10 for FMN (44), FAD (77), NADH (1599), and NADPH (553), it was selected as the injection duration for cell extracts.

4.4.1.3 Peak identification

As shown in Figure 4.7, FAD, FMN, NADH, and NADPH were cleanly separated in the CHO cell extracts. Peak identification was achieved by spiking the electropherogram with standard solutions of these endogenous fluorophores. The contribution of nicotinamides to the total fluorescence is several times higher than the contributions from flavins, as illustrated in the inset of Figure 4.7, which is consistent with the results of tissue spectroscopy.

4.4.1.4 Reproducibility of CE-LIF separation of CHO cell extracts

The reproducibility of separation for CHO cell extracts was evaluated with the relative standard deviations of migration times and peak areas, both within days and between days. The relative standard deviations of CE parameters are summarized in Table 4.2. The RSD in migration times for all four compounds was lower than 0.4% for both within day and between days, which indicates that the migration times provide a good parameter for identifying the four compounds. The RSDs in peak areas between 3 days were lower than 5% for all four compounds, suggesting that the extracts are stable at least for 3 days when they are stored at 4ºC in the dark. The within-day RSDs in peak areas were lower than 5% for FAD, NADH, and NADPH but higher for FMN. The concentrations of the compounds in the cell extracts were about 8, 180, 35, and 7 times as high as their respective detection limits. The magnitudes of RSDs are consistent with the signal-to-noise levels in the experiments. To reduce the RSDs, it will be advantageous to implement sensitivity-enhancing methods, such as dynamic pH junction-sweeping [104, 181].

The sample electropherograms of CHO cell extracts on different days after extraction are shown in Figure 4.8. Besides the variation reflected in Table 4.2, we also observed that two unidentified peaks around 160 seconds grew significantly over days. These two peaks did not always appear in every extract and they may be random pieces of peptides decomposed from proteins. This fact also reminds us that for biological systems extracted from living cells, the biological variation can sometimes be overwhelming. To minimize the possible variations, especially for quantitative experiments, it is necessary to keep the manipulation of cells and the extraction conditions as consistent as possible.

4.4.2 Optimization of extraction conditions

4.4.2.1 Optimization of extraction buffer pH and final extracts pH

Since the oxidized flavins prefer acidic environments while the reduced nicotinamides are more stable under basic conditions, the extraction pH is the most important parameter to optimize to effectively extract flavins and nicotinamides simultaneously. During the extraction of CHO cells, two solution pHs are crucial for the extraction efficiency – the pHs of the initial extraction solution and of the final extracts.

Figure 4.9 and Figure 4.10 show the effects of extraction solution pH and final extracts pH, respectively, on the peak area of the four compounds in the electropherogram.

As shown in Figure 4.9, the extraction efficiencies for NADH and NADPH keep improving when the pH of the initial extraction solution increases while the FAD and FMN extraction efficiencies reach their maxima at pH 13.0. As a compromise between the two types of compounds, pH 13.0 was selected for the initial extraction solution.

As illustrated in 4.10, the extraction efficiencies of all compounds reach their peaks when the final extracts pH is ~9.4. The extraction method was thus established to use hydrochloric acid to adjust the pH after sonication to this target pH. As in the examples shown in the figure, for extraction of cells in the 25 cm^2 flask (~ 2.0×10^6 cells), 400 μL extraction solution is needed and 20 μL 1.2 M HCl is used to adjust to the target pH. It is worthwhile to mention that although we attempt to control the final extracts pH with the high concentration extraction buffer and the addition of hydrochloric acid, the different quantity of the cells in the flask and their different conditions could alter the final pH significantly. In practice, with our method, the final extract pH can be controlled within the range of 9.0 to 9.5.

4.4.2.2 Necessity of adjusting pH after breaking cells

The necessity of adjusting pH after breaking cells with high pH surfactant solution has been emphasized. Figure 4.11 illustrates that if a pH 9.2 extraction solution is directly used instead of a pH 13.0 extraction solution with pH adjustment after breaking cells, the intensities of all the four compounds interested are decreased by at least two to three times. This is due to the inefficiency of breaking cell membrane when the surfactant (CHAPS) solution is at a lower pH environment. The surfactant is a sulfobetaine derivative of cholic acid. As a zwitterionic compound, it does not have a net charge between pH 2 to 12. The critical micellar concentration (CMC) for CHAPS ranges between 3-10 mM depending on solution conditions [182]. The concentration we used is about 7 mM. The formation of micelles is thus highly possible. In all, using CHAPS and sonication to break cell membranes and mitochondria, a higher pH is desired but this pH has to be adjusted back to around 9.0-9.5 after breaking the cells to preserve the interested molecules.

4.4.2.3 Cell quantities for extraction

The extraction method we adapted breaks cells on the surface of the culture flask/dish without digesting them. The advantage of this manipulation is to minimize the pipetting process and lower the possibility of sample loss or introduction of interferences [98]. However, it also brings two issues in the extraction. One issue is that the exact number of the cells extracted cannot be counted before extraction. The cell numbers can only be estimated by counting cells in a parallel culture. The second issue is that the cell quantities for extraction are limited by the device used for cell culture. In Figure 4.12, the electropherograms of CHO cell extracts from a T-25 flask (with surface area 25 cm^2) and a T-75 flask (with surface area 75 cm^2) are compared. As expected, the concentrations of the compounds in the cell extracts are increased with the cell quantity. The signal-to-noise ratios corresponding to these electropherograms are summarized in Table 4.3. With the cell quantity increased by 4 to 5 times, the signal-to-noise ratios are also increased about 3 to 5 times. Therefore, it is an option to extract the cells from a larger culture flask to improve the signal-to-noise ratio of the electropherogram. In practice, the T-25 flasks are still easier to manipulate, especially for condition optimization experiments, which require large amounts of extracts. Therefore, the T-25 flasks were used to culture cells for extraction as long as the cell quantities in the T-25 flasks offered sufficient signal-to-noise ratios (>10) for all the compounds.

4.4.3 Quantification of FMN, FAD, NADH and NADPH in CHO cell extracts

The mass of each compound per cell under the extraction conditions was estimated from linear fitting of the standard addition curve and corresponding cell numbers obtained in parallel cell counting. (Table 4.4) The cell extract is a complicated matrix that affects the signal and the quantification of fluorescent compounds in the extract. To minimize matrix effects, the standard addition method was used to quantify the four identified fluorophores. Briefly, small amounts of standard solutions with known concentrations were added into the cell extract and the CE separation was performed for the extract after each addition. The ratio of peak areas for the compound of interest after/before standard addition showed linear dependence on the added volumes as shown in Table 4.4. Three replicate CE runs were performed for each sample. The concentrations of FMN, FAD, NADH, and NADPH were detected to be 0.033, 0.18, 1.8, and 0.37μM, respectively. The extracted masses of these compounds were estimated to be 1.58, 8.5, 90 and 18 attomoles in each CHO cell.

4.5 Conclusion

The protocols for extraction and separation of endogenous fluorophores, FAD, FMN, NADH and NADPH, from CHO cells have been established. The standard addition method proved to be effective for quantitative determination of the four compounds. These protocols form the basis for the extraction and separation of endogenous fluorophores in normal and diseased cells and tissue. Quantification of fluorophore composition in cells and tissue at various physiological stages will provide guidance to optical biopsy for cancer diagnosis. The separation of CHO cell extracts suggests that NADPH and FMN when excited at 325 nm may contribute to the autofluorescence at a similar level to NADH and FAD. It is envisioned that separation of cell and tissue extracts will identify the correct collection of fluorophores to be included in statistical models for optical biopsy.

Table 4.1 Comparison of resolution (R) and efficiency (N) of NADH and NADPH in separation of CHO cell extracts with different sample injection duration

Injection duration	R	N_{NADH}	N_{NADPH}
3 seconds 0.5 psi	35.2	3.0×10^5	4.4×10^5
5 seconds 0.5 psi	35.8	3.1×10^5	4.8×10^5
10 seconds 0.5 psi	32.8	2.8×10^5	4.9×10^5
15 seconds 0.5 psi	29.3	2.3×10^5	5.5×10^5
20 seconds 0.5 psi	25.6	0.20×10^5	5.8×10^5

Note: The resolutions and efficiencies were calculated by Equation 2.3 and 2.4 based on the electropherograms in Figure 4. 6.

Table 4.2 Repeatability of CE-LIF separation of CHO cell extracts

	RSD in Migration time		RSD in Peak area	
	Within days (n=4)	Day-to-day (n=20)	Within days (n=4)	Day-to-day (n=12)
FMN	0.18%	0.27%	11.46%	3.87%
FAD	0.21%	0.26%	5.53%	3.60%
NADH	0.32%	0.39%	2.64%	1.71%
NADPH	0.17%	0.31%	1.48%	5.08%

Table 4.3 Comparison of signal-to-noise ratios of FMN, FAD, NADH, and NADPH in electropherograms of CHO cell extracts from T-25 flask and T-75 flasks with different extraction solution volumes

	Cell number extracted (n=3)	Signal-to-noise Ratio			
		FMN	FAD	NADH	NADPH
T-25 flask with 400 µL extraction solution	(1.01±0.04) × 10^7	10.3	16.1	207	31.9
T-75 flask with 600 µL extraction solution	(5.7±0.1) × 10^7	40.4	40.7	648	147

Table 4.4 Quantification of the four endogenous fluorophores in CHO cell extracts

	Standard Addition Results		Conc. in extracts/μM	Number of cells extracted	Estimated mass in each cell/amol
	Equation*	r^2			
FMN	y=(1.1±0.2)+(4.4±0.1)x	0.99	0.033±0.001	$(5.8\pm0.9)\times10^6$	1.58±0.07
FAD	y=(1.0±0.1)+(1.14±0.08)x	0.92	0.18±0.01	$(5.8\pm0.9)\times10^6$	8.5±0.7
NADH	y=(1.007±0.009)+(0.101±0.008)x	0.90	1.8±0.2	$(5.8\pm0.9)\times10^6$	90±10
NADPH	y=(0.98±0.03)+(0.53±0.03)x	0.96	0.37±0.02	$(5.8\pm0.9)\times10^6$	18±1

Note: *y and x stand for peak area and added standard volume respectively.

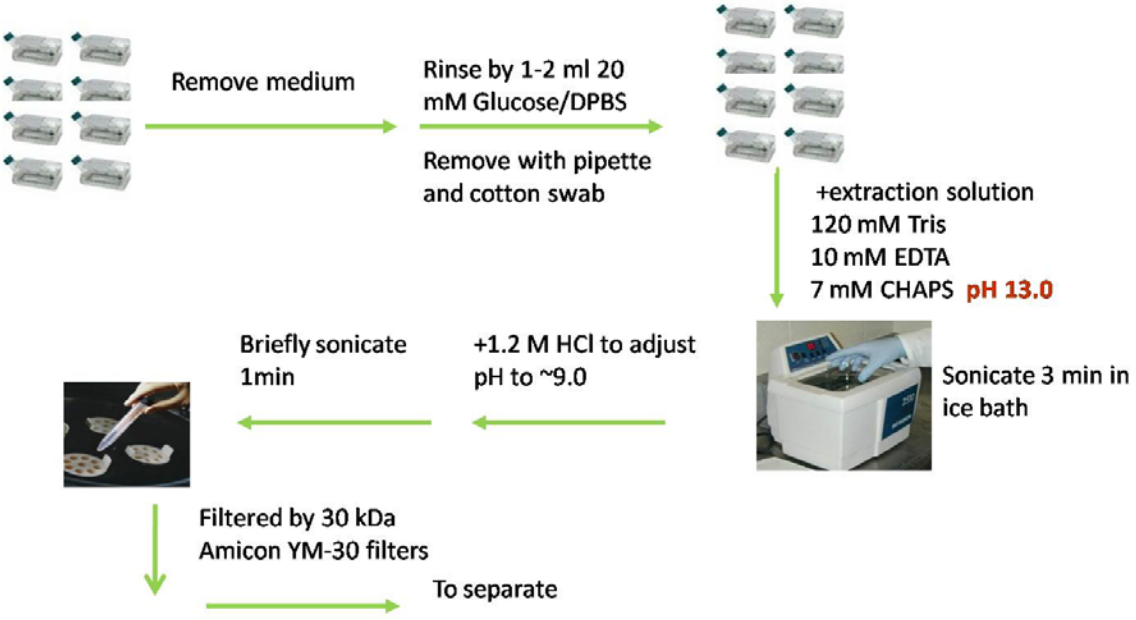

Figure 4.1 CHO cell extraction procedure

Note: The extraction method is adapted from Wise, D. D.; Shear, J. B., Tracking variations in nicotinamide cofactors extracted from cultured cells using capillary electrophoresis with multiphoton excitation of fluorescence. *Analytical Biochemistry* **2004,** *326* (2), 225-233.

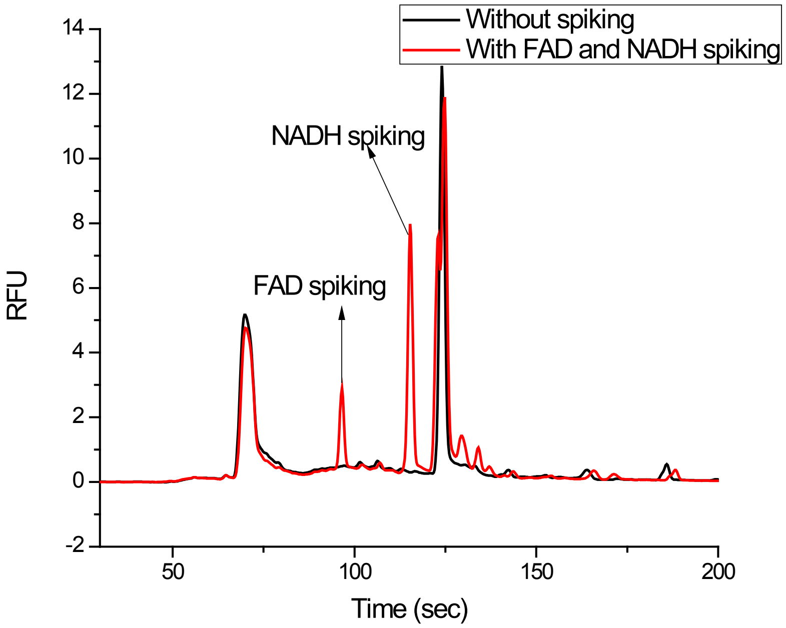

Figure 4.2 Electropherogram of *E. coli* cell extracts separated in phosphate buffer

Note: Separation conditions: buffer: 30 mM phosphate buffer (pH 8.0), high voltage 20 kV, effective capillary length: 20.5 cm, capillary i.d. 50 µm, injection: 0.5 psi 5 sec, LIF excitation at 325 nm (He-Cd Laser), emission collected though 345 nm long pass filter.

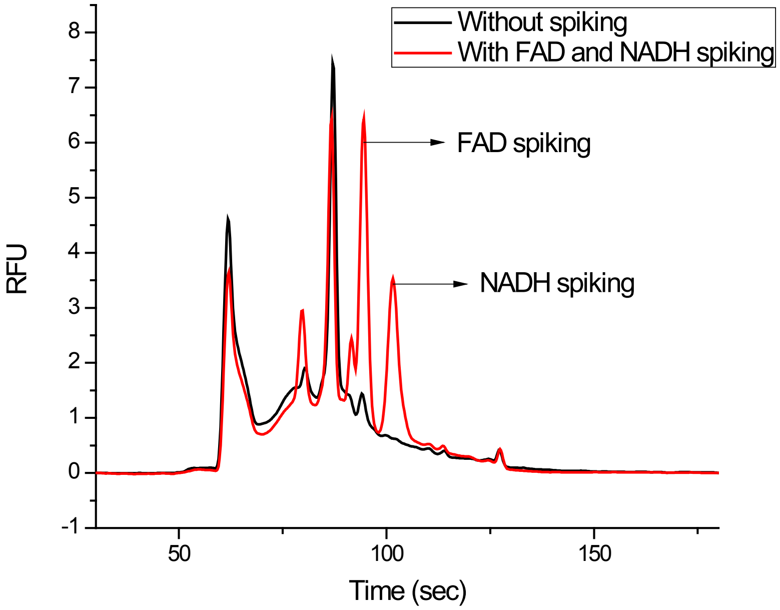

Figure 4.3 Electropherogram of *E. coli* cell extracts separated in borate buffer

---

Note: Separation conditions: buffer: 40 mM borate buffer (pH 9.0), high voltage 15 kV, effective capillary length: 20.5 cm, capillary i.d. 50 µm, injection: 0.5 psi 5 sec, LIF excitation at 325 nm (He-Cd Laser), emission collected though 345 nm long pass filter.

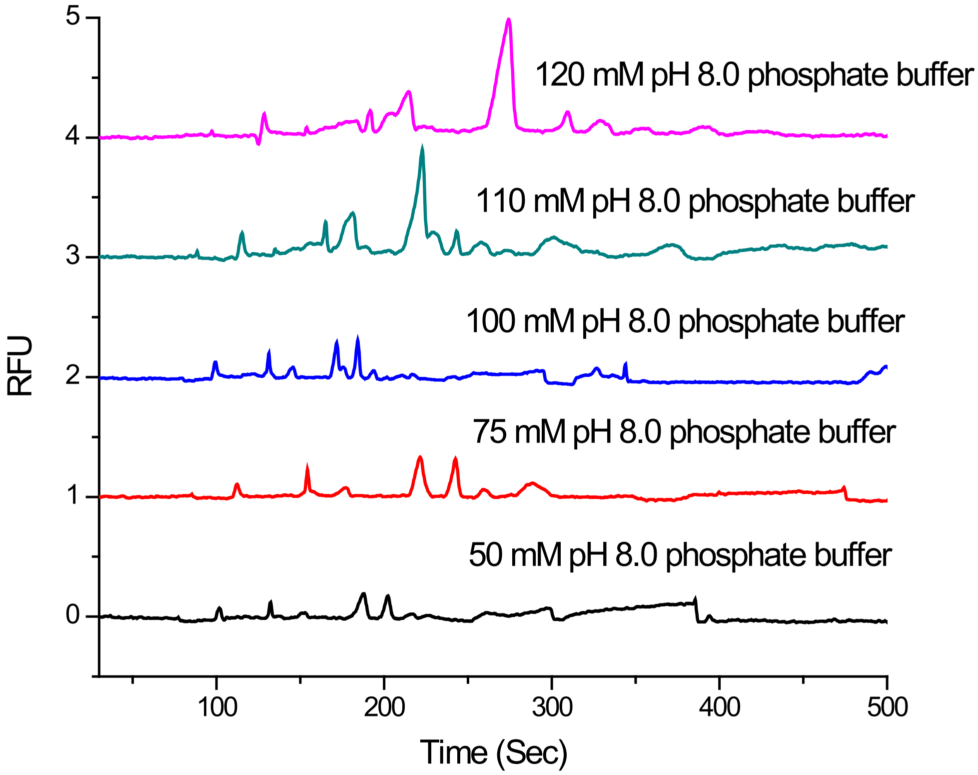

Figure 4.4 Effects of phosphate buffer concentration on CE separation of CHO cell extracts

---

Note: Separation conditions: buffer as shown in the figure, high voltage: 20 kV, effective capillary length: 20.5 cm, capillary i.d. 50 µm, injection: 0.5 psi 5 sec, LIF excitation at 325 nm (He-Cd Laser), emission collected though 345 nm long pass filter.

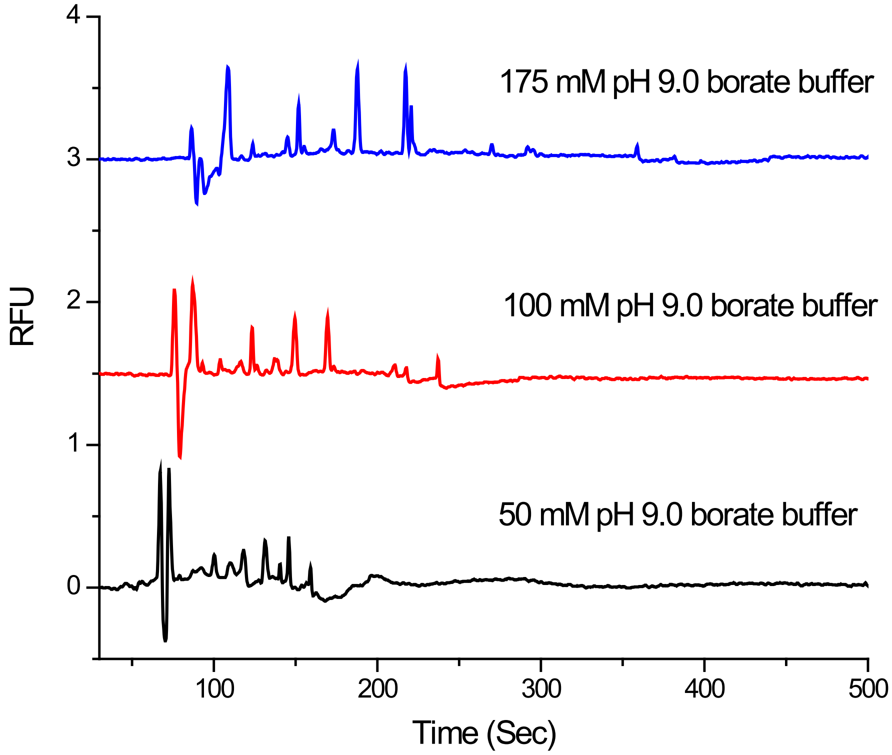

Figure 4.5 Effects of borate buffer concentration on CE separation of CHO cell extracts

Note: Separation conditions: buffer as shown in the figure, high voltage: 15 kV, effective capillary length: 20.5 cm, capillary i.d. 50 μm, injection: 0.5 psi 5 sec, LIF excitation at 325 nm (He-Cd Laser), emission collected though 345 nm long pass filter.

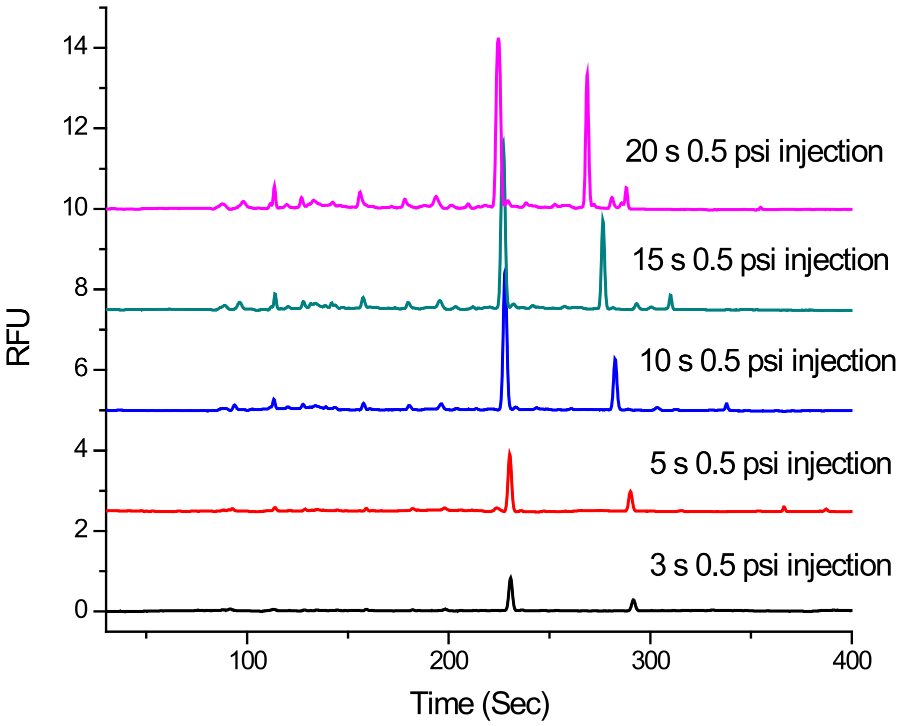

Figure 4.6 Effects of injection time on CE separation of CHO cell extracts

---

Note: The cell number extracted was (5.8 ± 0.8) × 10^6.

Separation conditions: injection duration and pressure as shown in the figure, buffer: 175 mM borate buffer (pH 9.0), high voltage 15 kV, effective capillary length: 20.5 cm, capillary i.d. 50 µm, LIF excitation at 325 nm (He-Cd Laser), emission collected though 345 nm long pass filter.

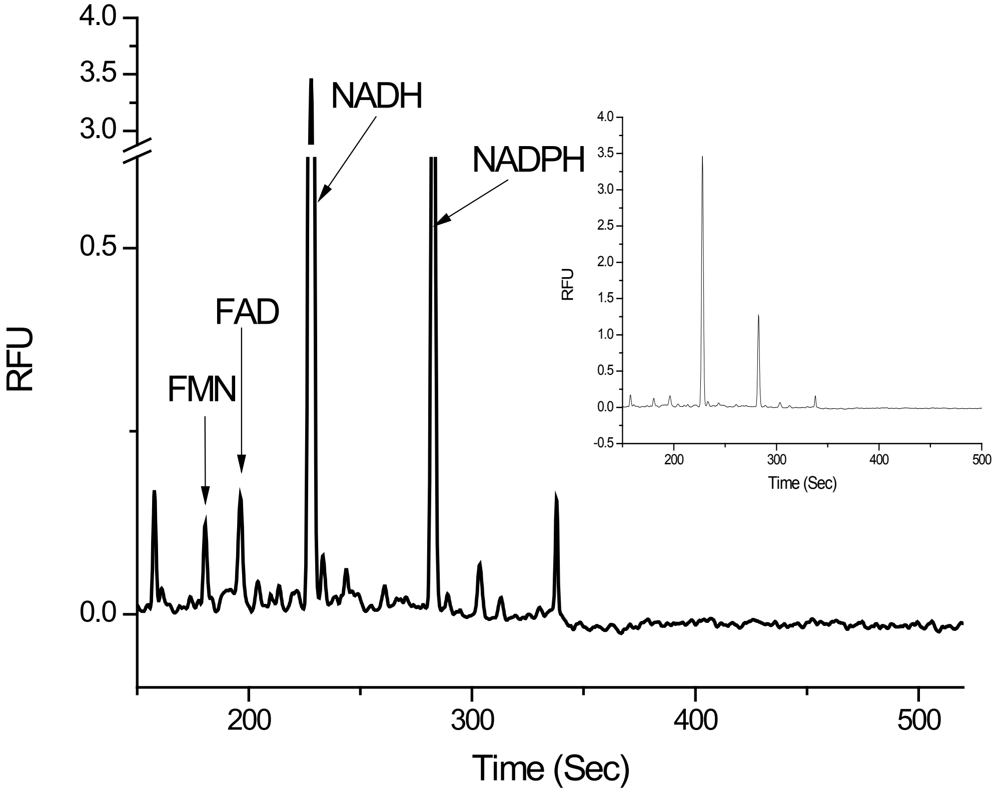

Figure 4.7 Electropherogram of CHO cell extracts with extraction buffer pH13.0

Note: Separation conditions: Capillary total length 30.5cm, the effective length 20.5 cm; capillary i.d. 50 µm, 175 mM borate buffer at pH 9.0; High voltage 15 kV; Injection at 0.5 psi for 10 sec; LIF excitation at 325 nm (He-Cd Laser), emission collected though 345 nm long pass filter. (These optimized separation conditions are used for separations presented in subsequent tables and figures unless specified otherwise.)

The insert is the overview of the electropherogram.

Peaks are identified by spiking the extracts with standard solutions.

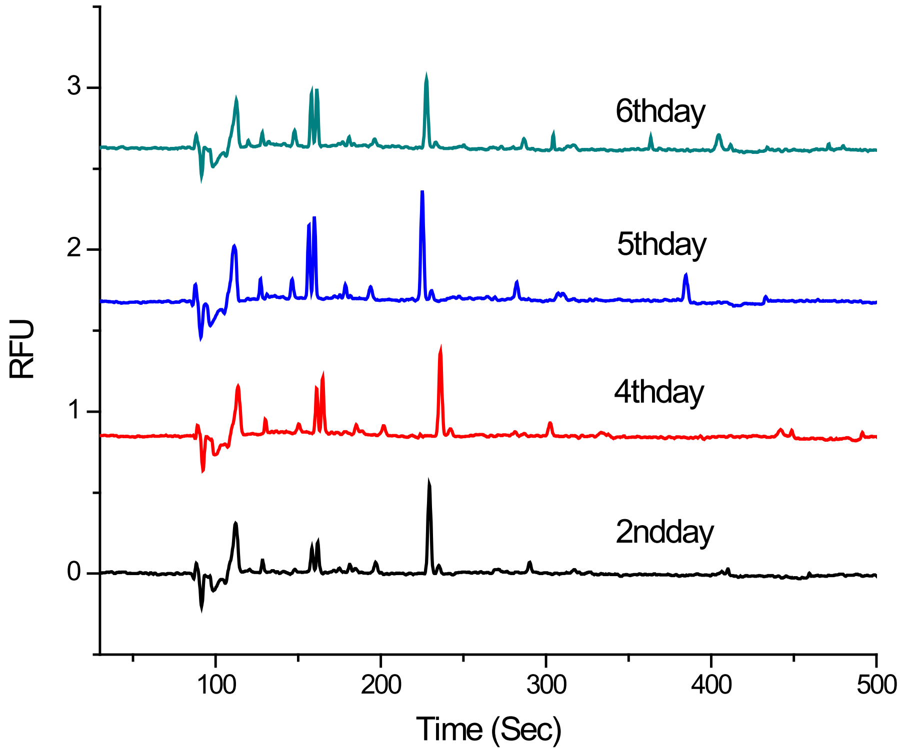

Figure 4.8 Electropherograms of CHO cell extracts on different days after extraction

---

Note: Separation conditions: Injection at 0.5psi for 3sec; Other conditions are the same as the conditions shown in Figure 4.7.

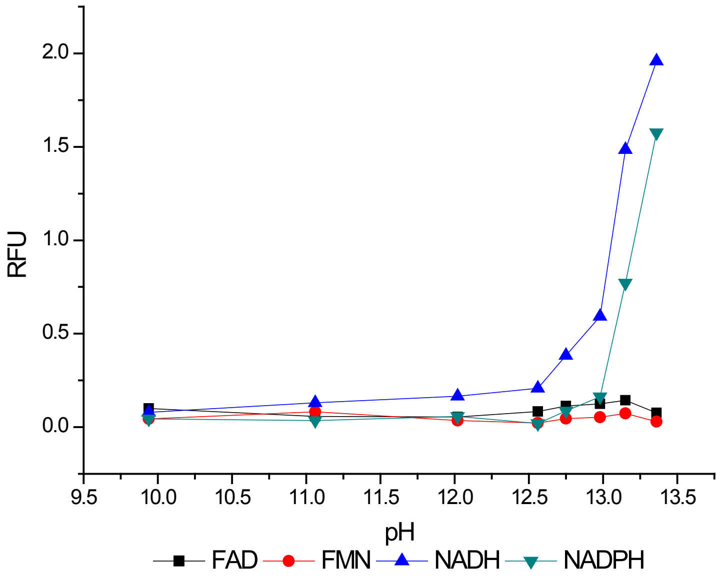

Figure 4.9 Effects of the initial extraction solution pH on extraction efficiencies of FAD, FMN, NADH and NADPH

Note: each signal was measured as the peak area of the corresponding compound in an electropherogram.

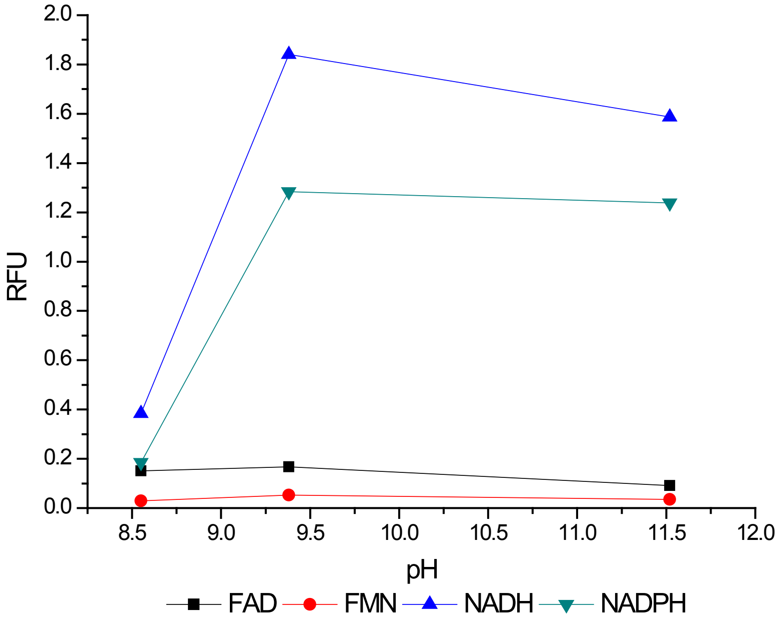

Figure 4.10 Effects of the final extracts pH on extraction efficiencies of FAD, FMN, NADH and NADPH

Note: each signal was measured as the peak area of the corresponding compound in an electropherogram.

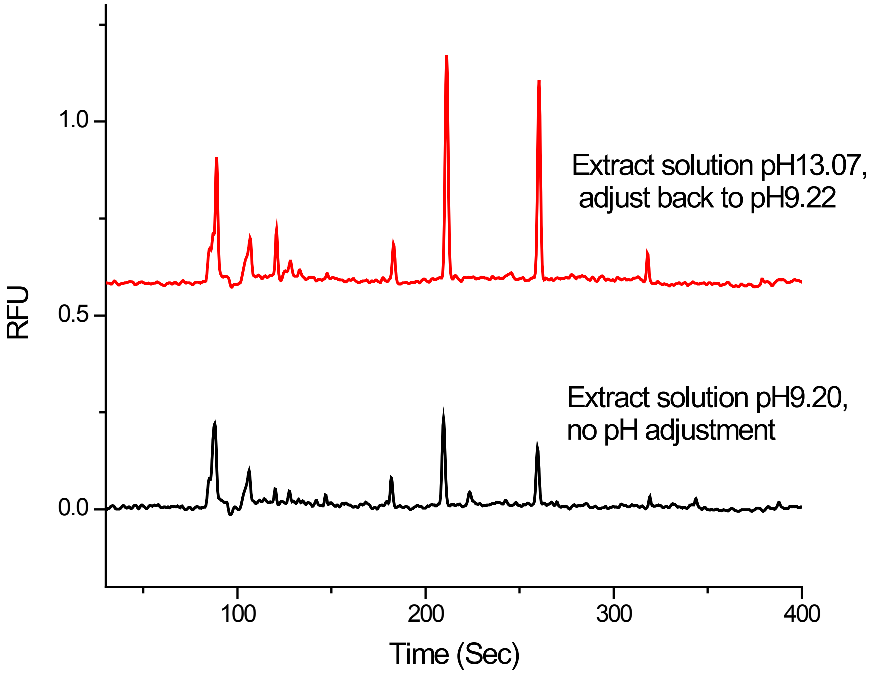

Figure 4.11 Comparison of electropherograms of CHO cell extracts using pH adjustment and not using pH adjustment after breaking cells

---

Note: Cell numbers in both extractions are approximately 2.6×10^6 .

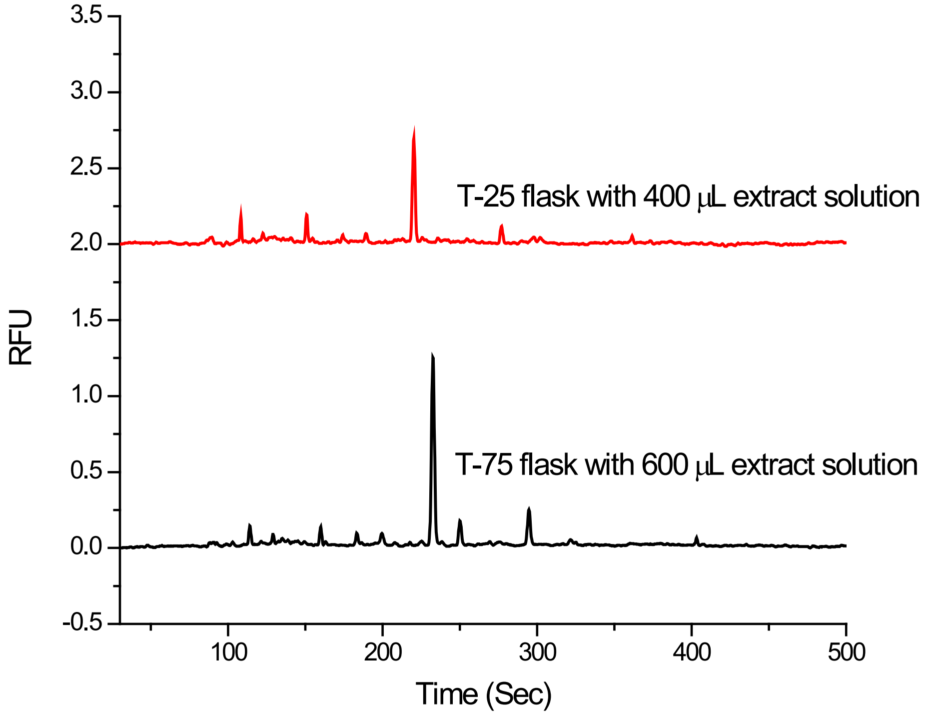

Figure 4.12 Comparison of electropherograms of CHO cell extraction from T-25 flask and T-75 flasks

Note: The cell number in the T-25 flask is (1.01±0.04) × 10^7. The cell number in the T-75 flask is (5.7±0.1) × 10^7.

CHAPTER 5

HT-29 AND FHC CELL EXTRACTION, SEPARATION AND COMPARISON

5.1 Introduction

The optimization of CE-LIF separation conditions for flavins and nicotinamide nucleotides (Chapter 2) and extraction methods for CHO cells (Chapter 4) have well prepared us to study the human colorectal adenocarcinoma cell HT-29. As a typical cell line derived from human colorectal adenocarcinoma, HT-29 cells have been used widely for cancer and metabolism research. For example, HT-29 cells were used to monitor oligosaccharide biosynthesis in single cells by capillary electrophoresis [183]. We selected this readily available cell line to be the model for human cancer cells to develop the extraction and separation protocols. These protocols can be easily adapted to the analysis of other cell lines. In this chapter, we discuss how to apply and modify the extraction and separation protocols to HT-29 cells for comparison with normal cell models. Since the human cell HT-29 has properties different from animal cells like CHO, the extraction conditions including the extraction solution pH and final extracts pH effects were re-evaluated. To prepare for the comparison with normal cells, the effects of cell densities and growth stages on extraction and separation were also investigated. Last, the quantification results of the endogenous fluorophores in HT-29 cells are presented.

The human normal colon cell FHC was selected as the normal cell model opposed to the cancer cell model HT-29. We applied the optimized extraction and separation protocols of the HT-29 cells to the FHC cells. The results of chemical separations are compared to identify the differences between the two cell extracts.

To statistically demonstrate the difference between HT-29 and FHC two-dimensional statistical correlation analysis was applied to the electropherograms from the two types of cell extracts. Two-dimensional correlation analysis uses statistical parameters, such as covariance and the correlation coefficient, to evaluate correlations between variables or samples [184-185]. The method has been applied to various spectroscopic analyses. For example, covariance mapping was first utilized in mass spectrometry by Fransinski *et al.* to identify the relationships between fragments [186]. Barton *et al.* applied correlation coefficient mapping to infrared spectroscopy [187]. Ozaki and coworkers further developed correlation coefficient mapping by introducing the autoscaling pretreatment to experimental data and also used the method for sample-sample correlation [188]. Traditional two-dimensional correlation spectroscopy usually focuses on variable-variable correlation. The sample-sample correlation spectroscopy concept was first proposed by Ozaki's group to reveal the species' perturbation-dependent dynamics [189]. Therefore, it is a good tool to classify spectra with perturbation depending on different species. In the Geng research lab, correlation coefficient mapping was applied to the classification of cancerous and normal tissue fluorescence spectra [9]. In order to demonstrate the difference between electropherograms of normal and cancer cell extracts, we proposed to apply the sample-sample correlation coefficient mapping to analyze the electropherograms. For a set of electropherograms from *m* samples with *n* time points, the sample-sample covariance between each pair of signals is $c(s_1,s_2)$, which can be represented by equation 5.1.

$$c(s_1,s_2)=\frac{1}{n-1}\sum_{j=1}^{n}[x_j(s_1)-x_{av}(s_1)][x_j(s_2)-x_{av}(s_2)] \qquad [5.1]$$

The sample-sample correlation coefficient is defined as $p(s_1,s_2)$ as shown in equation 5.2.

$$p(s_1,s_2)=\frac{c(s_1,s_2)}{\sigma(s_1)\sigma(s_2)} \qquad [5.2]$$

Here, $x_{av}(s)$ and $\sigma(s)$ are the mean and the standard deviation in signals of *n* time points of sample *s* respectively. The plot of $p(s_i,s_j)$ with respect to two sample axes is the correlation coefficient map. The function "corrcoef" from MATLAB 7.4.0 (The

MathWorks Inc., Natick, MA, USA) was used to calculate the correlation coefficient map.

The correlation coefficient $p(s_i,s_j)$ ranges between -1 to 1. When it is equal to 1, it means sample s_i and s_j have perfect similarity; while -1 means perfect antisimilarity and 0 means no similarity/antisimilarity at all. Those values between correspond to different extents of similarity/antisimilarity.

Correlation coefficient mapping is a purely mathematical method, without subjective experimental assumptions involved, to evaluate the correlation and it is very sensitive to noise [188]. Therefore, it is beneficial to select the data range with higher signal-to-noise ratios to calculate the correlation coefficients.

5.2 Experimental

5.2.1 Chemicals and Materials

FAD (95%), β-NADH (98%), FMN, (~95%), RF, (>98%), β-NADPH (97%) and Pyridoxine (VB6, ≥98%) were obtained at the highest purity from Sigma (St. Louis, MO, USA) and used as received. Sodium dihydrogen phosphate, disodium hydrogen phosphate, boric acid and sodium hydroxide were purchased from Aldrich (Milwaukee, WI, USA). EDTA disodium salt (Amresco, Solon, OH, USA), Tris[hydroxymethyl] aminomethane (>99.9%, Sigma, St. Louis, MO,USA), and [3-[3-chloramidopropyl]-dimethylamminio]-1-propanesulfonate (CHAPS, >99.0%, Research Products International Corp. Mt. Prospect, IL, USA) were used as received. Ultra pure Milli-Q (Millipore, Bedford, MA, USA) water was used to prepare all solutions. Stock solutions were prepared daily and CE separation was performed no later than 5 hours after sample preparation. A 170 mM borate buffer was prepared, and the run buffer was adjusted to the target pH 9.0 using 0.1 M sodium hydroxide solution. All solutions were filtered through 0.20 μm syringe filters (Cole-Parmer Instrument Co., Vernon Hills, IL, USA) and sonicated prior to measurement.

5.2.2 HT-29 cell culture and extraction

Human colorectal adenocarcinoma cells HT-29 (ATCC Number: HTB-38) was obtained from American Type Culture Collection (ATCC), Manassas, VA. The HT-29 cells were maintained in modified McCoy's 5a medium (Invitrogen, Carlsbad, CA, USA) supplemented with 10% fetal bovine serum (Atlanta Biologicals, Lawrenceville, GA, USA) and seeded in 25 cm^2 canted tissue culture flasks with vent cap (Corning Incorporated, Corning, NY, USA). The cells were cultured in a 37°C incubator with 5% CO_2 until they reached 100% confluency.

For each batch of extraction, one flask of cells was digested by 0.05% Trypsin/EDTA (Invitrogen, Carlsbad, CA, USA) and counted with a hemocytometer to assist the quantification of compounds per cell. Adapted from extraction methods by Wise and Shear [98], the metabolites were extracted from the cell monolayer without being digested by Trypsin. As depicted in Figure 5.1, after the medium was removed with pipettes and cotton swabs, the cell monolayer in the flask was rinsed by iced 20mM glucose in Delbecco's phosphate buffered saline without Calcium and Magnesium (Invitrogen, Carlsbad, CA, USA). The DPBS was then removed thoroughly with pipettes and cotton swabs. The extraction buffers (120 mM Tris, 10 mM EDTA, and 7 mM CHAPS) were added to the flask. Then, the flasks were put on ice in a Branson 2210 sonicator (Branson Ultrasonics Corporation, Danbury, CT, USA) to sonicate for 5 min and the pHs of the extracts were immediately adjusted to ~9.0 by iced 1.2 M HCl, followed by 60 sec sonication for mixing. The resulted extracts were transferred into Millipore Amicon® Ultra-4 30kD NMWL 4mL centrifugal filter units (Millipore, Bedford, MA, USA) and filtered for 15 min at 4500 rpm using a Beckman Coulter Allegra 21R Centrifuge (Beckman Coulter, Fullerton, CA, USA). The centrifugal filter units were rinsed with water and 0.1 M NaOH to remove glycerol before use. The filtrate was collected and analyzed by CE-LIF immediately. In the T-25 culture flasks, HT-29 cells usually reach 100% confluency on the fourth day after seeding, which is considered the day for cell extraction unless specified otherwise.

5.2.3 FHC cell culture and extraction

Human normal colon cells FHC (ATCC Number: CRL-1831) was obtained from ATCC (Manassas, VA). The FHC cells were maintained in Ham's F12 medium 45% and Dulbecco's modified Eagle's medium 45% (Invitrogen, Carlsbad, CA, USA) supplemented with 10% fetal bovine serum (Atlanta Biologicals, Lawrenceville, GA, USA) and seeded in 25 cm^2 canted tissue culture flasks with vent cap (Corning Incorporated, Corning, NY, USA). Some additives are necessary for the FHC medium, including 25 mM HEPES (Invitrogen, Carlsbad, CA, USA), 10 ng/ml cholera toxin (from Vibro cholera, 95%, Sigma, St. Louis, MO, USA), 0.005 mg/ml insulin (from bovine pancreas, 27 USP units/mg by HPLC, 3% loss on drying, Sigma, St. Louis, MO, USA), 0.005 mg/ml apo-transferrin human (>97%, Sigma, St. Louis, MO, USA), and 100 ng/ml hydrocortisone (Sigma, St. Louis, MO, USA). The cells were cultured in a 37°C incubator with 5% CO_2 until they reached 60% confluency (the highest confluency possible). The extraction methods are the same for FHC cells as for the HT-29 cells described above. With the seeding density about $4 \sim 6 \times 10^3$ /cm^2, the cells reach 60% confluency around the eighth day after seeding, which is usually the day for extracting FHC cells.

5.2.4 Instrumentation and CE separation conditions

A Beckman P/ACE™ MDQ system (Beckman Coulter, Fullerton, CA, USA) was used to perform the CE separations. The separation conditions were described in Chapter 2. Briefly, in LIF detection, the excitation was provided by a He-Cd laser at 325 nm and the fluorescence emission was collected through a 345 nm long pass filter to reduce scattered laser light. The excitation power was typically 1 mW. Polyimide coated fused silica capillaries (Polymicro Technologies, Phoenix, AZ) with an effective length of 20 cm (30 cm × 50 μm I.D.) were used in the experiment. Prior to use, the capillaries were preconditioned with sodium hydroxide and run buffer. Between runs, the capillary was conditioned consecutively with 0.1 M sodium hydroxide, 0.1 M hydrochloric acid, deionized water and run buffer. Samples were introduced by pressure injection for 10 seconds at 0.5 psi (~3.5 kPa). The temperature of the capillary was maintained at 25ºC with the instrument's thermostating system. Separations of HT-29 cell extracts and FHC cell extracts were performed under15 kV in 170 mM, pH 9.0 borate buffer. In the parallel extraction and separation of HT-29 and FHC cells for comparison purposes, three parallel extractions were performed for each batch. For each of the three extracts, five replicate separations were performed.

5.2.5 Identification and quantification of endogenous fluorophores in cell extracts

The flavins and NAD(P)H were identified by spiking the cell extracts with standard solutions of NAD(P)H, RF, FMN and FAD. To quantify the identified compounds in the cell extracts, the standard addition method was used for each compound. Briefly, 0.5 μL, 1.0 μL, 1.5 μL, and 2.0 μL standard solutions with appropriate concentrations were added into 50 μL cell extracts. The concentration of each compound in the extracts could be calculated from the fitted standard addition curves as described in section 4.2.5. The mass of each compound in a cell was estimated according to the cell numbers obtained from parallel cell counting as shown in equation 4.3.

5.3 HT-29 cell extraction and separation

5.3.1 HT-29 cell extracts separation

5.3.1.1 Peak identification

Before spiking the cell extracts with standards to identify peaks, four types of blanks were investigated to exclude the impurity peaks. The resulting electropherograms and comparison with the HT-29 electropherogram are shown in Figure 5.2. The first type of blank is injection of pure water to verify if there are any impurity peaks from the running buffer itself. A small dip at about 85 seconds and a small spike at 100 seconds are observed in the electropherogram. The water plug is observed as a dip because of the difference in refractive indices between the running buffer and the water plug. The position of this dip also represents the EOF since water is neutral. The second type of blank is the injection of the extraction buffer only and the third type is the injection of the extraction buffer after passing through the Amicon 30 kDa centrifugal filter. Both injections result in four impurity peaks as shown in Figure 5.2. The fourth blank is the blank extracts with the cell culture medium in the culture flask being extracted. This blank followed the exact extraction and separation procedures for HT-29, but only with a blank culture flask filled with medium and without any cells. As can be seen in Figure 5.2, three of the four impurity peaks from the extraction buffer still exist, but the peak at about 110 seconds disappears in the fourth blank, which means the culture medium may have reacted with that component resulting in the disappearance of the peak. This peak did not appear in the real cell extracts either. In summary, the two prominent impurity peaks (labeled by red and blue arrows in Figure 5.2) in the cell extracts brought by the extraction buffer are the peaks with typical migration times longer than 340 seconds. It is also noticed that these two peaks are shifting more significantly than other peaks in the cell extracts. They can be easily identified in the electropherograms by the researcher according to their intensity and time-lapse pattern.

FMN, FAD, NADH and NADPH were identified in the electropherogram of the HT-29 cell extracts by spiking the extracts with standards (Figure 5.3). As shown in Figure 5.4, attempts were also made to identify pyridoxine in the cell extracts but no peak for the compound was found.

5.3.2 Optimization of extraction conditions

5.3.2.1 Optimization of extraction solution pH

Although the pH of the extraction solution has been optimized for CHO cells, the HT-29 cells are human cells and there is a need to perform similar optimization to ensure the best extraction efficiency for the pH sensitive molecules, the oxidized flavins and reduced nicotinamide nucleotides. The optimization results are shown in Figures 5.5 and 5.6.

When the pH of the extraction solution is elevated, the efficiency of the surfactant is better for breaking the cell membrane. As a consequence, the peaks for the four compounds become more intense. This trend continues for the nicotinamides, but the peak areas for FMN and FAD reach a maximum when the extraction solution is at pH 12.8 because the oxidized flavins are not stable at higher pHs. Although NADH and NADPH peak areas increase with pH up to 13.0, pH 12.8 is selected to be the extraction solution pH for HT-29 cells. Plus, as experiences indicated, the reproducibility of electropherograms of the cell extracts from pH 12.8 is better than extracts from higher pHs.

5.3.2.2 Optimization of final extracts pH

The optimization results of final extracts pH are shown in Figures 5.7 and 5.8. The efficiencies for extracting the four compounds improve when the final pH increases to ~pH 9.5 (Figure 5.8). Further increase of the final pH causes irreproducibility of separation and lower extraction efficiency for the flavins. For FMN, FAD and NADH, the peak areas stay at a comparatively stable level when the pH is between 9.0 to 9.5. For NADPH, the peak area increases more sharply when pH goes higher than 9.4. As discussed in the CHO cell separation, with the extraction solution and pH adjustment by hydrochloric acid after sonication, the final extracts pH is not easily controlled very accurately due to the various interferences from the cell contents and trace medium.

Therefore, we selected adding 10 µL 1.2 M HCl to the extracts after sonication to control the final extracts pH between 9.0 ~ 9.5.

5.3.2.3 Effects of cell densities on extraction

The effects of cell densities on extraction were investigated and are shown in Figures 5.9 and 5.10. As expected, with higher cell density, more cells are available for extraction in the flask, and larger amount of flavins and nicotinamides nucleotides are recovered. The peak areas of the four compounds show the steepest increase when the cell density grows from 3×10^6 to 4×10^6 cells/T-25 flask. It is also worth noting that the increments of the four compounds are not the same. The pHs of the final extracts for the four samples are all around 9.4 so this variation in increments is not pH-related. It is concluded with this set of experiments that in order to obtain comparatively reproducible extraction and separation results, it is important to be consistent with the cell density for extraction.

5.3.2.4 Effects of cell growth stages on extraction

Cell growth stages are determined by the growth time (typically expressed as the number of days) after seeding the cells into the culture flask. In the late stage of cell growth, besides the fact that more cells are available for extraction, there are also differences in the chemical compositions caused by the average activities of the cells. With our extraction methods, the effect of the growth stages is evaluated in Figures 5.11 and 5.12. Similar concentration increases for all the four components were observed in the growth stage effects as in the cell density effects. The increments of the four compounds are also not the same. Again, being consistent with the growth stage at the time of extraction will help to improve the consistency of the extraction results.

5.3.3 Quantification of FMN, FAD, NADH and NADPH in HT-29 cell extracts

The standard addition methods were again used to quantify FMN, FAD, NADH and NADPH in the HT-29 cell extracts to account for the matrix effects. The extraction of HT-29 cells was performed on the fifth day after seeding the cells with the optimized extraction protocol. The quantification results are summarized in Table 5.1. The masses of each compound per cell were calculated to be 0.5, 2.3, 15, and 10 amol for FMN, FAD, NADH and NADPH, respectively. These amounts are significantly lower than the amount we measured in CHO cells. The difference may come from the efficiency of extraction on the two different cell lines and/or the biochemical difference of the two cell lines.

5.4 Extraction and separation of FHC cells

The extraction and separation protocol optimized for HT-29 cells was applied to FHC cells. Figure 5.13 shows the electropherograms of FHC cell extracts. Since the FHC cell is a normal cell line, the growth of the cell is not as fast as the cancer cell HT-29 and the maximum confluency the FHC cell can reach is only 60%. The maximum amount of cells for extraction in each culture flask is limited to about $3 \sim 6 \times 10^5$ cells. As can be seen in the electropherogram of FHC, the signal-to-noise ratios for FMN and FAD are not as high as in the HT-29 cell electropherograms but the peaks are still identifiable by spiking. If only for the purpose of improving the signal-to-noise ratios for these two compounds, larger cell culture flasks can be used for extraction to include more cells in the extraction. But for comparison with the HT-29 cell extracts, the extraction conditions for the FHC cells were the same as for HT-29 cells.

5.5 Comparison of HT-29 and FHC cell extracts

With the optimized extraction and separation protocol for HT-29 cells, batches of HT-29 cells and FHC cells were extracted and separated in parallel. Some of the electropherograms of these batches are shown in Figure 5.14 for FHC cell extracts and Figure 5.15 for HT-29 cell extracts. In Figure 5.15, the electropherograms are presented in two sets for HT-29 cells. The first set (Figure 5.15(a)) includes electropherograms from HT-29 cells extracted at comparatively lower cell densities (8.0 ~ 10 × 10^5/T-25 flask), which are closer to the maximum cell density of FHC cells (3.0 ~ 6.0 × 10^5/T-25 flask) for extraction. The second set (Figure 5.15(b)) includes electropherograms from HT-29 cells extracted at higher cell densities (4.0 ~11 × 10^6/T-25 flask). With the two sets of HT-29 cell extracts, we can potentially take into account the cell density effects when we compare the two types of cells.

In order to compare FHC and HT-29 cells, 2D statistical correlation analysis, specifically 2D correlation coefficient mapping, was used to analyze the electropherograms of these two types of cells. The correlation coefficient calculation and mapping were carried out in MATLAB. Figure 5.16 shows a simple correlation coefficient mapping of the 42 electropherograms for FHC (electropherograms 1-12, ~3.3 × 10^5 cells/T-25 flask) and HT-29 (electropherograms 13-28, ~8.7 × 10^5 cells/T-25 flask, and electropherograms 29-42, ~8.7 × 10^5 cells/T-25 flask). The sections between 100 to 375 seconds of the electropherograms were used for the calculation of correlation coefficients without any pretreatments. As expected, the correlation coefficient map in Figure 5.16 does not present any useful information. The only strong correlation is the autocorrelation of each electropherogram with itself. There are several reasons for the irregular correlation, including the peak shifting and broadening as well as the marginal signal-to-noise ratio. With correlation analysis methods, peak shifting and broadening usually disrupt the correlation and it is necessary to correct the peak shifting and broadening to obtain reliable correlation results [184-185, 188, 190-191]. Regarding the noise level, since our signal-to-noise level is limited by the FHC cell numbers for extraction, its effect will not be focused at this stage of our research.

Since the 2D correlation coefficient mapping is based on the covariance of two electropherograms, it is beneficial to analyze the sources of variation in our system. The variations in electropherograms of cell extract can originate in the cell culture, extraction and the separation processes. Here are some examples of sources of variation.

- Biological variations - e.g. cell number variations, cell growth stage variations and environment variations such as medium variations, etc.
- Extraction variations – e.g. variations in extraction solution pHs and concentrations, variations in enzyme effects on interested compounds after breaking cell membranes, and variations in filter efficiencies, etc.
- Separation variations – e.g. variations in EOF, variations in background electrolytes, variations in injection volumes, variations in laser intensity, sharp peaks caused by air bubble and variations of capillary surfaces caused by interactions of peptides or other small debris in cell extracts and the capillary surface, etc.

Since the variance caused by differences between the two cell species is the major variance we intend to probe, all the above variations should be minimized during experiments to avoid overwhelming the cell species differences. Therefore, the extraction and separation procedures were kept as consistent as possible. However, it was not possible to completely eliminate these variations. One obvious result of these variations is the peak shifting in the electropherograms. As can be seen in Figure 5.17(a), in both types of cell extracts, the peak shifting is significant and not only caused by EOF shifting. For the purpose of comparison between electropherograms, we propose to align peak(s) with mathematical processing so that the correlation could reveal the difference in peak intensity (concentration) profiles of the two types of extracts. The assumption of using this alignment method is that the difference of cell species does not cause significant changes in migration times of the interested compounds.

Two types of basic alignment methods were explored for the electropherograms. One was to align one of the prominent peaks (NADH or NADPH). This method was carried out in MATLAB by the function shown in Appendix A.1. Another was to align and interpolate/extrapolate the electropherograms using the two prominent peaks (NADH and NADPH) as references, which could be performed in MATLAB with the function shown in Appendix A.2. The procedure of this method is illustrated in Figure 5.17. Figures 5.18 (b) and (c) show the results of these two types of alignments. The effects of the two types of alignments to 2D correlation coefficient mapping of electropherograms are examined next.

The correlation results after aligning NADH peaks of the 42 electropherograms, which were correlated without pretreatment in Figure 5.16, are shown in Figure 5.19. In Figure 5.19 (a), the whole electropherograms with the migration time from 0 seconds to 600 seconds are used for correlation while in Figure 5.19 (b), only the sections between 100 seconds to 375 seconds of the electropherograms are used for correlation. Figure 5.19(c) shows the cross sections of Figure 5.19(b) at x=28 to x=42, where the HT-29 cell extracts with higher cell densities correspond to. Figure 5.19(d) is the cross section of Figure 5.19(b) at x=40.

Comparing to the correlation without pretreatment, in Figures 5.19(a) and (b), the correlation of all the electropherograms of HT-29 cells with higher cell density (electropherograms 28 to 42) is more consistent. And as shown in Figures 5.19(c) and (d), the correlation between the HT-29 cells with higher cell density set and the other two sets (HT-29 with lower cell density set and FHC set) are closer to 0. That is to say, if we have an electropherogram of an unknown sample, it is possible to determine if it is from HT-29 cells with higher cell density based on the correlation coefficients of this electropherogram to the HT-29 with higher cell density set. But, we cannot determine if it belongs to either HT-29 with lower cell density or FHC cell extracts just based on the correlation coefficients.

Another observation in Figure 5.19 is that choosing the whole section of electropherograms (Figure 5.19(a)) to analyze or choosing the section between 100 seconds to 375 seconds (Figure 5.19(b)), where the cell extracts information are more concentrated, appears not to make significant difference on the correlation results. Hereafter, we use the 100 seconds to 375 seconds sections of electropherograms for 2D correlation analysis.

The same sets of electropherograms are also subjected to the second type of pretreatment – align and interpolate/extrapolate electropherograms to align both NADH and NADPH peaks. The 2D correlation results of electropherograms after this pretreatment are shown in Figure 5.20. In Figure 5.20(a) and (b), the three sets of electropherograms, 1-12 FHC cell extracts, 13-27 HT-29 cell extracts with lower cell density, and 28-42 HT-29 cell extracts with higher cell density, are aligned and interpolated/extrapolated, respectively, to align both NADH and NADPH peaks. Then, the resulting 42 electropherograms are all aligned to the NADH peak and the correlation coefficients are calculated. Figure 5.20(b) is the cross section of Figure 5.20(a) at x = 40. In Figure 5.20(c) and (d), all the 42 electropherograms are aligned and interpolated/extrapolated to align both NADH and NADPH peaks and then used for calculation of the correlation coefficients. Figure 5.20(d) is the cross section of Figure 5.20(c) at x = 40.

From Figures 5.20(a), (b), (c) and (d), we can see that aligning both NADH and NADPH peaks brings more consistency for the correlation of HT-29 cell extracts with higher cell density than only aligning the NADH peak. Thus, in Figure 5.20(b) and (d), the cross sections at x = 40 shows more significant differences between the correlation of the electropherogram 40 with the HT-29 cell extracts with higher cell density and the correlation of this electropherogram with other two types of cell extracts. Between these two, Figure 5.20 (b) shows better consistency with no correlation between the HT-29 cell extracts with higher density and the other two sets. That is to say, we can draw clearer thresholds between them for the classification of an unknown electropherogram. Potentially, with this correlation after the second type of pretreatment, we can be more certain to classify an unknown electropherogram to be HT-29 cell extracts with higher cell density. However, we still cannot differentiate HT-29 cell extracts with lower cell density from FHC cell extracts.

The above correlations were performed on small sets of electropherograms. Each of the three sets of electropherograms is collected on the same day. Next, we will include extractions and separations performed on different days for calculation of correlation coefficients to see if between days variation would change the correlation significantly.

Once again, the electropherograms are categorized into three sets. The electropherograms 1-65 are from FHC cells extracted on the eighth day after seeding (cell density $3.0{\sim}6.0 \times 10^5$/T-25 flask). The electropherograms 66-92 are from HT-29 cells extracted on the second day after seeding (cell density $8.7{\sim}10 \times 10^5$/T-25 flask), while the electropherograms 93-149 are from HT-29 cells extracted on the fourth day (cell density $4.0{\sim}11 \times 10^6$/T-25 flask).

For the pretreatment of electropherograms used for correlation in Figure 5.21, the 149 electropherograms were aligned and extrapolated to align both NADH and NADPH peaks. The correlation coefficients were then calculated. Clearly, the difference of the correlation between HT-29 cell extracts with higher density and HT-29 cell extracts with lower density and the correlation between HT-29 cell extracts with FHC cells are not sufficient to draw two thresholds to differentiate the three types of cell extracts as shown in Figure 5.21 (b) and (c). But the correlation of HT-29 cell extracts with higher density within the set is still consistent and close to 1. And it is still possible to differentiate HT-29 cell extracts with higher density from HT-29 cell extracts with lower density and FHC cell extracts.

In all, the original expectation for the 2D correlation analysis was to reveal the difference between the HT-29 cell extracts and FHC cell extracts. However, our current analysis only allows us to differentiate the HT-29 cell extracts with higher cell density from the FHC cell extracts and HT-29 cell extracts with lower cell density. One possible reason for this situation is that the correlations within the FHC cell extracts and HT-29 cell extracts with lower cell density sets are not consistent enough due to the lower signal-to-noise ratios in these two sets of electropherograms and the high sensitivity of statistical 2D correlation to the noise. Another possible reason is that the cell density is a more influential factor to fluorophore concentration profiles than the cell species factor.

As discussed in section 4.4.2, the signal-to-noise ratio can possibly be improved by extracting cells from larger culture flasks. If the correlation of cell extracts with lower density show better correlation within the set because of the improved signal-to-noise ratio, we would be able to confirm if the signal-to-noise ratio is the major reason overwhelmed the difference caused by cell species in 2D correlation.

We also took a closer examination of the two most prominent peaks in the electropherograms, the NADH and NADPH peaks. The ratios of the two peaks were calculated and plotted against the corresponding cell density of the extracts (Figure 5.22) and the corresponding cell extracts pH (Figure 5.23). Clearly, as shown in Figure 5.22, the higher density of cells corresponds to a higher ratio of NADH/NADPH. Furthermore, this correlation does not relate to the final extracts pH as shown in Figure 5.23. Therefore, assuming that the NADH/NADPH ratio change represents the metabolic changes in the cell, we can hypothesize that the cell density probably plays an important role in metabolism of the cells. Even if they are cancer cells, the altered metabolism only emerges when the cells grow to a higher cell density. In order to test this hypothesis, we will need to show that this phenomenon is not introduced by our extraction and separation procedures. Tu et al. has discovered the cyclic changes of NADPH concentration during the metabolic cycle of a yeast cell with 2D GC-MS [192]. The extraction methods they used were ethanol and formic acid extraction of yeast cells. They were both harsh extraction conditions but the authors tended to believe that the influences of these manipulations were consistent for all the extractions. Thus the cyclic changes of NADPH they observed reflected real metabolic changes. In our case, Figure 5.23 excludes the final extracts pH as a factor. But there might be other factors involved such as the unknown and complicated enzyme actions after breaking the cell membranes. Therefore, we are cautious in claiming the hypothesis but meanwhile it would be an interesting topic to explore.

5.6 Conclusion

In this Chapter, the optimization of extraction and separation of fluorophores in HT-29 cells was discussed. The optimized protocols were applied to HT-29 cells and FHC cells. FMN, FAD, NADH and NADPH were all identified in both cell extracts and were quantified in HT-29 cell extracts. The effects of cell densities and growth stages were also investigated. The electropherograms of the cell extracts were compared with 2D correlation coefficient mapping. With the correlation coefficient map, we could differentiate the HT-29 cell extracts with higher cell density from the FHC cell extracts based on the electropherogram but could not differentiate the HT-29 cell extracts with lower cell densities from the FHC cell extracts. The peak area ratios between NADH/NADPH also demonstrated the similarity between the FHC cells and HT-29 cells at lower cell densities. This phenomenon may be because the difference in metabolism caused by cell densities overwhelms the difference caused by cell species.

Table 5.1 Quantification of the four endogenous fluorophores in HT-29 cell extracts (n=15)

	Standard Addition Results		Conc. in extracts/µM	Number of cells extracted	Estimated mass in each cell/amol
	Equation*	r^2			
NADH	y=(0.8±0.1)+(2.25±0.09)x	0.98	0.47±0.02	$(8\pm2)\times10^6$	15±3
FAD	y=(0.8±0.3)+(2.8±0.2)x	0.93	0.075±0.006	$(8\pm2)\times10^6$	2.3±0.6
FMN	y=(0.3±0.9)+(14.7±0.7)x	0.97	0.0173±0.0009	$(8\pm2)\times10^6$	0.5±0.1
NADPH	y=(0.9±0.2)+(2.8±0.1)x	0.97	0.31±0.02	$(8\pm2)\times10^6$	10±2

Note: The extraction and separation were performed on the fifth day after seeding the cells.

* y and x stand for peak area and added standard volume respectively.

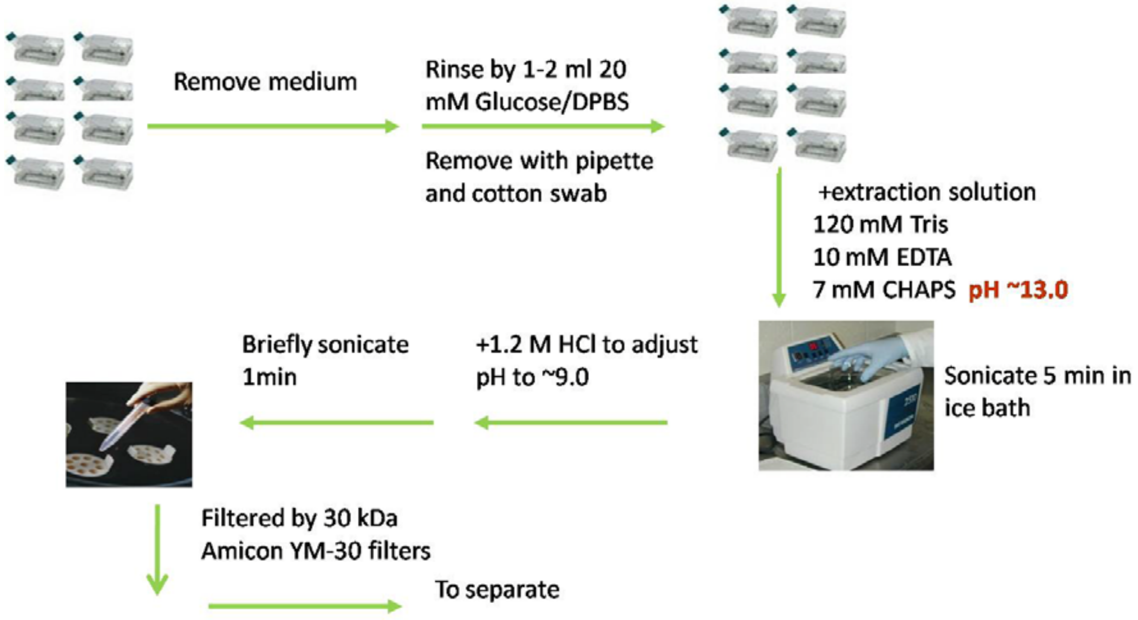

Figure 5.1 HT-29 cell extraction procedure

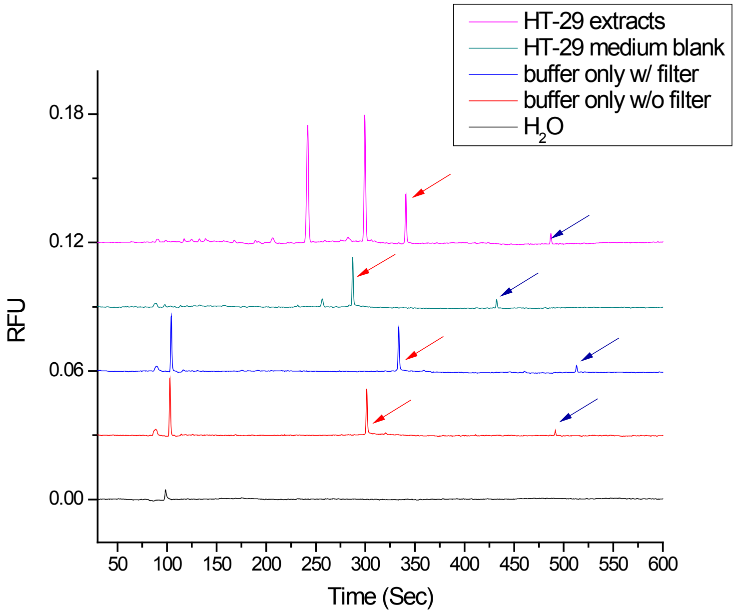

Figure 5.2 Comparison of electropherograms of HT-29 cell extracts and various types of blank

---

Separation conditions: Capillary total length 30.5 cm, the effective length 20.5 cm; capillary i.d. 50 µm, 170 mM borate buffer at pH 9.0; High voltage 15 kV; Injection at 0.5 psi for 10sec; LIF excitation at 325 nm (He-Cd Laser), emission collected though 345 nm long pass filter. (These separation conditions are used for the separations presented in the subsequent figures unless specified otherwise.)

The blanks are the water only blank, the extraction buffer without passing through the Millipore Amicon® Ultra-4 30kD NMWL 4mL centrifugal filter, the extraction buffer after passing through the filter, and the extracts of a blank culture flask filled with medium but without any cells.

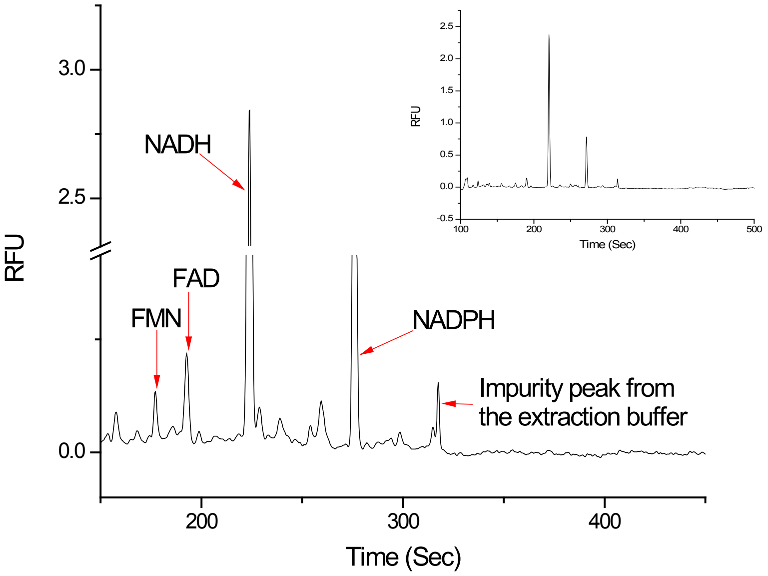

Figure 5.3 Peak identification on the electropherogram of HT-29 cell extracts

Note: The insert is the overview of the electropherogram.

Peaks are identified by spiking the extracts with standard solutions.

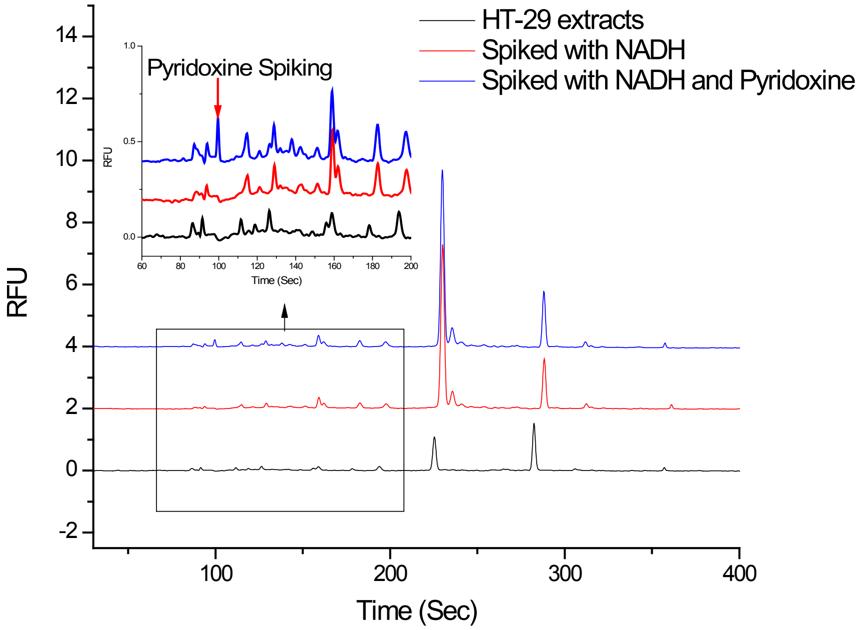

Figure 5.4 Pyridoxine and NADH spiking of the HT-29 cell extracts

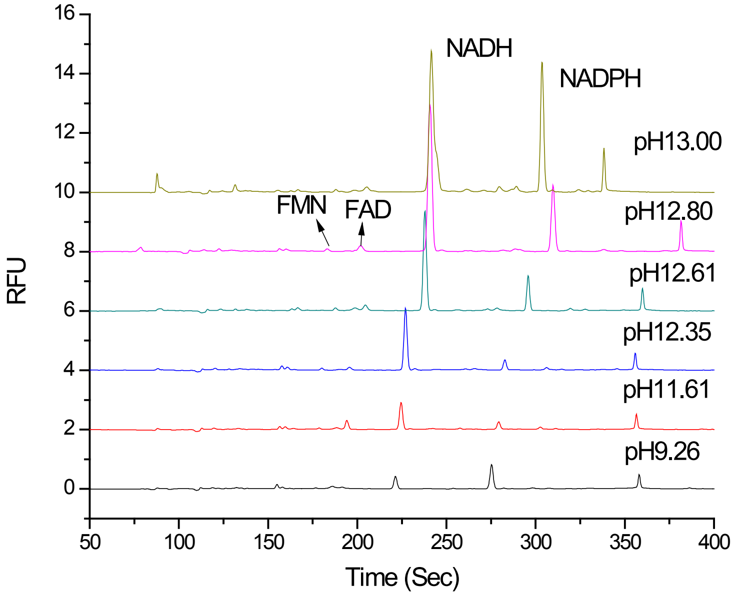

Figure 5.5 Electropherograms of cell extracts with extraction solution at different pH

Note: 8~10 × 10^6 HT-29 cells in T-25 culture flask were extracted for each extraction. For each extraction, 400 µL extraction solution at different pH was used and the final pH was adjusted by adding 10 µL 1.2 M HCl to the sonicated extracts.

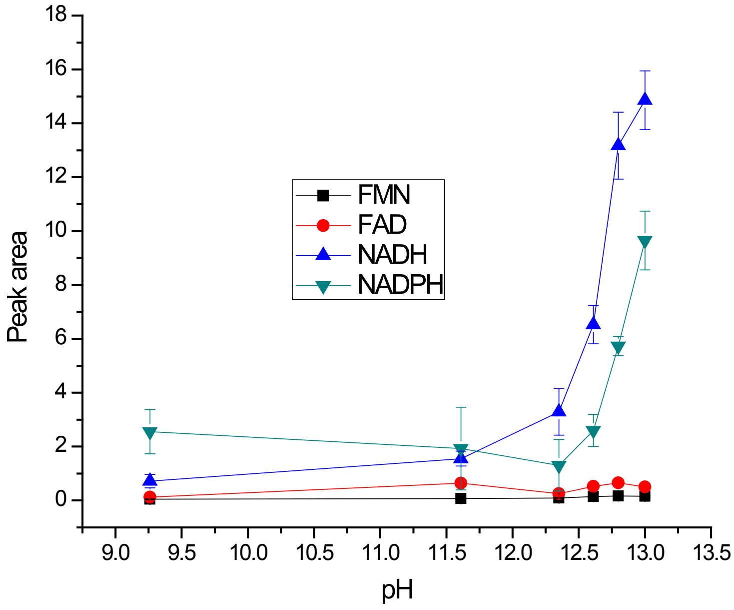

Figure 5.6 Effects of the different extraction solution pH on peak areas of flavins and nicotinamide nucleotides in HT-29 cell extracts

---

Note: Each peak area plotted was calculated as the average of three replicate electropherograms. The error bars represent the standard deviations of peak areas of the three replicates.

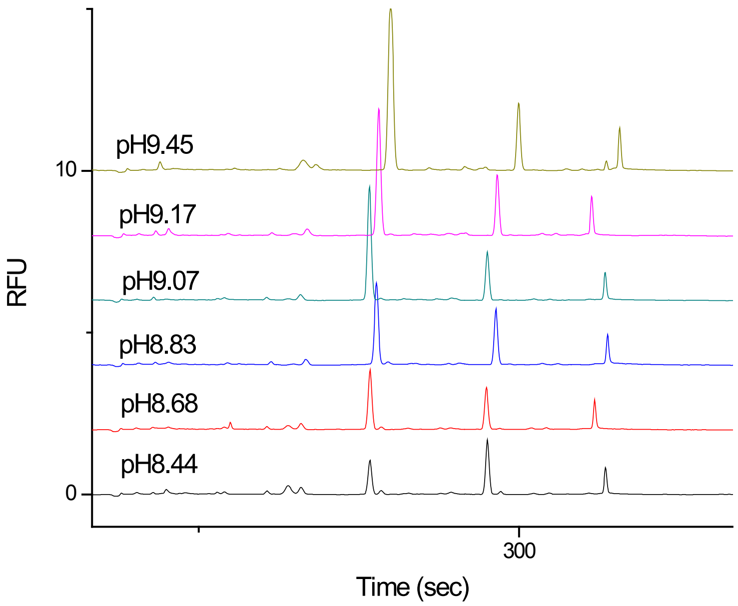

Figure 5.7 Electropherograms of cell extracts with different final extracts pH

Note: 8.0~10 × 10^6 HT-29 cells in T-25 culture flask were extracted for each extraction. For each extraction, 400 µL extraction solution at pH 13.0 was used and the final pH was adjusted by adding 5, 10, 15, 20, 25 and 30 µL of 1.2 M HCl to the sonicated extracts.

.

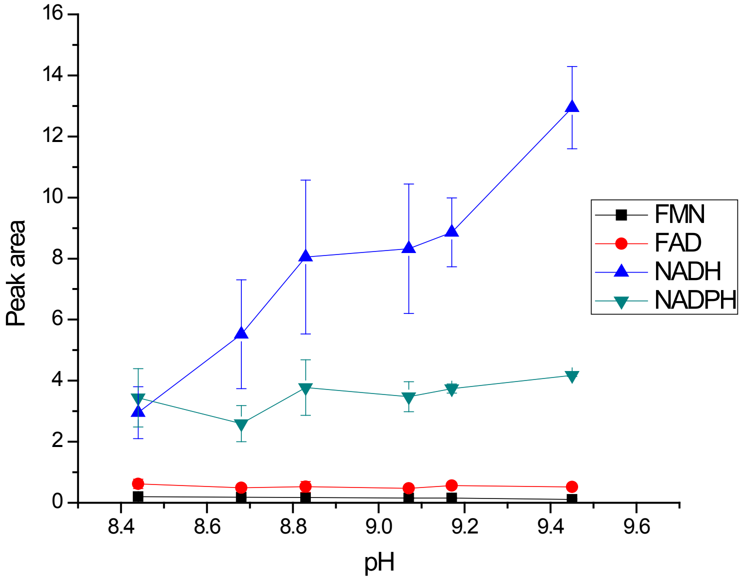

Figure 5.8 Effects of the different pHs of final extracts on peak areas of flavins and nicotinamide nucleotides in HT-29 cell extracts

---

Note: Each peak area plotted was calculated as the average of three replicate electropherograms. The error bars represent the standard deviations of peak areas of the three replicates.

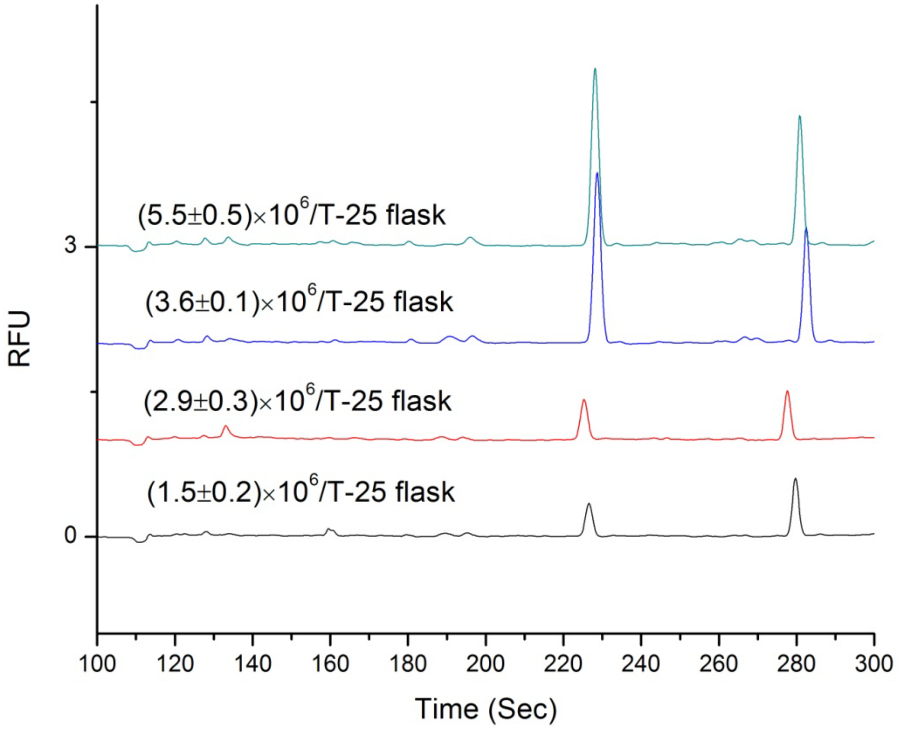

Figure 5.9 Electropherograms of HT-29 cell extracts with different cell densities

---

Note: The extractions were done on the third day after seeding by 400 µL extraction solution at pH 12.8 and 10 µL of 1.2 M HCl to the sonicated extracts. (These extraction conditions are used for results shown in subsequent tables and figures unless specified otherwise.)

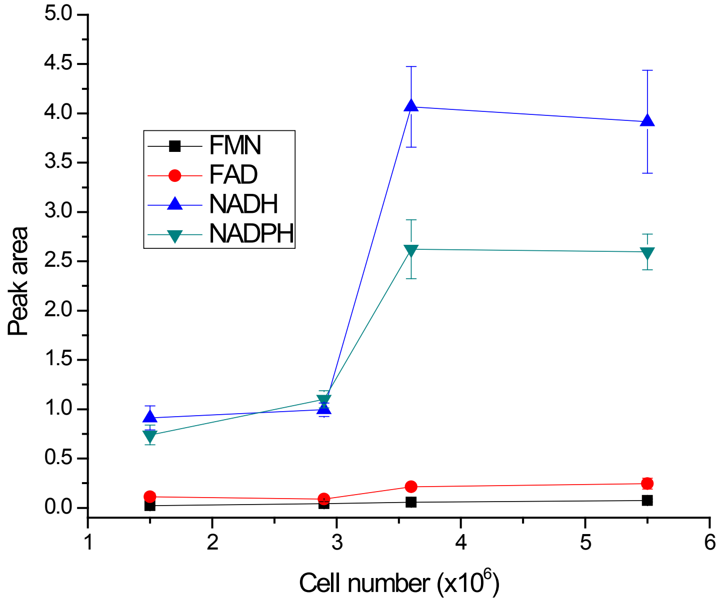

Figure 5.10 Effects of cell densities on peaks areas of flavins and nicotinamide nucleotides in HT-29 cell extracts

---

Note: Each peak area plotted was calculated as the average of three replicate electropherograms. The error bars represent the standard deviations of peak areas of the three replicates.

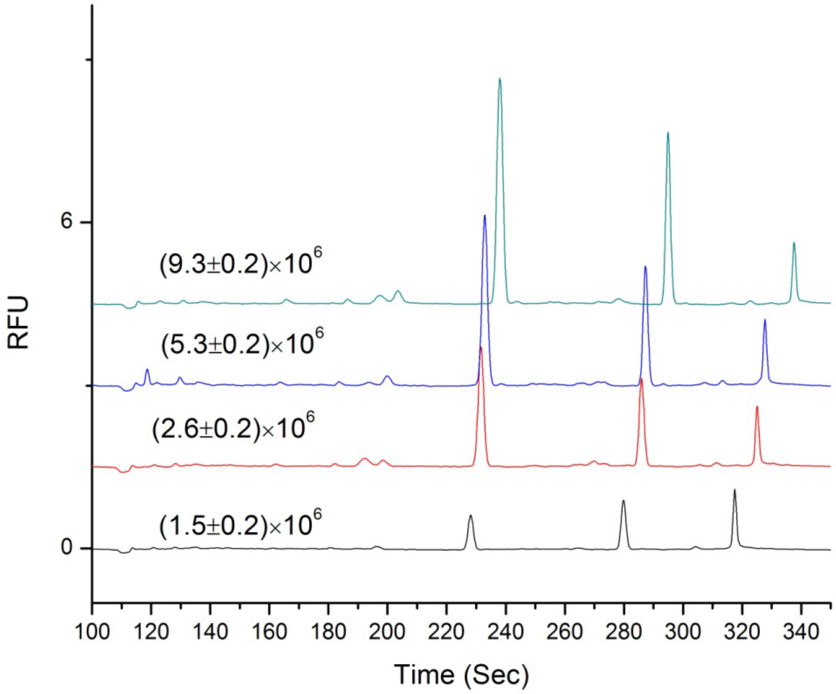

Figure 5.11 Electropherograms of HT-29 cell extracts with different cell growth stages

---

Note: The extractions were performed on the third, fourth, fifth and sixth days after seeding.

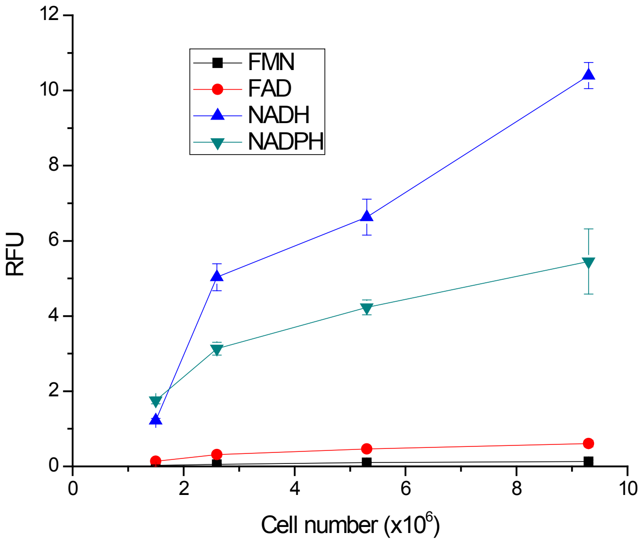

Figure 5.12 Effects of cell growth stages on peak areas of flavins and nicotinamide nucleotides in HT-29 cell extracts

---

Note: Each peak area plotted was calculated as the average of three replicate electropherograms. The error bars represent the standard deviations of peak areas in the three replicates.

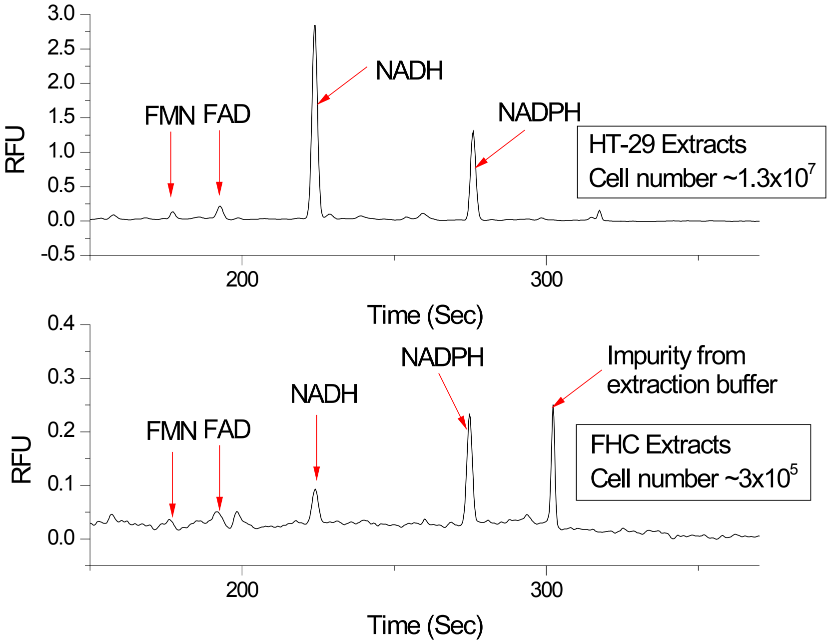

Figure 5.13 Comparison of electropherograms of HT-29 and FHC cell extracts

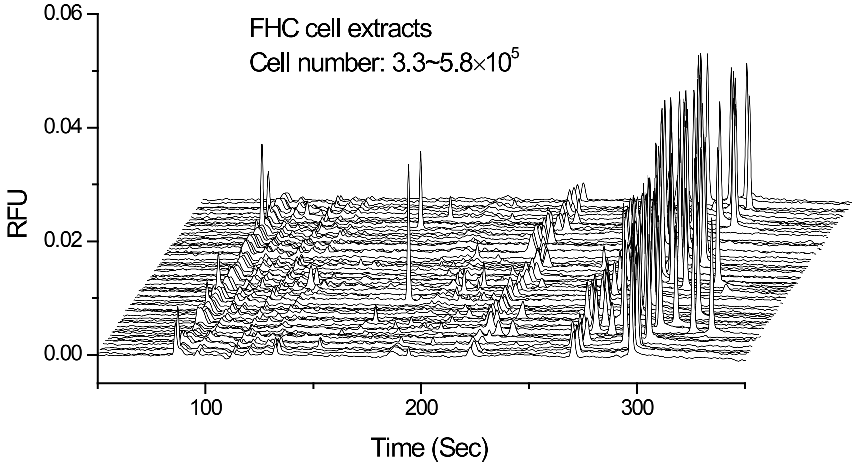

Figure 5.14 Electropherograms of FHC cell extracts under the optimized extraction and separation conditions

Note: The number of cells extracted ranges 3.0 ~ 6.0 × 10^5.

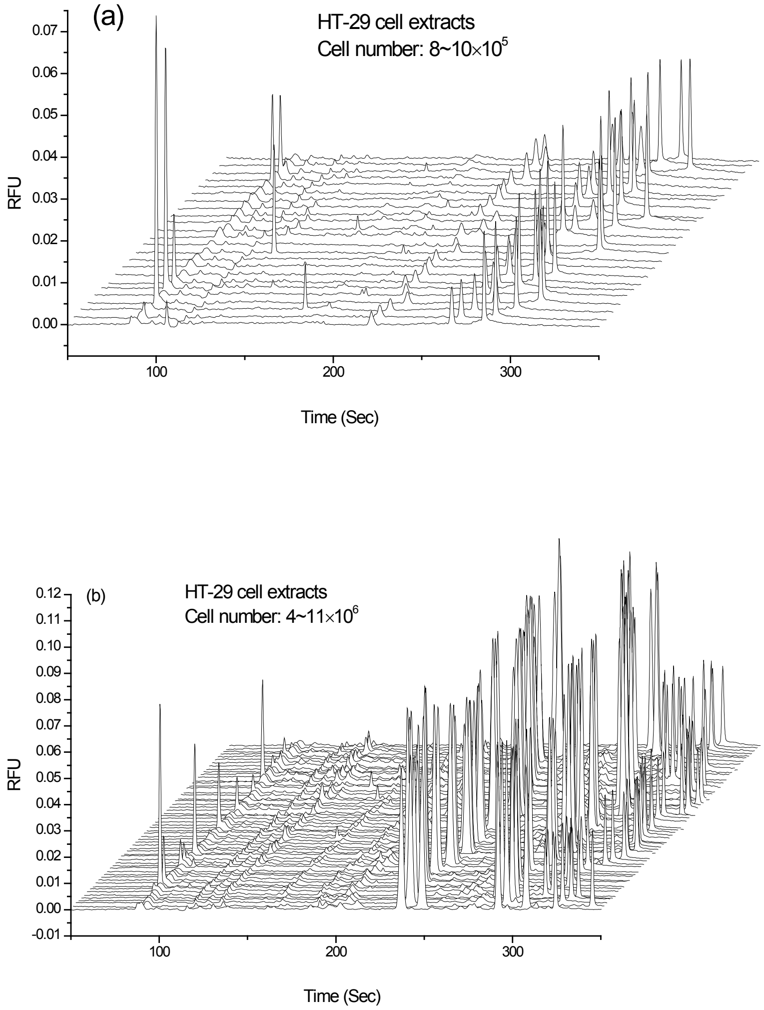

Figure 5.15 Electropherograms of HT-29 cell extracts under the optimized extraction and separation conditions

---

Note: (a) Extracted on the second day after seeding (b) Extracted on the fourth day after seeding. The number of cells extracted ranges (a) 8.0 ~ 10 × 10^5 and (b) 4.0 ~ 11 × 10^6.

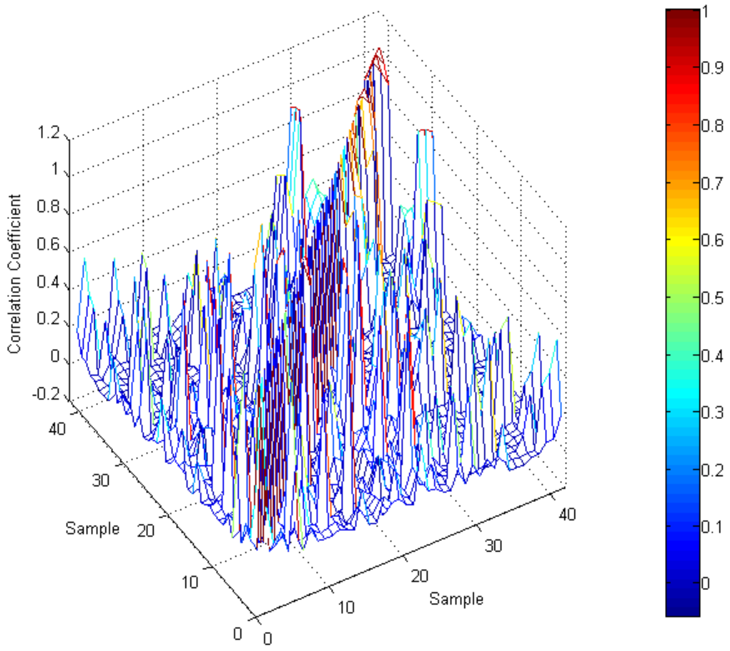

Figure 5.16 Correlation coefficient map of electropherograms of FHC cells and HT-29 cells without pretreatments

---

Note: The electropherograms 1-12 are electropherograms from FHC cells extracted on the eighth day after seeding (cell density ~3.3×10^5/T-25 flask). The electropherograms 13-27 are electropherograms from HT-29 cell extracted on the second day after seeding (cell density ~8.7×10^5/T-25 flask). The electropherograms 28-42 are electropherograms from HT-29 cell extracted on the fourth day after seeding (cell density ~4.0×10^6/T-25 flask).

The sections between 100 seconds to 375 seconds (1101 data points) of the electropherograms are used for calculation of correlation coefficients.

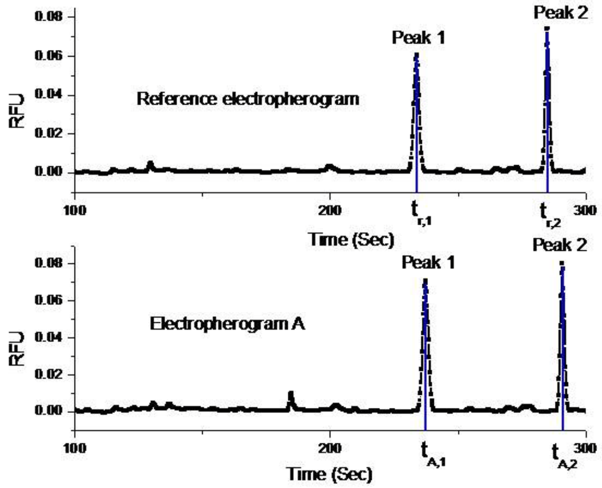

To align both peak 1 and peak 2 in electropherogram A to the corresponding peaks in the reference electropherogram, following procedures are performed.

1. **Calculate the re-spacing factor** $F = \frac{t_{r,1} - t_{r,2}}{t_{A,1} - t_{A,2}}$
2. **Calculate the shifting factor** $\Delta t = t_{A,1} - F \cdot t_{A,2}$
3. **Calculate the new set of x axis, t_A', for electropherogram A.** $t_A' = t_A \cdot F + \Delta t$
4. **Interpolate the signal based on the original electropherogram A and the new t_A' vector. Plot the vector y_A' vs. t_r to obtain the aligned electropherogram A to the reference electropherogram.**

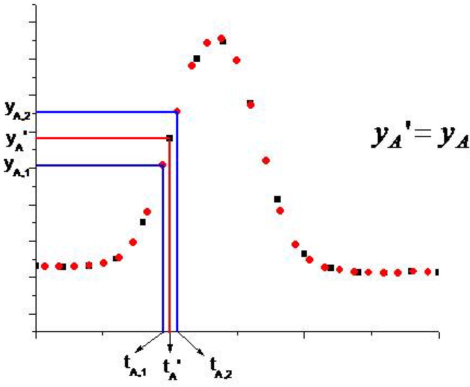

$$y_A' = y_{A,1} + \frac{t_A' - t_{A,1}}{t_{A,2} - t_{A,1}}(y_{A,2} - y_{A,1})$$

Figure 5.17 Procedure of aligning two peaks in two electropherograms

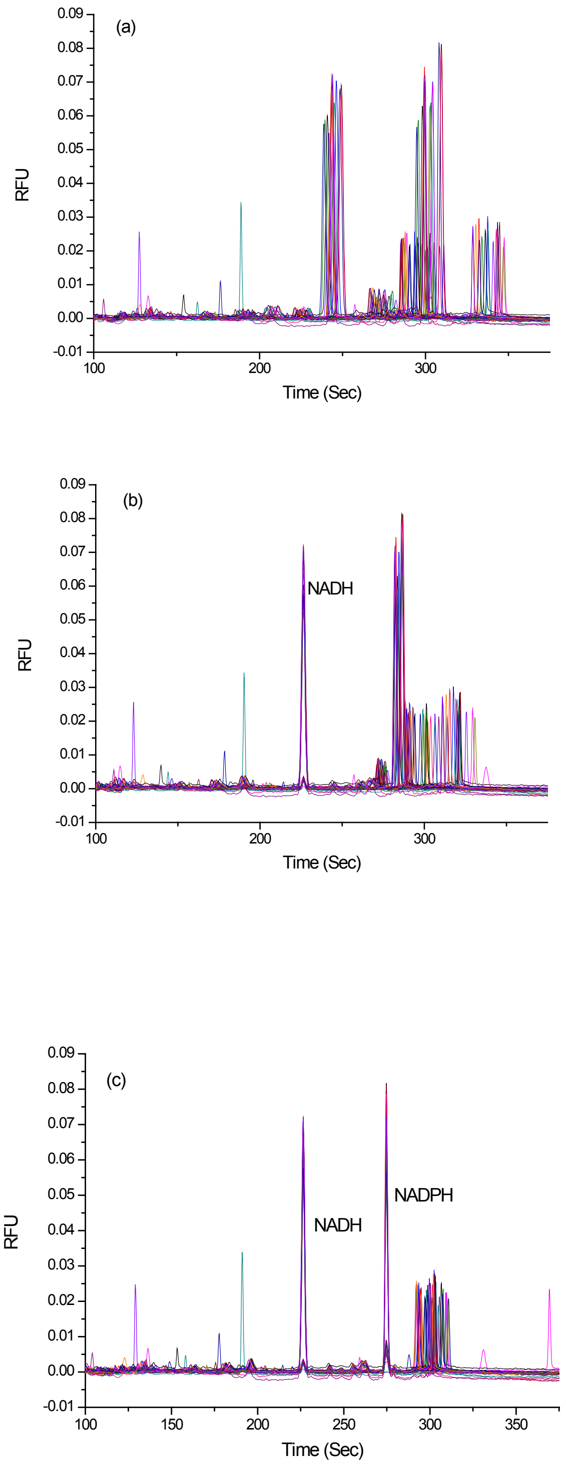

Figure 5.18 Examples of electropherograms (a) before pretreatment; (b) after aligning them to their NADH peak; (c) after aligning them using both NADH and NADPH peaks as references

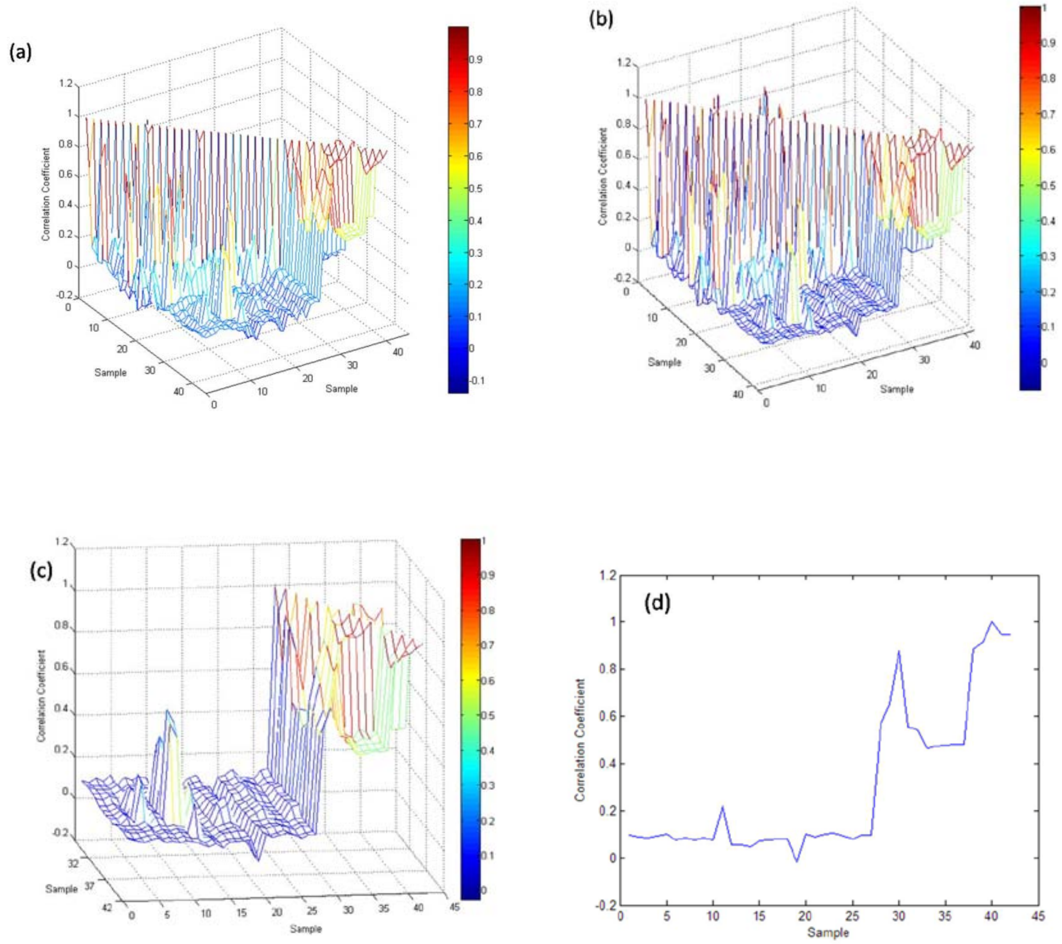

Figure 5.19 Correlation coefficient map of electropherograms of FHC cells and HT-29 cells with aligning NADH peaks for all electropherograms

---

Note: The electropherograms 1-12 are electropherograms from FHC cell extracted on the eighth day after seeding (cell density ~3.3 × 10^5/T-25 flask). The electropherograms 13-27 are electropherograms from HT-29 cell extracted on the second day after seeding (cell density ~8.7 × 10^5/T-25 flask). The electropherograms 28-42 are electropherograms from HT-29 cell extracted on the fourth day after seeding (cell density ~4.0 × 10^6/T-25 flask).

In (a), the electropherograms with migration time from 0 seconds to 600 seconds (2401 data points) are used for calculation of correlation coefficients. In (b), (c) and (d), only the sections between 100 seconds to 375 seconds (1101 data points) of the electropherograms are used for calculation of correlation coefficients. (c) is the cross sections of (b) at x = 28 to x=42. (d) is the cross section of (b) at x = 40.

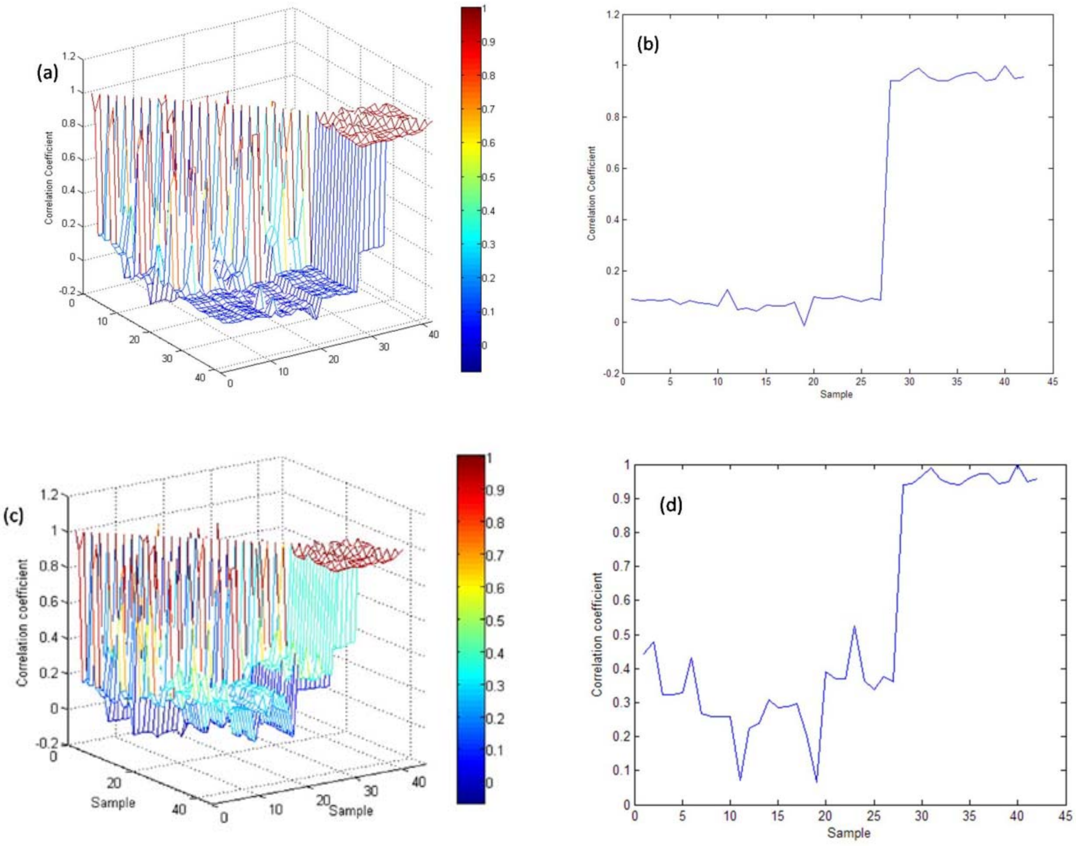

Figure 5.20 Correlation coefficient map of electropherograms of FHC cells and HT-29 cells with aligning both NADH and NADPH peaks for the electropherograms

---

Note: The electropherograms 1-12 are electropherograms from FHC cell extracted on the eighth day after seeding (cell density ~3.3 × 10^5/T-25 flask). The electropherograms 13-27 are electropherograms from HT-29 cell extracted on the second day after seeding (cell density ~8.7 × 10^5/T-25 flask). The electropherograms 28-42 are electropherograms from HT-29 cell extracted on the fourth day after seeding (cell density ~4.0 × 10^6/T-25 flask).

The sections between 100 seconds to 375 seconds (1101 data points) of the electropherograms are used for calculation of correlation coefficients. (a) is the correlation result of electropherograms which are first aligned with both NADH and NADPH peaks as references for the electropherogram sets 1-12, 13-27, and 28-42, respectively, and then all aligned to NADH peak. (b) is the cross section of (a) at x = 40; (c) is the correlation result of electropherograms aligned to both NADH and NADPH peaks for all the electropherograms; (d) is the cross section of (c) at x=40.

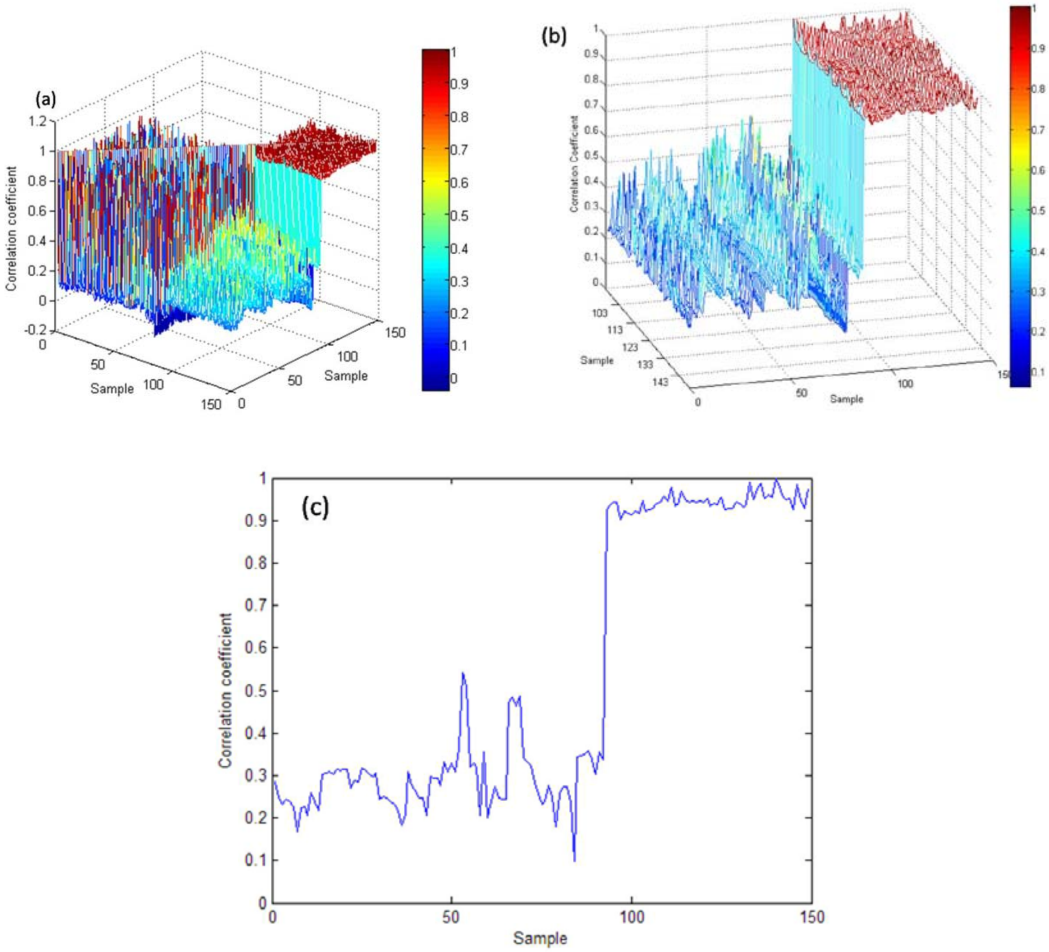

Figure 5.21 Correlation coefficient map of electropherograms with aligning both NADH and NADPH peaks for all electropherograms

---

Note: The electropherograms 1-65 are electropherograms from FHC cells extracted on the eighth day after seeding (cell density 3.0~6.0 × 10^5/T-25 flask). The electropherograms 66-92 are electropherograms from HT-29 cell extracted on the second day after seeding (cell density 8.7~10 × 10^5/T-25 flask). The electropherograms 93-149 are electropherograms from HT-29 cell extracted on the fourth day after seeding (cell density 4.0~11 × 10^6/T-25 flask).

The sections between 100 seconds to 375 seconds (1101 data points) of the electropherograms are used for calculation of correlation coefficients. (a) is the correlation result of the electropherograms aligned and extrapolated to both NADH and NADPH peaks for all the electropherograms; (b) is the cross sections of (a) at x = 93 to x = 149; (c) is the cross section of (a) at x = 140.

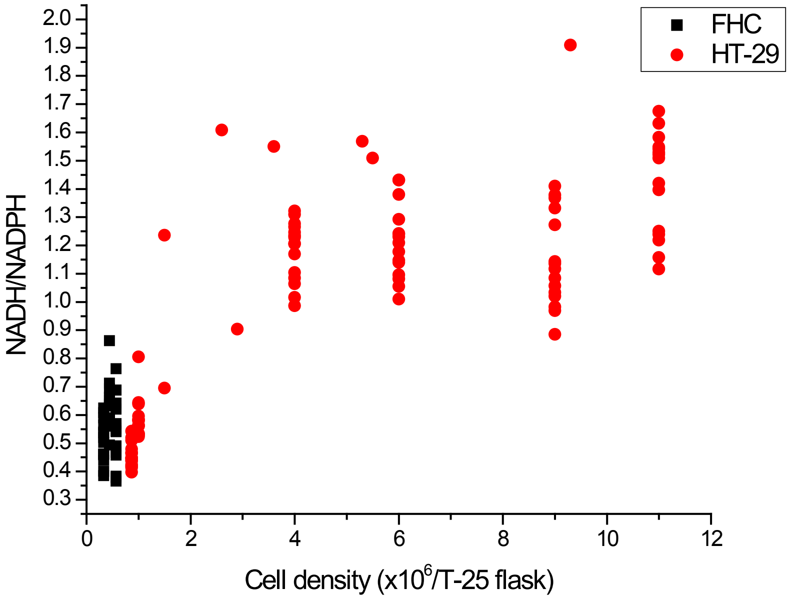

Figure 5.22 Peak area ratios of NADH/NADPH in HT-29 and FHC cell extracts with different cell densities

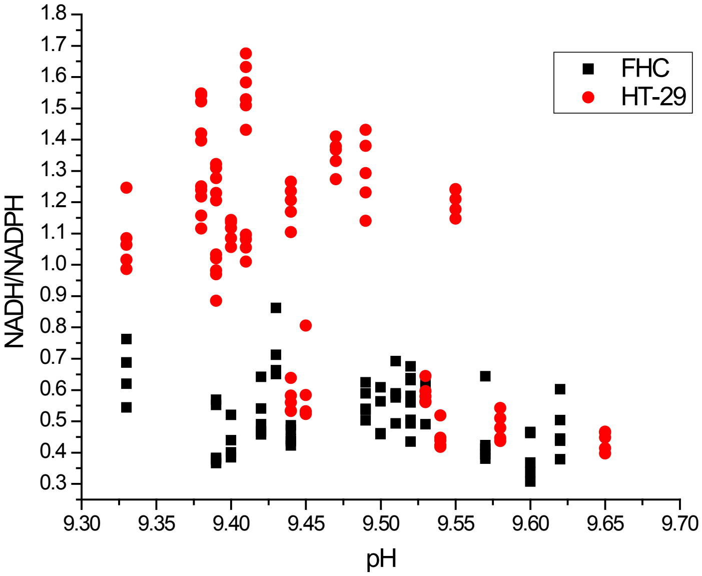

Figure 5.23 Peak area ratios of NADH/NADPH in HT-29 and FHC cell extracts with different final extract pHs

CHAPTER 6

TWO DIMENSIONAL CORRELATION ANALYSIS OF ELECTROPHEROGRAMS AND FLUORESCENCE SPECTRA

6.1 Introduction

Fluorescence spectroscopy is a powerful tool for probing molecular structures and intra/intermolecular interactions and for chemical and biological sensing. Among spectroscopic techniques, fluorescence enjoys the distinction of superior signal-to-noise ratio and sensitivity to the micro environmental changes around the probe molecules [111]. With these advantages, fluorescence spectroscopy, imaging and probes are being applied in a wide array of fields in biology and medicine [193]. However, in biological samples containing a vast number of molecular components, multiple endogenous fluorophores exist in the system and contribute to the overall fluorescence spectroscopy of the system [6]. The overlap of fluorescent bands from different fluorophores or the same fluorophore in different cellular and extracellular micro environments makes the analysis of the fluorescence spectra a challenge. The tissue and cell fluorescence spectra are good examples of this complexity (Figure 6.1). Figure 6.1(a) shows the tissue fluorescence spectra at normal and cancerous stages, while the spectra of HT-29 cell extracts are depicted in Figure 6.1(b). The HT-29 cells were extracted as described in Chapter 5 and the spectra were collected on an Aminco Bowman Series 2 Luminescence Spectrometer at the excitation wavelength of 325 nm.

Two-dimensional correlation spectroscopy (2D COS) has been shown to be a very effective approach to resolving overlapped spectral peaks and correlating spectral bands with the same origins [184-185]. It has been applied to a number of spectroscopic techniques, including IR, Raman, fluorescence, and NMR. Three techniques have been developed for two-dimensional fluorescence correlation spectroscopy (2D FCS), dynamic, statistical and generalized two-dimensional correlation analysis. Among them, statistical 2D FCS uses statistical parameters such as the covariance or correlation coefficient to evaluate correlation between variables as described in Chapter 5. Statistical two-dimensional correlation analysis of fluorescence spectra has been developed in the Geng research lab for tissue classification in cancer detection and in other biological systems [9, 12-13, 194]. The dynamic 2D FCS was first introduced in the Geng research lab [195-197]. Briefly, the dynamic 2D FCS evaluates the correlation between variables through a sinusoidal perturbation on the excitation. This technique is also extended to 2D correlation capillary electrophoresis to perform cross-correlation between elution times in separation [197-198]. The generalized 2D correlation analysis was first formulated by Noda [185, 199]. The basic principle of the generalized 2D correlation analysis is that any form of perturbation, including time, temperature, pressure, concentration, voltage, etc., can be used to generate the synchronous and asynchronous 2D correlation to reveal the correlation between variables. The generalized 2D correlation can even be applied to find relations between two different types of analytical signals, as in 2D hetero-correlation analysis [185].

Laser induced fluorescence is one of the detectors of choice for capillary electrophoresis because its high sensitivity perfectly matches the requirement of CE. Our effort to separate and quantify endogenous fluorophores in cell extracts by CE-LIF is described in the previous chapters. With an LIF detector, an electropherogram is a plot of the fluorescence intensity versus the migration time. All endogenous fluorophores are baseline separated when the separation conditions are optimized. The hetero-correlation between these isolated CE peaks with the fluorescence spectra of the cell extracts should help resolve the overlapped fluorescence spectra into their individual components. Although not a focus of this work, another potential of this hetero-analysis between CE and spectroscopy is that the correlation between an electrophoretic peak and specific spectroscopic bands can verify the identity of the CE peak. This technique is potentially a complementary tool to spiking samples with standards for identifying peaks from cell extracts. This chapter establishes the 2D generalized correlation analysis between electropherograms and fluorescence spectra using the concentration ratio change as the perturbation, explores advantages and characteristics of the technique through simulation, and demonstrates its resolution power through detailed correlation between experimental electropherograms and spectra of FAD/NADH mixtures.

6.2 Theory

The discrete Hilbert scheme is used to describe the mathematical procedure of the generalized 2D correlation by Noda [200]. Here, we adapt this scheme to demonstrate the evaluation of the correlation between the fluorescence signals of electropherograms and spectra.

The electropherograms from CE-LIF separations arise from the spread of the fluorescence of the system along the migration time vector. Similarly, the fluorescence spectra arise as the fluorescence intensity spreads along the wavelength vector. In order to evaluate the correlation between these two fluorescence intensities with changes caused by the perturbation-concentration change, the electropherogram and the corresponding fluorescence spectrum for a solution are concatenated into a single vector. With concentration perturbation, c_j ($j = 1, 2, ..., m$), the fluorescence intensity matrix can be expressed as

$$I_j(x) = I(x, c_j) \text{ where } j = 1,2,...,m \qquad [6.1]$$

where variable x refers to the migration time for the electropherogram and wavelength for the fluorescence spectrum. For any two dynamic fluorescence intensities measured at x_1 and x_2, the synchronous and asynchronous 2D correlation intensities can be evaluated by equations 6.2 and 6.3, respectively.

$$\Phi(x_1, x_2) = \frac{1}{m-1}\sum_{j=1}^{m} I_j(x_1) \cdot I_j(x_2) \qquad [6.2]$$

$$\Psi(x_1,x_2) = \frac{1}{m-1}\sum_{j=1}^{m} I_j(x_1)\cdot\sum_{k=1}^{m} N_{jk}\cdot I_j(x_2)\text{, where } N_{jk} = \begin{cases} 0 & \text{if } j = k \\ \dfrac{1}{\pi(k-j)} & \text{if } j \neq k \end{cases} \qquad [6.3]$$

The N_{jk} term is called the Hilbert-Noda transformation matrix [200]. When the concentration intervals are not equally spaced, the N_{jk} term should be modified as shown in equation 6.4 [201].

$$N_{jk} = \begin{cases} 0 & \text{if} j = k \\ \dfrac{c_{k+1} - c_{k-1}}{2\pi(c_k - c_j)} & \text{if } j \neq k \end{cases} \qquad [6.4]$$

Here, the synchronous correlation intensity $\Phi(x_1,x_2)$ shows how coincident the fluorescence signals x_1 and x_2 are. The asynchronous correlation intensity $\Psi(x_1,x_2)$ shows how out-of-phase the fluorescence signal x_1 and x_2 are. In our system, with the concentration change in the mixture, the CE peak of a particular molecule and the fluorescence peak of this molecule will change at the same rate. If the concentrations of two components in the system change at different rates, the asynchronous correlation intensity map will show two pairs of associated CE and fluorescence peaks belonging to the two components, respectively.

The synchronous correlation intensity matrix can be plotted as a contour map called the synchronous correlation contour plot. It is a symmetrical plot about the main diagonal line corresponding to $x_1 = x_2$. The correlation peaks appear on the diagonal line (autopeak) which is mathematically equal to the autocorrelation function of the fluorescence signal variations. A higher autocorrelation peak usually represents the fluorescence signal changes to a greater extent due to the given perturbation, i.e., as the concentration changes. The off-diagonal peaks (cross peaks) are positive or negative peaks, which represent the coincidental changes of two fluorescent signals at x_1 and x_2. The positive cross peak at the coordinate (x_1, x_2) means the two fluorescence signals at x_1 and x_2 are increasing or decreasing together. A negative peak at the coordinate (x_1, x_2)

means that when the fluorescence signal at x_1 is increasing/decreasing, the fluorescent signal x_2 is changing in the opposite direction (decreasing/increasing).

The asynchronous correlation contour plot is not symmetrical. When the intensities of two fluorescent signals at x_1 and x_2 change out of phase to each other due to the perturbation, the cross peak will appear at the coordinate (x_1, x_2). There are no diagonal peaks in the asynchronous correlation contour plot. The positive and negative peaks in the asynchronous correlation contour map usually can be used to determine the sequential order of the two signal changes.

6.3 Experimental

6.3.1 Chemicals and Materials

FAD (95%) and β-NADH (98%) were obtained at the highest purity from Sigma (St. Louis, USA) and used as received. Boric acid and sodium hydroxide were purchased from Aldrich (Milwaukee, WI, USA). Ultra pure Milli-Q (Millipore, Bedford, MA, USA) water was used to prepare all solutions. Stock solutions were prepared daily and CE separation was performed no later than 5 hours after sample preparation. A 170 mM pH 9.0 borate buffer was prepared. The buffer was adjusted to the target pH using 0.1 M sodium hydroxide solution. All solutions were filtered through 0.20 µm syringe filters (Cole-Parmer Instrument Co., Vernon Hills, IL, USA) and sonicated prior to experiment.

6.3.2 Instrumentation

A Beckman P/ACE™ MDQ system (Beckman Coulter, Fullerton, CA, USA) was used to perform the CE separations. The separation conditions were those optimized for cell extracts so that it could be easily adapted for cell analysis later. In LIF detection, the excitation was provided by a He-Cd laser at 325 nm and the fluorescence emission was collected through a 345 nm long pass filter to reduce scattered laser light. The excitation power was typically 1 mW. Polyimide coated fused silica capillaries (Polymicro

Technologies, Phoenix, AZ) with an effective length of 20 cm (30 cm × 50 µm I.D.) were used in the experiment. Prior to use, the capillaries were preconditioned with sodium hydroxide and run buffer. Between runs, the capillary was conditioned consecutively with 0.1 M sodium hydroxide, 0.1 M hydrochloric acid, deionized water and run buffer. Samples were introduced by pressure injection for 10 seconds at 0.5 psi (~3.5 kPa). The temperature of the capillary was maintained at 25ºC with the instrument thermostating system. Separation of the FAD and NADH mixtures was performed under15 kV in 170 mM, pH 9.0 borate buffer.

An Aminco Bowman Series 2 Luminescence Spectrometer was used to collect the fluorescence spectra of the mixtures. The excitation wavelength was 325 nm and the emission is collected between 375 nm to 600 nm. The bandpass width was set as 4 nm and the step size for collection was 1 nm. The scanning rate was set to 1 nm/second. The high voltage for detector was set as 785 Volts to ensure that the highest peak at 460 nm of the sample with the highest concentration was at 70% of the full detection range.

6.4 Simulated correlation between electropherograms and fluorescence spectra

To explore the characteristics and potential advantages of the generalized 2D correlation analysis, we simulated a two-component mixture system. A set of electropherograms and corresponding fluorescence spectra were generated for a series of mixtures of FAD and NADH based on their individual fluorescence spectra excited at 325 nm.

The concentration ranges of the two components were designed based on their fractional intensity contributions to tissue fluorescence in optical biopsy. As shown in Table 1.2, statistical decomposition of the tissue spectra recovered that the FAD contribution to tissue fluorescence is 1.0%±0.2% to 4.7%±2.1% and the NADH contribution is 11.6%±1.3% to 53.8%±7.0%. The ratio of the two compounds is in the range from 0.06 to 0.10. Additional consideration is from the separation of HT-29 cell extracts shown in Chapter 5, where the ratio between the flavins (FMN and FAD) and nicotinamides (NADH and NADPH) is approximately 0.11. Therefore, in our simulation, the ratio between the two compounds was selected to be between 0.06 and 0.11. It is noted that FMN and FAD have similar emission spectra and so do NADH and NADPH as shown in Figure 1.11. Thus, in the statistical decomposition of the tissue fluorescence spectra, it is not possible to differentiate the contributions from FMN and FAD or the contributions from NADH and NADPH.

The simulation of the electropherograms and spectra was performed in MATLAB 7.4.0 (The MathWork Inc., Natick, MA, USA) with a function simulation.m as included in Appendix A.3 and the result is shown in Figure 6.2. The peak intensities of FAD and NADH were varied from 1 to 7 and 10 to 60, respectively (Table 6.1). Twenty pairs of electropherograms and fluorescence spectra were generated according to the 20 evenly spaced concentration pairs. An impurity peak in the NADH sample was also simulated as a peak migrating right after the NADH peak.

The synchronous correlation and asynchronous correlation were evaluated for this set of simulated data according to equations 6.2 and 6.3. The MATLAB program used to calculate and plot the correlation matrices is shown in Appendix A.4.

The correlation spectra (Figures 6.3 and 6.4) are composed of four quadrants. The two on the diagonal line are the homo-correlation spectra of the electropherograms and fluorescence. The other two areas contain the hetero-correlation spectra between capillary electrophoresis and fluorescence spectroscopy of the samples. In the synchronous correlation spectrum (Figure 6.3), a strong peak is observed on the diagonal at the 460 nm maximum of the fluorescence spectra. Additional intense correlation features on the diagonal correspond to the CE peaks for FAD and NADH. These features are expected for the autocorrelation, where the changes on two axes are naturally synchronized. The strengths of the autocorrelation depend on the squared intensity of the one-dimensional spectra, thus accentuating the fluorescence peak. The autocorrelation feature for the CE peak of FAD is relatively weak in comparison as a result. Off-diagonal correlation peaks are also observed between the CE peaks of FAD and NADH because their intensities are changing in the same direction across the samples, although at different rates. The strength of the correlation is determined by the intensities of the one-dimensional spectra on both axes, and the how synchronized the two peaks are in their intensity changes. Interestingly, there is rather strong hetero-correlation between the fluorescence peak and all CE peaks, with strengths exceeding those of the CE-CE homo-correlation. The high intensity of the 1D fluorescence spectra dictated these intense correlation peaks.

The contour map of the asynchronous correlation is shown in Figure 6.4. The homo-correlation regions of the spectrum feature the classical characteristics of the two-dimensional spectra. There is no asynchronous correlation on the diagonal line because the variables on both axes are identical and thus naturally in phase on the diagonal. This is an important feature of the asynchronous spectrum that enables spectral resolution. For example, in the CE homo-correlation region, the two CE peaks for NADH sample have identical rates of change and thus do not exhibit any asynchronous correlation. On the other hand, the CE peak for FAD asynchronously correlates with both NADH peaks. As a result, a cross section of the asynchronous spectrum at the FAD peak recovers the electropherogram of NADH cleanly and vice versa. The pattern of two split peaks in the fluorescence region of the asynchronous correlation spectra clearly indicates that the 1D fluorescence spectra contain contributions from two bands, although the second band is not evident at all in 1D. The hetero-correlation region has the most important feature we are investigating: spectral resolution assisted by chemical separations. Specifically, the CE peaks of FAD and NADH correlate with different sections of the fluorescence peak (Figure 6.4), effectively resolve it into two bands.

As shown in Figures 6.4 and 6.5, at the cross section of 157 seconds, the time of FAD migration, three cross peaks appear signifying that their intensity changes are not in phase with FAD. Two cross peaks are located at 266 and 289 seconds of the electropherogram, where NADH and its impurity appear, respectively. Another cross peak is located at 460 nm of the fluorescence spectra, the maximum of NADH fluorescent emission. In the meantime, the cross section at 266 seconds, the CE peak for NADH, two cross peaks also appear due to the out-of-phase changes in their signals compared to NADH (Figures 6.4 and 6.6). One is located at 157 seconds, where FAD migrates. The other cross peak shows an important correlation with a fluorescence band at 525 nm. This band corresponds to the fluorescence emission of the FAD peak. This fluorescence spectrum of FAD is buried in the 1D spectra that is dominated by the strong NADH fluorescence. Since the signal from NADH in the mixture fluorescence spectra is synchronized with the signal in the CE peak of NADH, the asynchronous correlation analysis *completely* removes the intensity contribution of NADH to the fluorescence, thus resolving the FAD spectrum out of the mixture. Clearly, for any two-component system, as long as the two components have different fluorescence emission maxima and can be separated by CE-LIF, we can correlate their CE peak and their fluorescence emission peak respectively. For systems with more than two components, we can still identify the correlation between a CE peak and a fluorescence emission peak by observing its cross section to see where the cross peak do not appear as long as (1) all components have different fluorescence emission peaks, (2) they can be separated by CE-LIF, and (3) their concentrations change at different paces.

In the simulation, the peaks in the electropherograms were kept at the same migration times and the peak widths were kept constant. The resulting correlation pattern is very clean as shown in Figure 6.4. With this clean correlation, even small changes in the concentration ratio as listed in Table 6.1 could give us the expected correlation. In a real CE separation, however, there may be several interfering factors: (1) shifting of the peak locations due to changing EOF and variations in separation, (2) peak broadening due to variations in separation, and (3) impurity peaks in the samples. We evaluated the influence of these experimental factors on the correlation analysis. The effect of EOF shifting is simulated in MATLAB with the program in Appendix A.5 at two levels of variations. In Figure 6.7, the EOF shifts randomly for each electropherogram within the range of ±2% of the total analysis time. In Figure 6.8, a higher level of variation in EOF shifts is simulated: up to ±5%. Clearly, with EOF shifting, each cross peak is split into a number of cross peaks around the original position. In addition, a number of false cross peaks appearing at the 266 seconds section. And with the variation from EOF shifting increasing, the false cross peaks eventually overwhelm the original cross peak at 525 nm as shown in Figure 6.8.Therefore, even the EOF shifting alone can fail the correlation evaluation. With experimental data, pretreatments of data such as aligning peaks are necessary for a successful correlation evaluation.

6.5 Correlation between electropherograms and fluorescence spectra of FAD and NADH

Mixtures of FAD and NADH standards were made with the concentration ranges of 1 to 7 μM and 10 to 60 μM, respectively. These ranges are determined based on the contributions of FAD and NADH to the tissue fluorescence spectra. The concentrations of the ten samples are listed in Table 6.2.

The 2D asynchronous correlation spectrum in Figure 6.9 was constructed from the raw experimental data and shows that the variations in the electropherograms brought cross peak splitting and false cross peaks in the plot. For example, a cross section at 229 seconds has false peaks at 229 seconds in the electropherogram and at 460 nm in the fluorescence spectrum. Significantly, the false peak at 460 nm overwhelmed the expected cross peak at 525 nm. Clearly, a pretreatment to align all the peaks in the electropherograms is necessary for the correlation analysis.

The complications brought by peak shifting have been studied in 2D correlation spectroscopy by many groups as reviewed by Noda [184-185]. For example, to account for the peak shifting and band widening, Lefèvre *et al.* used the simulation of actual data by curve fitting based on the experimental data to perform the 2D analysis [190].

Considering the sources of variation in CE discussed in section 6.4, correction for EOF by shifting alone does not achieve alignment of all the peaks because a lengthened EOF will delay the migration times of all peaks but will not change the time between peaks. In reality, the distance between peaks could vary in CE as the results of other experimental fluctuations. To better account for these variations, we used a bracketing method for alignment. Specifically, two prominent peaks in the electropherograms are chosen as the reference peaks. Both peaks are aligned across all electropherograms. The entire electropherogram is then recalculated through interpolation in order to keep an identical variable axis for all electropherograms in the correlation analysis. The alignment was performed using the MATLAB program in Appendix A.2. Altering the migration time does not cause any loss of relevant correlation since the perturbation in the experiments is molecular concentrations and the migration time of a compound is not related to the perturbation. The electropherograms before and after the alignment are shown in Figure 6.10. Close examination of the electropherograms after alignment reveals that the peak widths vary significantly, which can still be a potential interference to the evaluation of correlation.

The 2D asynchronous correlation spectrum of the aligned electropherograms and the fluorescence emission spectra is shown in Figure 6.11. At the cross section of 197 seconds, there are mainly three cross peaks as expected (Figures 6.11 and 6.12). Two of them are at 229 and 235 seconds of the electropherogram, migration times for NADH sample. The third one is at 460 nm of the fluorescence, the peak maximum of NADH fluorescence emission. At the cross section of 229 seconds, several cross peaks appeared (Figures 6.11 and 6.13). The cross peak at 197 seconds and 525 nm are expected as the FAD out-of-phase correlation. The split peak at 229 seconds and the small peak at 460 nm are caused by the NADH peak broadening in the original electropherograms. The smaller peaks at the migration time lower than 197 seconds appear to be impurities in the FAD sample. Therefore, if this correlation method is applied to a multiple-component system, more pretreatments than aligning peaks such as correction for peak widths are needed to exclude false correlation information.

One way to standardize the peak width is to simulate Gaussian peaks with fixed peak widths based on the integrated peak areas of the experimental electropherograms. These simulated Gaussian peaks can be plotted against the average migration times of the peaks. As long as the relative peak ratios are preserved, the correlation information will be preserved. With this simulation method, we also eliminate the interference from those irrelevant noises.

The MATLAB function included in Appendix A.6 can be used to perform the simulation of the electropherograms. Based on the electropherograms we obtained from FAD/NADH mixture, there are 10 peaks from FAD, NADH and their impurities to simulate and the average peak base width is about 4.5 seconds. The average migration times were calculated for each of the ten peaks to be used as the center of the simulated Gaussian peak. Since all the simulated Gaussian peaks share the same peak width, multiplying the Gaussian peaks by the experimental peak areas as the intensity of the Gaussian peaks will preserve the relative peak ratios from the experimental data.

The 2D asynchronous correlation spectrum of the electropherograms simulated based on the experimental electropherograms and fluorescence spectra of FAD/NADH mixtures are shown in Figure 6.14. Compared to the asynchronous correlation of the raw experimental data (Figure 6.9) and the asynchronous correlation of the aligned data (Figure 6.11), those expected cross peaks are stronger and those split cross peaks are eliminated in Figure 6.14. The cross section at the average FAD migration time 191.5 seconds (Figure 6.15), there are still three cross peaks, two at the NADH sample migration time and the other at the maximum of NADH emission 460 nm. As shown in the cross section at the average NADH migration time 222 seconds (Figure 6.16), the initial split peaks caused by peak broadening of NADH disappears and the FAD sample out-of-phase correlation remain, including those from the impurities. In all, it demonstrates that we can eliminate the interference from peak broadening as well as preserve the major correlations with the electropherograms simulation method to standardize the peak widths.

6.6 Conclusion

The 2D generalized correlation analysis of the electropherograms and the fluorescence spectra has been demonstrated to be useful for mutual identification of peaks between them through the simulated data and experimental data. The perturbation employed is the concentration changes at different rates. To successfully evaluate the correlation of experimental data, pretreatments of electropherograms such as peak alignments and peak widths standardizations are necessary. More components could be added to the system in the future to really use the identification power. Eventually, we can apply the method to electropherograms and spectra of cell and tissue samples so that the components of these biological samples could be verified. The idea of correlating signals from separation technique and spectroscopy technique for the same sample can also be generalized to other separation and spectroscopy techniques other than CE and fluorescence spectroscopy.

Table 6.1 Peak heights and their ratios of FAD and NADH used for simulation of electropherograms and fluorescence spectra of the mixtures

FAD	NADH	Ratio
7	60.0	0.1167
6.7	57.5	0.1165
6.4	55.0	0.1164
6.1	52.5	0.1162
5.8	50.0	0.1160
5.5	47.5	0.1158
5.2	45.0	0.1156
4.9	42.5	0.1153
4.6	40.0	0.1150
4.3	37.5	0.1147
4.0	35.0	0.1143
3.7	32.5	0.1138
3.4	30.0	0.1133
3.1	27.5	0.1127
2.8	25.0	0.1120
2.5	22.5	0.1111
2.2	20.0	0.1100
1.9	17.5	0.1086
1.6	15.0	0.1067
1.3	12.5	0.1040
1.0	10.0	0.1000

Table 6.2 Concentrations of FAD and NADH of the samples used for in the CE and fluorescence experiments

FAD (μM)	NADH (μM)	Concentration Ratio
7.0	25	0.28
6.0	45	0.13
5.0	28	0.18
4.0	10	0.40
3.5	15	0.23
3.0	60	0.05
2.5	12	0.21
2.0	18	0.11
1.5	35	0.04
1.0	40	0.03

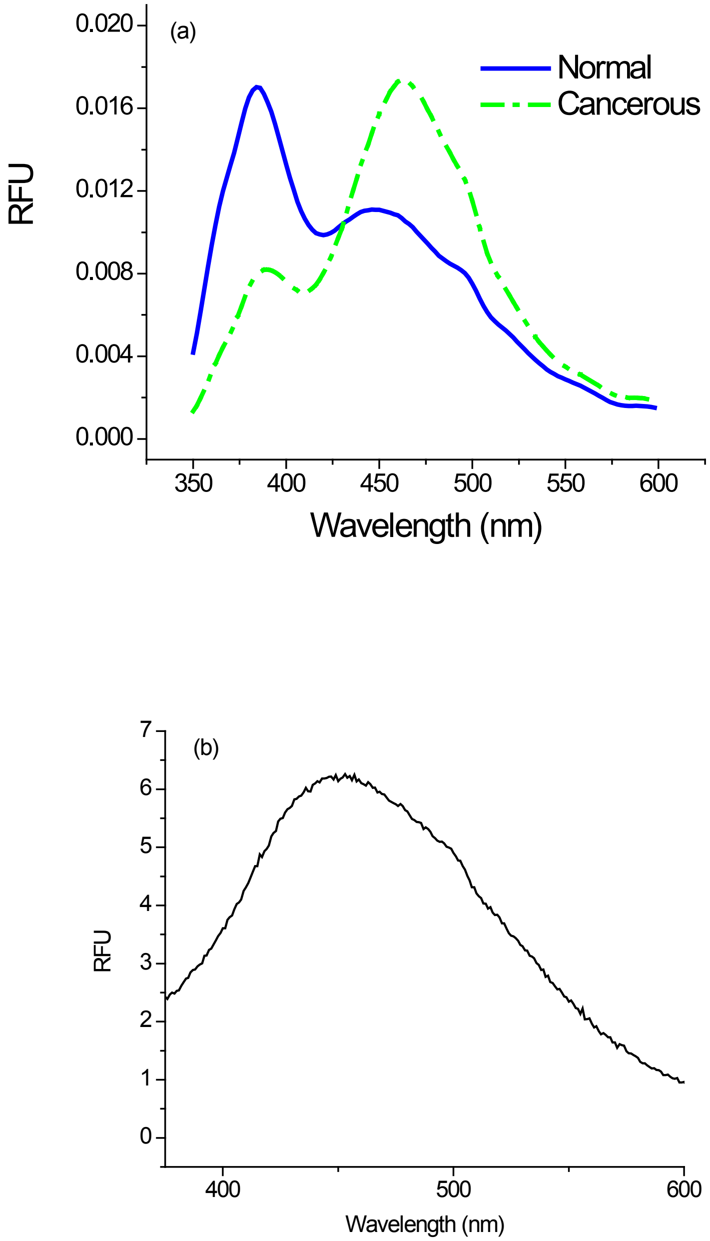

Figure 6.1 Fluorescence spectra of (a) tissue at normal and cancerous stages and (b) HT-29 cell extracts with excitation wavelength at 325 nm.

Source: (a) is adapted from Wang, G. F.; Platz, C. P.; Geng, M. L., Probability-based differential normalized fluorescence bivariate analysis for the classification of tissue autofluorescence spectra. *Applied Spectroscopy* 2006, 60 (5), 545-550.

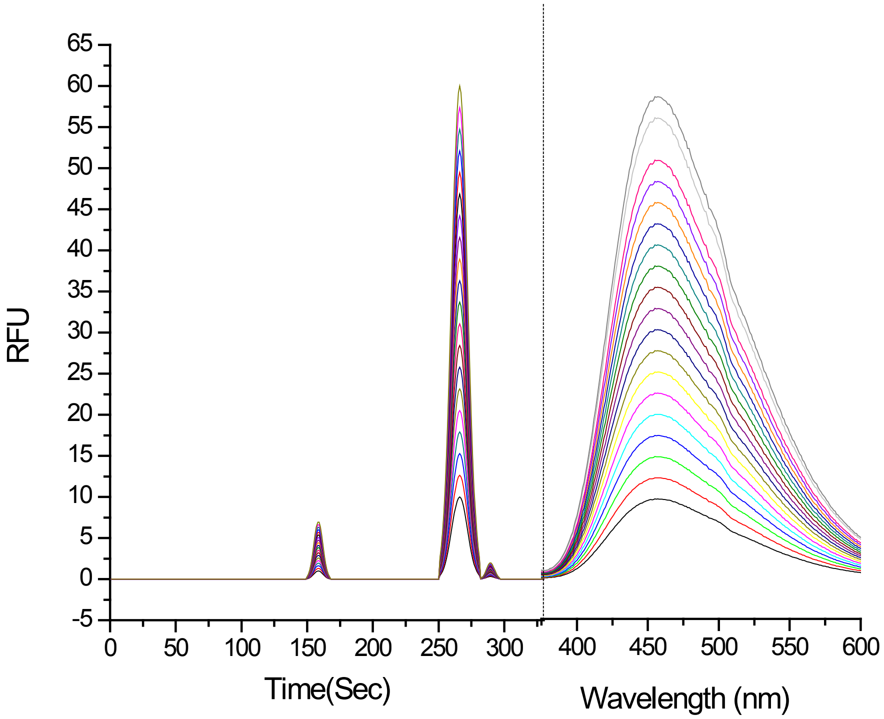

Figure 6.2 Simulated electropherograms and fluorescence spectra for mixture of FAD and NADH

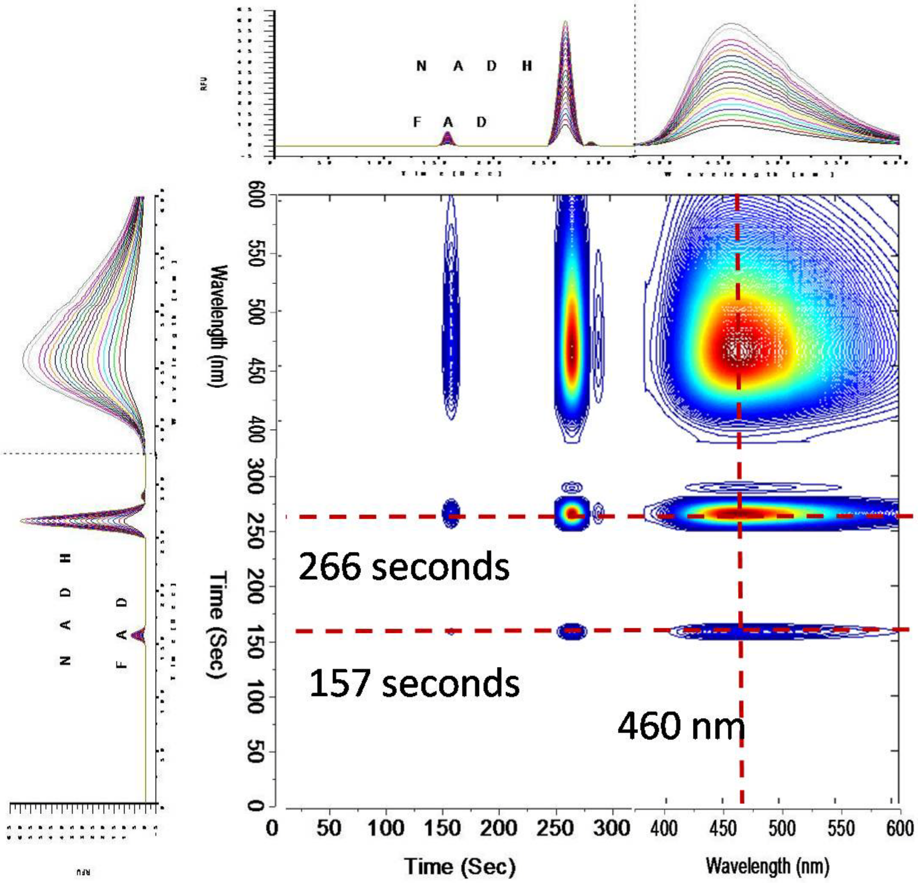

Figure 6.3 Two dimensional synchronous correlation spectrum of the simulated electropherograms and fluorescence spectra of FAD/NADH mixtures

---

Note: The simulated electropherograms and fluorescence spectra are plotted on the side bar of the 2D asynchronous correlation spectrum to demonstrate the cross peaks.

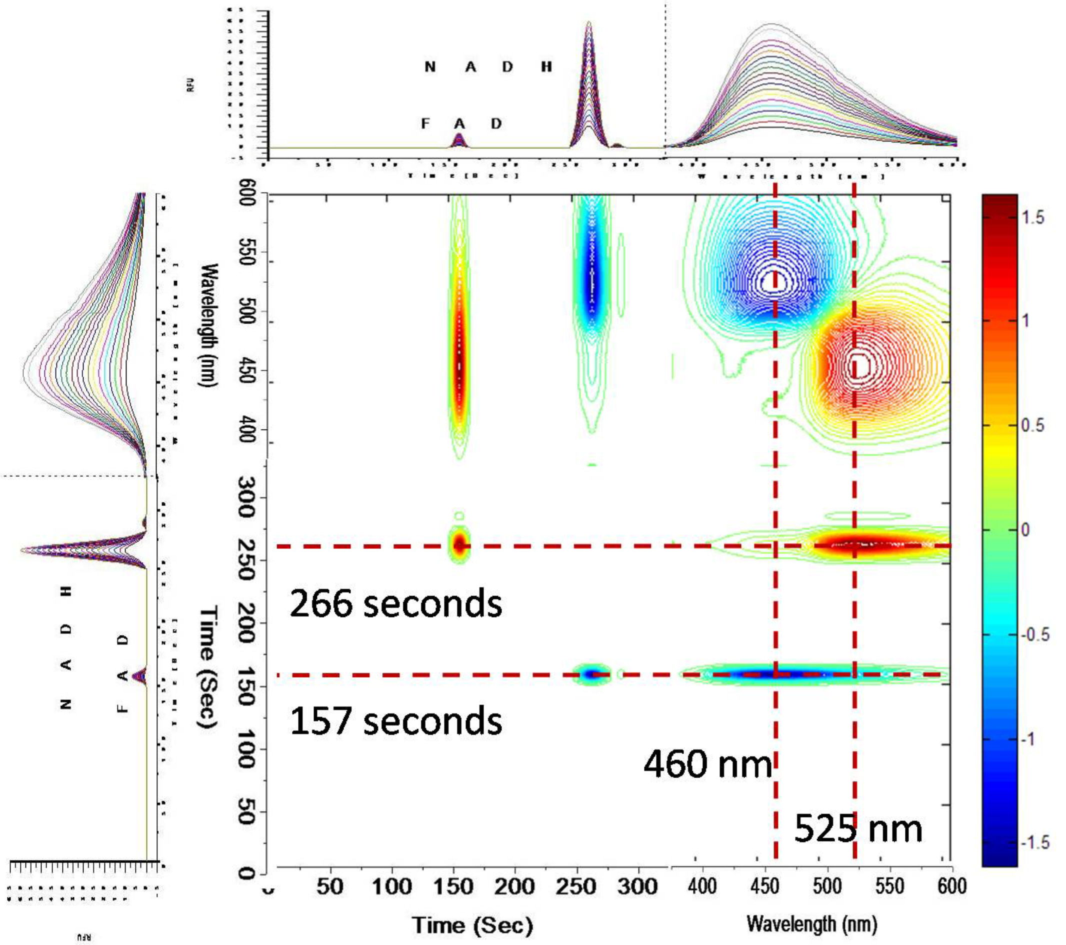

Figure 6.4 Two dimensional asynchronous correlation spectrum of the simulated electropherograms and fluorescence spectra of FAD/NADH mixtures

---

Note: The simulated electropherograms and fluorescence spectra are plotted on the side bar of the 2D asynchronous correlation spectrum to demonstrate the cross peaks.

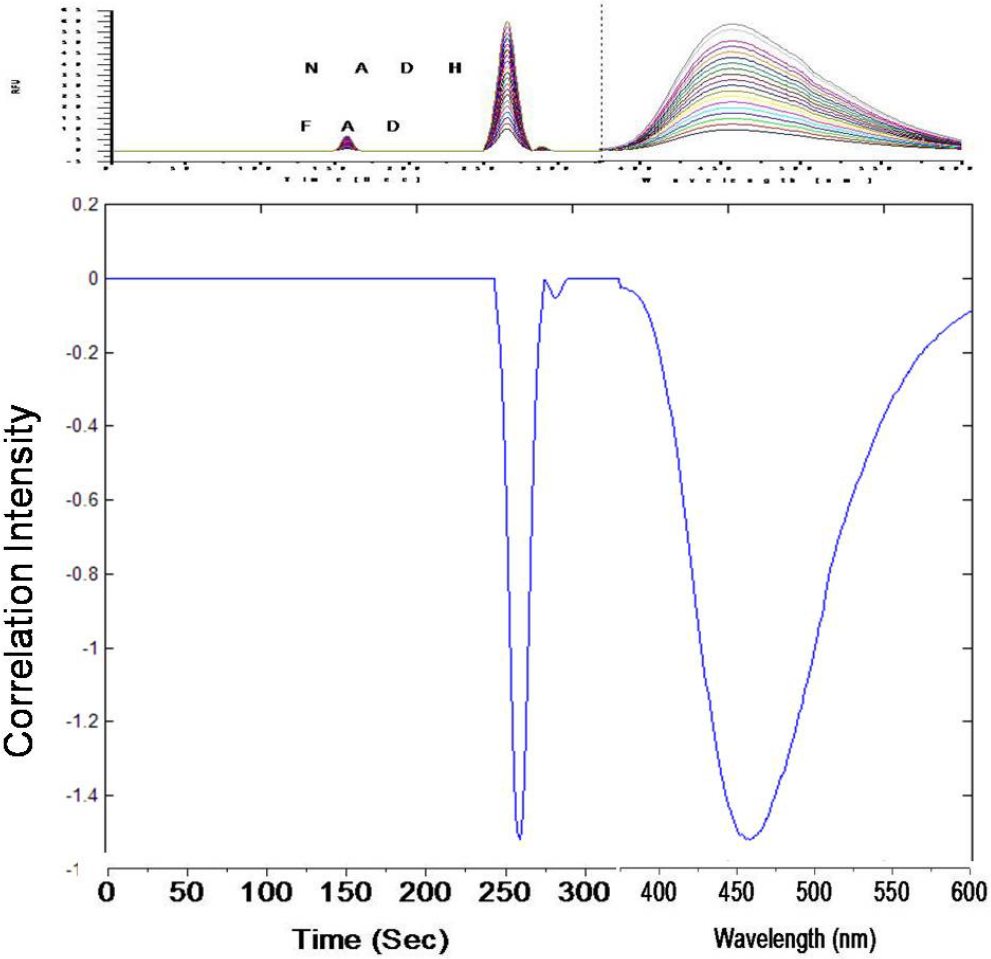

Figure 6.5 Cross section of the asynchronous correlation spectrum at 157 seconds of the electropherograms and fluorescence spectra

---

Note: The migration time of FAD is 157 seconds. The cross peaks in this cross section appear at 266 seconds of the electropherogram and 460 nm of the fluorescence spectra, which means both of the fluorescence signals come from the other component, NADH.

The simulated electropherograms and fluorescence spectra are plotted on the top of the cross section plot to demonstrate the cross peaks.

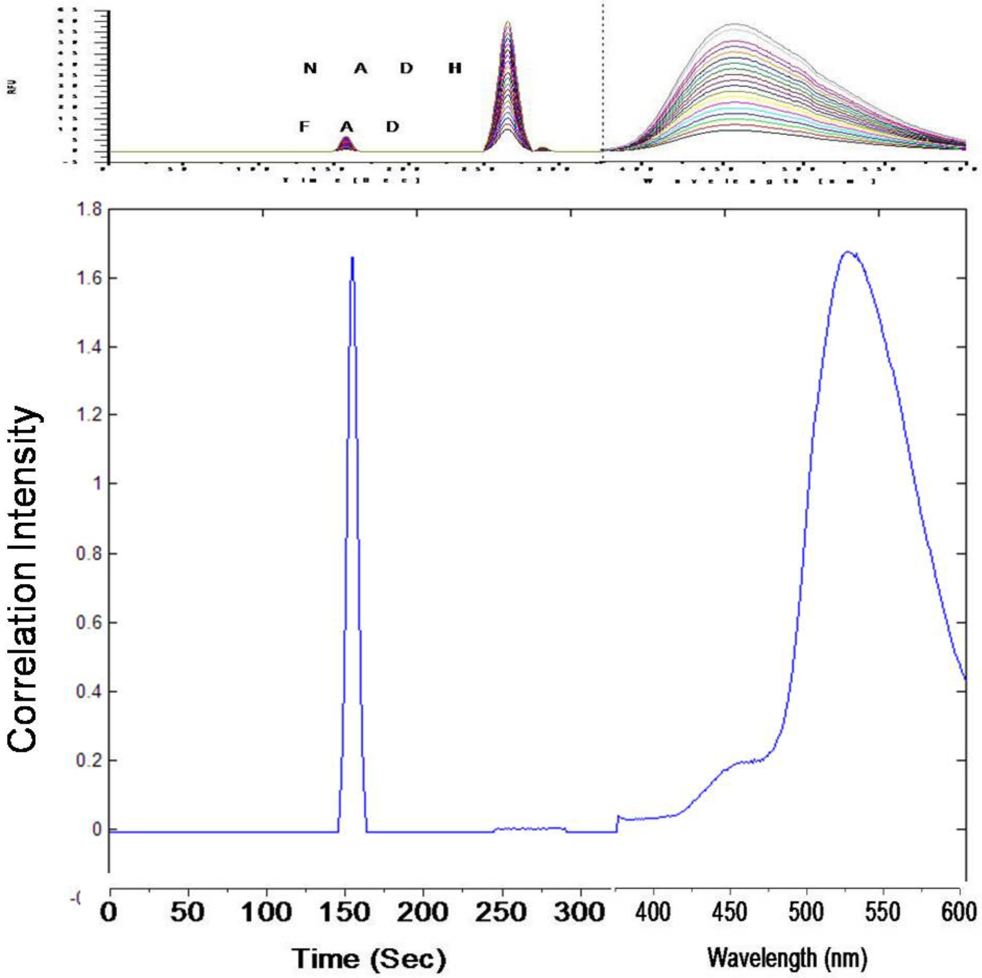

Figure 6.6 Cross section of the asynchronous correlation spectrum at 266 seconds of the electropherograms

---

Note: The migration time of NADH is 266 seconds. The cross peaks in this cross section appear at 157 seconds of the electropherogram and 525 nm of the fluorescence spectra, which means both of the fluorescence signals come from the other component, FAD.

The simulated electropherograms and fluorescence spectra are plotted on the top of the cross section plot to demonstrate the cross peaks.

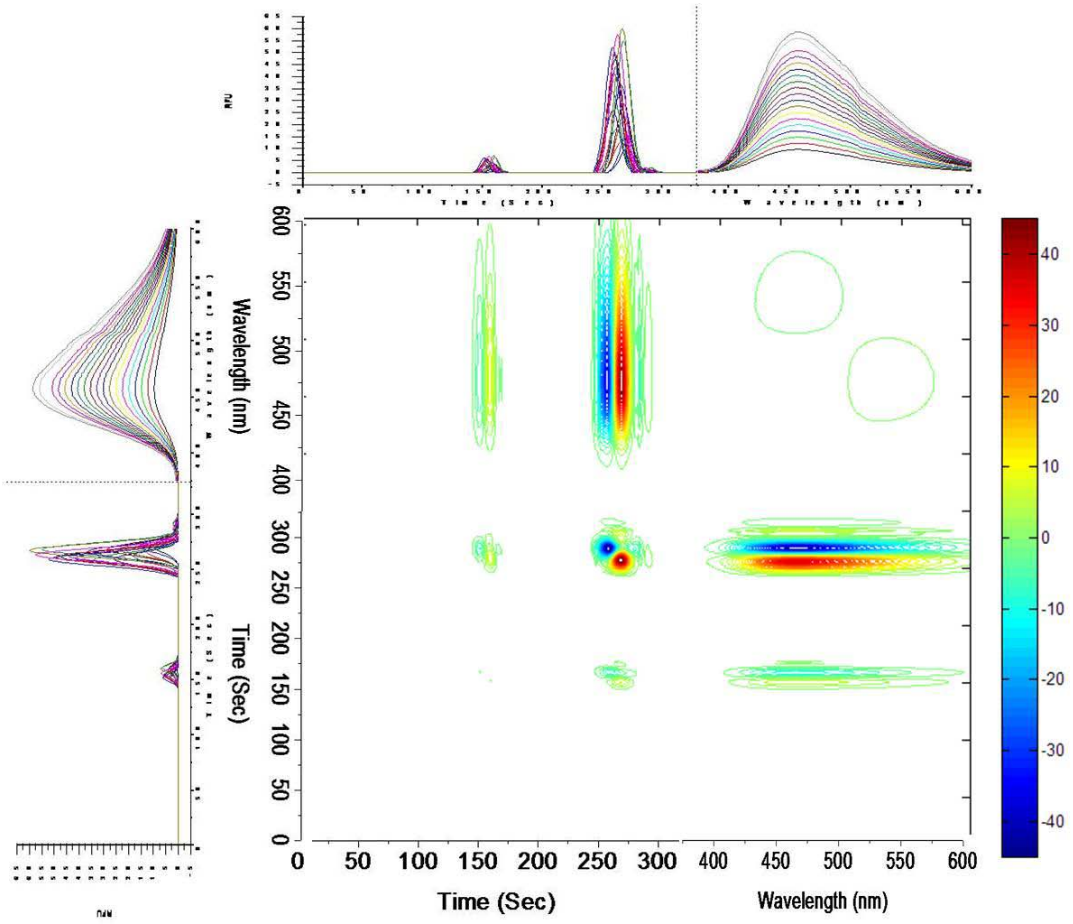

Figure 6.7 Two-dimensional asynchronous correlation spectrum of the simulated electropherograms and fluorescence spectra of FAD/NADH mixture with 2% random EOF shifts in the electropherograms

Note: The simulated electropherograms and fluorescence spectra are plotted on the side bar of the 2D asynchronous correlation spectrum to demonstrate the cross peaks.

The peaks in the simulated electropherograms are shifted randomly within 2% of the total analysis time.

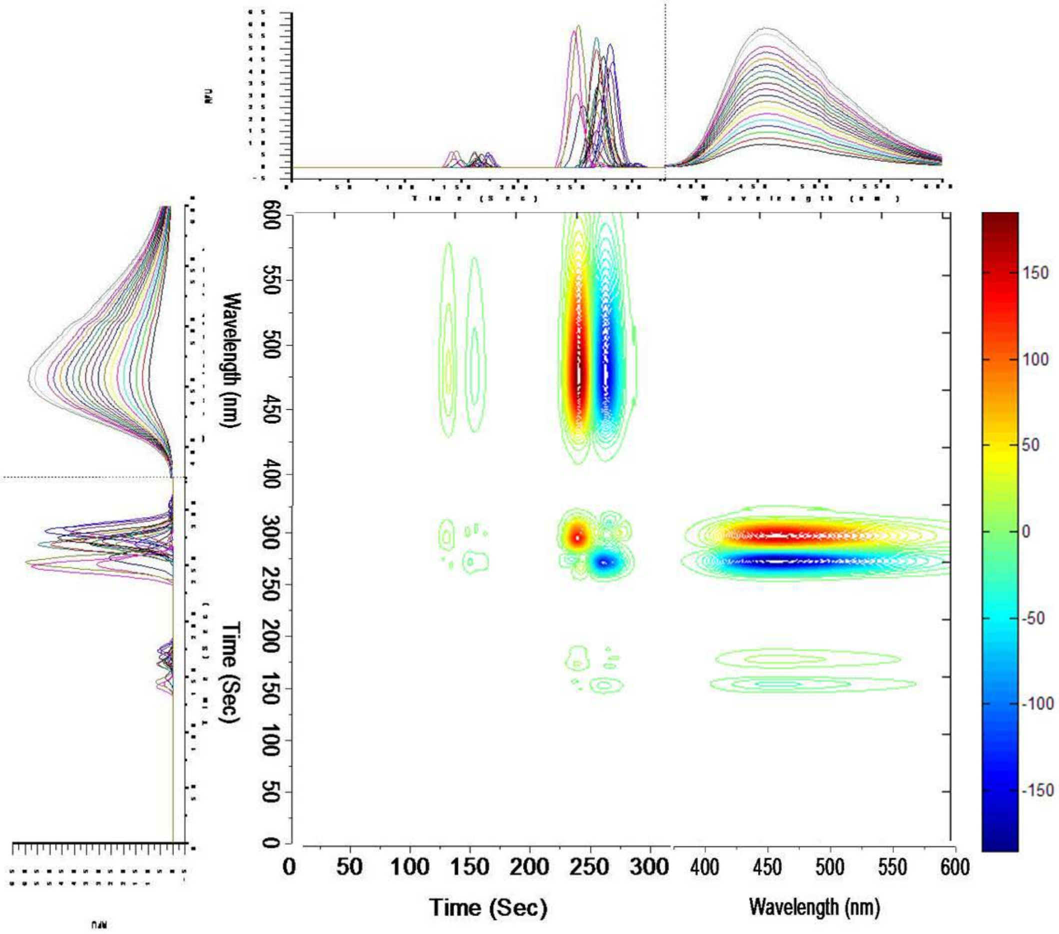

Figure 6.8 Two-dimensional asynchronous correlation spectrum of the simulated electropherograms and fluorescence spectra of FAD/NADH mixture with 5% random EOF shifts in the electropherograms

Note: The simulated electropherograms and fluorescence spectra are plotted on the side bar of the 2D asynchronous correlation spectrum to demonstrate the cross peaks.

The peaks in the simulated electropherograms are shifted randomly within 5% of the total analysis time.

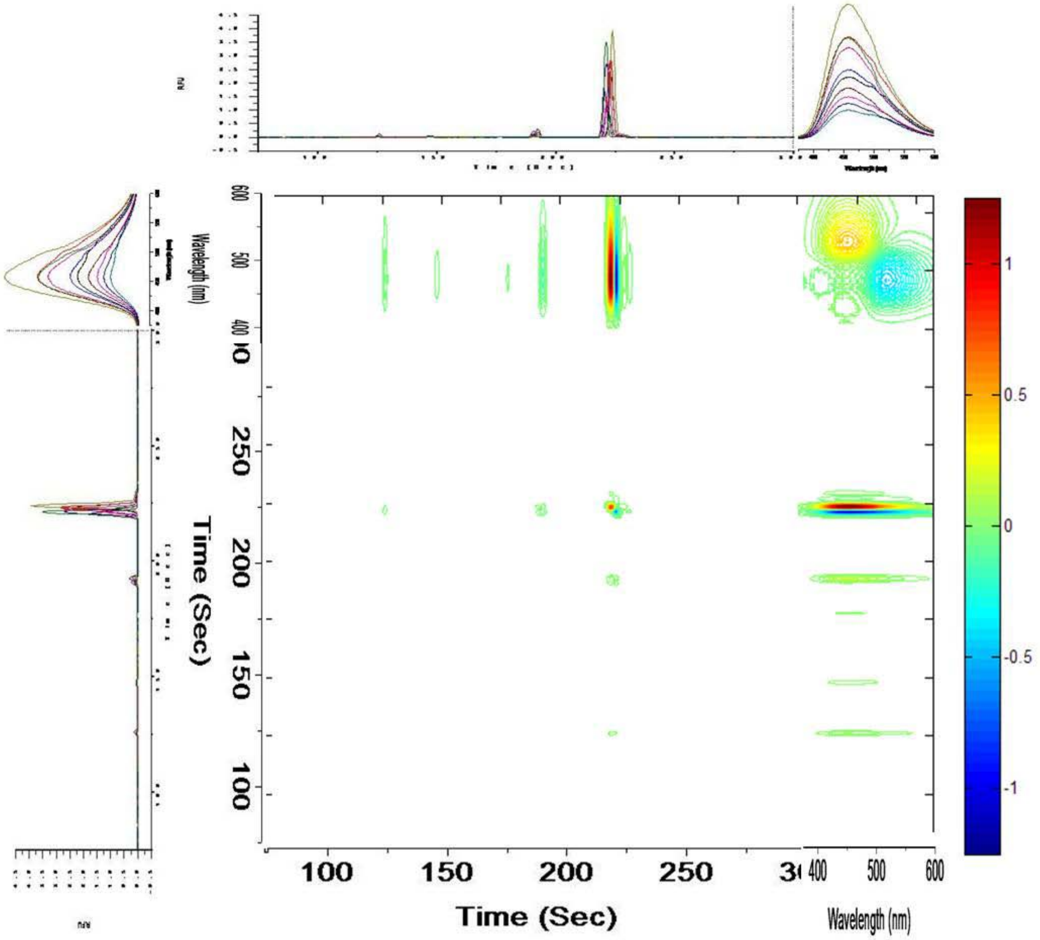

Figure 6.9 Two-dimensional asynchronous correlation spectrum of experimental electropherograms and fluorescence spectra of FAD/NADH mixtures

---

Note: The experimental electropherograms and fluorescence spectra are plotted on the side bar of the 2D asynchronous correlation spectrum to demonstrate the cross peaks.

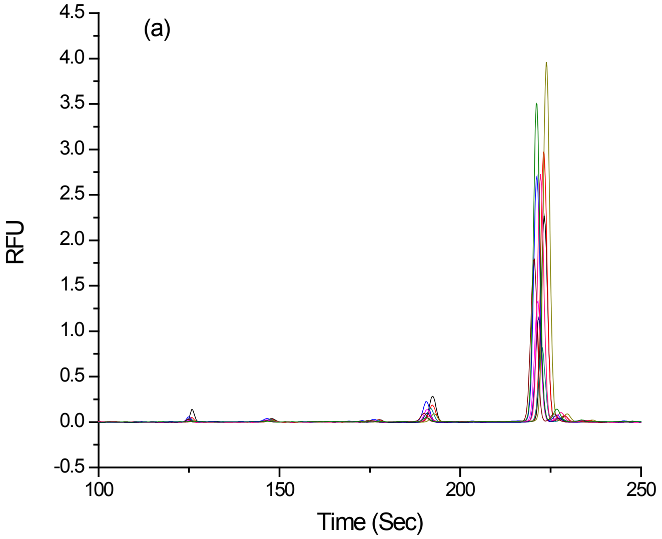

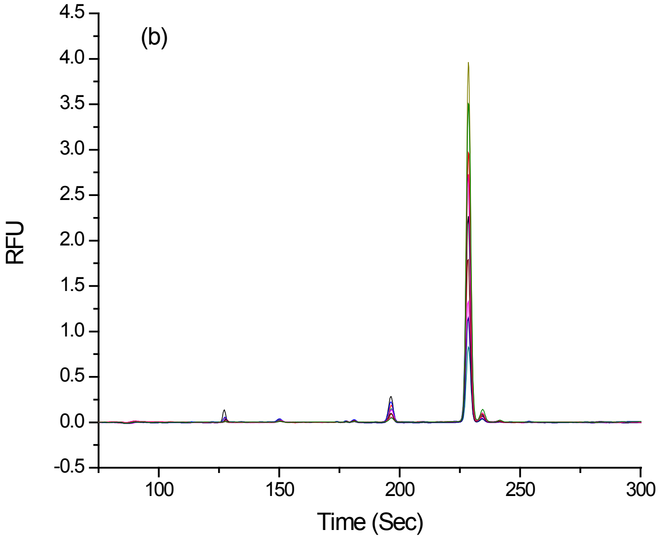

Figure 6.10 Electropherograms of FAD and NADH (a) before and (b) after alignment of peaks

---

Separation conditions: Capillary total length 30.5cm, effective length 20.5 cm; capillary i.d. 50 µm, 170 mM borate buffer at pH 9.0; High voltage 15 kV; Injection at 0.5psi for 5sec; LIF excitation at 325 nm (He-Cd Laser), emission collected though 345 nm long pass filter).

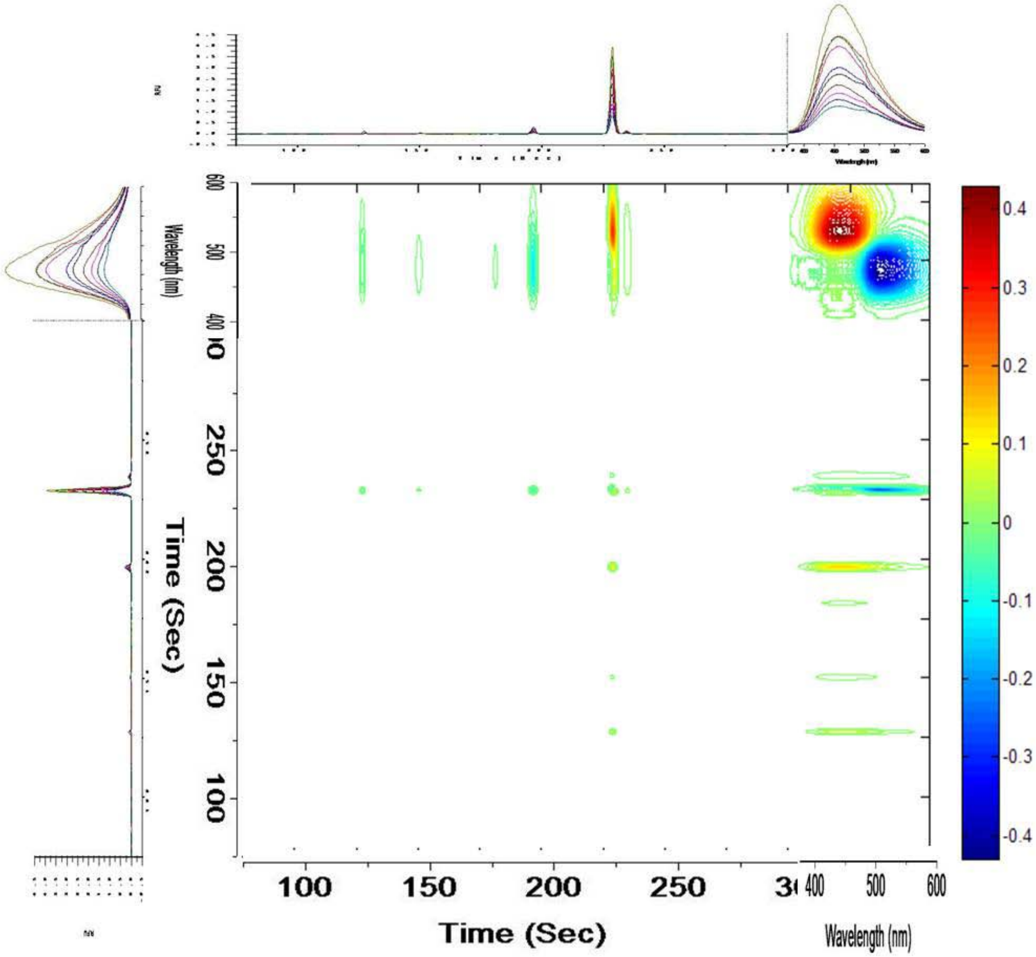

Figure 6.11 Two-dimensional asynchronous correlation spectrum of the experimental electropherograms and fluorescence spectra of FAD/NADH mixtures after alignment of electropherogram peaks

---

Note: The experimental electropherograms with aligned peaks and fluorescence spectra are plotted on the side bar of the 2D asynchronous correlation spectrum to demonstrate the cross peaks.

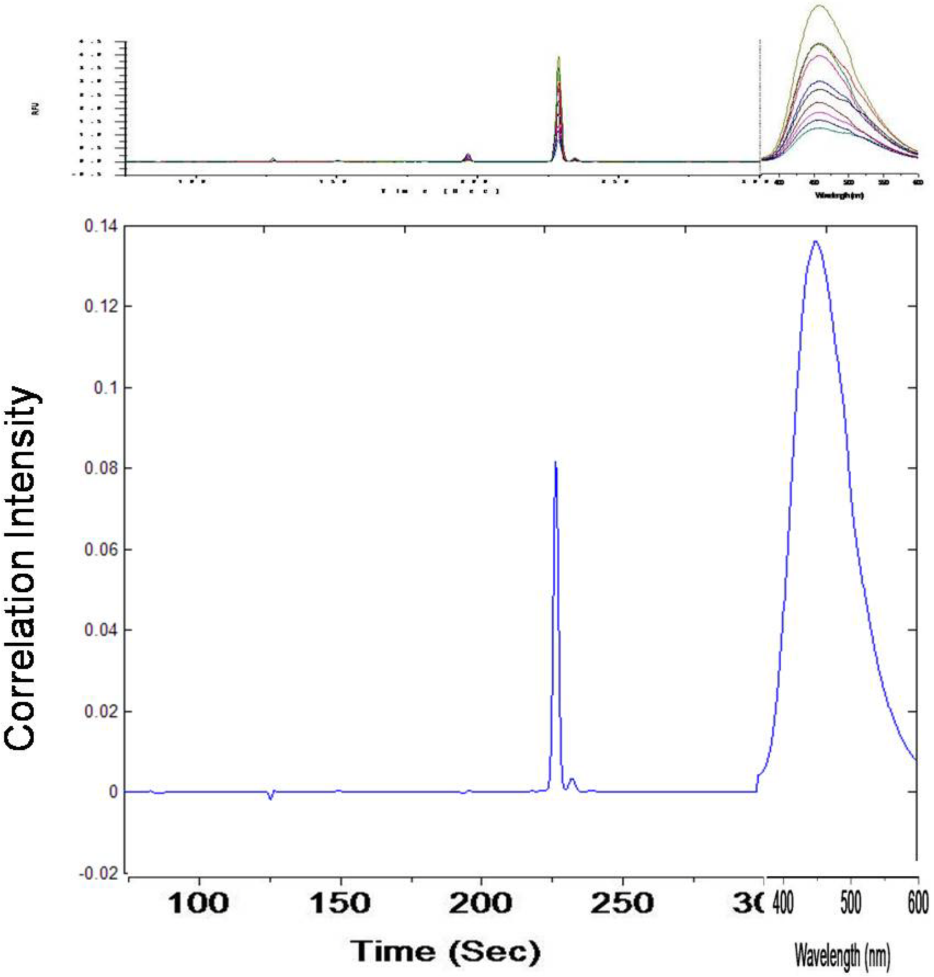

Figure 6.12 Cross section at 197 seconds of the asynchronous correlation spectrum of the experimental electropherograms with aligned peaks and fluorescence spectra

Note: The migration time of FAD is 197 seconds. The cross peaks in this cross section appear at 229 seconds of the electropherogram and 460 nm of the fluorescence spectra, which means both of the fluorescence signals come from the other component, NADH.

The experimental electropherograms with aligned peaks and fluorescence spectra are plotted on the top of the cross section plot to demonstrate the cross peaks.

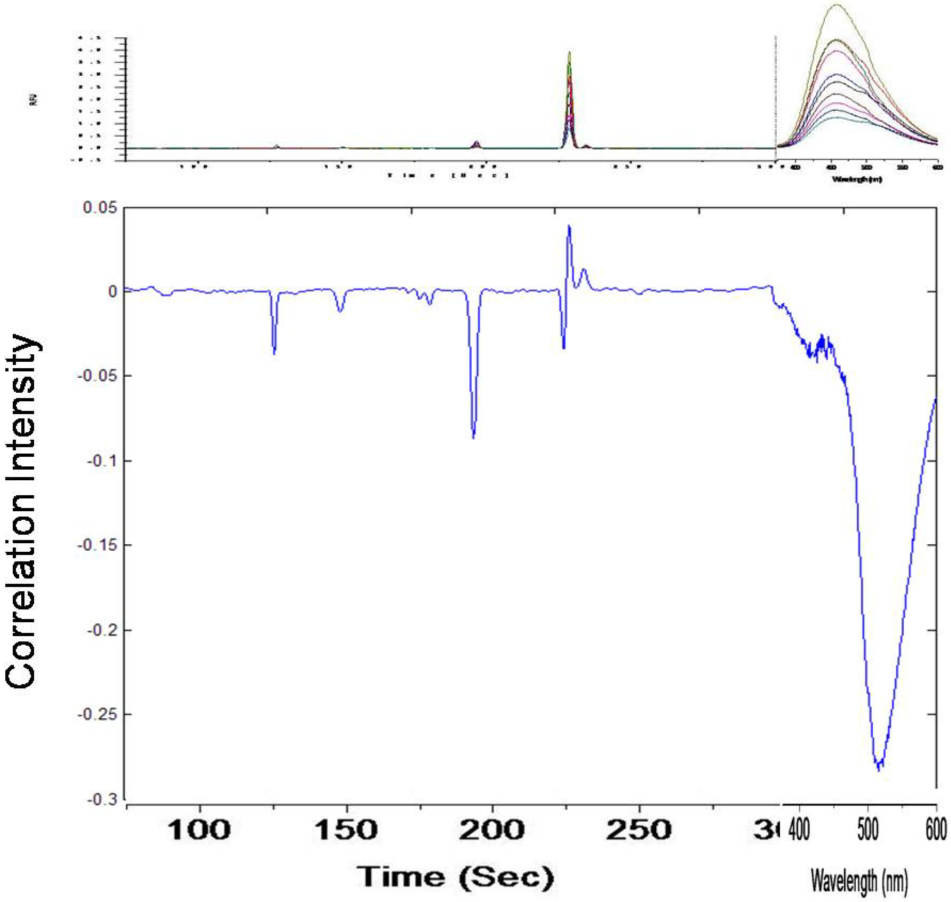

Figure 6.13 Cross section at 229 seconds of the asynchronous correlation spectrum of the experimental electropherograms with aligned peaks and fluorescence spectra

---

Note: The migration time of NADH is 229 seconds. The cross peaks in this cross section appear at several place including 197 seconds of the electropherogram and 525 nm of the fluorescence spectra, which means both of the fluorescence signals come from the other component, FAD. Other smaller cross peaks may represent impurities in FAD sample.

The experimental electropherograms and fluorescence spectra are plotted on the top of the cross section plot to demonstrate the cross peaks.

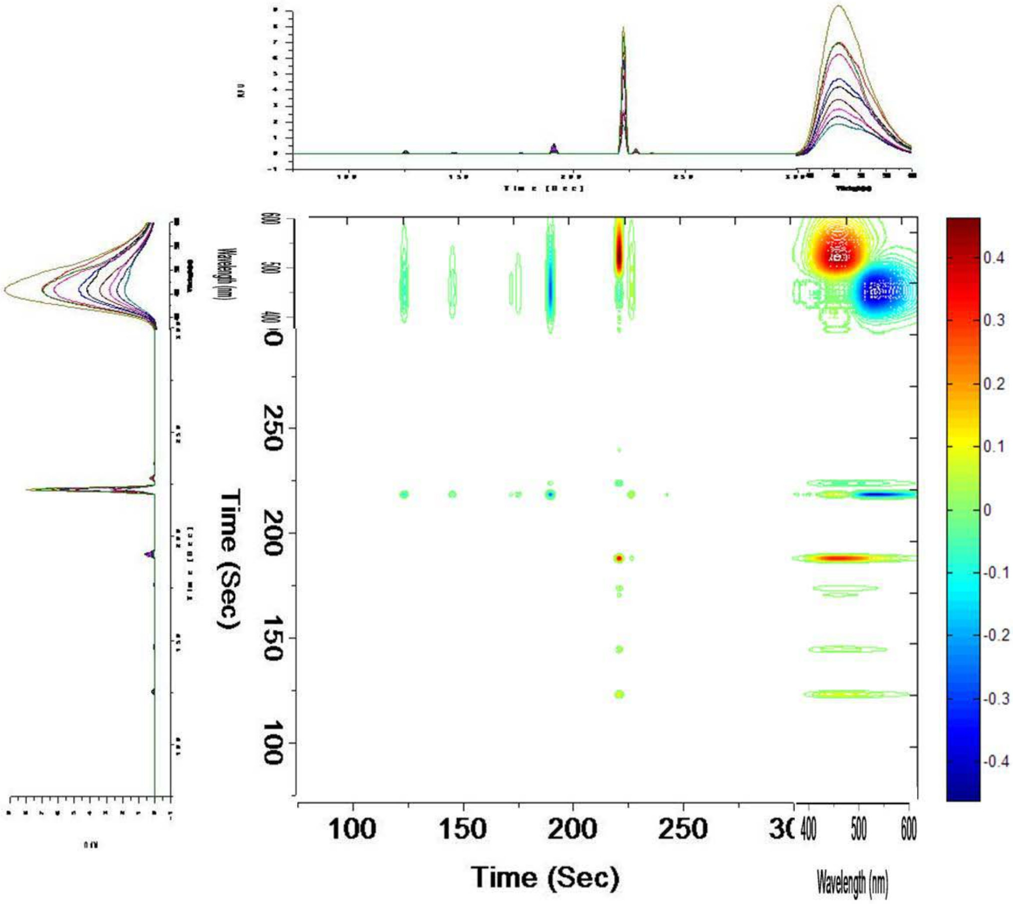

Figure 6.14 Two-dimensional asynchronous correlation spectrum of the electropherograms simulated based on the experimental electropherograms and fluorescence spectra of FAD/NADH mixtures

---

Note: The electropherograms simulated based on the experimental electropherograms and fluorescence spectra are plotted on the side bar of the 2D asynchronous correlation spectrum to demonstrate the cross peaks.

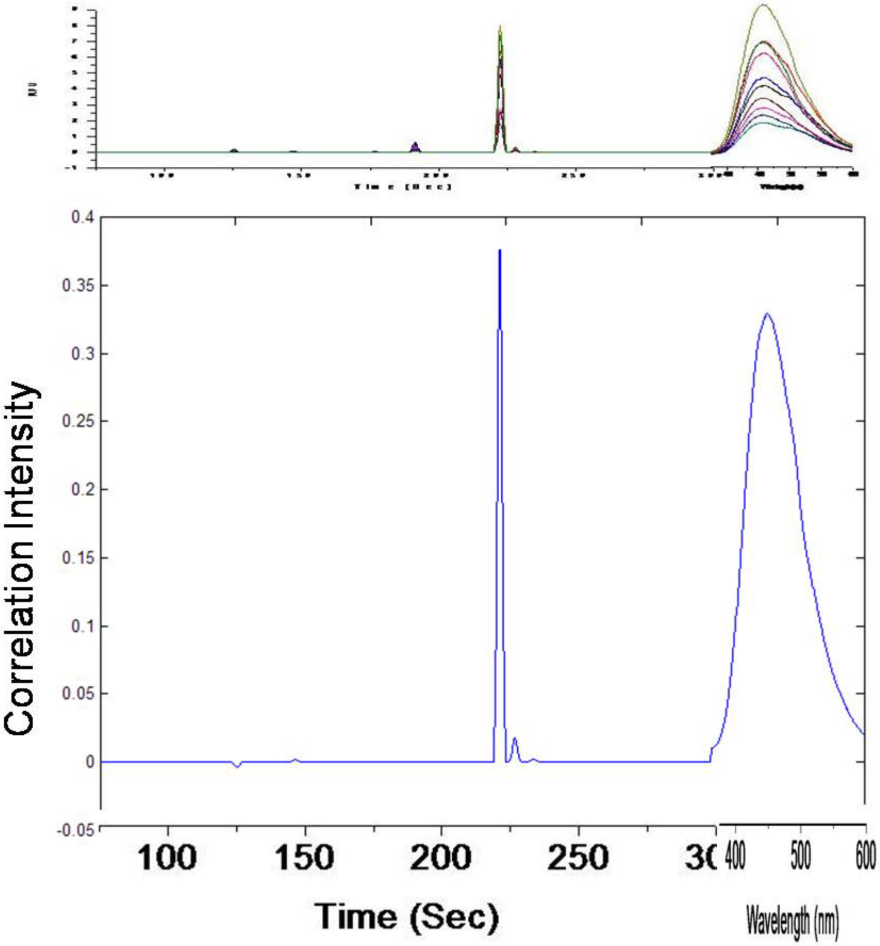

Figure 6.15 Cross section at 191.5 seconds of the asynchronous correlation spectrum of the electropherograms simulated based on the experimental electropherograms and fluorescence spectra

---

Note: The electropherograms simulated based on the experimental electropherograms and fluorescence spectra are plotted on the side bar of the cross section plot to demonstrate the cross peaks.

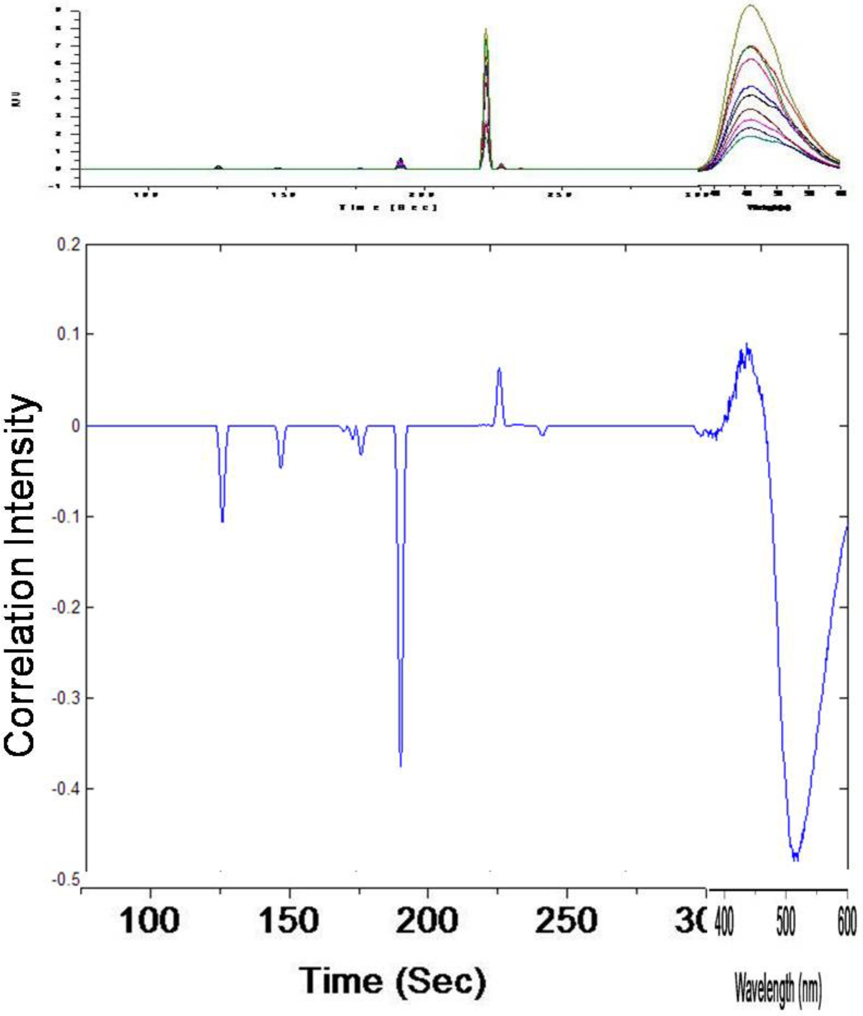

Figure 6.16 Cross section at 222 seconds of the asynchronous correlation spectrum of the electropherograms simulated based on the experimental electropherograms and fluorescence spectra

---

Note: The electropherograms simulated based on the experimental electropherograms and fluorescence spectra are plotted on the side bar of the cross section plot to demonstrate the cross peaks.

CHAPTER 7

FUTURE DIRECTIONS

With the optimized protocols for cell extraction and separation, we have identified endogenous fluorophores including FMN, FAD, NADH, and NADPH in CHO, HT-29 and FHC cell extracts and quantified them in CHO and HT-29. The two-dimensional correlation coefficient mapping of the electropherograms of cell extracts and the peak area ratios of NADH/NADPH demonstrate that there are significant differences between the endogenous fluorophore profiles in cancer cell HT-29 with higher cell density and the normal cell FHC. But the difference between HT-29 cells and FHC cells at similar cell densities are not observed in 2D correlation coefficient map or the comparison of NADH/NADPH peak ratios. This finding leaves us the following questions to address. Does the cell density influence the endogenous fluorophores profile more than the cell species? Do the observed differences between cofactors profiles reflect the real differences in cofactor profiles of cells with different cell densities? To address these questions, more understanding of the factors altering the concentration of the extracted fluorophores during extraction and separation is desired.

In the meantime, with the preparation of cell extraction and separation, we are prepared for extraction and separation of endogenous fluorophores in tissue at different physiological stages. How to process the tissues to preserve the fluorescence of the extracellular matrix, including collagen and elastin, consistently during extraction will be the major challenge.

The two-dimensional generalized correlation analysis has been demonstrated to be useful to mutually identify peaks between electropherograms from CE-LIF and fluorescence spectra with the FAD/NADH system. Later on, this technique of hetero-correlation analysis can be applied to other techniques such as correlation between electropherograms and Raman spectra, which will offer valuable identification of Raman peaks in a mixture. Also, if the variations in cell extracts can be appropriately treated, we can apply this analysis to peak identification in cell extracts' electropherograms or chromatograms.

APPENDIX

PROGRAMS FOR CALCULATIONS IN MATLAB

A.1 Program to align electropherograms with the reference to a specific peak

```
function [Aligned]=aligntopeak(A)

%This function is used to align electropherograms to a specific peak.
%The input is the matrix of electropherograms.
%The user will also be prompted to input the range they need to look
for
%the reference peak.x is the lower limit and y is the higher limit of
the
%range, respectively
%The user will also be asked to input which electropherogram is desired
to
%be used as reference. This number will be given to r.
%find the dimension of the matrix
n=size(A,1);
m=size(A,2);
I=[]; C=[];

%plot the matrix to allow users choosing the range to seek reference
peak
plot(A);

%prompt users to input the range and the number of reference
%electropherogram
input('lower limit x=? higher limit y=? r=? electropherogram as
reference');
keyboard;

%find out the maximum (the peak)and their indice in the range given
[C,I]=max(A(x:y, :));

%shift the electropherograms with respect to the reference peak in the
%reference elctropherogram
for v=1:m
    if I(v)>=I(r)
        for w=1:(n-(I(v)-I(r))-1)
            B(w, v)=A(w+(I(v)-I(r)), v);
        end
    else
        for w=(1+(I(r)-I(v))+1):n
            B(w, v)=A(w-(I(r)-I(v)), v);
        end
    end
end
```

```
Aligned=B;
```

A.2 Function to align peaks in electropherograms by shifting and interpolating/extrapolating with the reference of two specific peaks

```
function [alignpolated]=alignpolate(A)

%This function is used to align and interpolate/extrapolate peaks in
%electropherograms so that the peaks from the same species will be at
the same position and ready to further analysis.

%The input is the matrix of electropherograms with only y values of the
%electropherograms.
%User will be asked to select two ranges to find the two peaks used to
%define the alignment.
%Which electropherogram to be used as standard will also be asked.

%find the dimension of the matrix
n = size(A,1);
m = size(A,2);

%define intermediate variables needed
C1=[];
I1=[];
C2=[];
I2=[];

%plot the matrix to allow users choosing the range to seek peaks
plot(A);

%prompt users to input the range and the number of reference
%electropherogram
input('Peak1 lower limit a1=? higher limit b1=? ; Peak 2 lower limit
a2=? b2=?; r=? electropherogram as reference (r <= m)');
keyboard;

%find out the maximum (the peak)and their indices in the range given
[C1,I1]=max(A(a1:b1, :));
[C2,I2]=max(A(a2:b2, :));

for i=1:m
    I1(i) = a1+I1(i)-1;
    I2(i) = a2+I2(i)-1;
end

%find the conversion factor for each electropherogram
F = [];
```

```
F = (I2(r)-I1(r))./(I2-I1);

%Generate the original x-axis, based on the frequency of data is 4
%points/sec.
Xr = (0:0.25:((n-1)/4));

%Get new x-axes
X=[];
for i = 1:m
     w = I1(r);
        s = I1(i);
        W(i) = Xr(w)-(Xr(s).*F(i));
     for j=1:n
    X(j,i) = Xr(j).*F(i)+ W(i);
    end
end

%interpolate the values
Y = [];
for j = 1:m
      Y(:,j) = interp1(X(:,j),A(:,j),Xr);
end

alignpolated = Y;
```

A.3 Function to simulate electropherograms and spectra based on FAD and NADH spectra

```
function [simulated]=simulation(FAD,NADH)

%This function is used to simulate electropherogram and spectram of FAD
and NADH mixture.%
%With the input of FAD and NADH spectra from 375nm-600nm. The result
will be a matrix with simulated electropherogram and spectra.%

%create three Gaussian peaks with different width to represent NADH,
FAD, %and NADH impurity peak in electropherogram.%
N=gausswin(31);
F=gausswin(18);
NI=gausswin(16);
%Decrease the intensity of impurity peak to 1/30 of NADH.
NI=NI/30;

%Ask for input of how many curves to simulate, what is the lowest and
the highest percentage for FAD and NADH, respectively.
input('How many curve to simulate x=? FAD percentage a1=? b1=? NADH
percentage a2=? b2=?');
keyboard;

%calculate FAD and NADH ratios.
```

```
Fr=(a1:(b1-a1)/(x-1):b1);
Nr=(a2:(b2-a2)/(x-1):b2);
NIr=Nr;

%simulate the elecropherogram, the migration time is determined based
on real separation of the two compounds.
E=zeros(330,x);
for n=1:x
    E(1:149,n)=0.001;
    E(150:167,n)=F.*Fr(n);
    E(168:250,n)=0.001;
    E(251:281,n)=N.*Nr(n);
    E(282:297,n)=NI*NIr(n);
    E(297:330,n)=0.001;
end

%normalize FAD spectra
FS=FAD;
a=max(FS);
FS=FS./a;

%normalize NADH spectra
NS=NADH;
b=max(NS);
NS=NS./b;

%simulate mixture spectra
MixS=zeros(226,x);
for n=1:x
    for m=1:226
    MixS(m,n)=FS(m).*Fr(n)+NS(m)*Nr(n);
    end
end

%put the electropherogram and spectra together
simulated=zeros(556,x);
simulated(1:330,:)=E;
simulated(331:556,:)=MixS;
```

A.4 Program to calculate and plot synchronous and asynchronous correlation intensity for electropherograms and spectra with evenly spaced concentration changes as perturbation

```
%THIS PROGRAM IS MODIFIED BASED ON A PROGRAM WRITTEN BY GUFENG WANG IN
%2005.
```

```
% This program calculates the generalized 2D correlation with original data.
% Each time you need to clear the Matlab memory, load the original spectra matrix in columns,
% and assign your data to the matrix temp1, reset m and n values.
% m: column numbers, number of measurements/samples
% n: row numbers, number of wavelengths plus number of time points
%
% It out puts
% syn_vv:  generalized variable-variable 2D synchronous correlation spetrum
% asyn_vv: generalized variable-variable 2D asynchronous correlation spetrum

%%%%%%%%%%%%%%%%%%%%%%%%%%%%%%%%%%%%%%%%%%%%%%%%%%%%%%%%%%%%%%%%%%%%%%%
% Parameters in this paragraph should be edited as needed.
clear;
load Simu_F1_7_N10_60.txt;

temp1=Simu_F1_7_N10_60';
m=20;
n=556;
%%%%%%%%%%%%%%%%%%%%%%%%%%%%%%%%%%%%%%%%%%%%%%%%%%%%%%%%%%%%%%%%%%%%%%



%%%%%%%%%%%%%%%%%%%%%%%%%%%%%%%%%%%%%%%%%%%%%%%%%%%%%%%%%%%%%%%%%%%%%%
% Generalized 2D correlation
%%%%%%%%%%%%%%%%%%%%%%%%%%%%%%%%%%%%%%%%%%%%%%%%%%%%%%%%%%%%%%%%%%%%%%
% Calculates the Noda matrix
nmatrix(n,n)=0;
for p=1:n;
for q=1:n;
if p==q;
nmatrix(p,q)=0;
else
nmatrix(p,q)=1/3.1415926536/(q-p);
end
end;
end;

% Calculates the variable-variable correlation
syn_vv(n,n)=0;
asyn_vv(n,n)=0;
syn_vv=temp1'*temp1/(m-1);
asyn_vv=(temp1'*(nmatrix(1:m,1:m)*temp1))/(m-1);



% Plot the 2D spectra
% Variable-variable synchronous
figure;mesh(syn_vv);
figure;contour(syn_vv, 50);
% Variable-variable asynchronous
figure;mesh(asyn_vv);
figure;contour(asyn_vv, 50);
```

A.5 Function to shift simulated electropherogram randomly within certain range to mimic EOF shifting

```
function [withEOF]=shift(elegram_spec)

%This function is used to shift the elegram_spec to mimic the EOF
change in
%electropherogram.

%Ask which part of the input matrix is electropherogram, how much the
%EOF shifts?
input ('Electropherograms start with a=? end with b=? shifts +-x%=?');
keyboard;

%Take the electropherogram part out.
E=elegram_spec(a:b,:);
[m,n]=size(E);

%suppose the EOF shifts +-x%, the points shift range will be total
%points*+-x/100. round the range to get the integer to generate random
%number for EOF shifts.
c=(b-a+1)*(-x/100);
c=round(c);
d=(b-a+1)*(x/100);
d=round(d);

%generate set of n random integer between c and d.
EOFsh=randint(1,n,[c,d]);

%shift the elegram with different EOF shifts
F=zeros(m,n);
for v=1:n
    sh=EOFsh(1,v);
    for w=1:m
        if w-sh<=0
            F(w,v)=0;
        else
            if w-sh<=m
            F(w,v)=E(w-sh,v);
            end
        end
    end
end

elegram_spec(a:b,:)=F;
withEOF=elegram_spec;
```

A.6 Function to simulate electropherograms based on peak areas and migration times in experimental electropherograms

```
function
[simulatedele]=elegramsimu(t,peakbasewidths,migrationtimes,peakareas)

%This function is used to simulate electropherograms based on the peak
area and migration time of real electropherograms.
%The input requested are t,the total length of the electropherograms in
seconds,the average peak base width in seconds for each peak, matrix of
migration times for n peaks (the average of a peak in m
electropherograms), matrix of peak areas for m electropherograms and n
peaks.

%Create the time vector of the electropherograms based on the total
time t and frequency 4 points/seconds.
T=0:0.25:t;

%calculate the average sigma for peaks.
sigma=mean(peakbasewidths)/6;

%Simulate the Gaussian peaks separately
[a b]=size(peakareas);
[c d]=size(T);
G=zeros(d,b);
for m=1:b
    G(:,m)=gaussmf(T, [sigma migrationtimes(m,1)]);
end
plot(T,G);

%Scale peaks according to peak areas matrix and add all peaks to
%electropherograms.
E=zeros(d,b);
for i=1:b
    for j=1:a
    E(:,i)=E(:,i)+G(:,j).*peakareas(j,i);
    end
end
plot(T,E);

simulatedele=E;
```

REFERENCES

1. American Cancer Society *Cancer facts & figures 2009*; American Cancer Society: Atlanta, GA, **2009**.

2. Schulz, W. A., *Molecular biology of human cancers : An advanced student's textbook*. Springer: Dordrecht; Norwell, MA, **2005**.

3. American Cancer Society *Colorectal cancer facts & figures 2008-2010*; American Cancer Society: Atlanta, GA, **2008**.

4. American Cancer Society *Cancer prevention & early detection facts & figures 2009*; American Cancer Society: Atlanta, GA, **2009**.

5. Alfano, R. R. In *Advances in optical biopsy and optical mammography*, New York, New York Academy of Sciences: New York, **1998**.

6. Richards-Kortum, R.; Sevick-Muraca, E., Quantitative optical spectroscopy for tissue diagnosis. *Annual Review of Physical Chemistry* **1996,** *47* (1), 555-606.

7. Sokolov, K.; Follen, M.; Richards-Kortum, R., Optical spectroscopy for detection of neoplasia. *Current Opinion in Chemical Biology* **2002,** *6* (5), 651-658.

8. Zonios, G.; Cothren, R.; Crawford, J. M.; Fitzmaurice, M.; Manoharan, R.; Van Dam, J.; Feld, M. S., Spectral pathology. *Advances in Optical Biopsy and Optical Mammography* **1998,** *838*, 108-115.

9. Crowell, E.; Wang, G. F.; Cox, J.; Platz, C. P.; Geng, L., Correlation coefficient mapping in fluorescence spectroscopy: Tissue classification for cancer detection. *Analytical Chemistry* **2005,** *77* (5), 1368-1375.

10. Schomacker, K. T.; Frisoli, J. K.; Compton, C. C.; Flotte, T. J.; Richter, J. M.; Deutsch, T. F.; Nishioka, N. S., Ultraviolet-laser induced fluorescence of colonic polyps. *Gastroenterology* **1992,** *102* (4), 1155-1160.

11. Schomacker, K. T.; Frisoli, J. K.; Compton, C. C.; Flotte, T. J.; Richter, J. M.; Nishioka, N. S.; Deutsch, T. F., Ultraviolet laser-induced fluorescence of colonic tissue - basic biology and diagnostic potential. *Lasers in Surgery and Medicine* **1992,** *12* (1), 63-78.

12. Skvortsova, Y.; Wang, G. F.; Geng, M. L., Statistical two-dimensional correlation coefficient mapping of simulated tissue phantom data: Boundary determination in tissue classification for cancer diagnosis. *Journal of Molecular Structure* **2006,** *799* (1-3), 239-246.

13. Skvortsova, Y. A. Simulation of tissues for biomedical applications. The University of Iowa, Iowa City, **2009**.

14. Wang, G. F.; Platz, C. P.; Geng, M. L., Probability-based differential normalized fluorescence bivariate analysis for the classification of tissue autofluorescence spectra. *Applied Spectroscopy* **2006,** *60* (5), 545-550.

15. Wang, T. D.; Crawford, J. M.; Feld, M. S.; Wang, Y.; Itzkan, I.; Van Dam, J., In vivo identification of colonic dysplasia using fluorescence endoscopic imaging. *Gastrointest Endosc* **1999,** *49* (4 Pt 1), 447-55.

16. Meric-Bernstam Funda, P. R. E., Chapter 9. Oncology. In *Schwartz's principles of surgery*, 8e ed.; Brunicardi FC, A. D., Billiar TR, Dunn DL, Hunter JG, Matthews JB, Pollock RE, Schwartz SI, Ed. The McGraw-Hill Companies, Inc.: **2005**.

17. Talbot, I.; Price, A.; Salto-Tellez, M., *Biopsy pathology in colorectal disease*. 2nd ed.; Hodder Arnold: London, Great Britain, **2006**.

18. Martin Lipkin, Phase 1 and phase 2 proliferative lesions of colonic epithelial cells in diseases leading to colonic cancer. *Cancer* **1974,** *34* (S3), 878-888.

19. Warburg, O.; Wind, F.; Negelein, E., The metabolism of tumors in the body. *The Journal of General Physiology* **1927,** *8* (6), 519-530.

20. Warburg, O., On the origin of cancer cells. *Science* **1956,** *123* (3191), 309-14.

21. Zu, X. L.; Guppy, M., Cancer metabolism: Facts, fantasy, and fiction. *Biochemical and Biophysical Research Communications* **2004,** *313* (3), 459-465.

22. Moreno-Sánchez, R.; Rodríguez-Enríquez, S.; Marín-Hernández, A.; Saavedra, E., Energy metabolism in tumor cells. *FEBS Journal* **2007,** *274* (6), 1393-1418.

23. Bishop, J. M., Molecular themes in oncogenesis. *Cell* **1991,** *64* (2), 235-248.

24. Varmus, H., The new era in cancer research. *Science* **2006,** *312* (5777), 1162-1165.

25. Gatenby, R. A.; Gillies, R. J., Why do cancers have high aerobic glycolysis? *Nature Reviews Cancer* **2004,** *4* (11), 891-899.

26. Moreno-Sanchez, R.; Rodriguez-Enriquez, S.; Saavedra, E.; Marin-Hernandez, A.; Gallardo-Perez, J. C., The bioenergetics of cancer: Is glycolysis the main ATP supplier in all tumor cells? *Biofactors* **2009,** *35* (2), 209-25.

27. Gillies, R. J.; Robey, I.; Gatenby, R. A., Causes and consequences of increased glucose metabolism of cancers. *Journal of Nuclear Medicine* **2008,** *49* (Suppl_2), 24S-42S.

28. Boros, L. G.; Lee, P. W. N.; Brandes, J. L.; Cascante, M.; Muscarella, P.; Schirmer, W. J.; Melvin, W. S.; Ellison, E. C., Nonoxidative pentose phosphate pathways and their direct role in ribose synthesis in tumors: Is cancer a disease of cellular glucose metabolism? *Medical Hypotheses* **1998,** *50* (1), 55-59.

29. Cox, D. L. N. M. M., *Lehninger principles of biochemistry*. 4th ed.; W H Freeman & Co: **2004**.

30. Hanahan, D.; Weinberg, R. A., The hallmarks of cancer. *Cell* **2000,** *100* (1), 57-70.

31. Garber, K., Energy deregulation: Licensing tumors to grow. *Science* **2006,** *312* (5777), 1158-1159.

32. Kritikou, E., Metabolism: Warburg effect revisited. *Nature Reviews Cancer* **2008,** *8* (4), 247-247.

33. Ramanathan, A.; Wang, C.; Schreiber, S. L., Perturbational profiling of a cell-line model of tumorigenesis by using metabolic measurements. *Proceedings of the National Academy of Sciences of the United States of America* **2005,** *102* (17), 5992-5997.

34. Frangioni, J. V., New technologies for human cancer imaging. *J Clin Oncol* **2008,** *26* (24), 4012-21.

35. Koenig, F.; Knittel, J.; Stepp, H., Diagnosing cancer in vivo. *Science* **2001,** *292* (5520), 1401-1403.

36. Weissleder, R., Molecular imaging in cancer. *Science* **2006,** *312* (5777), 1168-1171.

37. Luker, G. D.; Luker, K. E., Optical imaging: Current applications and future directions. *J Nucl Med* **2008,** *49* (1), 1-4.

38. Fass, L., Imaging and cancer: A review. *Molecular Oncology* **2008,** *2* (2), 115-152.

39. Weissleder, R.; Pittet, M. J., Imaging in the era of molecular oncology. *Nature* **2008,** *452* (7187), 580-9.

40. Ballou, B.; Ernst, L. A.; Waggoner, A. S., Fluorescence imaging of tumors in vivo. *Curr Med Chem* **2005,** *12* (7), 795-805.

41. Brown, J. Q.; Vishwanath, K.; Palmer, G. M.; Ramanujam, N., Advances in quantitative uv-visible spectroscopy for clinical and pre-clinical application in cancer. *Curr Opin Biotechnol* **2009,** *20* (1), 119-31.

42. Gill, E. M.; Palmer, G. M.; Ramanujam, N.; Gerard Marriott and Ian, P., [21] steady-state fluorescence imaging of neoplasia. In *Methods in enzymology*, Academic Press: **2003**; Vol. Volume 361, pp 452-481.

43. Haringsma, J.; Tytgat, G. N., Fluorescence and autofluorescence. *Baillieres Best Pract Res Clin Gastroenterol* **1999,** *13* (1), 1-10.

44. Prosst, R. L.; Gahlen, J., Fluorescence diagnosis of colorectal neoplasms: A review of clinical applications. *Int J Colorectal Dis* **2002,** *17* (1), 1-10.

45. Ramanujam, N., Fluorescence spectroscopy of neoplastic and non-neoplastic tissues. *Neoplasia* **2000,** *2* (1-2), 89-117.

46. Romer, T. J.; Fitzmaurice, M.; Cothren, R. M.; Richards-Kortum, R.; Petras, R.; Sivak, M. V., Jr.; Kramer, J. R., Jr., Laser-induced fluorescence microscopy of normal colon and dysplasia in colonic adenomas: Implications for spectroscopic diagnosis. *Am J Gastroenterol* **1995,** *90* (1), 81-7.

47. Sud, D.; Zhong, W.; Beer, D. G.; Mycek, M. A., Time-resolved optical imaging provides a molecular snapshot of altered metabolic function in living human cancer cell models. *Opt Express* **2006,** *14* (10), 4412-26.

48. Wagnieres, G. A.; Star, W. M.; Wilson, B. C., In vivo fluorescence spectroscopy and imaging for oncological applications. *Photochem Photobiol* **1998,** *68* (5), 603-32.

49. Zonios, G. I.; Cothren, R. M.; Arendt, J. T.; Wu, J.; Van Dam, J.; Crawford, J. M.; Manoharan, R.; Feld, M. S., Morphological model of human colon tissue fluorescence. *IEEE Trans Biomed Eng* **1996,** *43* (2), 113-22.

50. Cothren, R. M.; Richards-Kortum, R.; Sivak, M. V., Jr.; Fitzmaurice, M.; Rava, R. P.; Boyce, G. A.; Doxtader, M.; Blackman, R.; Ivanc, T. B.; Hayes, G. B.; et al., Gastrointestinal tissue diagnosis by laser-induced fluorescence spectroscopy at endoscopy. *Gastrointest Endosc* **1990,** *36* (2), 105-11.

51. Cothren, R. M.; Sivak, M. V., Jr.; Van Dam, J.; Petras, R. E.; Fitzmaurice, M.; Crawford, J. M.; Wu, J.; Brennan, J. F.; Rava, R. P.; Manoharan, R.; Feld, M. S., Detection of dysplasia at colonoscopy using laser-induced fluorescence: A blinded study. *Gastrointest Endosc* **1996,** *44* (2), 168-76.

52. Eker, C.; Montan, S.; Jaramillo, E.; Koizumi, K.; Rubio, C.; Andersson-Engels, S.; Svanberg, K.; Svanberg, S.; Slezak, P., Clinical spectral characterisation of colonic mucosal lesions using autofluorescence and delta aminolevulinic acid sensitisation. *Gut* **1999,** *44* (4), 511-8.

53. Mycek, M. A.; Schomacker, K. T.; Nishioka, N. S., Colonic polyp differentiation using time-resolved autofluorescence spectroscopy. *Gastrointest Endosc* **1998,** *48* (4), 390-4.

54. Testoni, P. A., Optical coherence tomography. *ScientificWorldJournal* **2007,** *7*, 87-108.

55. Testoni, P. A.; Mangiavillano, B., Optical coherence tomography in detection of dysplasia and cancer of the gastrointestinal tract and bilio-pancreatic ductal system. *World J Gastroenterol* **2008,** *14* (42), 6444-52.

56. Nishioka, N. S., Optical biopsy using tissue spectroscopy and optical coherence tomography. *Can J Gastroenterol* **2003,** *17* (6), 376-80.

57. Tromberg, B. J.; Shah, N.; Lanning, R.; Cerussi, A.; Espinoza, J.; Pham, T.; Svaasand, L.; Butler, J., Non-invasive in vivo characterization of breast tumors using photon migration spectroscopy. *Neoplasia* **2000,** *2* (1-2), 26-40.

58. Mourant, J. R.; Bigio, I. J.; Boyer, J.; Conn, R. L.; Johnson, T.; Shimada, T., Spectroscopic diagnosis of bladder cancer with elastic light scattering. *Lasers in Surgery and Medicine* **1995,** *17* (4), 350-357.

59. Perelman, L. T., Optical diagnostic technology based on light scattering spectroscopy for early cancer detection. *Expert Rev Med Devices* **2006,** *3* (6), 787-803.

60. Chang, S. K.; Mirabal, Y. N.; Atkinson, E. N.; Cox, D.; Malpica, A.; Follen, M.; Richards-Kortum, R., Combined reflectance and fluorescence spectroscopy for in vivo detection of cervical pre-cancer. *Journal of Biomedical Optics* **2005,** *10* (2), -.

61. Nijssen, A.; Koljenovic, S.; Bakker Schut, T. C.; Caspers, P. J.; Puppels, G. J., Towards oncological application of raman spectroscopy. *J Biophotonics* **2009,** *2* (1-2), 29-36.

62. Boustany, N. N.; Manoharan, R.; Dasari, R. R.; Feld, M. S., Ultraviolet resonance raman spectroscopy of bulk and microscopic human colon tissue. *Applied Spectroscopy* **2000,** *54* (1), 24-30.

63. Anandasabapathy, S., Endoscopic imaging: Emerging optical techniques for the detection of colorectal neoplasia. *Curr Opin Gastroenterol* **2008,** *24* (1), 64-9.

64. Kiesslich, R.; Goetz, M.; Neurath, M. F., Confocal laser endomicroscopy for gastrointestinal diseases. *Gastrointest Endosc Clin N Am* **2008,** *18* (3), 451-66, viii.

65. Kiesslich, R.; Goetz, M.; Vieth, M.; Galle, P. R.; Neurath, M. F., Confocal laser endomicroscopy. *Gastrointest Endosc Clin N Am* **2005,** *15* (4), 715-31.

66. Benninger, R. K.; Hao, M.; Piston, D. W., Multi-photon excitation imaging of dynamic processes in living cells and tissues. *Rev Physiol Biochem Pharmacol* **2008,** *160*, 71-92.

67. Sokolov, K.; Follen, M.; Richards-Kortum, R., Optical spectroscopy for detection of neoplasia. *Curr Opin Chem Biol* **2002,** *6* (5), 651-8.

68. Masters, B. R.; Chance, B., Redox confocal imaging intrinsic fluorescent probes of cellular metabolism. In *Fluorescent and luminescent probes for biological activity : A practical guide to technology for quantitative real-time analysis*, 2nd ed.; Mason, W. T., Ed. Academic Press Limited: London. San Diego, **1999**.

69. Puppels, G. J.; Coremans, J. M. C. C.; Bruining, H. A., In vivo semiquantitative NADH-fluorescence imaging. In *Fluorescent and luminescent probes for biological activity : A practical guide to technology for quantitative real-time analysis*, 2nd ed.; Mason, W. T., Ed. Academic Press Limited: London. San Diego, **1999**.

70. Esmans, E. L.; Broes, D.; Hoes, I.; Lemiere, F.; Vanhoutte, K., Liquid chromatography mass spectrometry in nucleoside, nucleotide and modified nucleotide characterization. *Journal of Chromatography A* **1998,** *794* (1-2), 109-127.

71. Klawitter, J.; Schmitz, V.; Klawitter, J.; Leibfritz, D.; Christians, U., Development and validation of an assay for the quantification of 11 nucleotides using LC/LC-electro spray ionization-MS. *Analytical Biochemistry* **2007,** *365* (2), 230-239.

72. Emmerie, A., Separation of flavin and phosphorylated flavin. *Nature* **1938,** *141*, 416-416.

73. Peel, J. L., A method for the separation of riboflavin, flavin mononucleotide and flavin-adenine dinucleotide by ionophoresis on paper and its application to the determination of these compounds in micro-organisms. *Biochemical Journal* **1954,** *58* (3), R30-R30.

74. Peel, J. L., Separation of flavins by paper electrophoresis and its application to the examination of the flavin contents of micro-organisms. *Biochemical Journal* **1958,** *69*, 403-416.

75. Maso–wski, K., Chromatographic determination of riboflavin and flavin nucleotides in yeast. *Journal of Chromatography A* **1965,** *18*, 609-611.

76. Light, D. R.; Walsh, C.; Marletta, M. A., Analytical and preparative high-performance liquid-chromatography separation of flavin and flavin analog coenzymes. *Analytical Biochemistry* **1980,** *109* (1), 87-93.

77. Kozik, A.; Zak, Z., Flavin separation by affinity-chromatography on immobilized egg-white riboflavin-binding protein. *Analytical Biochemistry* **1982,** *121* (2), 224-226.

78. Hausinger, R. P.; Honek, J. F.; Walsh, C., Separation of flavins and flavin analogs by high-performance liquid-chromatography. *Methods in Enzymology* **1986,** *122*, 199-209.

79. Gong, B. Y.; Ho, J. W., Simultaneous separation and detection of ten common fat-soluble vitamins in milk. *Journal of Liquid Chromatography & Related Technologies* **1997,** *20* (15), 2389-2397.

80. Shamsi, S. A.; Danielson, N. D.; Warner, I. M., Flavin mononucleotide for indirect laser-induced fluorescence detection of anions separated by capillary electrophoresis. *Journal of Chromatography A* **1999,** *835* (1-2), 159-168.

81. Perez-Ruiz, T.; Martinez-Lozano, C.; Sanz, A.; Bravo, E., Determination of riboflavin, flavin mononucleotide and flavin adenine dinucleotide in biological tissues by capillary zone electrophoresis and laser-induced fluorescence detection. *Electrophoresis* **2001,** *22* (6), 1170-1174.

82. Britz-McKibbin, P.; Terabe, S., High-sensitivity analyses of metabolites introduction in biological samples by capillary electrophoresis using dynamic pH junction-sweeping. *Chemical Record* **2002,** *2* (6), 397-404.

83. Cataldi, T. R. I.; Nardiello, D.; De Benedetto, G. E.; Bufo, S. A., Optimizing separation conditions for riboflavin, flavin mononucleotide and flavin adenine dinucleotide in capillary zone electrophoresis with laser-induced fluorescence detection. *Journal of Chromatography A* **2002,** *968* (1-2), 229-239.

84. Cataldi, T. R. I.; Nardiello, D.; Scrano, L.; Scopa, A., Assay of riboflavin in sample wines by capillary zone electrophoresis and laser-induced fluorescence detection. *Journal of Agricultural and Food Chemistry* **2002,** *50* (23), 6643-6647.

85. Cataldi, T. R. I.; Nardiello, D.; Carrara, V.; Ciriello, R.; De Benedetto, G. E., Assessment of riboflavin and flavin content in common food samples by capillary electrophoresis with laser-induced fluorescence detection. *Food Chemistry* **2003,** *82* (2), 309-314.

86. Liu, B. F.; Hisamoto, H.; Terabe, S., Subsecond separation of cellular flavin coenzymes by microchip capillary electrophoresis with laser-induced fluorescence detection. *Journal of Chromatography A* **2003,** *1021* (1-2), 201-207.

87. Nardiello, D.; Bufo, S. A.; Cataldi, T. R. I., Riboflavin in dietary sources: Separation and detection by ce-lif. *Lc Gc Europe* **2003,** *16* (1), 30-35.

88. Hardwick, C. C.; Herivel, T. R.; Hernandez, S. C.; Ruane, P. H.; Goodrich, R. P., Separation, identification and quantification of riboflavin and its photoproducts in blood products using high-performance liquid chromatography with fluorescence detection: A method to support pathogen reduction technology. *Photochemistry and Photobiology* **2004,** *80* (3), 609-615.

89. Jia, L.; Tanaka, N.; Terabe, S., Capillary liquid chromatographic determination of cellular flavins. *Journal of Chromatography A* **2004,** *1053* (1-2), 71-78.

90. Qin, J. H.; Fung, Y. S.; Zhu, D. R.; Lin, B. C., Native fluorescence detection of flavin denvatives by microchip capillary electrophoresis with laser-induced fluorescence intensified charge-coupled device detection. *Journal of Chromatography A* **2004,** *1027* (1-2), 223-229.

91. Stocchi, V.; Cucchiarini, L.; Magnani, M.; Chiarantini, L.; Palma, P.; Crescentini, G., Simultaneous extraction and reverse-phase high-performance liquid-chromatographic determination of adenine and pyridine-nucleotides in human red blood-cells. *Analytical Biochemistry* **1985,** *146* (1), 118-124.

92. Northrop, D. B.; Duggleby, R. G., Preparation and storage of isotopically labeled reduced nicotinamide adenine-dinucleotide. *Analytical Biochemistry* **1987,** *165* (2), 362-364.

93. Noack, H.; Kunz, W. S.; Augustin, W., Evaluation of a procedure for the simultaneous determination of oxidized and reduced pyridine-nucleotides and adenylates in organic phenol extracts from mitochondria. *Analytical Biochemistry* **1992,** *202* (1), 162-165.

94. Klaidman, L. K.; Leung, A. C.; Adams, J. D., High-performance liquid-chromatography analysis of oxidized and reduced pyridine dinucleotides in specific brain-regions. *Analytical Biochemistry* **1995,** *228* (2), 312-317.

95. Meynial, I.; Paquet, V.; Combes, D., Simultaneous separation of nucleotides and nucleotide sugars using an ion-pair reversed-phase HPLC - application for assaying glycosyltransferase activity. *Analytical Chemistry* **1995,** *67* (9), 1627-1631.

96. Zhao, Z. X.; Wahl, J. H.; Udseth, H. R.; Hofstadler, S. A.; Fuciarelli, A. F.; Smith, R. D., Online capillary electrophoresis electrospray-ionization mass-spectrometry of nucleotides. *Electrophoresis* **1995,** *16* (3), 389-395.

97. Dillon, P. F.; Sears, P. R., Capillary electrophoretic measurement of tissue metabolites. *American Journal of Physiology-Cell Physiology* **1998,** *274* (3), C840-C845.

98. Wise, D. D.; Shear, J. B., Tracking variations in nicotinamide cofactors extracted from cultured cells using capillary electrophoresis with multiphoton excitation of fluorescence. *Analytical Biochemistry* **2004,** *326* (2), 225-233.

99. Ganzera, M.; Vrabl, P.; Worle, E.; Burgstaller, W.; Stuppner, H., Determination of adenine and pyridine nucleotides in glucose-limited chemostat cultures of penicillium simplicissimum by one-step ethanol extraction and ion-pairing liquid chromatography. *Analytical Biochemistry* **2006,** *359* (1), 132-140.

100. Sporty, J. L.; Kabir, M. M.; Turteltaub, K. W.; Ognibene, T.; Lin, S. J.; Bench, G., Single sample extraction protocol for the quantification of NAD and NADH redox states in saccharomyces cerevisiae. *Journal of Separation Science* **2008,** *31* (18), 3202-3211.

101. Xie, W. J.; Xu, A. S.; Yeung, E. S., Determination of NAD(+) and NADH in a single cell under hydrogen peroxide stress by capillary electrophoresis. *Analytical Chemistry* **2009,** *81* (3), 1280-1284.

102. Markham, K. A.; Sikorski, R. S.; Kohen, A., Purification, analysis, and preservation of reduced nicotinamide adenine dinucleotide 2 '-phosphate. *Analytical Biochemistry* **2003,** *322* (1), 26-32.

103. Markham, K. A.; Kohen, A., Analytical procedures for the preparation, isolation, analysis and preservation of reduced nicotinamides. *Current Analytical Chemistry* **2006,** *2* (4), 379-388.

104. Britz-McKibbin, P.; Markuszewski, M. J.; Iyanagi, T.; Matsuda, K.; Nishioka, T.; Terabe, S., Picomolar analysis of flavins in biological samples by dynamic pH junction-sweeping capillary electrophoresis with laser-induced fluorescence detection. *Analytical Biochemistry* **2003,** *313* (1), 89-96.

105. Markuszewski, M. J.; Britz-McKibbin, P.; Terabe, S.; Matsuda, K.; Nishioka, T., Determination of pyridine and adenine nucleotide metabolites in bacillus subtilis cell extract by sweeping borate complexation capillary electrophoresis. *Journal of Chromatography A* **2003,** *989* (2), 293-301.

106. Jia, L.; Liu, B. F.; Terabe, S.; Nishioka, T., Two-dimensional separation method for analysis of bacillus subtilis metabolites via hyphenation of micro-liquid chromatography and capillary electrophoresis. *Analytical Chemistry* **2004,** *76* (5), 1419-1428.

107. Jia, L.; Tanaka, N.; Terabe, S., Two-dimensional separation system of coupling capillary liquid chromatography to capillary electrophoresis for analysis of escherichia coli metabolites. *Electrophoresis* **2005,** *26* (18), 3468-3478.

108. Casey, T. M.; Dufall, K. G.; Arthur, P. G., An improved capillary electrophoresis method for measuring tissue metabolites associated with cellular energy state. *European Journal of Biochemistry* **1999,** *261* (3), 740-745.

109. Hustad, S.; Ueland, P. M.; Schneede, J., Quantification of riboflavin, flavin mononucleotide, and flavin adenine dinucleotide in human plasma by capillary electrophoresis and laser-induced fluorescence detection. *Clinical Chemistry* **1999,** *45* (6), 862-868.

110. Terabe, S.; Markuszewski, M. J.; Inoue, N.; Otsuka, K.; Nishioka, T., Capillary electrophoretic techniques toward the metabolome analysis. *Pure and Applied Chemistry* **2001,** *73* (10), 1563-1572.

111. Lakowicz, J. R., *Principles of fluorescence spectroscopy*. 3rd ed.; Springer US: **2006**.

112. Visser, A. J. W. G., Kinetics of stacking interactions in flavin adenine dinucleotide from time-resolved flavin fluorescence. *Photochemistry and Photobiology* **1984,** *40* (6), 703-706.

113. Weber, G., Fluorescence of riboflavin and flavin-adenine dinucleotide. *Biochemical Journal* **1950,** *47* (1), 114-121.

114. Leenders, R.; Kooijman, M.; van Hoek, A.; Veeger, C.; Visser, A. J., Flavin dynamics in reduced flavodoxins. A time-resolved polarized fluorescence study. *Eur J Biochem* **1993,** *211* (1-2), 37-45.

115. Koziol, J.; Donald, B. M. a. L. D. W., Fluorometric analyses of riboflavin and its coenzymes. In *Methods in enzymology*, Academic Press: **1971**; Vol. Volume 18, Part 2, pp 253-285.

116. Buchholz, A.; Hurlebaus, J.; Wandrey, C.; Takors, R., Metabolomics: Quantification of intracellular metabolite dynamics. *Biomolecular Engineering* **2002,** *19* (1), 5-15.

117. Kimball, E.; Rabinowitz, J. D., Identifying decomposition products in extracts of cellular metabolites. *Analytical Biochemistry* **2006,** *358* (2), 273-280.

118. Monton, M. R. N.; Soga, T., Metabolome analysis by capillary electrophoresis-mass spectrometry. *Journal of Chromatography A* **2007,** *1168* (1-2), 237-246.

119. Huck, C. W.; Bakry, R.; Bonn, G. K., Progress in capillary electrophoresis of biomarkers and metabolites between 2002 and 2005. *Electrophoresis* **2006,** *27* (1), 111-125.

120. Garcia-Perez, I.; Vallejo, M.; Garcia, A.; Legido-Quigley, C.; Barbas, C., Metabolic fingerprinting with capillary electrophoresis. *Journal of Chromatography A* **2008,** *1204* (2), 130-139.

121. Terabe, S., Metabolome analysis by capillary electrophoresis-mass spectrometry by M.R.N. Monton and T. Soga. *J Chromatogr A* **2007**.

122. Soga, T.; Ueno, Y.; Naraoka, H.; Ohashi, Y.; Tomita, M.; Nishioka, T., Simultaneous determination of anionic intermediates for bacillus subtilis metabolic pathways by capillary electrophoresis electrospray ionization mass spectrometry. *Analytical Chemistry* **2002,** *74* (10), 2233-2239.

123. Burton, R. M.; Kaplan, N. O., Reaction of reduced pyridine nucleotides with acid. *Archives of Biochemistry and Biophysics* **1963,** *101* (1), 150-&.

124. Chaykin, S., Nicotinamide coenzymes. *Annual Review of Biochemistry* **1967,** *36*, 149-170.

125. Chaykin, S.; King, L.; Watson, J. G., Reduction of DPN^+ and TPN^+ with sodium borohydride. *Biochimica et Biophysica Acta (BBA) - General Subjects* **1966,** *124* (1), 13-25.

126. Jeong, S. S.; Gready, J. E., A method of preparation and purification of (4r)-deuterated-reduced nicotinamide adenine-dinucleotide phosphate. *Analytical Biochemistry* **1994,** *221* (2), 273-277.

127. Lowry, O. H.; Rock, M. K.; Passonneau, J. V., Stability of pyridine nucleotides. *Journal of Biological Chemistry* **1961,** *236* (10), 2756-&.

128. Margolis, S. A.; Howell, B. F.; Schaffer, R., Purification and analysis of purity of NADH. *Clinical Chemistry* **1976,** *22* (8), 1322-1329.

129. Northrop, D. B.; Newton, C. J.; Faynor, S. M., Purification of reduced nicotinamide adenine-dinucleotide by ion-exchange and high-performance liquid-chromatography. *Methods in Enzymology* **1986,** *122*, 152-154.

130. Oppenhei.Nj; Kaplan, N. O., Structure of primary acid rearrangement product of reduced nicotinamide adenine-dinucleotide (NADH). *Biochemistry* **1974,** *13* (23), 4675-4685.

131. Wu, J. T.; Wu, L. H.; Knight, J. A., Stability of NADPH - effect of various factors on the kinetics of degradation. *Clinical Chemistry* **1986,** *32* (2), 314-319.

132. Alivisatos, S. G.; Ungar, F.; Abraham, G. J., Spontaneous reactions of 1,3-substituted 1,4-dihydropyridines with acids in water at neutrality. I. Kinetic analysis and mechanism of the reactions of dihydronicotinamide--adenine dinucleotide with orthophosphates. *Biochemistry* **1965,** *4* (12), 2616-30.

133. Gostkowski, M. L.; McDoniel, J. B.; Wei, J.; Curey, T. E.; Shear, J. B., Characterizing spectrally diverse biological chromophores using capillary electrophoresis with multiphoton-excited fluorescence. *Journal of the American Chemical Society* **1998,** *120* (1), 18-22.

134. Wise, D. D.; Shear, J. B., Quantitation of nicotinamide and serotonin derivatives and detection of flavins in neuronal extracts using capillary electrophoresis with multiphoton-excited fluorescence. *Journal of Chromatography A* **2006,** *1111* (2), 153-158.

135. Wise, D. D.; Shear, J. B., Circadian tracking of nicotinamide cofactor levels in an immortalized suprachiasmatic nucleus cell line. *Neuroscience* **2004,** *128* (2), 263-268.

136. Michaelis, L., Electric transport of ferments. (i) invertin. *Biochemische Zeitschrift* **1909,** *16*, 81.

137. Hjertén, S., Free zone electrophoresis. *Chromatographic Reviews* **1967,** *9* (2), 122-219.

138. Jorgenson, J. W.; Lukacs, K. D., Zone electrophoresis in open-tubular glass capillaries. *Analytical Chemistry* **1981,** *53* (8), 1298-1302.

139. Jorgenson, J. W.; Lukacs, K. D., Capillary zone electrophoresis. *Science* **1983,** *222* (4621), 266-72.

140. Mikkers, F. E. P.; Everaerts, F. M.; Verheggen, T. P. E. M., High-performance zone electrophoresis. *Journal of Chromatography* **1979,** *169*, 11-20.

141. Kraly, J.; Fazal, M. A.; Schoenherr, R. M.; Bonn, R.; Harwood, M. M.; Turner, E.; Jones, M.; Dovichi, N. J., Bioanalytical applications of capillary electrophoresis. *Analytical Chemistry* **2006,** *78* (12), 4097-4110.

142. Huang, W. H.; Ai, F.; Wang, Z. L.; Cheng, J. K., Recent advances in single-cell analysis using capillary electrophoresis and microfluidic devices. *Journal of Chromatography B-Analytical Technologies in the Biomedical and Life Sciences* **2008,** *866* (1-2), 104-122.

143. Kostal, V.; Arriaga, E. A., Recent advances in the analysis of biological particles by capillary electrophoresis. *Electrophoresis* **2008,** *29* (12), 2578-2586.

144. Kostal, V.; Katzenmeyer, J.; Arriaga, E. A., Capillary electrophoresis in bioanalysis. *Analytical Chemistry* **2008,** *80* (12), 4533-4550.

145. Landers, J. P., *Handbook of capillary electrophoresis*. CRC Press: Boca Raton, **1997**.

146. Camilleri, P., *Capillary electrophoresis : Theory and practice*. CRC Press: Boca Raton, Fla., **1998**.

147. Lacroix, M.; Poinsot, V.; Fournier, C.; Couderc, F., Laser-induced fluorescence detection schemes for the analysis of proteins and peptides using capillary electrophoresis. *Electrophoresis* **2005,** *26* (13), 2608-2621.

148. Dolnik, V., Capillary electrophoresis of proteins 2005-2007. *Electrophoresis* **2008,** *29* (1), 143-156.

149. Metzger, J.; Luppa, P. B.; Good, D. M.; Mischak, H., Adapting mass spectrometry-based platforms for clinical proteomics applications: The capillary electrophoresis coupled mass spectrometry paradigm. *Critical Reviews in Clinical Laboratory Sciences* **2009,** *46* (3), 129 - 152.

150. Ahmed, F. E., The role of capillary electrophoresis-mass spectrometry to proteome analysis and biomarker discovery. *Journal of Chromatography B* **2009,** *877* (22), 1963-1981.

151. Weissinger, E. M.; Hertenstein, B.; Mischak, H.; Ganser, A., Online coupling of capillary electrophoresis with mass spectrometry for the identification of biomarkers for clinical diagnosis. *Expert Review of Proteomics* **2005,** *2* (5), 639-647.

152. Bakry, R.; Huck, C. W.; Najam-ul-Haq, M.; Rainer, M.; Bonn, G. K., Recent advances in capillary electrophoresis for biomarker discovery. *Journal of Separation Science* **2007,** *30* (2), 192-201.

153. Mischak, H.; Coon, J. J.; Novak, J.; Weissinger, E. M.; Schanstra, J. P.; Dominiczak, A. F., Capillary electrophoresis-mass spectrometry as a powerful tool in biomarker discovery and clinical diagnosis: An update of recent developments. *Mass Spectrometry Reviews* **2009,** *28* (5), 703-724.

154. Nelson, A. R.; Allbritton, N. L.; Sims, C. E., Rapid sampling for single-cell analysis by capillary electrophoresis. In *Laser manipulation of cells and tissues*, **2007**; Vol. 82, pp 709-722.

155. Soga, T.; Heiger, D. N., Amino acid analysis by capillary electrophoresis electrospray ionization mass spectrometry. *Analytical Chemistry* **2000,** *72* (6), 1236-1241.

156. Soga, T.; Ohashi, Y.; Ueno, Y.; Naraoka, H.; Tomita, M.; Nishioka, T., Quantitative metabolome analysis using capillary electrophoresis mass spectrometry. *Journal of Proteome Research* **2003,** *2* (5), 488-494.

157. Min S. Chang, Q. J. J. Z. T. A. E.-S., Historical review of sample preparation for chromatographic bioanalysis: Pros and cons. *Drug Development Research* **2007,** *68* (3), 107-133.

158. Solis, A.; Rex, M.; Campiglia, A. D.; Sojo, P., Accelerated multiple-pass moving average: A novel algorithm for baseline estimation in ce and its application to baseline correction on real-time bases. *Electrophoresis* **2007,** *28* (8), 1181-1188.

159. Szymanska, E.; Markuszewski, M. J.; Capron, X.; van Nederkassel, A. M.; Heyden, Y. V.; Markuszewski, M.; Krajka, K.; Kaliszan, R., Increasing conclusiveness of metabonomic studies by cheminformatic preprocessing of capillary electrophoretic data on urinary nucleoside profiles. *Journal of Pharmaceutical and Biomedical Analysis* **2007,** *43* (2), 413-420.

160. Vallejo, M.; Angulo, S.; García-Martínez, D.; García, A.; Barbas, C., New perspective of diabetes response to an antioxidant treatment through metabolic fingerprinting of urine by capillary electrophoresis. *Journal of Chromatography A* **2008,** *1187* (1-2), 267-274.

161. Aranas, A. T.; Guidote, A. M.; Quirino, J. P., Sweeping and new on-line sample preconcentration techniques in capillary electrophoresis. *Analytical and Bioanalytical Chemistry* **2009,** *394* (1), 175-185.

162. Britz-McKibbin, P.; Terabe, S., On-line preconcentration strategies for trace analysis of metabolites by capillary electrophoresis. *Journal of Chromatography A* **2003,** *1000* (1-2), 917-934.

163. Kartsova, L. A.; Bessonova, E. A., Preconcentration techniques in capillary electrophoresis. *Journal of Analytical Chemistry* **2009,** *64* (4), 326-337.

164. Simpson, S. L.; Quirino, J. P.; Terabe, S., On-line sample preconcentration in capillary electrophoresis fundamentals and applications. *Journal of Chromatography A* **2008,** *1184* (1-2), 504-541.

165. Quirino, J. P.; Terabe, S., Exceeding 5000-fold concentration of dilute analytes in micellar electrokinetic chromatography. *Science* **1998,** *282* (5388), 465-468.

166. Edwards, J. L.; Chisolm, C. N.; Shackman, J. G.; Kennedy, R. T., Negative mode sheathless capillary electrophoresis electrospray ionization-mass spectrometry for metabolite analysis of prokaryotes. *Journal of Chromatography A* **2006,** *1106* (1-2), 80-88.

167. Tanaka, N.; Takahashi, H.; Kitano, H.; Matsuoka, M.; Akao, S.; Uchimiya, H.; Komatsu, S., Proteome approach to characterize the methylmalonate-semialdehyde dehydrogenase that is regulated by gibberellin. *Journal of Proteome Research* **2005,** *4* (5), 1575-1582.

168. Power, P. P.; Woods, W. G., The chemistry of boron and its speciation in plants. *Plant and Soil* **1997,** *193* (1-2), 1-13.

169. ATCC Product description of cho-k1. http://www.atcc.org/ATCCAdvancedCatalogSearch/ProductDetails/tabid/452/Default.aspx?ATCCNum=CCL-61&Template=cellBiology (accessed 09/18/2009).

170. ATCC Product description of ht-29. http://www.atcc.org/ATCCAdvancedCatalogSearch/ProductDetails/tabid/452/Default.aspx?ATCCNum=HTB-38&Template=cellBiology (accessed 09/18/2009).

171. ATCC Product description of fhc. http://www.atcc.org/ATCCAdvancedCatalogSearch/ProductDetails/tabid/452/Default.aspx?ATCCNum=CRL-1831&Template=cellBiology (accessed 09/18/2009).

172. Health Protection Office University of Iowa, Biological safety manual. Iowa City, 2006.

173. Environmental Health & Safety University of Iowa, Biological safety manual. Iowa City, 2009.

174. Freshney, R. I., *Culture of animal cells : A manual of basic technique*. Wiley-Liss: Hoboken, N.J., **2005**.

175. Prasad Maharjan, R.; Ferenci, T., Global metabolite analysis: The influence of extraction methodology on metabolome profiles of escherichia coli. *Analytical Biochemistry* **2003,** *313* (1), 145-154.

176. Pecheur, I.; Peyruchaud, O.; Serre, C. M.; Guglielmi, J.; Voland, C.; Bourre, F.; Margue, C.; Cohen-Solal, M.; Buffet, A.; Kieffer, N.; Clezardin, P., Integrin alpha v beta 3 expression confers on tumor cells a greater propensity to metastasize to bone. *Faseb Journal* **2002,** *16* (10), 1266-1268.

177. Orczyk, J.; Morre, D.; Morre, D. J., Periodic fluctuations in oxygen consumption comparing hela (cancer) and cho (non-cancer) cells and response to external NAD(P)(+)/NAD(P)H. *Molecular and Cellular Biochemistry* **2005,** *273* (1-2), 161-167.

178. Kochanowski, N.; Blanchard, F.; Cacan, R.; Chirat, F.; Guedon, E.; Marc, A.; Goergen, J. L., Intracellular nucleotide and nucleotide sugar contents of cultured cho cells determined by a fast, sensitive, and high-resolution ion-pair RP-HPLC. *Analytical Biochemistry* **2006,** *348* (2), 243-251.

179. Feng, H. T.; Wong, N.; Wee, S.; Lee, M. M., Simultaneous determination of 19 intracellular nucleotides and nucleotide sugars in chinese hamster ovary cells by capillary electrophoresis. *Journal of Chromatography B-Analytical Technologies in the Biomedical and Life Sciences* **2008,** *870* (1), 131-134.

180. Li, Y.; de Silva, P. G.; Xi, L.; van Winkle, A.; Lin, J. J.; Ahmed, S.; Geng, M. L., Separation of flavins and nicotinamide cofactors in chinese hamster ovary cells by capillary electrophoresis. *Biomed Chromatogr* **2008,** *22* (12), 1374-84.

181. Britz-McKibbin, P.; Otsuka, K.; Terabe, S., On-line focusing of flavin derivatives using dynamic pH junction-sweeping capillary electrophoresis with laser-induced fluorescence detection. *Analytical Chemistry* **2002,** *74* (15), 3736-3743.

182. Giacomelli, C. E.; Vermeer, A. W. P.; Norde, W., Micellization and adsorption characteristics of CHAPS. *Langmuir* **2000,** *16* (11), 4853-4858.

183. Krylov, S. N.; Arriaga, E. A.; Chan, N. W. C.; Dovichi, N. J.; Palcic, M. M., Metabolic cytometry: Monitoring oligosaccharide biosynthesis in single cells by capillary electrophoresis. *Analytical Biochemistry* **2000,** *283* (2), 133-135.

184. Noda, I. In *Progress in two-dimensional (2d) correlation spectroscopy*, The Third International Symposium on Two-Dimensional Correlation Spectroscopy (2DCOS-3), Delavan, Wisconsin, USA, Nov 6; Elsevier Science Bv: Delavan, Wisconsin, USA, **2005**; pp 2-15.

185. Noda, I.; Ozaki, Y., *Two-dimensional correlation spectroscopy applications in vibrational and optical spectroscopy*. John Wiley & Sons: Chichester, West Sussex, England; Hoboken, NJ, **2004**.

186. Frasinski, L. J.; Codling, K.; Hatherly, P. A., Covariance mapping: A correlation method applied to multiphoton multiple ionization. *Science* **1989,** *246* (4933), 1029-1031.

187. Barton, F. E.; Himmelsbach, D. S.; Duckworth, J. H.; Smith, M. J., Two-dimensional vibration spectroscopy: Correlation of mid- and near-infrared regions. *Applied Spectroscopy* **1992,** *46*, 420-429.

188. Sasic, S.; Ozaki, Y., Statistical two-dimensional correlation spectroscopy: Its theory and applications to sets of vibrational spectra. *Analytical Chemistry* **2001,** *73* (10), 2294-2301.

189. Sasic, S.; Muszynski, A.; Ozaki, Y., A new possibility of the generalized two-dimensional correlation spectroscopy. 1. Sample−sample correlation spectroscopy. *The Journal of Physical Chemistry A* **2000,** *104* (27), 6380-6387.

190. Lefèvre, T.; Arseneault, K.; Pézolet, M., Study of protein aggregation using two-dimensional correlation infrared spectroscopy and spectral simulations. *Biopolymers* **2004,** *73* (6), 705-715.

191. Pierce, K. M.; Wright, B. W.; Synovec, R. E., Unsupervised parameter optimization for automated retention time alignment of severely shifted gas chromatographic data using the piecewise alignment algorithm. *Journal of Chromatography A* **2007,** *1141* (1), 106-116.

192. Tu, B. P.; Mohler, R. E.; Liu, J. C.; Dombek, K. M.; Young, E. T.; Synovec, R. E.; McKnight, S. L., Cyclic changes in metabolic state during the life of a yeast cell. *Proceedings of the National Academy of Sciences* **2007,** *104* (43), 16886-16891.

193. Wolfbeis, O. S., Fluorescence methods and applications: Spectroscopy, imaging, and probes. *Ann N Y Acad Sci* **2008,** *1130* (Fluorescence Methods and Applications: Spectroscopy, Imaging, and Probes).

194. Wang, G. F.; Geng, L., Statistical and generalized two-dimensional correlation spectroscopy of multiple ionization states. Fluorescence of neurotransmitter serotonin. *Analytical Chemistry* **2005,** *77* (1), 20-29.

195. He, Y.; Wang, G. F.; Cox, J.; Geng, L., Two-dimensional fluorescence correlation spectroscopy with modulated excitation. *Analytical Chemistry* **2001,** *73* (10), 2302-2309.

196. Geng, L.; Cox, J. M.; He, Y., Dynamic two-dimensional fluorescence correlation spectroscopy. Generalized correlation and experimental factors. *Analyst* **2001,** *126* (8), 1229-1239.

197. Wang, G. Fluorescence studies of apomyoglobin folding and two-dimensional fluorescence correlation spectroscopy. The University of Iowa, Iowa City, **2004**.

198. Wang, G. F.; Geng, L., Two-dimensional fluorescence correlation in capillary electrophoresis for peak resolution and species identification. *Analytical Chemistry* **2000,** *72* (19), 4531-4542.

199. Noda, I., Generalized 2-dimensional correlation method applicable to infrared, raman, and other types of spectroscopy. *Applied Spectroscopy* **1993,** *47*, 1329-1336.

200. Noda, I., Determination of two-dimensional correlation spectra using the hilbert transform. *Applied Spectroscopy* **2000,** *54* (7), 994-999.

201. Noda, I., Two-dimensional correlation analysis of unevenly spaced spectral data. *Applied Spectroscopy* **2003,** *57* (8), 1049-1051.